NUMERICAL METHODS FOR UNSTEADY FILM COOLING IN GAS TURBINE



Muting Hao

Rolls-Rolls Gas Turbine Aerodynamics UTC

Oxford Thermofluids Institute

University of Oxford

A thesis submitted for the degree of

Doctor of Philosophy

Michaelmas 2022





Copyright ©2023 University of Oxford
©2023 Rolls Royce UTC

First edition, December 6, 2022

"Courage is not the absence of fear; it is the making of action in spite of fear, the moving out against the resistance engendered by fear into the unknown and into the future."

—— *The road less traveled, M. Scott Peck*

"Dare and the world always yields; or if it beats you sometimes, dare it again and it will succumb."

— *William Thackeray*

Acknowledgements

This thesis marks the end of a long and memorable journey of studying at The University of Oxford when it is a great opportunity to express my sincere appreciation to all those who offered me invaluable support.

Words cannot express my heartfelt gratitude to my respectable supervisor Professor Luca di Mare for his consistent support and illuminating instruction throughout my DPhil studies. I want to thank him for his patience, help, and the academic profession. The completion of this research wouldn't have been possible without the sheer support of knowledge and expertise from my supervisor. He offered me excellent chances of working on a valuable research project on the gas turbine which I am super fond of, and dedicated time to providing me helpful training in coding, useful advice in writing research papers, and constructive feedback to help me work better. It is like still yesterday when I first time stepped into his office, where I can never forget the neat white shirt and black suit, the powerful hand-shaking greeting, and the energetic smiling face. This continuous energetic smile together with his passion for research, concern, and ever-cheery disposition have been encouraging me to keep progressing every day through my research, to fight for the project meeting from early morning under the moon, to get over the pandemic, to gain joy from the writing process, and to fight for Orion light at the bottom of my life. Working with Professor Luca di Mare was definitely one of the most cheerful experiences in my life!

Furthermore, I want to acknowledge Rolls Royce plc. for funding my research project. I want to show appreciation to Dr. Goenaga Frederic, Dr. Adami Paolo, Dr. Romero Eduardo who provided me with the most valuable asset of time devoted to this project. Many thanks to Dr. Haidong Li and Dr. Cristian Orozco Pineiro who contribute time on providing useful comments on my research papers. The participation of these specialists in Rolls Royce in my research including listening to my reports and providing helpful suggestions to me in the constant telephone meeting or in person made my data presentation not only successful but also high-efficient and interesting, which reconfirmed my passion throughout the research.

I also feel lucky to meet a few world great scientists during my Dphil. I appreciate the time when I talked to Dr. John Adamczyk from NASA as

well as when I showed my research to him. His enthusiasm to science and great ability of doing mathematics derivation in CFD gives me remarkable inspiration and let me set a role model.

I further want to present a huge amount of gratitude to my office fellows who helped me with their knowledge to formulate my research questions. I would like to offer my special thanks to Dr. Feng Wang for sharing his expertise on CFD and work experience, and for discussing research questions with me, which gives me inspiration. And my great thanks to Dr. Ahmad Nawab, Dr. Max Rife, Dr. Mario, Dr. Yuewen Jiang, Dr Ioan Hadade, Joshua Hope-Collins for helping me with many technical aspects at the start of my doctoral project. Many thanks to both my previous and current colleagues for the lovely atmosphere provided by them during my lab time.

I must also thank my examiners, Prof. David Gillespie and Dr. Salvador Navarro-Martinez, who reviewed my thesis very carefully, went through every detail of the text and pictures, and provided useful minor correction comments. With their suggestions, the thesis has been improved to be more accurate.

Finally, I want to present my dearest gratitude to my parents who always give me unconditional support, being my emotional support, and letting me grow up with the best resources they can offer. When fighting on their side, they teach me how to face every hurdle with intelligence and confidence.

All these words recorded here are an extract of work with successful results based on failures hundreds of times. These experiences enabled my mentality to be torn, dismantled, rebuilt, and improved. My mind has become tougher when having the chance to touch the boundary of knowledge in this world. This allows me to imagine the unknown dimension of both the physical and philosophical worlds from a different perspective. Now when I look back and forward, my mind passes through the memory palace as if all the time periods are fixed. Every step I have passed is shown in front of me, and there is light further away which should be the place I carry on targetting along this path. Nice memories during DPhil will be treasured in my mind as a fortune of my whole life. I will carry this precious experience with me and keep going.

"Those who sow with tears will reap with joy".

Abstract

Large eddy simulation (LES) of film cooling flows are focused on, not only because the complexity of film cooling flows brings challenges to accurate numerical simulations, but also because to improve the RANS model which is the main source of inaccuracies of RANS, a systematic set of Reynolds stress and turbulent heat flux data are needed. Achieving high accuracy of prediction for the film cooling flows mandates the exploitation of all the available elements of numerical modelling and computation methods. These methods as a whole should be able to result in reliable budgets of Reynolds-stress tensor and heat flux tensor in scale-resolving simulations. The LES framework for this flowfield is designed by including key ingredients of accuracy – i) a meshing system (automatic hexahedral mesh generator) resolving small scales and representing complex geometries, ii)a high-resolution scheme (a thrid-order limiter), handling unwanted oscillations while retaining high order accuracy; iii)an efficient inflow generation (synthetic generator based on eigen-decoposition from realistic approximations of the covariance tensor) minimizing the required inlet development length. Results reveal that the set of modelling methodologies is valid for calculating film-cooling performance in terms of velocity, turbulence, heat flux profiles, and discharge coefficient for fan-shaped and cylindrical holes. The energy-carrying turbulence structures in and near the cooling holes are illustrated from a standpoint of turbulent Reynolds stresses. The mechanisms by which energy is extracted from the mean flow and distributed among the normal Reynolds stresses are highlighted. A qualitative summary of the structure of the film in terms of jet edge, potential core, the lower edge of the jet, and confined region is proposed on the basis of their positions and relative magnitudes of the mean temperature, turbulent heat fluxes, and temperature variance in each region. A scaling law for the outer part of a three-dimensional wall jet has been proposed. Similarity patterns of velocity, turbulent heat fluxes, non-dimensional temperature, Reynolds stresses, and budget profiles are discussed. Far downstream of the cooling films, the Reynolds stress budgets near the wall present similarities with the Reynolds stress budgets in a boundary layer, while the Reynolds stress budgets further away from the

wall resemble budgets in a free-shear flow. Results show that the dynamic balance of all budget terms is significantly influenced by the cooling hole shape, while each budget term may scale with the velocity defect, temperature deficit, and the normalized streamwise distance to the power of an exponent dependent on the hole shape.

Contents

Contents **ix**

1 Introduction **1**
1.1 Motivation 1
1.2 Thesis Contributions 3
1.3 Thesis Outline 5

2 Background **9**
2.1 Trends in film cooling of gas turbine 9
2.1.1 The importance of turbine cooling 9
2.1.2 Historical development of cooling systems 10
2.1.3 Modern external cooling 14
2.2 Numerical and experimental studies of film cooling 17
2.2.1 Numerical methods during 1960-1990 17
2.2.2 Shaped film cooling holes 20
2.2.3 Experiment of film cooling flowfield 21
2.2.4 Numerical methods for film cooling flowfield from the late 90s 24
2.2.5 Modern LES of film cooling 27
2.3 Targets and challenges for film cooling 28
2.3.1 The thermodynamic penalty for film cooling 28
2.3.2 Adiabatic film effectiveness 30

2.3.3 Ideal cooling system designing 30
2.4 Current design barrier 31
2.5 Implications for thermodynamical design 32

3 High Resolution Numerical Scheme 33
3.1 Preface 33
3.2 Related Work 34
3.3 Methodology 37
3.3.1 Conservation law 37
3.3.2 Finite volume 38
3.3.3 Spatial reconstruction 40
3.3.4 Approximate Riemann Solvers-Roe's 49
3.3.5 Time marching scheme 52
3.4 Results and Discussions 53
3.4.1 Preliminary tests on WENO scheme 53
3.4.2 Comparison with limiter methods 64

4 Efficient generation of high-quality hex multiblock grids 69
4.1 Preface 69
4.2 Technical Paper 1 73
4.3 Interpolation of the control function 101
4.3.1 Quadratic interpolation 104
4.3.2 Linear interpolation 105
4.3.3 Exponential interpolation 107
4.3.4 Results 108

5 Generation of correlated fields by Synthetic inflow generator 113
5.1 Preface 113
5.2 Technical Paper 2 115

6 Large eddy simulation of film cooling holes 167

6.1 Technical Paper 3 170
6.2 Technical Paper 4 194

7 Reynolds stress budgets and turbulent heat flux budgets in film cooling 239
7.1 Preface 239
7.2 Technical Paper 5 242
7.3 Technical Paper 6 278

8 Conclusions 329
8.1 Reviews of Major Findings 329
8.2 Future Work 335

9 Appendix 337

References 339
*



1 Introduction

1.1 | Motivation

Film cooling is an effective technique to achieve reliable operation at high temperatures in gas turbine engines. In its simplest form, film cooling is performed by discharging cold air through a number of orifices, usually referred to as cooling holes. Whilst essential, turbine cooling comes at a thermodynamic price because of the work needed to compress the cooling air and because of the reduction in free energy of the turbine stream. Therefore, the main challenge in designing cooling systems is to use as little air as possible for a given reduction in wall temperature. This requires high accuracy of numerical prediction and resolution for small-scale features of flow in cooling geometries. However, the complexity of film cooling flows brings great challenges to accurate numerical simulations. Reynolds-Averaged Navier-Stokes (RANS) turbulence models commonly used nowadays show poor agreement with experimental data in terms of both detailed distributions and average quantities.

This is mainly because these numerical models do not predict the Reynolds stress tensor and Reynolds flux vector correctly. Consequently, achieving high accuracy of prediction for the film cooling flows mandates the exploitation of all the available elements of numerical modeling and computation methods. These methods as a whole should be able to result in reliable budgets of Reynolds-stress tensor and heat flux tensor in scale-resolving simulations.

The research presented in this thesis is a fundamental study funded by Rolls-Royce plc. The target investigated is the flowfield in the vicinity of film-cooling holes. The overall project involves developing a whole Computational Fluid Dynamics (CFD) package for numerical modeling as well as computation in the Large Eddy Simulation(LES) framework that can be used on this flowfield.

Scale resolving simulations of cooling devices, however, impose stringent requirements on a major ingredient – 1)accurate and efficient methods for flow. These include requirements i) on the meshing system, because of the contrasting needs of resolving small scales and representing complex geometries or even representing domains of a large number of devices; ii)on the high-resolution scheme, because of the unwanted appearance of oscillations in the numerical solutions of complex flow interactions while using the second order or higher order schemes which are needed for high order accuracy on smooth solutions; iii)on an efficient inflow generator, because, due to which, a minimum inlet development length for the computational domain of complex film cooling cases is feasible and can considerably save computational time and resources; iv) on the parallelism, making use of modern processors that can lead to speed-ups. Another major ingredient is 2) an efficient conjugate heat transfer method. The topics 1.i, 1.ii, 1.iii are the main focus of this Dphil

thesis.

The main attention of this research is devoted to designing a CFD code that consists of an automatic mesh generator handling multiblock topologies for complex film-cooled blade geometries, a synthetic turbulence inflow generator, and options for finite volume third-order schemes for scale-resolving simulations of film cooling flow predictions in gas turbine engines. Additionally, an efficient conjugate heat transfer method is also implemented and tested on channels as a early step before applied to the film cooling. It is finally removed from this thesis as a compromise of the page size limit suggested from the university.

1.2 | Thesis Contributions

This thesis makes the following contributions:

(i) Demonstrates the importance of making good use of the nonlinear conservation equations by introducing of limiters and developing high-resolution, monotone schemes without numerical wiggles.

(ii) Demonstrates the utility of using an automatic mesh generation system based on templates for turbine cooling geometries and the merits of elliptic smoothing on the generated multi-block hexahedral mesh. The proposed system can be utilized either as a standalone tool or as a postprocessing tool to decorate the existing hexahedral grid with cooling features. The system is implemented as a portable library of C++ classes.

(iii) Demonstrates the benefit of modal decomposition in the spatial correlation, the benefit of digital filters in terms of maintaining spatial correlation. These

techniques facilitate the establishment of an instantaneous inlet flow field by a linear combination of the modes via uncorrelated random weights with unit variance.

(iv) Demonstrates the feasibility of generating modes in a computationally inexpensive processing step, that is, a preliminary RANS simulation with an explicit algebraic Reynolds stress model (EASMR) closure, as well as the efficiency during matching a realistic set of two-point statistics with minimal input.

(v) Demonstrates a credible and most cost-effective LES methodology, including a high-resolution numerical scheme, an efficient multiblock hexahedra mesh generation, a synthetic turbulence inflow generator, and other numerical schemes, which can allow for accurate prediction of mean quantity profiles, turbulence intensity profiles and discharge characteristics.

(vi) Illustrates the energy-carrying turbulence structures in and near the cooling holes from a standpoint of turbulent Reynolds stresses.

(vii) Presents Reynolds stresses and turbulent heat fluxes based on different blowing ratios and two types of cooling holes in a parametric study which has been the first time for film cooling flows to the author's knowledge

(viii) Proposed a theory of scaling law for the three-dimensional jet of cooling films, with self-similar parameters including velocity defect, temperature deficit, and boundary layer thickness successfully collapsing mean profiles and turbulence profiles for the outer part of three-dimensional wall jets in the high-Reynolds-number limit are obtained.

(ix) Demonstrates similarity patterns of velocity profiles, non-dimensional temperature profiles, Reynolds stresses profiles, turbulent heat flux profiles, budgets of Reynolds stresses, and budgets of turbulent heat flux.

(x) Demonstrates the importance of an understanding of unsteady turbulent flow physics and heat transfer mechanism in cooling film flows. The cooling effect induced by the cooling hole is shown. The prediction can provide guidance for future cooling device design.

(xi) Demonstrates the advantage of a high-resolution LES code in capturing budgets of Reynolds stress and turbulence heat flux, and the importance of evaluating these budgets in the film cooling flows. The LES data can be used as a benchmark for improving RANS turbulence models in simulating unsteady flows.

1.3 | Thesis Outline

The thesis is a hybrid thesis made up of 8 chapters. 6 journal papers - published or in review - are included in the thesis along with 1 conference paper.

Chapter 2 gives the general background of cooling technologies, fundamentals of the gas turbine cooling system, and current challenges for cooling method designs in aircraft gas turbines are introduced. A review of previous work on external film cooling is presented with an emphasis on numerical studies, CFD methods, and Reynolds stress budget analysis. Achievements in understanding flow physics and thermodynamics are shown.

Chapter 3 introduces the high-resolution numerical schemes adopted. The chosen scheme is capable of obtaining minimal dissipation at least on smooth regions while capturing strong discontinuities without oscillations. Comparison is made to fundamental Basic experiments with known uncertainty to select the most suitable methods. The method is tested on a 2D Euler equation. Two ways to achieve high order accuracy, the TVD limiter and the adaptive stencil method (WENO) are compared.

Chapter 4 presents a novel method that allows high-quality multiblock grids to be generated for configurations with large numbers of cooling holes. The method combines the usual advantages of multiblock grids - accuracy of the solution and efficient execution - with flexibility and robustness normally associated with unstructured grids, whilst avoiding difficulties related to non-conformal interfaces or block placement seen in earlier contributions. ***One conference paper on this meshing method is included.***

Chapter 5 presents a novel synthetic inflow generator capable of producing a random field matching a realistic set of two-point statistics with minimal input. The method is based on two main elements. The first element is a procedure to infer realistic two-point covariance tensors from readily available data. The second element is an efficient eigen-decomposition step of the two-point correlation tensor which determines a set of modes. The proposed method is shown to produce a realistic turbulent channel flow and boundary layer which contains statistics that are in good agreement with results from DNS. ***One published journal paper on the theory of the proposed inflow generator is included.***

Chapter 6 presents LES results of film cooling. ***Two journal papers are***

included, presenting the two components of this chapter. For better analyzing the turbulence data, a theory has been first proposed explaining the power laws ruling the decay of velocity defect and the growth of the wall jet generated by fan-shaped films and cylindrical films. The power laws describing the streamwise decay of the Reynolds stresses are shown. An upper bound to the power law describing the downstream evolution of the wall shear stress is also indicated. Estimates for the entrainment rate and power laws describing the wall-normal and transversal velocity scales are obtained. The derivations are based on a small-perturbation expansion for the strength of velocity and density defects.

The second part of **Chapter 6** examined the credibility of the current LES for fan-shaped and cylindrical films in terms of the discharge characteristics, velocity, and turbulence intensity profiles of two types of films by comparing them with published measured data on the same flow configurations. The energy-carrying turbulence structures in and near the cooling holes have been illustrated from a standpoint of turbulent Reynolds stresses. Reynolds stresses and turbulent heat fluxes have been compared for different blowing ratios and two types of cooling holes in the parametric study. Similarity patterns of velocity profiles, non-dimensional temperature profiles, and Reynolds stresses profiles are discussed.

Chapter 7 presents the budgets in the transport equations of Reynolds stresses and turbulence heat flux in film cooling cases captured using data obtained from LES shown in 6. ***Two journal papers on budgets are included.*** The analysis of these budget terms is shown for the first time in the open literature to the author's knowledge. The similarity laws for budgets of the Reynolds stresses and turbulent heat fluxes are discovered. The exponents in the scaling laws are also

studied in terms of their dependence on the film configuration, on the blowing ratio, or on the flow regime. A qualitative criterion has been proposed to identify the regions constituting a cylindrical film wall jet based on the relative magnitude of non-dimensional temperature, turbulent heat flux, and temperature fluctuations. Individual terms in the heat flux budgets have been analyzed and the main physical processes contributing to those budgets have been identified.

Chapter 8 draws conclusions about the thesis and gives an outlook of future research focus based on this work.



2

Background

2.1 | Trends in film cooling of gas turbine

2.1.1 | The importance of turbine cooling

Cooling technologies have become key to improving gas turbines engine performance in aircraft propulsion, power generation and industrial applications alike.

Thermodynamic considerations encourage designers to use higher and higher turbine inlet gas temperatures, to improve both efficiency and power output. As an example, the specific work of a typical aircraft engine can be doubled by increasing inlet temperature from today's 1700°C to 2000°C [41] - assuming the same amount of cooling air is used. Over the years, performance considerations have led to the adoption of turbine entry temperatures well above the melting point of the materials used for the turbine nozzles, rotor blades and discs. Hence, safe operation for any length of time can only be achieved by cooling blades and end-walls using air at

suitably lower temperature bled from the compression system. Even if a cooling system is adopted, the life of hot components in gas turbines is determined by the temperatures they are exposed to. As an example, the life of blade can be increased by a factor of two if blade temperature is reduced by 25°C [13].

Whilst essential, turbine cooling does come at a thermodynamic price because the cooling air still needs to be compressed and also because the injection of air at lower total enthalpy reduces the free energy of the turbine flow, thereby reducing its ability to do mechanical work. Therefore, the main challenge in designing cooling systems is to use as little air as possible for a given reduction in wall temperature.

It is therefore critical to optimise the cooling method for gas turbine engine designs, and better understanding of fluid mechanism should be available for any given turbine operation condition and geometry.

2.1.2 | Historical development of cooling systems

Early turbojet engines (e.g. the BMW003 which is an early axial turbojet engine) featured uncooled turbine blades which limited the turbine entry temperature to a value below the melting point of the brass used for the turbine blades and nozzles. Component life was limited to few missions. The effect of temperature on disc life was acknowledged very early and the Rolls-Royce Nene already featured a small impeller to supply cooling air to the disc. As more and more ambitious aircrafts and power-plants were planned, it was recognised that metallurgy alone could not allow the adoption of suitably high turbine entry temperatures and that the hot

parts needed to be shielded from the main gas stream. The first air-cooled turbine blading was first done on the Conway engine.

In the 1960s[42] airfoils were cooled on the inside by high-pressure bleed air from the compressor. This was the earliest application of convective cooling. In the 1970s film cooling started being applied. Film cooling requires the creation of orifices (cooling holes) on the surfaces to be cooled. The cooling action is performed by the air ejected from the internal cooling passages into small holes on the blade/vane surfaces. Surface with holes rather than porous surfaces or slots were chosen to maintain the rigidity of structure in case of large stresses by blades and vanes.

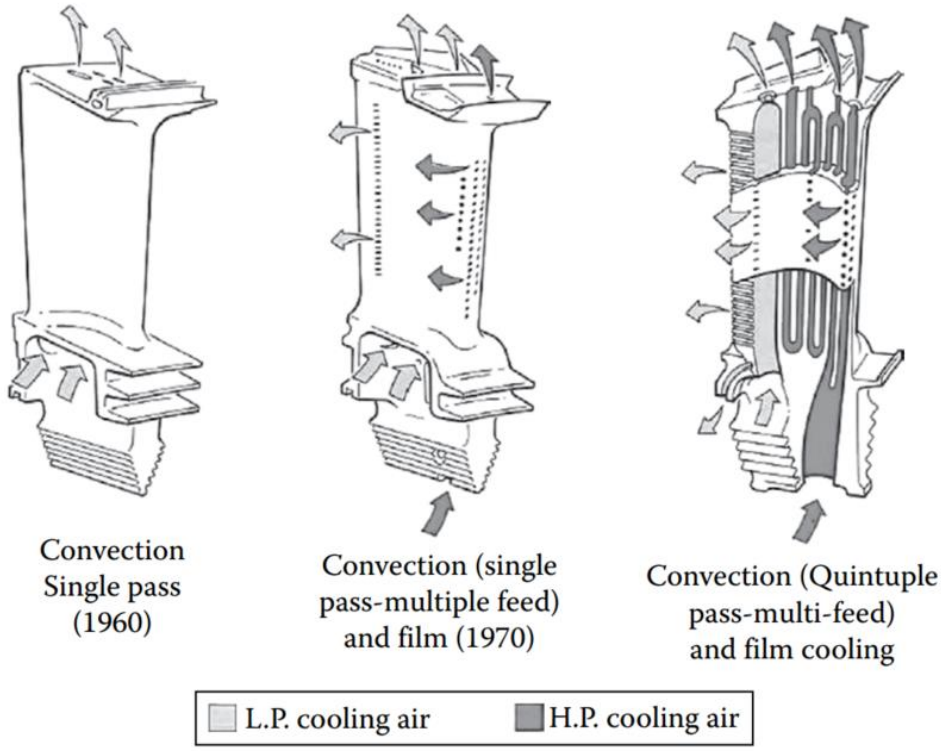


Figure 2.1: General development of cooling technologies, from Rolls-Royce plc, Copyright Rolls-Royce plc 2007[23]

There are a number of publications presenting state-of art designs of gas turbine

cooling systems and discussing associated heat transfer issues since 1970s[11, 31, 39]. The general development of cooling technologies is shown in Fig.2.1.

Along the development history of cooling designs, heat is removed from the airfoil by both internal cooling and external cooling. The details in the design of cooling systems is hardly disclosed because of confidentiality, but the general cooling method is similar, including external cooling as shown in Fig.2.2(left) and internal cooling as shown in Fig.2.2(right) for a cutaway view.

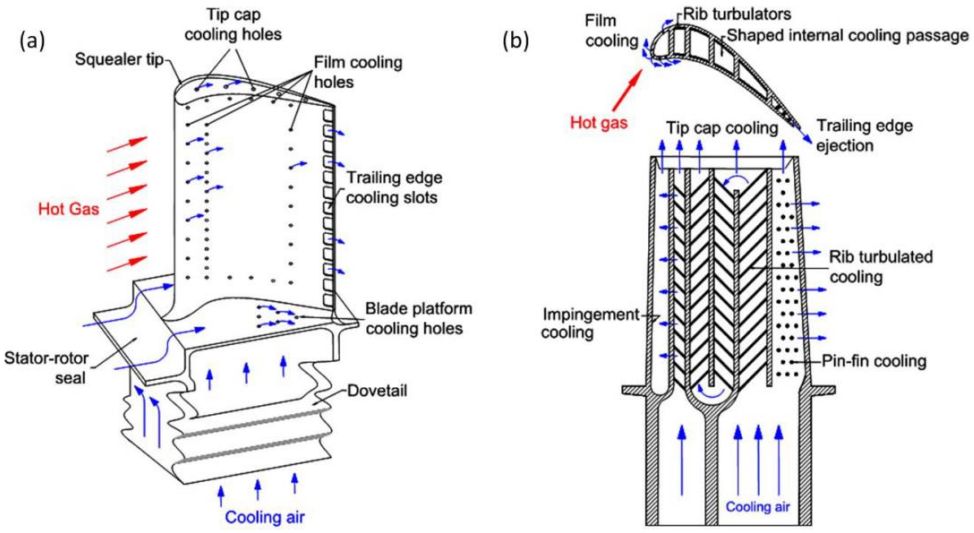


Figure 2.2: Gas turbine blade cooling schematic: external(left), internal(right)[41]

Internal and external cooling devices may be combined in a single blade. In these cases the internal cooling system also acts as supply for the external cooling. A state-of-art gas turbine with a combination of different cooling technologies is presented in Fig.2.3. In this case, both low-pressure and high-pressure compressors deliver the cool air for the cooling purpose[29].

In detail, Fig. 2.4[22] shows the cooling strategies for a nozzle vane and a blade, each of which combines both internal and external cooling. In the nozzle vane,

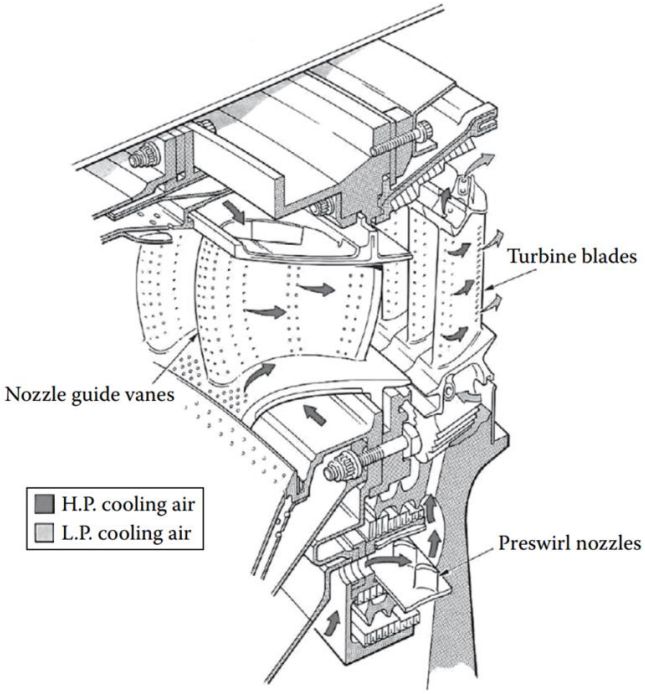


Figure 2.3: Cooling for a high-pressure turbine, from Rolls-Royce plc, Copyright Rolls-Royce plc 2007[23]

coolant air is routed through two internal channels for invective cooling. Cooling holes are set on the pressure side of both the two channels and the leading edge for film cooling, while impinging cooling is designed on the inner suction surface of the second channel only. After passing through the two internal channels, the coolant finally leaves through trailing pin-fin cooling arrays and from slots on the trailing cut-back pressure side wall. For the rotor blade, there are three inside channels with the middle serpentine channel guiding coolant air three times. Besides film cooling, inside suction and pressure surfaces are roughened with ribs for rib turbulated cooling.

In summary, internal cooling includes four conventional methods: convection[25, 40, 67], impingement[29, 95], rib turbulated[1, 94] and pin-fins cooling[105], which

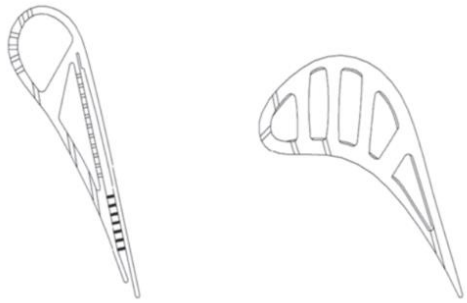


Figure 2.4: Cooling strategy sketch: the nozzle vane(left), the blade(right)[22]

are usually adopted at different positions[42], and a currently popular method: transpiration cooling[29]. These methods are shown in Fig.2.5. External cooling uses injection of a secondary flow (coolant) out through holes or slots on blade surfaces all over the external surface. As external cooling is the main subject of this study, it will be explained in detail in the following subsection.

2.1.3 | Modern external cooling

This practice is called film cooling, as a coolant film acting as an insulating layer is generated on blade surfaces, protecting the blade outside surface from hot combustion gases, at the same time removing heat from the blade. To achieve uniform film cooling effect, coolant air should be injected both at the leading edge, and at multiple locations on the downstream pressure and suction sides of the blade.

Fig.2.6 shows a typical arrangement of film cooling holes first promoted by Nirmalan[71] on the basis of extending two earlier geometries: leading edge film cooled[98] and non-film cooled blades. The leading edge cooling adopts a 'showerhead' arrangement of five equally spaced rows of cooling holes with the middle row placed at the estimated aerodynamic stagnation point, while downstream film

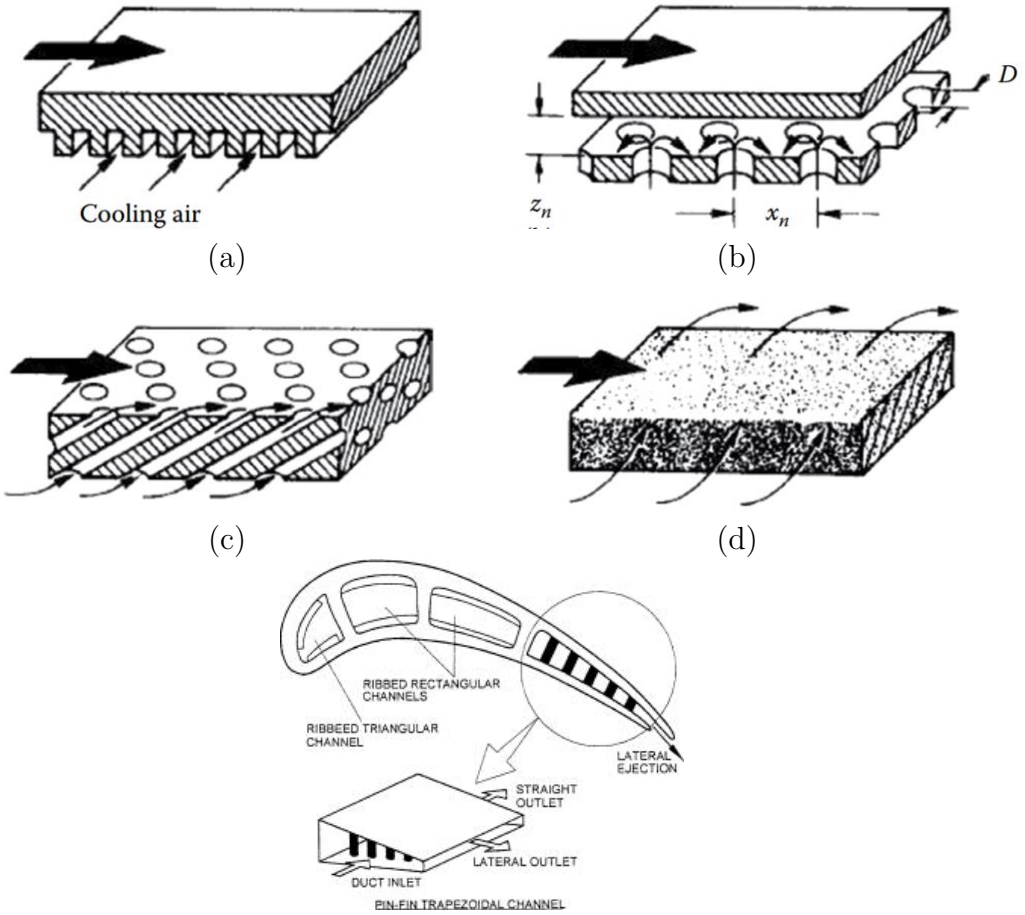
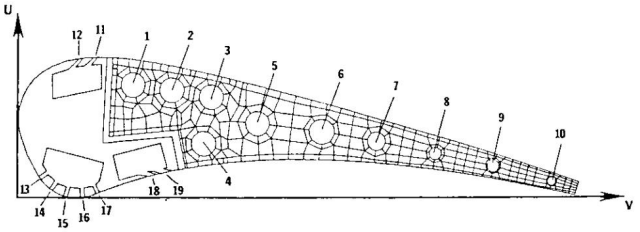


Figure 2.5: Cooling method sketch: (a)convection cooling (b)impinge cooling (c)full coverage film cooling (d)transpiration cooling, *from Glassman[29], NASA, 1994* ,(e)Rib and pin-fins cooling



Radial cooling holes					Film cooling holes		
Hole No.	U, mm	V, mm	Diameter, mm	Cr	Hole No.	U, mm	V, mm
1	28.70	29.92	6.30	1.118	11	35.92	20.24
2	27.33	39.98	6.30	1.118	12	35.56	16.31
3	25.55	49.91	6.30	1.118	13	4.98	5.41
4	13.64	47.88	6.30	1.118	14	2.11	8.28
5	18.69	61.82	6.30	1.118	15	0.41	11.96
6	16.66	77.47	6.30	1.118	16	0.05	16.00
7	14.12	92.35	4.70	1.090	17	1.09	19.94
8	10.87	107.59	3.10	1.056	18	5.59	35.05
9	7.37	122.53	3.10	1.056	19	6.43	38.91
10	3.45	137.57	1.98	1.025			

Figure 2.6: Film cooling hole arrangement, from Nirmalan[71]

cooling arrays are placed on the pressure and suction sides, each with two rows of cooling holes at comparable locations to the blade. Leading edge holes are inclined at 45° to the blade surface in the spanwise direction but perpendicular to the surface in the chordwise direction. These hole arrays are staggered, as the cooling holes of the second row are placed midway between the first and third row holes in the spanwise directions. As for downstream film cooling, cooling hole arrays are placed at 25.2% of the surface distance on the suction side and 22.5% of the surface distance on the pressure side from the geometric stagnation point, which is defined as the tangency point on the blade of the cascade inlet plane. These two locations are just upstream of the pressure recovery region on each surface side in the case without film cooling so that the highest film cooling effectiveness can be expected. The method of staggered hole arrays is again used. The holes on the suction side are angled at 35° to the surface, whereas those on the pressure side are angled at 20° in the chordwide direction. Holes on both suction and pressure sides are placed normal to the blade surface in the spanwise direction.

The effect of parameters such as exit Mach number, true chord exit Reynolds number, coolant-to-gas absolute temperature ratio, and coolant-to-gas pressure ratio, on film cooling performance should be discussed for design[71] (explained below).

2.2 | Numerical and experimental studies of film cooling

2.2.1 | Numerical methods during 1960-1990

Early from the 20^{th} century, the interest in turbulence at the practical level has been in the larger scales of motion, as they control, on the one hand, most of the Reynolds stress, and on the other hand, the viscous dissipation rates in finer grids through vortex-stretching process[61]. In the 60s and 70s, when production-line digital computers such as the IBM 7090 were introduced into universities, the considerable progress in the numerical methods for turbulence in turbomachine-related flows led to an evolution in the numerical methods. Famous numerical procedures appeared including Patanka and Spalding's boundary layer solver [89], the steady two-dimensional recirculating flow solver by Spalding's group [33] and a few numerical schemes, including a few Finite Difference schemes and integral schemes at the 1968 Stanford Conferences [62] on turbulence boundary layers.

In this period, countless papers were published on turbulence models for solving the averaged Navier-Stokes equations. Closures were proposed to involve correlations between different fluctuating quantities. The three most important closure models

are the Boussinesq viscosity model, the Reynolds stress transport model and the algebraic stress model. Their definitions are shown as below with the definition of Reynolds stress is $\tau_{ij} = -\overline{\rho u_i'' u_j''}/\overline{\rho}$:

- Boussinesq viscosity model in Equ. 2.1:

$$-\rho\left(\overline{u_{\mathrm{i}}u_{\mathrm{j}}} - \frac{1}{3}\delta_{\mathrm{ij}}\overline{u_{\mathrm{k}}u_{\mathrm{k}}}\right) = \mu_{\mathrm{T}}\left(\frac{\partial U_{\mathrm{i}}}{\partial x_{\mathrm{j}}} + \frac{\partial U_{\mathrm{j}}}{\partial x_{\mathrm{i}}}\right) \tag{2.1}$$

  where the turbulent viscosity is to be determined μ_{T}. There are two models determining μ_{T}: one is the Prandtl-Taylor mixing length hypothesis

$$\mu_{\mathrm{T}} = \rho l_{\mathrm{m}}^2 \left|\frac{\partial U}{\partial t}\right| \tag{2.2}$$

  , and the other is a series of two-equation models with:

$$\mu_{\mathrm{T}} = c_\mu \rho k^2/\varepsilon \tag{2.3}$$

- Reynolds stress transport model in Equ. 2.2.1:

$$\frac{D\overline{u_{\mathrm{i}}u_{\mathrm{j}}}}{Dt} = P_{\mathrm{ij}} + \phi_{\mathrm{ij}} - \varepsilon_{\mathrm{ij}} + D_{\mathrm{ij}} \tag{2.4}$$

- Algebraic stress model in Equ. 2.2.1:

$$\left(\overline{u_{\mathrm{i}}u_{\mathrm{j}}} - \frac{2}{3}\delta_{\mathrm{ij}}k\right) = \frac{(1-c_2)}{c_1}\frac{k}{\varepsilon}\left(P_{\mathrm{ij}} - \frac{1}{3}\delta_{\mathrm{ij}}P_{\mathrm{kk}}\right) \tag{2.5}$$

An analogy with, the closure of transport equations for the turbulent heat flux is

$$\overline{u_{\mathrm{i}t}} \propto -\frac{k}{\varepsilon}\overline{u_{\mathrm{i}}u_{\mathrm{j}}}\frac{\partial T}{\partial x_{\mathrm{j}}} \tag{2.6}$$

Vast efforts were contributed to computations related to film cooling slots/holes. Patankar[77] simulated a deflected jet, and he gave the trajectory of jet and velocity profiles with three-dimensional effects by k-ϵ equations. Bergeles[7] developed a nonisotropic eddy-viscosity equation when simplifying the Reynolds stress model proposed by Launder et al.[61] and turbulent heat flux model [27]. As it cannot handle the reverse flow, they are restricted to a low blowing ratio for a normal hole or a medium blowing ratio for holes inclined to the mainstream. Bergeles [7] used the simplified partially parabolic equations together with the finite difference method to obtain injection through discrete holes in the plate surface, and later effectiveness in both single-row and double-row discrete holes [8]. The reverse flow was handled by Rodi and Srivatsa [81], who developed a locally-elliptic finite difference procedure, thus saving computer storage compared to the fully-elliptic procedure like Patankar[77]. Demuren [20] developed a locally elliptic program together with $k-\epsilon$ equations implementing higher-order finite difference schemes. A row of inclined jets was simulated. The elliptic equations relieved the restriction of low blowing ratio as they allowed the solution in the vicinity of jets. The modified $k-\epsilon$ model by Bergeles[7] included by Demuren [20] can consider the anisotropy of eddy viscosity and diffusivity. They used a high-order-accurate difference approximation for the convection terms in QUICK scheme, which provided better three-dimensional results than the hybrid scheme. A reasonable comparison with Kadotani and Goldstein [53] was obtained. They concluded that the $k-\epsilon$ turbulence model cannot adequately present the complexity in the jet discharge flows. White [102] confirmed the need for an elliptic procedure when predicting the recirculation near and downstream holes at higher injection rates. Demuren

et al [19] then extended Rodi and Srivatsa's approach[81] to the locally elliptic finite volume method to solve three-dimensional partial differential equations. The reverse flow in higher blowing ratio conditions resulted. The turbulent stresses and heat fluxes are compared with the nonisotropic result from Bergeles's [7] k-ϵ model in a range of conditions varying injection angles, hole spacings and blowing ratios.

With the introduction of Prandtl-Taylor mixing length hypothesis, a number of large-eddy-simulations (LES) have been made, for example by Schumann and Grotzbach in Karlsruhe [36], and Reynolds and Ferziger at Stanford [24]. However, due to the limitation of computer powers at that time, the LES procedures were not largely applied to applications.

2.2.2 | Shaped film cooling holes

A number of studies presented detailed physical mechanisms of the interaction and mixing process of coolant with the crossflow. A sketch of fundamental jet-in-crossflow is shown in Fig. 2.7 [44]. The vortical structures include a counter-rotating vortex pair (CVP). CVP is the dominant mechanism that affects the cooling performance. As the blowing ratio increases, the attached coolant jet at a low blowing ratio becomes detached and reattached in a moderate blowing ratio, and a fully detached jet at a high blowing ratio. The detachment of the jet decreases the cooling performance as the the lift-off of jet allows the entrained mainstream to go below the jet, which then increases the temperature near the plate.

To mitigate the CVP, film cooling holes are then often shaped in some manner. The shaped cooling holes permit better metal protection/lower coolant supply, thus improving the film cooling performance. A shaped film hole is composed of an

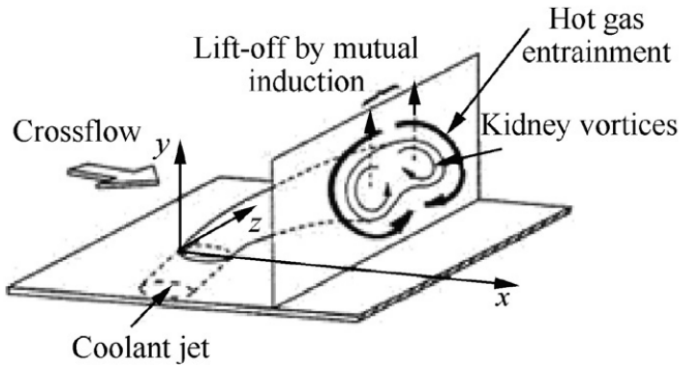


Figure 2.7: Cooling mechanism sketch [44]

initial round entry section acting as the metering role, and a following expanded diffuser section spreading the coolant laterally onto the main channel surface. Such shaped film holes are normally aimed at expanding the exit area of the jet by a factor of 2-3 times that of a cylindrical hole without separation [12]. The drilling of shapes and angles can be realized by electodishcharge machine, water-jet, and pulsed later approaches.

2.2.3 | Experiment of film cooling flowfield

Shaped film-cooling holes have been investigated since Goldstein [32] first measured holes with exit lateral expansion of 10° and an $L/D = 5.2$. The lateral expansion of holes can reduce the mean velocity, thus the momentum flux of the jet exiting the hole, leading to a reduction of penetration of the jet into the main channel and thus improved cooling efficiency. On the other hand, the higher level of lateral spreading promoted by lateral expansion makes a better coverage of cooling film, leading to a higher laterally-averaged film-cooling efficiency. Hay and Lampard [45] tested cylindrical holes with a lateral expansion angle of 12.5° and an additional

layback of 7.5°. They found that the flared geometries gained a higher discharge coefficient than cylindrical holes, but no further improvement was observed for additional layback. Haller and Camus [38] examined the aerodynamic loss of shaped film cooling on a two-dimensional cascade. The flare angle of 25° was seen as the optimum option in film cooling effectiveness with no loss penalty. Typical experimental research is the one by the Institut fur Thermische Stromungsmachinen (ITS), University of Karlsruhe, Germany[103]. They had an emphasis on a scaled-up cooling hole on a flat plate, with different parameters on adiabatic wall effectiveness, heat transfer coefficients, and discharge coefficients. The near-hole flowfield and interaction of the coolant jet with the mainstream were discussed. Three most concerned geometries are a cylindrical hole, a fan-shaped hole, and a laidback fan-shaped hole.

The studied case section consists of two loops, namely an external and an internal crossflow channel of a film-cooled airfoil. These two loops are independently controlled but connected by a scaled-up film cooling hole, as shown in Fig. 2.8. The two channels can be oriented parallel or perpendicular to each other. The main channel section is 90 mm in width and 41 mm in height, while the secondary channel section is 60 mm in width and 20 mm in height. In the experiments, the standard way for obtaining the flow rate in the coolant supply channel was by measuring the flow rates upstream and downstream of the hole location, followed by operating the difference between these two flow rates. For sake of an uncertainty consideration, they measured the flow rate through the film-cooling hole directly by using a 'closed loop' for the secondary loop instead.

The diameter of the cylindrical hole and the cylindrical inlet section of the

shaped holes are 10mm. The thickness of the wall is 30mm for all hole geometries. The lateral expansion angle of the shaped hole is 14°, giving rise to a hole width of 30mm at the hole exit. All the studied holes are inclined at 30°, with a hole length-to-diameter ratio of $L/D = 6$. In this study, only the cylindrical hole and the lateral hole are studied with the same operating conditions and test configuration in ITS's test rig. A sketch of the two holes are shown in Fig 2.9.

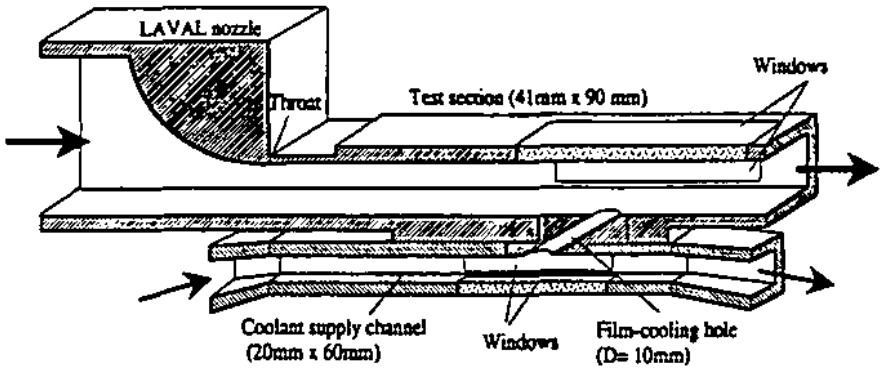


Figure 2.8: Schematic of the film-cooling test rig

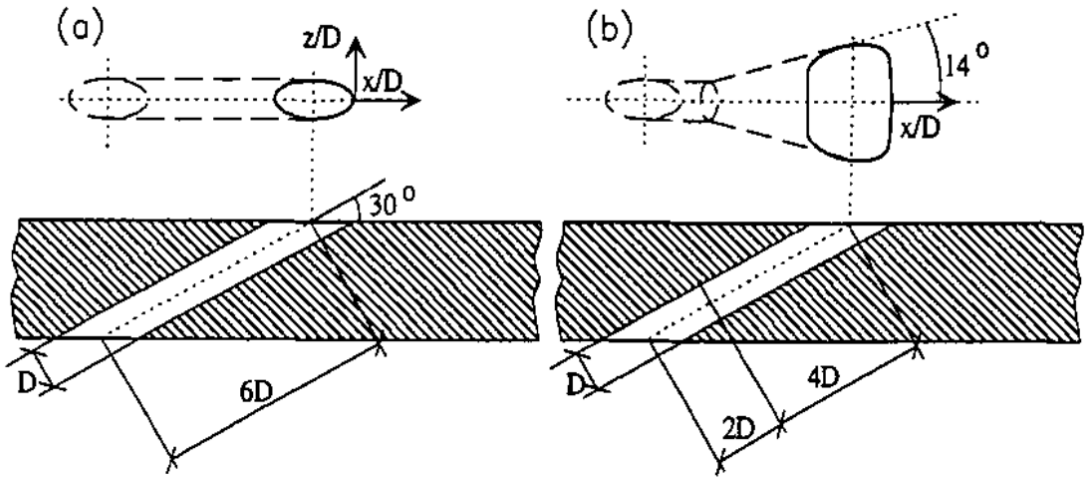


Figure 2.9: Film-cooling hole geometries

Moreover, the film cooling holes on the leading edge are specially focused on.

Goldstein [31] summarised early experimental studies. The stagnation region is particularly concerned as it is extensively exposed to the hot stream. Mehendale & Han [66] and Ou & Han[74] observed that for leading edge film cooling, effectiveness was decreased as the mainstream turbulence increases; less effect exits at bigger blowing ratio; the best effectiveness for spacing-to-diameter ratio 4 and 3 was found at mass flow ratios of 0.4 and 0.8. Mick & Mayle [68] and Gartshore et al [26] measured effectiveness for two rows of circular cooling orifices. NASA used in-house experimental research to give a full understanding of the influence of coolant flow conditions and geometry on film cooling effectiveness [76].

2.2.4 | Numerical methods for film cooling flow-field from the late 90s

Since Andreopouls[2] pointed out that the flow inside holes is perturbed by the mainstream crossflow, particularly at the low blowing ratio condition, more accurate numerical modeling and experiments of flow inside holes are concerned. Cho and Goldstein [17] summarised the four dominant parts of the flow mechanisms within the hole: the separated/backflow area near the hole entry, the reattachment area, the developing area, and the area at the exit downstream. Numerical studies found that the complex secondary flows and recirculation regions within the hole can largely influence the mixing process downstream in the mainstream, which is particularly studied in low length-to-diameter ratio cases [63, 100, 101]. Schmidt et al. [86] and Sen et al. measured laterally directed cooling holes with a compound angle of 60°, and streamwise directed round cooling holes at a range of momentum

ratios. They found that compound angle injection at high momentum flux ratios has higher effectiveness values than streamwise-directed holes when cooling performance behaves worse at a higher heat transfer level. Hayams et al. [50] studied the effect of inlet and exit shaping of the slot-jet on both flow and thermal fields on an unstructured grid by solving 2D $k - \epsilon$ equations.

Since 1997, full geometry, and three-dimensional predictions have been widely concerned for film cooling simulations.

Hayams et al. [49] was the first at that time to give systematic three-dimensional computational studies on the effect of different film hole configurations on the three-dimensional flow mechanism inside the hole and at the near-field interaction from a standpoint of vorticity. They used Walter and Leylek's [100] RANS code on an unstructured mesh. The holes are inclined at 35°. The mechanism in film cooling performance is dominantly influenced by the longitudinal vortex structure at the hole exit, and the strength of the exit vorticity is controlled by the boundary layer vorticity from the hole. The counter-rotating secondary structure from the hole can be reduced by decreasing the strength of crossflow-aligned vorticity exiting the hole so as to restrict the liftoff of the coolant downstream in the mainstream. (Weak longitudinal vorticity allows the film to remain attached to the surface. Less induction lift results from a separation of vortices.) Therefore, the dominating mechanism in determining downstream film cooling performance can be indicated by the aligned vorticity. Based on these observations, they proposed two sets of mechanisms to decrease the aligned vorticity: one is decreasing the through-flow vorticity, such as by using laterally-diffused holes; the second is increasing the secondary vorticity, like increasing the contour-rotating motion within the film hole.

Azzi and Jubran[4] adopted a multi-block mesh with a fully elliptic procedure using the standard $k-\epsilon$ used by Lakehal et al [59] and with Bergeles' modification. They compared two length-to-diameter ratios in terms of adiabatic effectiveness and turbulence. The mesh was generated separately for the different parts of the geometry. They found that the main source of turbulence is the shear layer between the coolant jet and mainstream at a blowing ratio of 0.5, yet the turbulence in the hole itself at at a higher blowing ratio of 1.0.

Saumweber [85] measured the effect of coolant supply crossflow in terms of the coolant crossflow orientation and Mach number for two types of cooling holes. They found that the coolant crossflow effects have a more influence on the fan-shaped holes in general compared to cylindrical holes. Increasing the blowing ratio to 1, the cylindrical holes present improved lateral spreading of coolant when the coolant crossflow is oriented both parallel to and perpendicular to the mainstream, while the fan-shaped holes are negatively affected by the perpendicular orientation of crossflow.

In addition, the sensitivity of different two-equation models to the features capturing of the film cooling hole flows is discussed. Turbulent models are pointed out as the main source of the inaccuracy of predicted film cooling performance. The standard $k-\epsilon$ model, even though widely used for film cooing simulations, have issues such as over-predictions of the penetration distance into the mainstream [48] and the under-prediction of the jet spreading [9]. Muldoon and Acharya [69] assessed terms in $k-\epsilon$ equations on channels by DNS. Budgets are obtained based on the difference between k and e equations in exact solutions and results by Boussinesq gradient approximation. They showed the eddy viscosity of the standard $k-\epsilon$

equations is greatly in error.

With the appearance of some more robust, more adaptive, more efficient grid generation techniques [106][57], more complex simulations are published in this period. film-cooling holes can be simulated along with the blades/vanes they are attached to, such as references[16, 51].

Besides shaped holes, new designs of film-cooling holes are also proposed based on a theory of reducing counter-rotating vortex, thus reducing liftoff of coolant boundary flow on the blade wall, such as [46][21, 46], or adding parts as disturbances such as an upstream ramp in front of the hole exit [70] or a trench [6][5].

2.2.5 | Modern LES of film cooling

With the development of computer power and geometry generation techniques, LES become available for understanding the detailed mechanisms in the film cooling flows.

Ziefle and Kleiser [109] studied the flow structures along a cylindrical cooling hole, which is selected from Sinha's [88] experiment, by a large-eddy simulation. A deep understanding of the mixing process was provided. However, a simplification of the turbulent boundary layer of inflow to a time-averaged profile prevents them from capturing realistic mixing processes suitably. Oilver et al. [72] found the Mach number of coolant flow may be several times higher than the mainstream Mach number, and the resulting comparability will influence the cooling performance. They gave an explanation of the decomposed mechanisms in the cooling holes in LES results of laterally-expanded holes under two Mach number conditions. Guo et al. [37] studied the effect of blowing ratio and incline angle through LES. They

observed that the counter-rotating vortex is more downstream in an inclined angle of 30 case compared to a normal jet case. Renze et al. [80] studied the effect of density ratio on the attachment/recirculation by LES of the jet in crossflow. Graf and Kleiser [35] carried out an LES study of double-row compound film cooling.

2.3 | Targets and challenges for film cooling

2.3.1 | The thermodynamic penalty for film cooling

As mentioned earlier, cooling imposes a thermodynamic penalty because work should be done by compressors to compress the coolant jet. On the one hand, this means that there needs to be a minimum supply of cooling air that ensures local temperatures compatible with safe operation over an extended period of time. On the other hand, it means that overcooling the turbine results in a performance penalty which will ultimately increase fuel burn. The highest overall cooling effectiveness should be achieved when the penalty on the thermodynamic performance should be the minimum. Han et al.[41] summarized the counteracting effect caused by thermodynamic parameters on the heat transfer coefficient in cases with different cooling methods. Dependent factors affect the thermodynamics in the flow field, and these parametric effects listed as follows should be provided to turbine designers to give the better design of film-cooled models.

2.3.1.1 | Blowing strength

At moderate blowing strengths ($\frac{P_c}{P_t} > 1.0$), the film cooling effect on the pressure surface is greatly dependent on blowing strength, while the effect on the suction surface shows little sensitivity to blowing strength where the coolant flow is choked. Conversely, at low blowing strengths ($\frac{P_c}{P_t} < 1.0$), both the suction and pressure surfaces present a dependence on blowing strength.[71]

2.3.1.2 | Exit Mach number

The exit Mach number has little effect on the film cooling performance at high thermal dilution levels (low coolant-to-gas temperature ratio), while much dependence is shown at low thermal dilution levels (high coolant-to-gas temperature ratio).[71]

2.3.1.3 | Reynolds number

Similarly, the heat transfer performance systematically increases with an increasing exit Reynolds number at high thermal dilution levels, whereas less relationship is presented at low thermal dilution levels.[71]

2.3.1.4 | Coolant-to-gas temperature ratio

The thermal dilution and the turbulence show the dominant effect at different coolant-to-gas temperature ratios, respectively[71].

2.3.2 | Adiabatic film effectiveness

Adiabatic film effectiveness is applied to measure the film cooling performance. The definition of adiabatic film effectiveness is

$$\eta = \frac{T_g - T_w}{T_g - T_c} \tag{2.7}$$

where T_g is the hot stream temperature, T_w is the temperature of the adiabatic wall and T_c is the temperature of the coolant. Adiabatic film effectiveness is associated with the blade shape(pressure gradient and blade curvature), boundary layer transition, free-stream turbulence behavior, blade surface roughness, and the film coolant injection location. Note that these factors not only influence flow behavior such as separation, reattachment, and the interaction between shock and boundary layer in a nonlinear way but also affect each other. Therefore a cooling system designer should consider these factors simultaneously. [10] showed a few factors that affect film effectiveness.

2.3.3 | Ideal cooling system designing

Therefore, the goal is to design a cooling system that can benefit the most from high inlet gas temperature with the minimum usage of compressor bleeding air for the cooling purpose. Besides, cooling systems should be designed to satisfy the material temperature requirement for the compatibility of blade life. Thermal stresses resulting from thermal gradients (steady) in the metal wall should also be satisfied.

The overall film cooling performance is related to a few factors, such as the cooling hole shape, the hole configuration, the angle of injection, and geometries,

Table 2.1: Factors influencing film-cooling

Coolant/mainstream conditions	Hole geometry and configuration	Airfoil geometry
Mass flux ratio[a]	Shape of the hole[a]	Hole location
Momentum flux ratio[a]	Injection angle and compound angle of the coolant hole[a]	Leading edge Main body Blade tip Endwall
Mainstream turbulence[a]	Spacing between holes, P/d	Surface curvature[a]
Coolant density ratio	Length of the hole, l/d	Surface roughness
Approach boundary layer	Spacing between rows of holes and number of rows	
Mainstream Mach number		
Unsteady mainstream flow		
Rotation		

shown in Table 2.1.

2.4 | Current design barrier

To enable modern gas turbines safely operate at higher inlet temperatures over the metal limitation, several cooling methods including augmentation internal cooling and film cooling are usually designed together. Details of flow and heat transfer mechanisms in the highly turbulent flow field should be well predicted. Note that current numerical predictions are still unable to show accurate heat load distribution as well as endwall flow patterns when the cooling jet flow is considered. Designs with an inappropriate amount of jet flow are thus always promoted, giving rise to a penalty to the thermal efficiency during operation. The non-optimized design will ultimately threaten the component safety.

2.5 | Implications for thermodynamical design

As above, the main challenge for cooling systems design is to use as little air as possible for a given reduction in wall temperature. This requires high accuracy of numerical prediction and resolution for small-scale features of flow in cooling geometries. Since the complexity of film cooling flows brings a great challenge to accurate numerical simulations, scale-resolving simulations, rather than simulations by RANS turbulence models commonly used nowadays, should be performed for predicting film cooling flows.



3

High Resolution Numerical Scheme

3.1 | Preface

The first key element for scale resolving of film cooling flows mentioned in Chapter 1 is the high-resolution numerical scheme. Current scale-resolving simulations of film cooling flows are either inaccurate or vulnerable to oscillations. Film cooling flows take place in complex geometries and are sensitive to flow fluctuations near the intersection between the cooling hole and the mainstream channel, therefore requiring a numerical scheme satisfying the following properties. First, the scheme should be suitable for scale-resolving simulations. Second, it can obtain least dissipation at least on smooth regions. Third, it should still capture strong discontinuities without oscillations. Based on these three requirements, a high-resolution numerical scheme is desired for LES of film cooling.

In this chapter, basic experiments with known methods are shown to select the most suitable methods. Section 3.2 introduces that there are two ways to achieve high order accuracy while retaining strong discontinuities without oscillations: one is to use a limiter, and the other is to use an adaptive stencil. Section 3.3 presents the methodology of implementing both the proposed limiter method and the adaptive stencil method used for reference, respectively. Section 3.4 shows successful results of the proposed high-order numerical scheme in terms of handling discontinuities, as well as maintaining high accuracy for smooth extrema, compared with the reference method.

3.2 | Related Work

A considerable number of numerical schemes have been published with the aim of improving stability, error properties, and order of accuracy in the past years. Despite higher orders of accuracy have been pursued, a major issue that dominated 30 years in CFD history is an unwanted appearance of wiggles, ie, numerical oscillations in the numerical solutions. The oscillations may cause regions of high error, thereby leading to non-physical phenomena. It has been discussed that the numerical oscillations are the consequence of the non-monotone behavior of the convection term when studying the second-order schemes [47]. The concept of Total Variation Diminishing (TVD) was then significant, which was first proposed by Harten in 1983[43]:

$$\mathrm{TV}(U(x,t)) = \max_{\text{all possible}} \sum_{i=-\infty}^{i=+\infty} |U(x_{j+1},t) - U(x_j,t)| \tag{3.1}$$

The TVD condition implies monotonicity preservation, and the monotonicity denotes that new extrema generated during the numerical procedure never goes beyond the

initial region of the solution. That is,

$$\begin{aligned} TV\left(U^{n+1}\right) &\leq TV\left(U^{n}\right), \quad \forall n > 0 \\ TV\left(U^{n}\right) &= \sum_{i=-\infty}^{i=+\infty} \mid U_{i+1}^{n} - U_{i}^{n} \mid \end{aligned} \tag{3.2}$$

The main advantage of imposing the TVD condition is that oscillations cannot grow infinitely so the unbounded development of oscillations can be avoided.

Van Leer[99] initially proposed a TVD limiter. It is based on the (Upstream-centered Scheme for Conservation Laws) MUSCL scheme. Van Leer[99] uses a piecewise linear approximation for spatial discretization and a second-order time scheme. Various limiting methods followed up resulting in second-order upwind schemes using modern high-resolution schemes. These limiters include superbee[84] , Sweby[91] , min-mod[82] , Koren[54] , etc. These limiters might lose their accuracy to the first order in the not smooth solution. Besides, there are some disadvantages of these classical second-order TVD limiters, such as 'smearing', 'clipping', and 'squaring' on the numerical approximation.

Some families of limiters have been defined. One example is the ALFA family:

$$\Psi(r) = \max[0, \min(2r, \alpha r + 1 - \alpha, (1-\alpha)r + \alpha, 2)] \tag{3.3}$$

where r is the ratio of successive gradients.

The ALFA family can become the Chakravarthy and Osher limiter when $\alpha = 1$, the SMART limiter when $\alpha = 3/4$, the Koren limiter when $\alpha = 2/3$ and close to the superbee limiter when $\alpha = 0$.

Updated limiting procedures are also designed with the expansion of the framework of TVD-MUSCL. Woodwar and Colella[18] developed a third-order scheme by using a limiter on a four-point stencil construction. Suresh and Huynh[90] obtained

higher order by using a limiter on a five-point stencil construction. Their limiters maintain monotonicity and accuracy for smooth extrema.

In addition, a number of non-polynomial reconstruction methods have been developed. Based on hyperbolas as the construction function proposed by Marquina[65], Artebrant and Schroll[3] developed a double logarithmic (LDLR) Ansatz function, with an additional parameter $q < 1$. The logarithmic pattern helps to get rid of spurious oscillations for discontinuities, as well as have locally bounded variation so that the order of accuracy for local extrema is not reduced. Based on the LDLR idea, Cada and Torrihon developed a third-order limiter [14]. The scheme using this third-order limiter has the good shock-capturing capability. Smearing, clipping, and squaring effects are got rid of. A large Courant number (CFL<=1.6) is permitted according to the von Neumann stability analysis.

Table 3.1: Review of limiters

Numerical scheme	**Limiter**	**Comments**
Second-order MUSCL	Van Leer[99]	$\Psi(r) = \frac{r+\|r\|}{1+r}$
	Mid mod[82]	$\Psi(r) = \text{mid mod(1,r)}$ $= \text{sgn}(x).\max[0, \min(\|x\|, \text{sgn}(x).y)]$
	Sweby[91]	$\Psi(r) = \max[0, \min(\beta r, 1), \min(r, \beta)] \quad 1 \leq \beta \leq 2$
	Roe (superbee)[83, 84]	$\Psi(r) = max[0, min(2r, 2), min(r, 2)]$
	ALFA family	$\Psi(r) = \max[0, \min(2r, \alpha r + 1 - \alpha, (1-\alpha)r + \alpha, 2)$
Higer-order MUSCL	Woodwar and Colella[18]	Limiting procedure development
	Suresh and Huynh[90]	Limiting procedure development
Non-polynomial reconstruction	Marquina[65]	a hyperbola function
	Artebrant & Schroll[3]	$\phi_{AS}(\theta_i, q) = \frac{2p\left[\left(p^2-2p\theta+1\right)\log(p)-(1-\theta)\left(p^2-1\right)\right]}{(p^2-1)(p-1)^2}$ $p = p(\theta_i, q) = 2\frac{\|\theta_i\|^q}{1+\|\theta_i\|^{2q}}$
	Cada & Torrihon[14]	based on LDLR

An alternative to tackle the oscillation issue is by using a procedure of searching adaptive stencils. Representatives are Harten et al.'s essentially nonoscillatory (ENO) scheme and Liu et al.'s weighted essentially nonoscillatory (WENO) scheme.

Both are approaches using polynomial reconstruction of interface values. When performing the interpolation, the ENO approach circumvents interpolation across discontinuities by picking up the stencil with the locally 'smoothest' reconstruction, while the WENO approach computes the interface values by a convex combination of all candidate stencils. Compared with TVD schemes, ENO and WENO present spurious but bounded variations, which are less apparent on a finer mesh.

In this work, both limiters and WENO schemes are tested. Results by WENO schemes are used as the reference for the search for the best option for limiter methods. The Cada and Torrihon limiter[14] and some of the classical second-order limiters are applied in different methods. Limiters are applied to different variables and in different combinations.

3.3 | Methodology

3.3.1 | Conservation law

The application of these numerical schemes has been to hyperbolic conservation laws. For one dimensional Euler equation, the PDE, conserved variables, and the vector of fluxes take the form:

$$\frac{\partial U}{\partial t} + \frac{\partial F(U)}{\partial x} = 0 \tag{3.4}$$

$$U = (\rho, \rho u, E)^t \qquad , F(U) = (\rho u, \rho u^2 + p, u(E+p))^t \tag{3.5}$$

For the three-dimensional Euler equation, the form is:

$$U_t + F(U)_x + G(U)_y + H(U)_z = 0 \tag{3.6}$$

with

$$U = \begin{bmatrix} \rho \\ \rho u \\ \rho v \\ \rho w \\ E \end{bmatrix}, F = \begin{bmatrix} \rho u \\ \rho u^2 + p \\ \rho uv \\ \rho uw \\ u(E+p) \end{bmatrix},$$
$$G = \begin{bmatrix} \rho v \\ \rho uv \\ \rho v^2 + p \\ \rho vw \\ v(E+p) \end{bmatrix}, H = \begin{bmatrix} \rho w \\ \rho uw \\ \rho vw \\ \rho w^2 + P \\ w(E+p) \end{bmatrix} \tag{3.7}$$

An important property of such hyperbolic conservation laws is that any linear combination of the Jacobians for $\sum_{j=1}^{d} \xi_j f_j'(u)$ for real ξ_j has only real eigenvalues with a set of independent eigenvectors.

3.3.2 | Finite volume

The Finite Volume method (FVM) is applied. Semi-discrete approach is used for the conservation laws so that time and space integration is decomposed.

$$\frac{\mathrm{d}}{\mathrm{d}t} \int_{\Omega} \boldsymbol{u}(x,t) \mathrm{d}x = - \int_{\partial\Omega} \boldsymbol{f}(\boldsymbol{u}(x,t)) \cdot \boldsymbol{n} \mathrm{d}S \tag{3.8}$$

The following explanation will show that the interface values of the flux $\boldsymbol{f}(\boldsymbol{u}(x,t))$ is reconstructed from available cell averages. The spatial domain is treated as finite volumes after discretisation.

(i) One-dimensional finite volume

Assume $I_i = [x_{i-\frac{1}{2}}, x_{i+\frac{1}{2}}]$, and Δx is the corresponding grid size. The FV method is based on cell-averaged values. Introducing the sliding average of the weak solution $u(x,t)$,

$$\bar{u}_i = \frac{1}{\Delta x}\int_{x_{i-\frac{1}{2}}}^{x_{i+\frac{1}{2}}} u(x,t)dx \tag{3.9}$$

for the solution $u(x,t)$ on the cell I_i, The conservation laws becomes

$$\bar{u}_i(x,t+\Delta t) - \bar{u}_i(x,t) = -\frac{1}{\Delta x_i}\Big[\int_{\tau=t}^{\tau=t+\Delta t}\Big(f(u(x_{i+\frac{1}{2}},\tau)d\tau - \int_{\tau=t}^{\tau=t+\Delta t} f\big(u(x_{i-\frac{1}{2}},\tau)\big)d\tau\Big] \tag{3.10}$$

In Godunov-type schemes, $f(u(x_{i+\frac{1}{2}}),t)$ can be replaced by a numerical flux $\hat{f}_{i+\frac{1}{2}}$, which is determined by

$$\hat{f}_{i+\frac{1}{2}} = h\Big(u^-_{i+\frac{1}{2}}, u^+_{i+\frac{1}{2}}\Big) \tag{3.11}$$

The function h is a function of two interface states (u_L, u_R), which constructs a Riemann problem. The solution of a Riemann problem consists of a set of nonlinear waves. This is solved by an approximate Riemann solver between every two neighboring cells in this study.

(ii) Two-dimensional finite volume

$$\begin{aligned}
\frac{d\tilde{\bar{u}}_{ij}(t)}{dt} &= -\frac{1}{\Delta x}\left(\hat{f}_{i+\frac{1}{2},j} - \hat{f}_{i-\frac{1}{2},j}\right) - \frac{1}{\Delta y}\left(\hat{g}_{i,j+\frac{1}{2}} - \hat{g}_{i,j-\frac{1}{2}}\right)\\
\hat{f}_{i+\frac{1}{2},j} &\approx \frac{1}{\Delta y}\int_{y_{j-\frac{1}{2}}}^{y_{j+\frac{1}{2}}} f\left(u\left(x_{i+\frac{1}{2}},y,t\right)\right)dy \equiv \tilde{f}_{i+\frac{1}{2},j},\\
\hat{g}_{i,j+\frac{1}{2}} &\approx \frac{1}{\Delta x}\int_{x_{i-\frac{1}{2}}}^{x_{i+\frac{1}{2}}} g\left(u\left(x,y_{j+\frac{1}{2}},t\right)\right)dx \equiv \bar{g}_{i,j+\frac{1}{2}}.
\end{aligned} \tag{3.12}$$

(iii) Three-dimensional finite volume

$$
\begin{aligned}
\frac{d\bar{U}_{ijk}(t)}{dt} &= -\left[\left(F_{i+\frac{1}{2},j,k} - F_{i-\frac{1}{2},j,k}\right) + \left(G_{i,j+\frac{1}{2},k} - G_{i,j-\frac{1}{2},k}\right) + \left(H_{i,j,k+\frac{1}{2}} - H_{i,j,k-\frac{1}{2}}\right)\right] \\
\bar{U}_{ijk}(t) &= \frac{1}{\Delta x \Delta y \Delta z} \int_{x_{i-\frac{1}{2}}}^{x_{i+\frac{1}{2}}} \int_{y_{i-\frac{1}{2}}}^{y_{i+\frac{1}{2}}} \int_{z_{i-\frac{1}{2}}}^{z_{i+\frac{1}{2}}} U(x,y,z,t) dz dy dx \\
F_{i+\frac{1}{2},j,k} &= \frac{1}{\Delta x \Delta y \Delta z} \int_{y_{i-\frac{1}{2}}}^{y_{i+\frac{1}{2}}} \int_{z_{i-\frac{1}{2}}}^{z_{i+\frac{1}{2}}} F(U(x+1/2,y,z,t)) \cdot \hat{n}_1 \cdot dz dy \\
G_{i,j+\frac{1}{2}k} &= \frac{1}{\Delta x \Delta y \Delta z} \int_{x_{i-\frac{1}{2}}}^{x_{i+\frac{1}{2}}} \int_{z_{i-\frac{1}{2}}}^{z_{i+\frac{1}{2}}} G(U(x,y+1/2,z,t)) \cdot \hat{n}_2 . dz dx \\
H_{i,j,k+\frac{1}{2}} &= \frac{1}{\Delta x \Delta y \Delta z} \int_{x_{i-\frac{1}{2}}}^{x_{i+\frac{1}{2}}} \int_{y_{i-\frac{1}{2}}}^{y_{i+\frac{1}{2}}} H(U(x,y,z+1/2,t)) \cdot \hat{n}_3 \cdot dy dx
\end{aligned}
\tag{3.13}
$$

With the aid of semi-discretization, two-dimensional and three-dimensional takes advantage of face values. A reconstruction similar to one dimension should be applied to higher dimensions.

The rest of this section will first introduce the spatial reconstruction of interface values, then illustrate how the Riemann problem is solved by the approximate Riemann solver. After that time integration methods are explained and the last part is the extension to higher dimensional Euler equations.

3.3.3 | Spatial reconstruction

The WENO reconstruction in a fifth-order WENO scheme and the interface value reconstruction with limiters in a third order MUSCL are shown. Both numerical schemes are performed on the most compact stencils including the control cell and its most direct neighbors.

3.3.3.1 | WENO reconstruction

WENO reconstruction is a convex combination of all the candidate stencils. The idea is to assign weights to each stencil corresponding to the contribution. Zero weight is set for the stencil passed across by discontinuities, identified by smoothness. This procedure enables its non-oscillatory property.

The One-dimensional WENO reconstruction is performed as follows:

(i) Stencils are first identified in a way that k sub-stencils are given for each stencil with $2k-1$points, with r cells to the left, and s cells to the right, in Fig.3.1:

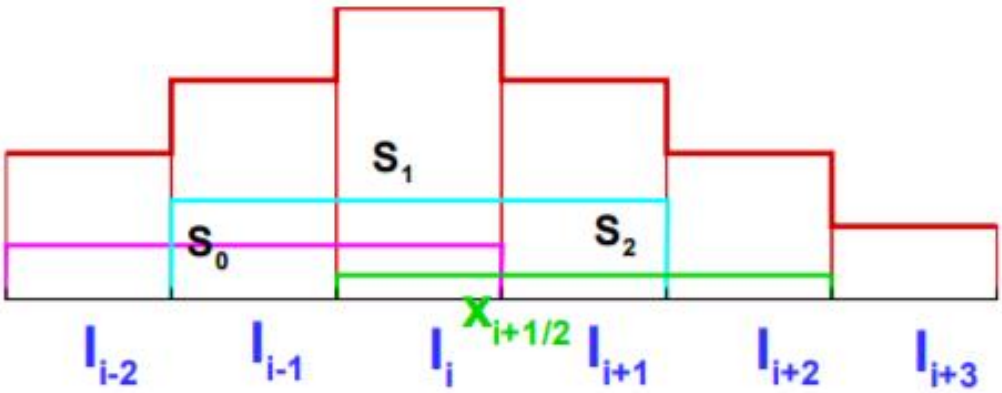


Figure 3.1: WENO stencils

$$S_r = \{x_{i-r}, ..., x_{i-r+k-1}\}, \qquad r = 0, ...k-1 \tag{3.14}$$

(ii) In each stencil, linear weights for k candidate sub-stencils are determined as

$$c_{rj}(x) = \prod \frac{x - x_{i-r+i}}{x_{i-r+j} - x_{i-r+l}} \tag{3.15}$$

satisfying

$$u_L^{(r)}(x) = \sum_{j=0}^{k-1} u_{i-r+j} c_{rj}(x) \tag{3.16}$$

(iii) The smooth indicator is used as a measure of smoothness to minimize the total variation for the reconstructed polynomial inside each stencil:

$$\beta_r = \sum_{l=1}^{k-1} \int_{x_{i-\frac{1}{2}}}^{x_{i+\frac{1}{2}}} \Delta x^{2l-1} \Big(\frac{\partial^l p_r(x)}{\partial^l x} \Big)^2 dx \tag{3.17}$$

(iv) Nonlinear weights are then achieved based on smoothness indicators as

$$w_j = \frac{\tilde{w}_j}{\sum_j \tilde{w}_j}, \quad \tilde{w}_j = \frac{d_j}{(\epsilon + \beta_j)^2}, \tag{3.18}$$

(v) The final WENO reconstruction is then given by

$$R(x^G) = \sum_{j=1}^{q} w_j p_j x^G \tag{3.19}$$

By far, point values $u^-_{i+\frac{1}{2}}$ for all cell boundaries have been reconstructed. For $k = 3$, the fifth-order WENO reconstruction has the polynomials,

$$\begin{aligned} p_0\left(x_{i+\frac{1}{2}}\right) &= \frac{1}{3}\bar{U}_{i-2} - \frac{7}{6}\bar{U}_{i-1} + \frac{11}{6}\bar{U}_i \\ p_1\left(x_{i+\frac{1}{2}}\right) &= \frac{1}{6}\bar{U}_{i-1} - \frac{5}{6}\bar{U}_i + \frac{1}{3}\bar{U}_{i+1} \\ p_2\left(x_{i+\frac{1}{2}}\right) &= \frac{1}{3}\bar{U}_i - \frac{5}{6}\bar{U}_{i+1} + \frac{1}{6}\bar{U}_{i+2} \end{aligned} \tag{3.20}$$

with weights as:

$$d_0 = \frac{1}{10} \quad d_1 = \frac{3}{5} \quad d_2 = \frac{3}{10} \tag{3.21}$$

The smoothness indicator for each stencil is

$$\begin{aligned} \beta_0 &= \frac{13}{12}\left(\bar{U}_{i-2} - 2\bar{U}_{i-1} + \bar{U}_i\right)^2 + \frac{1}{4}\left(\bar{U}_{i-2} - 4\bar{U}_{i-1} + 3\bar{U}_i\right)^2 \\ \beta_1 &= \frac{13}{12}\left(\bar{U}_{i-1} - 2\bar{U}_i + \bar{U}_{i+1}\right)^2 + \frac{1}{4}\left(\bar{U}_{i-1} - \bar{U}_{i+1}\right)^2 \\ \beta_1 &= \frac{13}{12}\left(\bar{U}_i - 2\bar{U}_{i+1} + \bar{U}_{i+2}\right)^2 + \frac{1}{4}\left(3\bar{U}_i - 4\bar{U}_{i+1} + \bar{U}_{i+2}\right)^2 \end{aligned} \tag{3.22}$$

3.3.3.2 | TVD-MUSCL with a switch of limiters

The CFD code is implemented with limiters as well as a switching function to apply limiters on the variables selected. A compact three-point stencil is built. Cada and Torrihon limiter[14] limiter is applied. Classical MUSCL methods based on a three-point stencil present second-order accuracy. The accuracy of the present MUSCL scheme is extended to the third order with the aid of limiters.

It shows that combined with an explicit TVD Runge-Kutta scheme for time integration, as well as the standard semi-discrete Monotonic Upstream-centered Scheme for Conservation Laws(MUSCL) algorithm, the numerical scheme as a whole can handle discontinuities and local extreme.

Considering a three-point stencil in one dimension, the interface values are defined as,

$$\begin{aligned} \hat{u}^{(-)}_{i+\frac{1}{2}} &\equiv L\left(\bar{u}_{i-1}, \bar{u}_i, \bar{u}_{i+1}\right) \\ \hat{u}^{(+)}_{i+\frac{1}{2}} &\equiv R\left(\bar{u}_i, \bar{u}_{i+1}, \bar{u}_{i+2}\right) \end{aligned} \tag{3.23}$$

(i) Second-order TVD-MUSCL schemes

Classical second-order TVD-MUSCL schemes assume a piecewise interpolation from cell-averaged values with non-linear limiter functions

$$\begin{aligned} \hat{u}^{(-)}_{i+\frac{1}{2}} &= \bar{u}_i + \frac{\Delta x}{2}\sigma_i \\ \hat{u}^{(+)}_{i-\frac{1}{2}} &= \bar{u}_i - \frac{\Delta x}{2}\sigma_i \end{aligned} \tag{3.24}$$

The downwind sloop is used to avoid Gibb's phenomenon:

$$\sigma_i = \left(\frac{\delta_{i+\frac{1}{2}}}{\Delta x}\right)\phi\left(r_i\right) \tag{3.25}$$

Examples of second-order MUSCL schemes are shown in Fig.3.2.

(ii) Third-order TVD-MUSCL schemes

On a local three-point stencil, the reconstruction of interface values is using a quadratic interpolation function.

The reformulation of third-order scheme reads

$$\begin{aligned} \hat{u}_{i+\frac{1}{2}}^{(-)} &= \bar{u}_i + \frac{1}{2}\phi\left(r_i\right)\delta_{i+\frac{1}{2}} \\ \hat{u}_{i-\frac{1}{2}}^{(+)} &= \bar{u}_i - \frac{1}{2}\phi\left(r_i^{-1}\right)\delta_{i-\frac{1}{2}} \end{aligned} \tag{3.26}$$

where

$$r_i = \frac{\delta_{i-\frac{1}{2}}}{\delta_{i+\frac{1}{2}}}, \quad \delta_{i+\frac{1}{2}} \neq 0 \tag{3.27}$$

is a local smoothness measurement, and $\delta_{i+\frac{1}{2}} = \bar{u}_{i+1} - \bar{u}_i$ is the difference across a cell interface.

The Cada and Torrihon's limiter was developed based on a local double logarithmic (LDLR) Ansatz function. Instead of using the log limiter, they recover

$$\phi(r) = \frac{2+r}{3} \tag{3.28}$$

so as to get rid of the complexity and the possible unstable property of both the LDLR and the logarithmic limiter function. Not only can they avoid

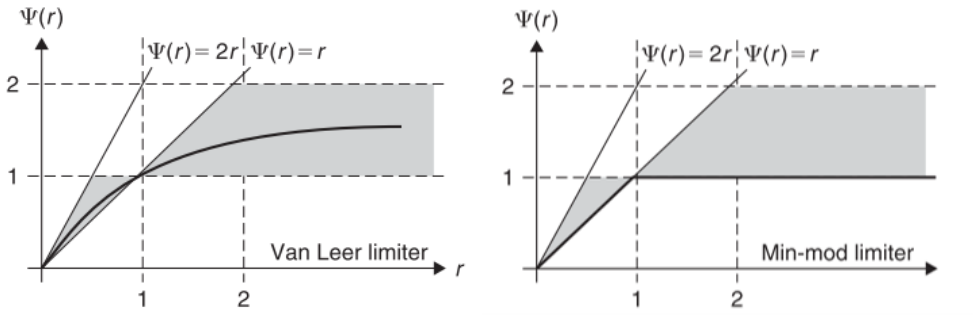


Figure 3.2: Second-order MUSCL schemes

troublesome singularities but also the TVD condition is better controlled. Numerical cost is decreased.

The improved Cada and Torrihon limiter[14] is

$$\hat{\phi}(r) = \max\left[0, \min\left(\frac{2+r}{3}, \max\left[-\alpha r, 0, \min\left(\beta r, \frac{2+r}{3}, \gamma\right)\right]\right)\right] \tag{3.29}$$

where the parameters α, β and γ should satisfy the conditions $0 \leq \alpha \leq 2$, $1 \leq \beta \leq 2$ and $1 \leq \gamma \leq 2$. These parameters control the limiter's shock capturing and total variation.

The scheme recovers the quadrature function in the smooth region as

$$\begin{aligned} \hat{u}^{(-)}_{i+\frac{1}{2}} &= \frac{5}{6}\bar{u}_i - \frac{1}{6}\bar{u}_{i-1} + \frac{1}{3}\bar{u}_{i+1} \\ \hat{u}^{(+)}_{i-\frac{1}{2}} &= \frac{5}{6}\bar{u}_i - \frac{1}{6}\bar{u}_{i+1} + \frac{1}{3}\bar{u}_{i-1} \end{aligned} \tag{3.30}$$

The shape of Cada and Torrihon limiter and second-order MUSCL limiters are shown in Fig. 3.3.

Compared with classical second-order MUSCL schemes, the shape-preserving properties of reconstruction are largely improved. Sharp, accurate, symmetric shock capturing is obtained. The smearing, clipping, and squaring effects of classical second-order limiters are avoided. A larger Courant number is allowed (CFL<=1.6) by Cada and Torrihon limiter.

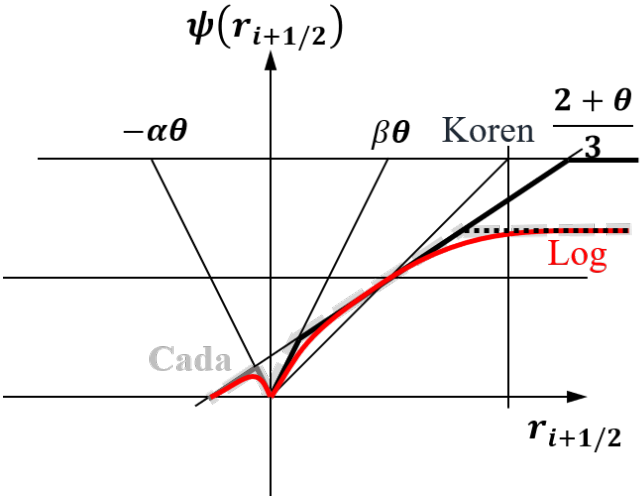


Figure 3.3: The adopted limiter compared with other limiters

3.3.3.3 | Characteristic decomposition for reconstruction

The WENO construction is performed on the characteristic field. Characteristic decomposition is applied for the simple and cost-effective component by component versions of WENO schemes. The limiters are imposed on either characteristic variables or primitive variables. Characteristic decomposition is imposed on the selective components for limiters.

(i) 1D Euler equation

The method is starting from a 1D Euler equation followed by a chain rule:

$$\frac{\partial U}{\partial t} + A(U)\frac{\partial U}{\partial x} = 0 \tag{3.31}$$

where $A(U)$ is the Jacobian matrix of the flux function F(U).

$$\mathbf{A} = \frac{\partial \mathbf{F}}{\partial \mathbf{U}} \tag{3.32}$$

$$A(U) = \begin{bmatrix} 0 & 1 & 0 \\ -\frac{1}{2}(\gamma-3)u^2 & (3-\gamma)u & \gamma-1 \\ u[\frac{1}{2}(\gamma-1)u^2 - H] & H-(\gamma-1)u^2 & \gamma u \end{bmatrix} \tag{3.33}$$

which has eigenvalues

$$\lambda = u-a,\ \lambda = u,\ \lambda = u+a \tag{3.34}$$

and the corresponding right eigenvectors are

$$\mathbf{K}^{(1)} = \begin{bmatrix} 1 \\ u-a \\ H-ua \end{bmatrix}, \mathbf{K}^{(2)} = \begin{bmatrix} 1 \\ u \\ \frac{1}{2}u^2 \end{bmatrix}, \mathbf{K}^{(3)} = \begin{bmatrix} 1 \\ u+a \\ H+ua \end{bmatrix}. \tag{3.35}$$

such that $AK = \lambda K$.

(ii) multi-dimensional characteristic equation

For multi-dimensional characteristic equation, Flux Vector Splitting Technique[28] is applied. The problem is spitted as solving fluxes in each dimension.

$$U_i^{n+1} = U_i^n - \frac{\Delta t}{\Delta x_i}\left(F_i^* - F_{j-1}^*\right) \tag{3.36}$$

Therefore, the Jacobian matrix of the x–split equations, its eigenvalues and corresponding right eigenvectors can be found:

$$\mathbf{A} = \frac{\partial \mathbf{F}}{\partial \mathbf{U}} = \begin{bmatrix} 0 & 1 & 0 & 0 & 0 \\ \hat{\gamma}H - u^2 - a^2 & (3-\gamma)u & -\hat{\gamma}v & -\hat{\gamma}w & \hat{\gamma} \\ -uv & v & u & 0 & 0 \\ -uw & w & 0 & u & 0 \\ \frac{1}{2}u\left[(\gamma-3)H - a^2\right] & H-\hat{\gamma}u^2 & -\hat{\gamma}uv & -\hat{\gamma}uw & \gamma u \end{bmatrix} \tag{3.37}$$

where

$$H = (E+p)/\rho = \frac{1}{2}\mathbf{V}^2 + \frac{a^2}{(\gamma-1)}, \mathbf{V}^2 = u^2+v^2+w^2, \hat{\gamma} = \gamma - 1$$

$$\lambda_1 = u - a, \lambda_2 = \lambda_3 = \lambda_4 = u, \lambda_5 = u + a. \tag{3.38}$$

A similar procedure can be done in other directions.

(iii) Transforming for reconstruction

The interface value reconstruction using characteristic variables is between two additional processes. One is transforming the conserved variables to characteristic variables before performing the reconstruction. Another is transforming the reconstructed characteristic variables back to conserved variables. This procedure will help prevent spurious oscillations. For the three-dimensional Euler equations, given eigenvalues $\lambda_1 \leq ... \leq \lambda_5$ and corresponding eigenvectors $K_1, ..., K_5$, which constitutes the columns of the matrix $K(U) = K_1, ..., K_5$ it gives

$$K^{-1}(U)A(U)K(U) = \Lambda(U) \tag{3.39}$$

The characteristic decomposition procedure takes the following steps:

- a. Approximating the flux Jacobian on the cell interface face by Roe average;
- b. Obtaining the eigenvalues, left eigenvectors, right eigenvectors of the Jacobian;
- c. Transforming the conservative variables to the characteristic form;
- d. Performing the interface value reconstruction for each selected characteristic variable;
- e. Transforming back each reconstructed interface value in the characteristic form back into conserved variables

- f. Solving the Riemann problem on the cell interface by the approximate solver introduced below.

3.3.3.4 | Primitive-Variable Formulation

Primitive variables may be used as the choice for the limiter. Thus it is necessary to have a brief introduction. The primitive variables in 1D Euler equation are $W = (\rho, u, p)^T$. Thus, we obtain

$$\mathbf{W}_t + \mathbf{A}(\mathbf{W})\mathbf{W}_x = \mathbf{0}$$
$$\mathbf{W} = \begin{bmatrix} \rho \\ u \\ p \end{bmatrix}, \quad \mathbf{A}(\mathbf{W}) = \begin{bmatrix} u & \rho & 0 \\ 0 & u & 1/\rho \\ 0 & \rho a^2 & u \end{bmatrix}. \tag{3.40}$$

A procedure of transformation to and back from conserved variables has been applied similarly to the above subsection.

3.3.4 | Approximate Riemann Solvers-Roe's

The Riemann problem for the 1D time-dependent Euler equation can be described as

$$\mathbf{U}_t + \mathbf{F}(\mathbf{U})_x = \mathbf{0},$$
$$\mathbf{U}(x,0) = \mathbf{U}^{(0)}(x) = \begin{cases} \mathbf{U}_L & \text{if } x < 0 \\ \mathbf{U}_\mathrm{R} & \text{if } x > 0 \end{cases} \tag{3.41}$$

The structure of the similarity solution $\mathbf{U}$ can be sketched in Fig.3.4. There are three families of waves associated with the three characteristic fields. Fig.3.5 shows a particular case presenting a rarefaction wave, a contact discontinuity, and a shock wave from left to right.

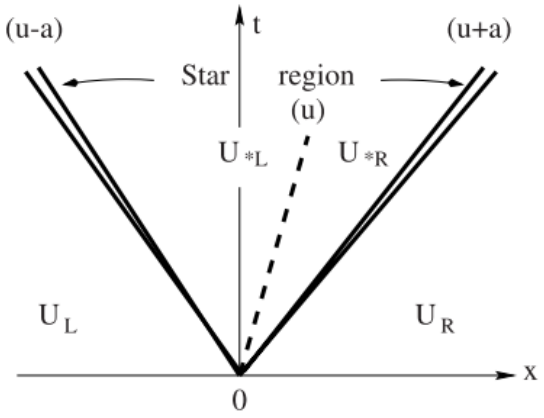


Figure 3.4: Structure of 1D Riemann problem solution: eigenvalues

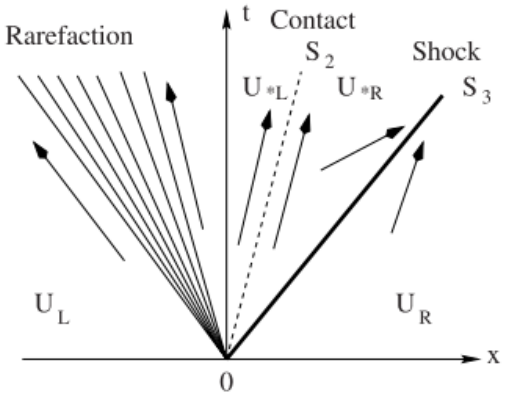


Figure 3.5: Structure of 1D Riemann problem solution: wave type

For the Riemann problem of the x-split three-dimensional Euler equation, there are five waves shown in Fig. 3.6. The solution to Riemann problem for the split three-dimensional equations is basically the same as for the one-dimensional Riemann problem.

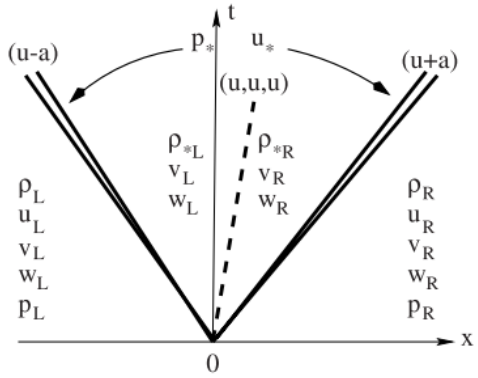


Figure 3.6: Structure of split 3D Riemann problem solution

Roe solver, one of the most well-known approximate Riemann solvers, is used as the numerical flux solver. The advantage of Roe's solver is its capability to capture discontinuities without any shock-fitting procedure. There are also other Riemann solvers, for example, HLLC that performs very well. However, the Roe solver is quicker as it only takes 25 operations in each solution while the HLLC takes over 30 operations. Roe [84] derived an approach that approximates systems of conservation laws by using a piecewise constant approximation.

$$w(x,t_n) = \begin{cases} w_L & x_L - \frac{\Delta x}{2} < x < x_L + \frac{\Delta x}{2} \\ w_R & x_R - \frac{\Delta x}{2} < x < x_R + \frac{\Delta x}{2} \end{cases}$$

The decomposition is $\Delta F = \sum_{k=1}^{M} \tilde{\alpha}_k \tilde{\lambda}_k \tilde{e}_k = \tilde{A}\Delta w.$ where $\tilde{A}(w_L, w_R) = \frac{\partial F}{\partial w}$ is the linearised Jacobian matrix and ˜ is the Roe average.So the method for the solution is obtaining the eigenvalues, eigenvectors, and wave strengths for solving Riemann

problems[97]. The Jacobian matrix of $F(U)$ is

$$w_i^{n+1} = w_i^n - s(F^*_{i+1/2} - F^*_{i-1/2}) \tag{3.42}$$

$$F^*_{i+1/2} = \frac{1}{2}(F^n_{i+1} + F^n_i) - \frac{1}{2}\left(\sum_{k=1}^{M} \tilde{\alpha}_k \mid \tilde{\lambda}_k \mid \tilde{e}_k\right)_{i+\frac{1}{2}} \tag{3.43}$$

The relevant averages are given as

$$\left.\begin{aligned} \tilde{u} &= \tfrac{\sqrt{\rho_L}u_L + \sqrt{\rho_R}u_R}{\sqrt{\rho_L}+\sqrt{\rho_R}} \\ \tilde{v} &= \tfrac{\sqrt{\rho_L}v_L + \sqrt{\rho_R}v_R}{\sqrt{\rho_L}+\sqrt{\rho_R}} \\ \tilde{w} &= \tfrac{\sqrt{\rho_L}w_L + \sqrt{\rho_R}w_R}{\sqrt{\rho_L}+\sqrt{\rho_R}} \\ \tilde{H} &= \tfrac{\sqrt{\rho_L}H_L + \sqrt{\rho_R}H_R}{\sqrt{\rho_L}+\sqrt{\rho_R}} \\ \tilde{a} &= \left((\gamma-1)\left(\tilde{H} - \tfrac{1}{2}\tilde{\mathbf{V}}^2\right)\right)^{\frac{1}{2}} \end{aligned}\right\} \tag{3.44}$$

3.3.5 | Time marching scheme

3.3.5.1 | Runge-Kutta scheme

High order TVD Runge-Kutta time discretization is implemented. Runge-Kutta time schemes are convex combinations of first-order forward Euler steps so that they have strong stability in any semi-norm of the forward Euler step. They were first designed in [34, 87]. A TVD third-order low-storage Runge–Kutta method is defined as

$$\begin{aligned} u^{(1)} &= u^n + \Delta t L\left(u^n\right) \\ u^{(2)} &= \frac{3}{4}u^n + \frac{1}{4}u^{(1)} + \frac{1}{4}\Delta t L\left(u^{(1)}\right) \\ u^{n+1} &= \frac{1}{3}u^n + \frac{2}{3}u^{(2)} + \frac{2}{3}\Delta t L\left(u^{(2)}\right) \end{aligned} \tag{3.45}$$

A fourth-order Runge–Kutta method is defined as:

$$\begin{aligned}
u^{(1)} =& u^n + \frac{1}{2}\Delta t L\left(u^n\right) \\
u^{(2)} =& \frac{649}{1600}u^{(0)} - \frac{10890423}{25193600}\Delta t\tilde{L}\left(u^n\right) + \frac{951}{1600}u^{(1)} + \frac{5000}{7873}\Delta t L\left(u^{(1)}\right) \\
u^{(3)} =& \frac{53989}{2500000}u^n - \frac{102261}{5000000}\Delta t\tilde{L}\left(u^n\right) + \frac{4806213}{20000000}u^{(1)} \\
& - \frac{5121}{20000}\Delta t\tilde{L}\left(u^{(1)}\right) + \frac{23619}{32000}u^{(2)} + \frac{7873}{10000}\Delta t L\left(u^{(2)}\right) \\
u^{n+1} =& \frac{1}{5}u^n + \frac{1}{10}\Delta t L\left(u^n\right) + \frac{6127}{30000}u^{(1)} + \frac{1}{6}\Delta t L\left(u^{(1)}\right) + \frac{7873}{30000}u^{(2)} + \frac{1}{3}u^{(3)} + \frac{1}{6}\Delta t L\left(u^{(3)}\right)
\end{aligned} \tag{3.46}$$

where

$$u^{n+1} = u^n - \Delta t\tilde{L}\left(u^n\right) \tag{3.47}$$

and $L(u,t)$ is a spatial discretization operator.

3.3.5.2 | Adams-Bashforth scheme

The Adams–Bashforth methods are explicit linear multistep methods. The two-step Adams–Bashforth method is defined as:

$$u^{n+2} = u^{n+1} + \frac{3}{2}hf\left(t^{n+1}, u^{n+1}\right) - \frac{1}{2}hf\left(t^n, u^n\right) \tag{3.48}$$

where $u' = f(t,u)$ with $u(t^0) = u^0$ and $h = t^n - t^{n-1} = t^{n+1} - t^n$.

3.4 | Results and Discussions

3.4.1 | Preliminary tests on WENO scheme

A preliminary test using the 5th order WENO scheme is performed on 2D Euler equations. The well-matching result by WENO can not only prove the correctness

of the CFD currently under design but also be used as a reference to compare with results by the MUSCL scheme with a limiter.

3.4.1.1 | Double Shock Problems

Two-dimensional Riemann problems of gas dynamics are 17 configurations initialized by constant in each quadrant, with one elementary wave, a 1D shock, a 1D rarefaction, or a 2D contact discontinuity shown on each interface.

The Riemann problem is solved with initial data as

$$(p,\rho,u,v)(x,y,0) = \begin{cases} (p_1,\rho_1,u_1,v_1)\,, & \text{if } x > 0.5 \text{ and } y > 0.5 \\ (p_2,\rho_2,u_2,v_2)\,, & \text{if } x < 0.5 \text{ and } y > 0.5 \\ (p_3,\rho_3,u_3,v_3)\,, & \text{if } x < 0.5 \text{ and } y < 0.5 \\ (p_4,\rho_4,u_4,v_4)\,, & \text{if } x > 0.5 \text{ and } y < 0.5 \end{cases} \tag{3.49}$$

The 17 configurations are separated by the three types of 1D centered waves, namely, rarefaction- ($\vec{R}$), shock- ($\overleftarrow{S}$) and contact waves ($J^{\pm}$). The arrow ($\vec{\cdot}$) and ($\overleftarrow{\cdot}$) superscript referring to negative, positive contacts. Each configuration is computed on a 400×400 grid domain.

Numerical results with each initial data given in[30] are shown as follows and listed below. For each configuration, the numerical solution is analyzed and shown by contour plots in Fig. 3.7 - 3.23. Density contour lines are set as reference[64] for comparison.

- Configuration 1

$$\begin{array}{ccc} & \vec{R_{21}} & \\ \vec{R_{32}} & & \vec{R_{41}} \\ & \vec{R_{34}} & \end{array}$$

with the initial condition:

$$\begin{array}{llll} p_2 = 0.4 & \rho_2 = 0.5197 & p_1 = 1 & \rho_1 = 1 \\ u_2 = -0.7259 & v_2 = 0 & u_1 = 0 & v_1 = 0 \\ p_3 = 0.0439 & \rho_3 = 0.1072 & p_4 = 0.15 & \rho_4 = 0.2579 \\ u_3 = -0.7259 & v_3 = -1.4045 & u_4 = 0 & v_4 = -1.4045 \end{array} \tag{3.50}$$

- Configuration 2

$$\begin{array}{ccc} & \vec{R_{21}} & \\ \overleftarrow{R_{32}} & & \vec{R_{41}} \\ & \overleftarrow{R_{34}} & \end{array}$$

with the initial condition:

$$\begin{array}{llll} p_2 = 0.4 & \rho_2 = 0.5197 & p_1 = 1 & \rho_1 = 1 \\ u_2 = -0.7259 & v_2 = 0 & u_1 = 0 & v_1 = 0 \\ p_3 = 1 & \rho_3 = 1 & p_4 = 0.4 & \rho_4 = 0.5197 \\ u_3 = -0.7259 & v_3 = -0.7259 & u_4 = 0 & v_4 = -0.7259 \end{array} \tag{3.51}$$

- Configuration 3

$$\begin{array}{ccc} & \overleftarrow{S_{21}} & \\ \overleftarrow{S_{32}} & & \overleftarrow{S_{41}} \\ & \overleftarrow{S_{34}} & \end{array}$$

with the initial condition:

$$\begin{array}{llll} p_2 = 0.3 & \rho_2 = 0.5323 & p_1 = 1.5 & \rho_1 = 1.5 \\ u_2 = 1.206 & v_2 = 0 & u_1 = 0 & v_1 = 0 \\ p_3 = 0.029 & \rho_3 = 0.138 & p_4 = 0.3 & \rho_4 = 0.5323 \\ u_3 = 1.206 & v_3 = 1.206 & u_4 = 0 & v_4 = 1.206 \end{array} \tag{3.52}$$

- Configuration 4

$$\begin{array}{ccc} & \overleftarrow{S_{21}} & \\ \vec{S_{32}} & & \overleftarrow{S_{41}} \\ & \vec{S_{34}} & \end{array}$$

with the initial condition:

$$\begin{array}{llll} p_2 = 0.35 & \rho_2 = 0.5065 & p_1 = 1.1 & \rho_1 = 1.1 \\ u_2 = 0.8939 & v_2 = 0 & u_1 = 0 & v_1 = 0 \\ p_3 = 1.1 & \rho_3 = 1.1 & p_4 = 0.35 & \rho_4 = 0.5065 \\ u_3 = 0.8939 & v_3 = 0.8939 & u_4 = 0 & v_4 = 0.8939 \end{array} \tag{3.53}$$

- Configuration 5

$$\begin{array}{ccc} & J_{21}^{-} & \\ J_{32}^{-} & & J_{41}^{-} \\ & J_{34}^{-} & \end{array}$$

with the initial condition:

$$\begin{array}{llll} p_2 = 1 & \rho_2 = 2 & p_1 = 1 & \rho_1 = 1 \\ u_2 = -0.75 & v_2 = 0.5 & u_1 = -0.75 & v_1 = -0.5 \\ p_3 = 1 & \rho_3 = 1 & p_4 = 1 & \rho_4 = 3 \\ u_3 = 0.75 & v_3 = 0.5 & u_4 = 0.75 & v_4 = -0.5 \end{array} \tag{3.54}$$

- Configuration 6

$$\begin{array}{ccc} & J_{21}^{-} & \\ J_{32}^{+} & & J_{41}^{+} \\ & J_{34}^{-} & \end{array}$$

with the initial condition:

$$\begin{array}{llll} p_2 = 1 & \rho_2 = 2 & p_1 = 1 & \rho_1 = 1 \\ u_2 = 0.75 & v_2 = 0.5 & u_1 = 0.75 & v_1 = -0.5 \\ p_3 = 1 & \rho_3 = 1 & p_4 = 1 & \rho_4 = 3 \\ u_3 = -0.75 & v_3 = 0.5 & u_4 = -0.75 & v_4 = -0.5 \end{array} \tag{3.55}$$

- Configuration 7

$$\begin{array}{ccc} & \vec{R}_{21} & \\ J_{32}^{-} & & \vec{R}_{41} \\ & J_{34}^{-} & \end{array}$$

with the initial condition:

$$\begin{array}{llll} p_2 = 0.4 & \rho_2 = 0.5197 & p_1 = 1 & \rho_1 = 1 \\ u_2 = -0.6259 & v_2 = 0.1 & u_1 = 0.1 & v_1 = 0.1 \\ p_3 = 0.4 & \rho_3 = 0.8 & p_4 = 0.4 & \rho_4 = 0.5197 \\ u_3 = 0.1 & v_3 = 0.1 & u_4 = 0.1 & v_4 = -0.6259 \end{array} \tag{3.56}$$

- Configuration 8

$$\begin{array}{ccc} & \overleftarrow{R_{21}} & \\ J_{32}^{-} & & \overleftarrow{R_{41}} \\ & J_{34}^{-} & \end{array}$$

with the initial condition:

$$\begin{array}{llll} p_2 = 1 & \rho_2 = 1 & p_1 = 0.4 & \rho_1 = 0.5197 \\ u_2 = -0.6259 & v_2 = 0.1 & u_1 = 0.1 & v_1 = 0.1 \\ p_3 = 1 & \rho_3 = 0.8 & p_4 = 1 & \rho_4 = 1 \\ u_3 = 0.1 & v_3 = 0.1 & u_4 = 0.1 & v_4 = -0.6259 \end{array} \tag{3.57}$$

- Configuration 9

$$\begin{array}{ccc} & J_{21}^{+} & \\ \vec{R_{32}} & & \vec{R_{41}} \\ & J_{34}^{+} & \end{array}$$

with the initial condition:

$$\begin{array}{llll} p_2 = 1 & \rho_2 = 2 & p_1 = 1 & \rho_1 = 1 \\ u_2 = 0 & v_2 = -0.3 & u_1 = 0 & v_1 = 0.3 \\ p_3 = 0.4 & \rho_3 = 1.039 & p_4 = 0.4 & \rho_4 = 0.5197 \\ u_3 = 0 & v_3 = -0.8133 & u_4 = 0 & v_4 = -0.4259 \end{array} \tag{3.58}$$

- Configuration 10

$$\begin{array}{ccc} & J_{21}^{-} & \\ \vec{R_{32}} & & \vec{R_{41}} \\ & J_{34}^{+} & \end{array}$$

with the initial condition:

$$\begin{array}{llll} p_2 = 1 & \rho_2 = 0.5 & p_1 = 1 & \rho_1 = 1 \\ u_2 = 0 & v_2 = 0.6076 & u_1 = 0 & v_1 = 0.4297 \\ p_3 = 0.3333 & \rho_3 = 0.2281 & p_4 = 0.3333 & \rho_4 = 0.4562 \\ u_3 = 0 & v_3 = -0.6076 & u_4 = 0 & v_4 = -0.4297 \end{array} \tag{3.59}$$

- Configuration 11

$$\begin{array}{ccc} & \overleftarrow{S_{21}} & \\ J_{32}^{+} & & \overleftarrow{S_{41}} \\ & J_{34}^{+} & \end{array}$$

with the initial condition:

$$\begin{array}{llll} p_2 = 0.4 & \rho_2 = 0.5313 & p_1 = 1 & \rho_1 = 1 \\ u_2 = 0.8276 & v_2 = 0 & u_1 = 0.1 & v_1 = 0 \\ p_3 = 0.4 & \rho_3 = 0.8 & p_4 = 0.4 & \rho_4 = 0.5313 \\ u_3 = 0.1 & v_3 = 0 & u_4 = 0.1 & v_4 = 0.7276 \end{array} \tag{3.60}$$

- Configuration 12

$$\begin{array}{ccc} & \vec{S_{21}} & \\ J_{32}^{+} & & \vec{S_{41}} \\ & J_{34}^{+} & \end{array}$$

with the initial condition:

$$\begin{array}{llll} p_2 = 1 & \rho_2 = 1 & p_1 = 0.4 & \rho_1 = 0.5313 \\ u_2 = 0.7276 & v_2 = 0 & u_1 = 0 & v_1 = 0 \\ p_3 = 1 & \rho_3 = 0.8 & p_4 = 1 & \rho_4 = 1 \\ u_3 = 0 & v_3 = 0 & u_4 = 0 & v_4 = 0.7276 \end{array} \tag{3.61}$$

- Configuration 13

$$\begin{array}{ccc} & J_{21}^{-} & \\ \overleftarrow{S_{32}} & & \overleftarrow{S_{41}} \\ & J_{34}^{-} & \end{array}$$

with the initial condition:

$$\begin{array}{llll} p_2 = 1 & \rho_2 = 2 & p_1 = 1 & \rho_1 = 1 \\ u_2 = 0 & v_2 = 0.3 & u_1 = 0 & v_1 = -0.3 \\ p_3 = 0.4 & \rho_3 = 1.0625 & p_4 = 0.4 & \rho_4 = 0.5313 \\ u_3 = 0 & v_3 = 0.8145 & u_4 = 0 & v_4 = 0.4276 \end{array} \tag{3.62}$$

- Configuration 14

$$\begin{array}{ccc} & J_{21}^{+} & \\ \overleftarrow{S_{32}} & & \overleftarrow{S_{41}} \\ & J_{34}^{-} & \end{array}$$

with the initial condition:

$$\begin{array}{llll} p_2 = 8 & \rho_2 = 1 & p_1 = 8 & \rho_1 = 2 \\ u_2 = 0 & v_2 = -1.2172 & u_1 = 0 & v_1 = -0.5606 \\ p_3 = 2.6667 & \rho_3 = 0.4736 & p_4 = 2.6667 & \rho_4 = 0.9474 \\ u_3 = 0 & v_3 = 1.2172 & u_4 = 0 & v_4 = 1.1606 \end{array} \tag{3.63}$$

- Configuration 15

$$\begin{array}{ccc} & \vec{R_{21}} & \\ J_{32}^{-} & & \overleftarrow{S_{41}} \\ & J_{34}^{+} & \end{array}$$

with the initial condition:

$$\begin{array}{llll} p_2 = 0.4 & \rho_2 = 0.5197 & p_1 = 1 & \rho_1 = 1 \\ u_2 = -0.6259 & v_2 = -0.3 & u_1 = 0.1 & v_1 = -0.3 \\ p_3 = 0.4 & \rho_3 = 0.8 & p_4 = 0.4 & \rho_4 = 0.5313 \\ u_3 = 0.1 & v_3 = -0.3 & u_4 = 0.1 & v_4 = 0.4276 \end{array} \tag{3.64}$$

- Configuration 16

$$\begin{array}{ccc} & \overleftarrow{R_{21}} & \\ J_{32}^{-} & & \vec{S_{41}} \\ & J_{34}^{+} & \end{array}$$

with the initial condition:

$$\begin{array}{llll} p_2 = 1 & \rho_2 = 1.0222 & p_1 = 0.4 & \rho_1 = 0.5313 \\ u_2 = -0.6179 & v_2 = 0.1 & u_1 = 0.1 & v_1 = 0.1 \\ p_3 = 1 & \rho_3 = 0.8 & p_4 = 1 & \rho_4 = 1 \\ u_3 = 0.1 & v_3 = 0.1 & u_4 = 0.1 & v_4 = 0.8276 \end{array} \tag{3.65}$$

- Configuration 17

$$\begin{array}{ccc} & J_{21}^{-} & \\ \overleftarrow{S_{32}} & & \vec{R_{41}} \\ & J_{34}^{-} & \end{array}$$

with the initial condition:

$$\begin{array}{llll} p_2 = 1 & \rho_2 = 2 & p_1 = 1 & \rho_1 = 1 \\ u_2 = 0 & v_2 = -0.3 & u_1 = 0 & v_1 = -0.4 \\ p_3 = 0.4 & \rho_3 = 1.0625 & p_4 = 0.4 & \rho_4 = 0.5197 \\ u_3 = 0 & v_3 = 0.2145 & u_4 = 0 & v_4 = -1.1259 \end{array} \tag{3.66}$$

3.4.1.2 | Double Mach Reflection

This problem [104] tracks a shock, initially a Mach 10 shock at a 60° angle to a reflecting wall, developing downwards a tube containing a wedge. Two Mach shocks and two contact discontinuities are shown in Fig.3.24,Fig.3.25 after $0.2s$.

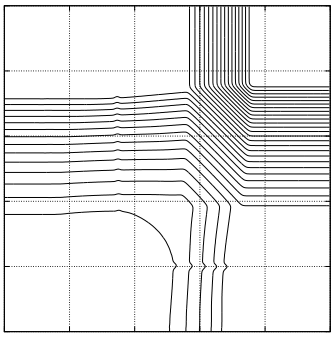


Figure 3.7: Configuration 1. dx=dy=1/399, dt/dx=0.2989

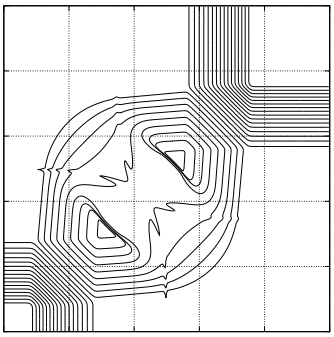


Figure 3.8: Configuration 2. dx=dy=1/399, dt/dx=0.2989

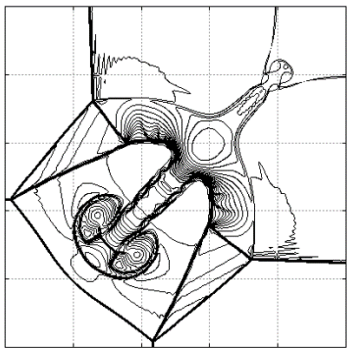


Figure 3.9: Configuration 3. dx=dy=1/399, dt/dx=0.2499

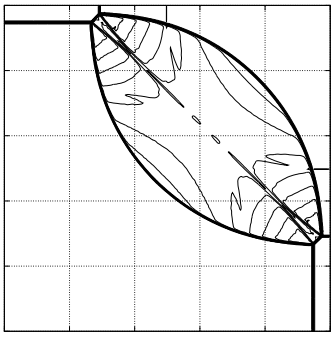


Figure 3.10: Configuration 4. dx=dy=1/399, dt/dx=0.25

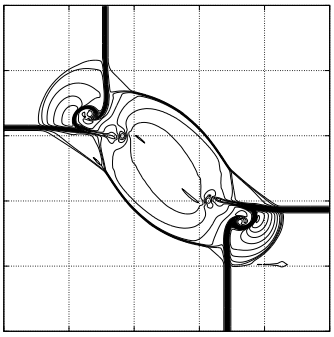


Figure 3.11: Configuration 5. dx=dy=1/399, dt/dx=0.2494

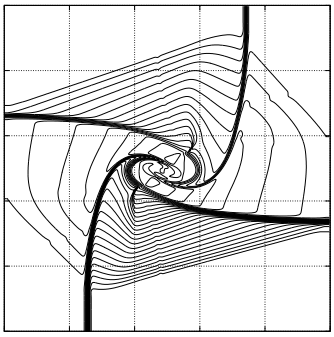


Figure 3.12: Configuration 6. dx=dy=1/399, dt/dx=0.2499

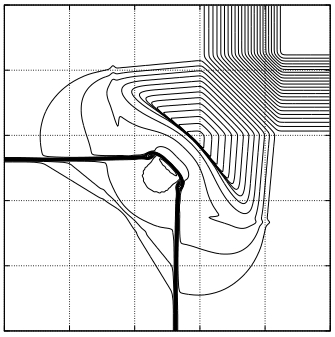


Figure 3.13: Configuration 7. dx=dy=1/399, dt/dx=0.25

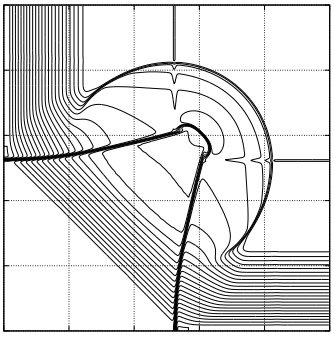


Figure 3.14: Configuration 8. dx=dy=1/399, dt/dx=0.25

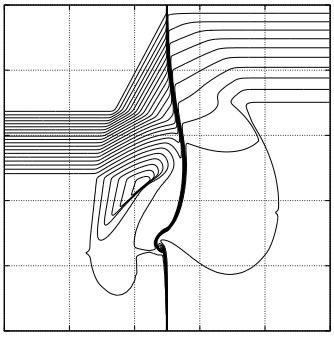


Figure 3.15: Configuration 9. dx=dy=1/399, dt/dx=0.2499

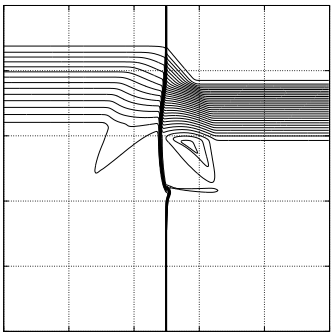


Figure 3.16: Configuration 10. dx=dy=1/399, dt/dx=0.2494

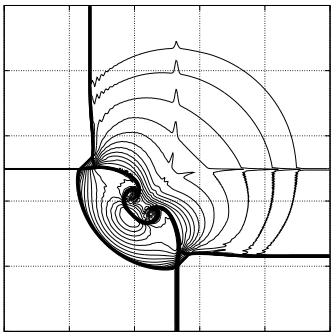


Figure 3.17: Configuration 11. dx=dy=1/399, dt/dx=0.3

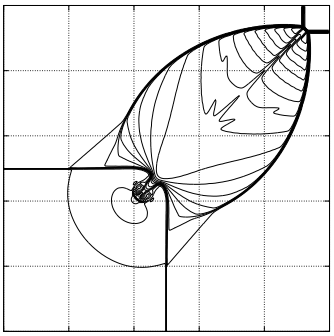


Figure 3.18: Configuration 12. dx=dy=1/399, dt/dx=0.25

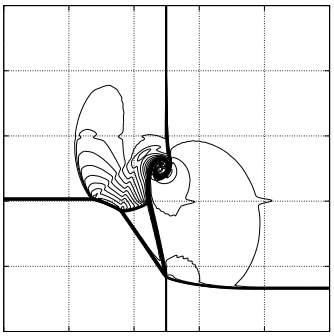


Figure 3.19: Configuration 13. dx=dy=1/399, dt/dx=0.3

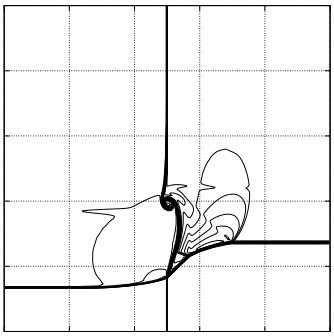


Figure 3.20: Configuration 14. dx=dy=1/399, dt/dx=0.1

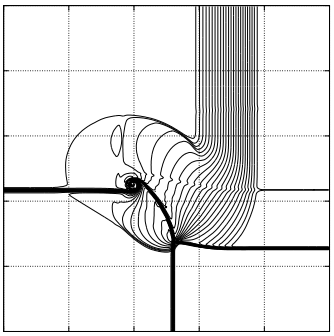


Figure 3.21: Configuration 15. dx=dy=1/399, dt/dx=0.2

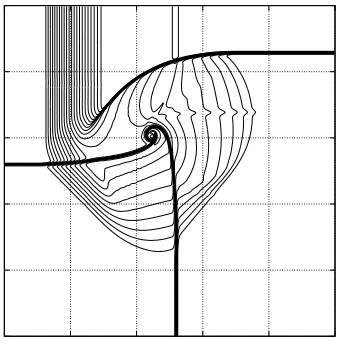


Figure 3.22: Configuration 16. dx=dy=1/399, dt/dx=0.2494

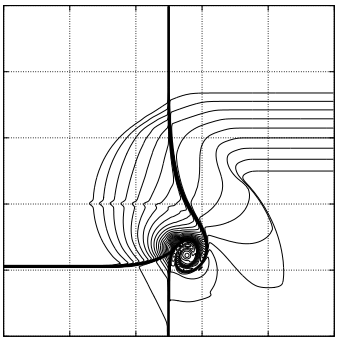


Figure 3.23: Configuration 17. dx=dy=1/399, dt/dx=0.2499

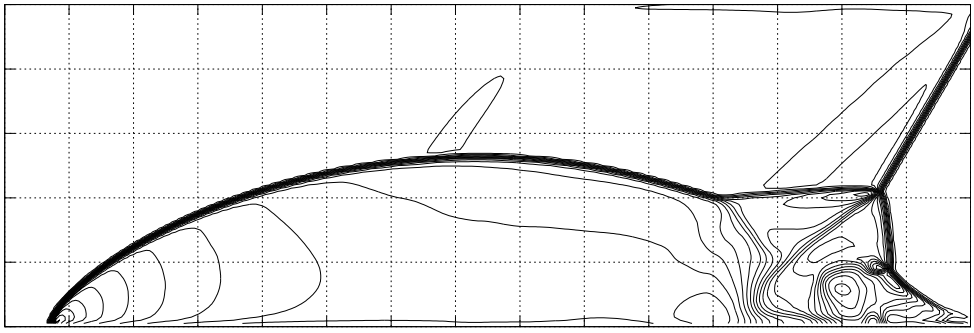


Figure 3.24: Double Mach reflection by 3^{rd} order WENO, dx=dy=1/399,dt/dx=0.6

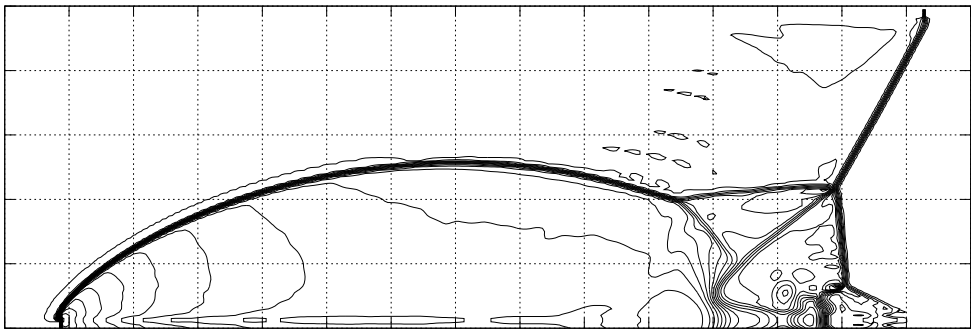


Figure 3.25: Double Mach reflection by 5^{th} order WENO, dx=dy=1/399,dt/dx=0.6

3.4.2 | Comparison with limiter methods

The MUSCL method with limiters is applied. The switching function facilitates the applying the tested limiter on the selected variables. Table 3.2 lists 9 methods of using limiters. Strategy 0 uses primititve variables. Strategy 1-strategy 8 apply characteristic variables (including vorticity, entropy, sound wave) but in difference combination of the way using limiters. Focus on Configuration 3 of the Riemann problem for two-dimensional gas dynamics, results of limiting methods in Fig.3.29-3.37 are compared with each other and the WENO result.

From the comparison, we conclude that: first, a scheme based on the reconstruction of interface values in the characteristic space performs better than that in primitive space. Second, the optimal scheme with limiter use is a third-order Cada

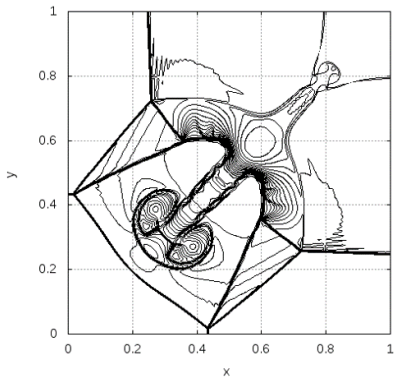


Figure 3.26: Configuration 3. dx=dy=1/399, dt/dx=0.2494, WENO

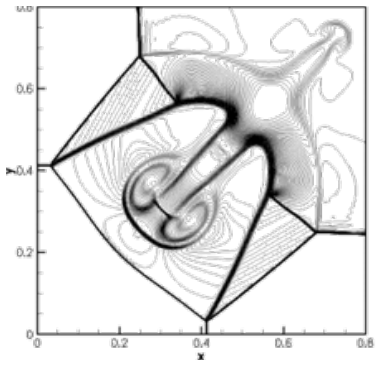


Figure 3.27: Configuration 3. dx=dy=1/399, dt/dx=0.2494, TVD-MUSCL with Van Leer limiter

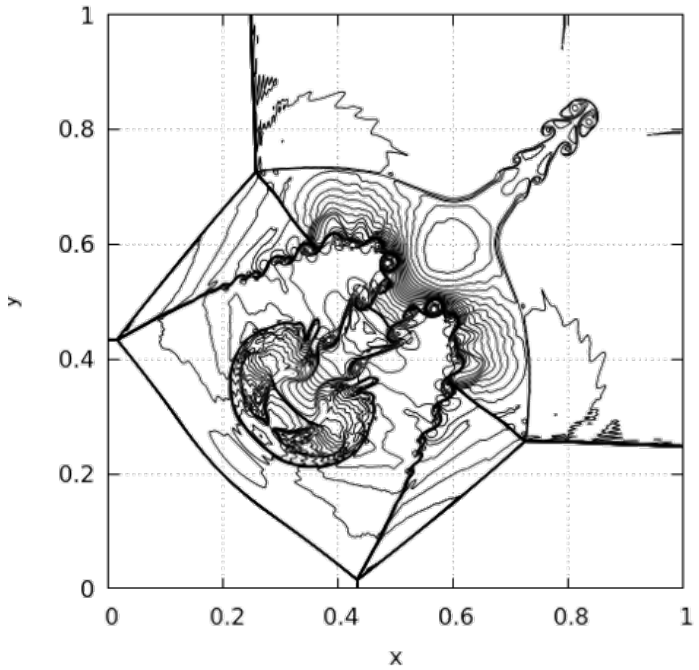


Figure 3.28: Configuration 3. dx=dy=1/799, dt/dx=0.2499, WENO

Table 3.2: Strategy of using limiters

No.	variables Type	**Strategy**
0	primitive	All variables are limited the same using Cada limiter
1	characteristic	All variables are limited the same using Cada limiter
2	characteristic	Vorticity extrapolated without limiter
3	characteristic	Entropy extrapolated without limiter
4	characteristic	Vorticity and entropy extrapolated without limiter
5	characteristic	Vorticity and entropy extrapolated without limiter, MINMOD for sound waves
6	characteristic	Vorticity and entropy extrapolated without limiter, Cada limiter for sound waves
7	characteristic	Vorticity and entropy extrapolated without limiter, Cada limiter for sound -modified variables
8	characteristic	Adams-Bashforth scheme, modified upper value of the Cada limiter

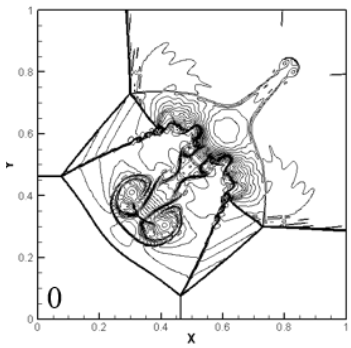


Figure 3.29: Configuration 3. dx=dy=1/399,strategy 0

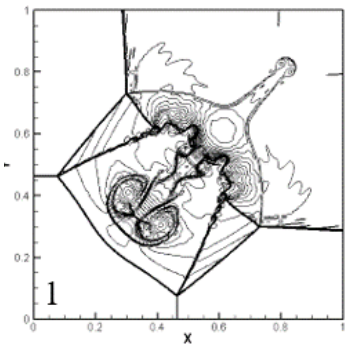


Figure 3.30: Configuration 3. dx=dy=1/399,strategy 1

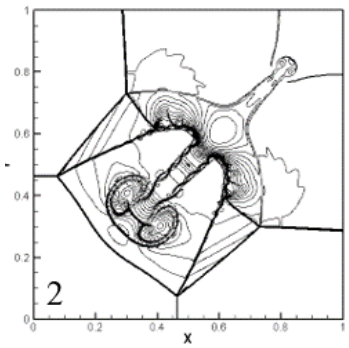


Figure 3.31: Configuration 3. dx=dy=1/399,strategy 2

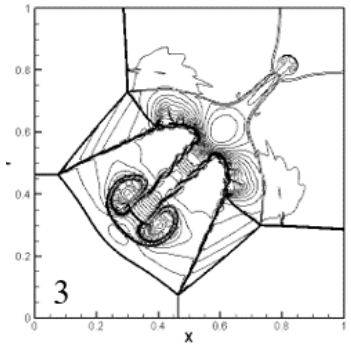


Figure 3.32: Configuration 3. dx=dy=1/399,strategy 3

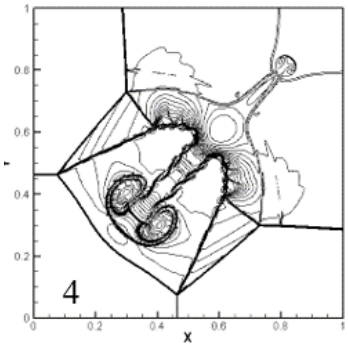


Figure 3.33: Configuration 3. dx=dy=1/399,strategy 4

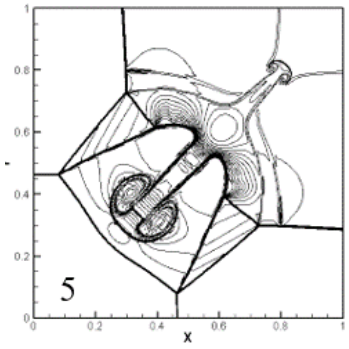


Figure 3.34: Configuration 3. dx=dy=1/399,strategy 5

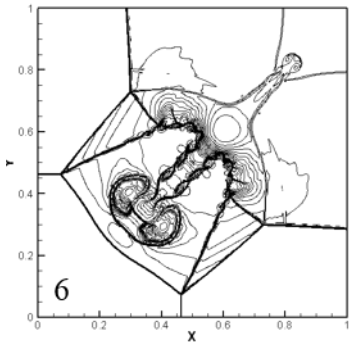


Figure 3.35: Configuration 3. dx=dy=1/399,strategy 6

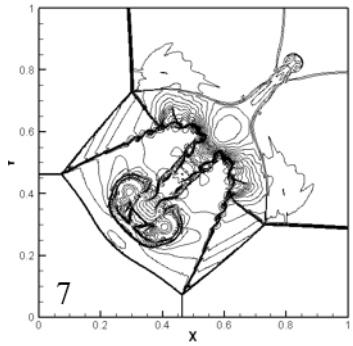


Figure 3.36: Configuration 3. dx=dy=1/399,strategy 7

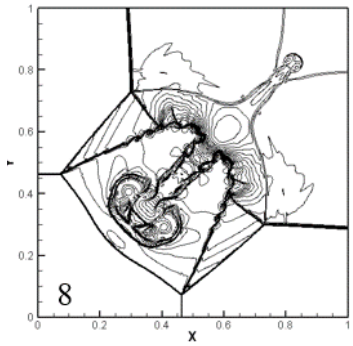


Figure 3.37: Configuration 3. dx=dy=1/399,strategy 8

limiter for sound waves and no limiter for entropy and vorticity waves. This limiter scheme can generally recover the scale structures shown by the WENO scheme. Third, first choosing a reasonable option, the result yields satisfactory results in terms of not damping instabilities in shear layers, as well as performing well for the shocks. Fourth, the scheme performs equally well with TVD-Runge-Kutta and Adams-Bashforth schemes. Fifth, both the optimal limiter scheme and WENO scheme are far superior to the VanLeer, which is too diffusive in that it largely smears out small vortical structures. Sixth, the scheme with Cada limiter runs faster than the WENO scheme. Using a scheme with a limiter rather than WENO can save computational resource. ***Therefore, a 3-point stencil with Cada limiter imposed on barely the sound waves is promising for scaling resolving calculations and is suitable for flux evaluation based on edge/face loops with pre-computed gradients.***



4

Efficient generation of high-quality hex multiblock grids

4.1 | Preface

The second key element for scale resolving of film cooling flows mentioned in Chapter 1 is an efficient generation of high-quality hex multiblock grids. Cooling film with the small size of film geometries compared to the overall size of turbine blades has posed challenges to the meshing techniques.

Current film cooling studies in literature largely rely on commercial software, which requires a great amount of manual work and is time-consuming while good quality grids cannot be guaranteed. There are other attempts at grid generation methods, such as the non-conformal method and immersed mesh block (IMB) method applied to film cooling. The non-conformal method is removing the interface between the film and the hot stream from the exit plane of the film by protruding the

film grids inside the hot stream domain [60], [93], Takahashi[92], Yamane[107],[15]. Although convenient and potentially effective, a non-conformal arrangement between the hot stream and film domain has some drawbacks that the dramatic effect of the interface at the film exit on the flow pattern, documented by Yavuzkurt[108]. Lad's Immersed Mesh Block (IMB) method [55, 56, 58] represented a potential compromise between the flexibility of chimera grids and the quality of multiblock grids for simple layouts by moving the interface away from the film/passage interface. However, non-conformal grids for The LES of the flow in a fan-shaped cooling film requires a careful arrangement of the blocks and a high-order interpolation procedure at block boundaries, see Oliver [73].

An efficient generation of good quality grids for cooled turbine configurations, especially with a large number of films added to the blade surface, is therefore needed. The scale resolving also poses requirements for the generated mesh. First, boundary orthogonality should be imposed. Second, the grid spacing should be small enough to solve the flow structures near the edge between the hole and the hot stream.

Hexahedral meshes are preferred to tetrahedral meshes, despite the flexibility of unstructured tet-dominant grids. Hexahedral grids are preferred because of their favorable error bounds for convection-dominated problems and in boundary layers[78]. For a given mesh density, a hex-dominant grid has fewer edges than a tetrahedral grid using the same set of vertices, and therefore it leads to a smaller operation count [79]. Hex-dominant grids give rise to more regular memory access patterns, which is advantageous on modern computer architectures for memory-bound problems. Finally, hex-dominant grids may require less data storage: a hex

mesh with finite elements requires seven times fewer elements than a tet mesh with the same number of vertices. [79]. The automatic generation of hex-dominant grids for complex geometries is still an open area of research. Due to the difficulty to generate hex mesh for complex configurations, advances have been largely seen with a variety of unstructured hex mesh methods proposed which are then categorized by Owen[75].

Multiblock grids have been historically popular for reasons of accuracy and computational efficiency. However, the generation of good-quality multiblock grids for general configurations is by no means a trivial task, and film cooling geometries can prove to be particularly challenging in locations where a number of film exit holes are crowded in a small area.

This chapter presents a novel method that allows high-quality multiblock grids to be auto-generated for configurations with large numbers of cooling holes. The method combines the usual advantages of multiblock grids, the accuracy of the solution, and efficient execution of the hexahedral meshes with flexibility and robustness normally associated with unstructured structures, whilst avoiding difficulties related to non-conformal interfaces or block placement seen in earlier contributions.

This study adopts the same approach of creating surfaces and extruding branches as [52].

In this study, the algorithm of automatically improving the mesh quality proposed in hexahedral meshing is based on elliptic smoothing. This algorithm adopts a newly proposed control function, rather than relying on Thompson's [96] construction of the control functions, as in the current algorithm the grid on the boundary is not fixed as Thompson [96] did during smoothing. A good reason to leave the grid on the

boundary - free to move along this boundary is to maximise orthogonality, especially in cases like turbines where there is hardly any quadrilateral tessellation for general boundary grids. This section introduces a new method to evaluate control functions for elliptic smoothing that allows the grid distribution to be determined as part of the smoothing process, and to perform elliptic smoothing robustly whilst allowing nodes to slide on the surface.

Section 4.2 contains a published ASME conference paper outlining the mathematical equations of this methodology as well as the procedure of generation of the templated layout, smoothing, refinement, and assembling. The good grid quality of generated mesh together with a comparison with an IMB grid of the same geometry configuration are presented. Section 4.3 presents some more details of the interpolation of elliptic smoothing. By using the optimal interpolation of smoothing, the final mesh of the film cooling cases is also shown. The meshing generator is implemented in an in-house CFD code named 'H4X' and is used in the following papers shown in this thesis.

4.2 | Technical Paper 1

Proceedings of ASME Turbo Expo 2020
Turbomachinery Technical Conference and Exposition
GT2020
June 22-26, 2020, London, England

GT2020-14660

TEMPLATE-BASED HEXAHEDRAL MESH GENERATION FOR TURBINE COOLING GEOMETRIES

Muting Hao, Feng Wang, Joshua Hope-Collins, Max. E. Rife, Luca di Mare

Oxford Thermo-Fluids Institute

Department of Engineering Science

University Of Oxford

UK

ABSTRACT

This paper describes a multiblock grid generation method for turbine cooling geometries. The method is based on the observation that cooling films are essentially branches inserted on a large trunk, represented by the passage or by the cooling duct. The small size of the films compared to the overall size of turbine blades allows simplifications to be introduced with respect to general-purpose trunk and branch algorithms. The grid generation starts from an existing layout for the passage or cooling duct grid and operates on a Cartesian patch of the trunk surface. The patch is hollowed and a templated branch layout is inserted. Padding blocks are created to connect the two layouts into a single, boundary conforming layout. The resulting multiblock grid is then smoothed using a modification of Thompson's Poisson system. The boundary mesh distribution is not prescribed. Instead, boundary orthogonality is enforced and elliptic

 Copyright © 2020 by Rolls-Royce plc.

smoothing is performed on the boundaries as well as inside the volume. The grid size control relies on a novel Newton-like update for the control functions of the Poisson system. The smoothing step is essential in achieving good grid quality throughout and determines, in part, the template for a given configuration. The algorithm is particularly suitable for large arrays of films or other cooling decoration and results show that the proposed method can produce grids of better quality than existing methods.

NOMENCLATURE

Roman symbols

r Cartesian position vector.

P_μ Control function in the μ-transformed coordinate, $\mu \in (\xi, \eta, \zeta)$.

R_u Residual of the Poisson system grid generation equation in the u-direction.

S_μ Residual of the grid spacing condition in the μ transformed direction.

g_{ij} Metric coefficients for the elliptic generation system.

g Trace of the metric tensor for the elliptic generation system.

Greek symbols

Δ_μ Assigned grid spacing in the μ-transformed direction.

ξ Transformed coordinate in the $i-$direction.

η Transformed coordinate in the $j-$direction.

ζ Transformed coordinate in the $k-$direction.

Acronyms

IMB Immersed Mesh Block.

1 INTRODUCTION

The need for rational design methods for turbine cooling devices led to attempts to simulate film cooling flows as soon as practical three-dimensional computational procedures became available: Patankar [1,2], Bergeles [3,4] and Demuren [5,6] reported early calculations of film cooling flows based on the parabolized, semi-parabolized

 Copyright © 2020 by Rolls-Royce plc.

or full Navier-Stokes equations, respectively. In these early contributions the cooling jet was introduced in the computation by assigning the velocity on a group of boundary faces in an otherwise Cartesian grid. Contemporary measurements by Bergeles [7] showed the high sensitivity of the flow development downstream of the film to the velocity profile at the film exit. This result indicated the need to include at least the terminal part of the film volume in calculations of cooling flows.

One way of including the film volume in the calculation of a film cooling flow is to mesh the hot stream and the film separately and apply some interpolation procedure at the interface. White [**?**] adopted two separate domains for the hot stream and the film and placed the interface at the exit of the film. The two solutions were coupled via the pressure field and the film exit velocity field. Choi [8], Fougères [9] and Hall [10] also used overlapping grids with the films meshed as simple cylindrical domains. The interface between the film and the hot stream was removed from the exit plane of the film by protruding the film grids inside the hot stream domain. Lapworth [11] used non-conformal Cartesian grids for the film and the hot stream domains and used hanging nodes to reconcile the two. Tartinville [12] used non-conformal film/passage grids, with interface plane at the film exit. Takahashi [13] also used structured grids arranged in multiple domains with non-conforming interfaces to simulate the full geometry of a cooled turbine blade. Yamane [14] showed how simple overset grids could be combined to generate a number of complex configurations for use in conjugate heat transfer simulations. In a similar spirit, Castillon [15] applied overset grid methods to a number of turbomachinery problems, ranging from casing treatment to film cooling and proposed the use of buffer grids to bridge the gap in resolution between the film grids and the passage grid. Peet [16] managed to use overset grids in a LES study of film cooling flow.

Although convenient and potentially effective, a non-conformal arrangement between hot stream and film domain has some drawbacks. Shih [17] examined issues encountered when using chimera grids for cooling and other flows of interest in propulsion systems and discussed, in particular, interpolation procedures and numerical boundary conditions at the block boundaries. Yavuzkurt [18] documented the dramatic effect of the interface at the film exit on the flow pattern, coolant placement and distribution of turbulent quantities. Lad's Immersed Mesh Block (IMB) method [19–21] represented a potential compromise between the flexibility of chimera grids and the quality of multiblock grids for simple layouts by moving the interface away from the film/passage interface.

 Copyright © 2020 by Rolls-Royce plc.

In later contributions to the IMB method, Jiang [22, 23] showed that marked improvements in the quality of the predictions could be made by appropriate treatment of the fluxes at the boundary of the chimera grid. Recently, Oliver [24] adopted non-comformal grids for their LES of the flow in a fan-shaped cooling film, but with a careful arrangement of the blocks and a high-order interpolation procedure at block boundaries.

For configurations with a small number of films feeding into a channel of relatively simple geometry, structured grids with Cartesian topology for both the film and the hot-stream domain can be easily generated. Zhou [25] used a Cartesian grid well adapted to the uncommon square film geometry adopted in their study. He [26, 27] and later Thakur [28] used a very simple multiblock grid arrangement to compute the film cooling flow around a leading edge. Lakehal [29] also used a two-block layout to study lateral injection from a row of films. Azzi [30, 31] used a simple multiblock layout for a numerical study of compound angle injection. The layout contained no special provisions for the film boundary layer.

The research groups at NASA Glenn and DLR were particularly active in the late 90s and early 2000s in applying increasingly sophisticated multiblock grids to turbine cooling problems. Vogel [32] and Bohn [33] used a multiblock arrangement with conformal block interfaces to study the flow field around the leading edge of a cooled turbine with two slots and an internal coolant duct. Bohn [34] used the same model to study conjugate heat transfer. Vogel [35] reported results on film cooling model development based on results obtained from carefully constructed multiblock grids featuring good resolution of the boundary layer inside the film. Bohn [36] published a CHT study of showerhead configuration using a more sophisticated multiblock arrangement featuring a passage grid, a cooling channel grid and film grids. Theodoridis [37] used a multiblock grid to study a smilar flow, with two leading edge films.

Heidmann [38] used a multiblock grid for a very complex geometry, featuring internal passages as well as twelve rows of cooling films. Heidmann [39] and Rigby [40] presented methods to determine the block layout for, among other configurations, turbine cooling problems. Garg [41] also used multiblock grids with complex layouts for film-cooled geometries. The same author [42] examined a showerhead configuration and discussed the effect grid resolution inside the films and its effect on film cooling predictions. Gaugler [43] and Garg [44] published further results based on very sophisticated multi-block arrangements for cooled turbine blades. A

 Copyright © 2020 by Rolls-Royce plc.

common feature of the NASA Glenn contribution was the need to specify only the layout of the multiblock grid, the indivual block grids being generated independently by any software capable of doing so. Medic [45] used a well designed multiblock layout to study film cooling from fan shaped films on a turbine blade. More recently, Goormans-Francke [46] used conformal grids in the films and around the pins of a cooled turbine blade, but inserted non-conformal interfaces away from the boundaries between components, e.g. at the boundary between a skin domain and a passage domain. Rozati [47] was among the first to address the issue of grid quality in scale resolving simulations of film cooling configurations and opted for a multiblock grid with manually generated layout of a showerhead configuration. Jorg [48] and Renze [49] adopted a similar solution for LES of film cooling on a flat plate.

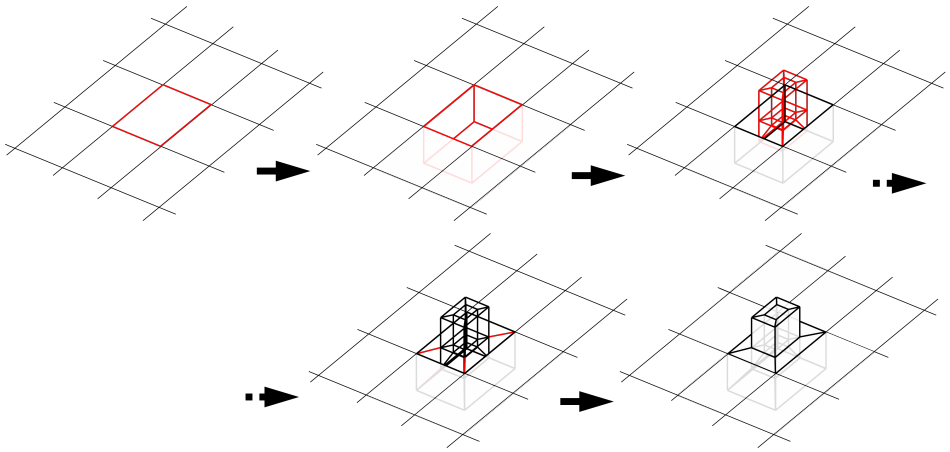


FIGURE 1. Insertion of a film template. *i*) branch patch is identified, *ii*) patch is hollowed out, *iii*) film template is inserted, *iv*) patch interface is stitched back *v*) final layout

Multiblock grids have been historically popular for reasons of accuracy and computational efficiency. However, the generation of good quality multiblock grids for general configurations is by no means a trivial task and film cooling geometries can prove to be particularly challenging in locations where a number of film exit holes are crowded in a small area. Gaugler [43] and Garg's [44] own reports showed a number of highly distorted cells. Charbonnier [50] presented multiblock grids with manually generated block layouts to study film cooling

 Copyright © 2020 by Rolls-Royce plc.

of turbine platforms but large distortions were present in the surface grids. Kusterer [51] reported computations on a pair of inclined holes using a multiblock grid arrangement where high levels of grid distortion in the region around the hole exits could be detected. Gräf [52] also showed similar issues in his LES of a pair of inclined holes.

Bergeles's [7] finding in 1976 also had direct implications for the design process of film-cooled blades as it implied the need to reliably generate good quality grids, including the hot stream, the films and the coolant ducts, for a potentially large number of configurations. Bell [53] discussed the needs of a turbine cooling design system in terms of computational and meshing infrastructure and highlighted the favourable characteristics of unstructured tetrahedral grids from the point of view of a design system. Unstructured grids have since been applied with success to the study of both fundamental physics and engineering solutions in film cooling problems, see for example the contributions by Walters [54], McGovern [55], Hyams [56, 57], York [58, 59], among many. Dawes [60] discussed openly the need for integrating the handling of the geometry, the grid generation and the flow solution. In a later contribution, Dawes [61] showed how oct-trees could be a powerful tool to represent operations on both the geometry and the computational grid to address, among other topics, the design of film cooling systems. Milli [62] presented a method for generating unstructured grids for geometries featuring regular arrays of cooling films, such as those often encountered in turbine cavities, but did not show their application to a fully featured film-cooled turbine blades.

In view of the favourable properties of multiblock grids from the point of view of accuracy and speed of execution - see e.g. Hadade [63] - there is considerable merit in studying the possibility of an efficient and robust method for grid generation for turbine cooling flows. Such a method can be tailored to the geometric properties and the solution requirements of such flows for the purpose of analysis and design calculations.

This paper presents a novel method that allows high-quality multiblock grids to be generated for configurations with large numbers of cooling holes. The method combines the usual advantages of multiblock grids - accuracy of the solution and efficient execution - with flexibility and robustness normally associated with unstructured grids,

 Copyright © 2020 by Rolls-Royce plc.

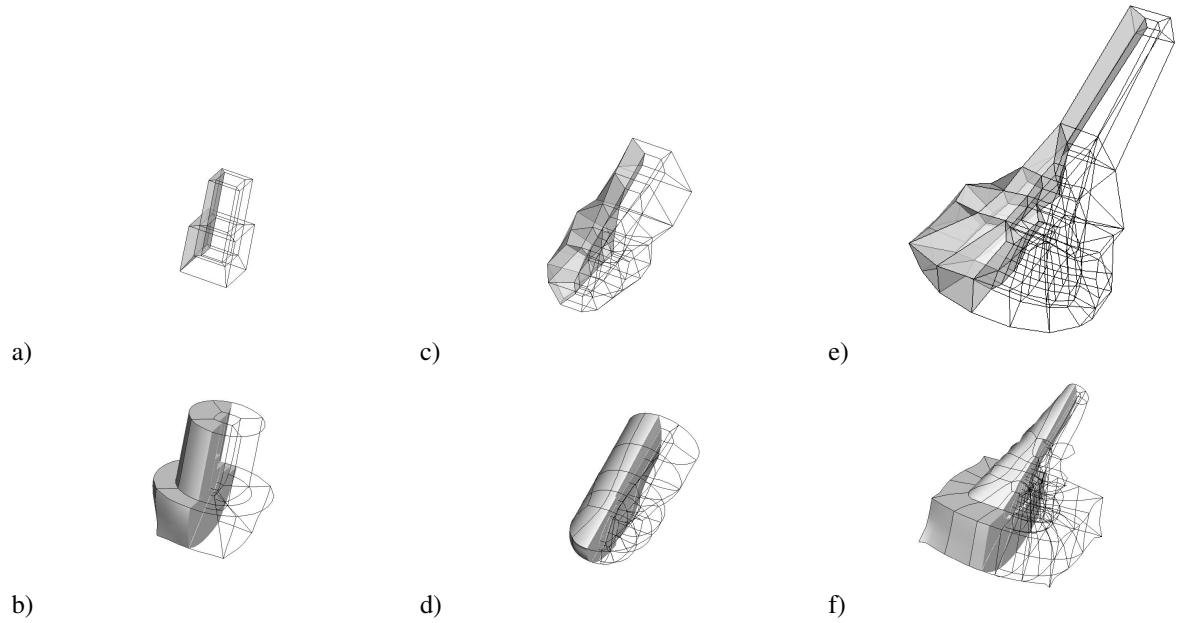


FIGURE 2. Templates for small branches in a trunk-and-branch geometry, such as turbine cooling films. The top row diagrams show the layout and the bottom row diagrams show the mapped and smoothed grid. a-b) orthogonal cylindrical films. c-d) inclined films. e-f) inclined fan-shaped films.

whilst avoiding difficulties related to non-conformal interfaces or block placement seen in earlier contributions. The main elements of the method are introduced in sections 2.1, 2.2 and 2.3. Examples of grids generated and preliminary results are introduced in section 3. Results and plans for future work are laid out in section 4.

2 Method

In analysing the generation of multiblock grids, this paper follows the approach by Heidmann [38], whereby the generation of the block layout and the generation of the block grids are treated as two separate operations. The layout is treated as an unstructured hexahedral grid, whereas the block grids are treated as structured grids of identical size in the three dimensions joined by conformal interfaces. The meshing process starts from an existing passage grid or cooling duct grid, to which the films are added as templated layouts, as outlined in sections 2.1 and 2.2. This procedure is not dissimilar to the generation of the geometry of a cooled turbine blade starting from a clean geometry and then decorating with cooling features. The new layout is then further modified e.g. by

 Copyright © 2020 by Rolls-Royce plc.

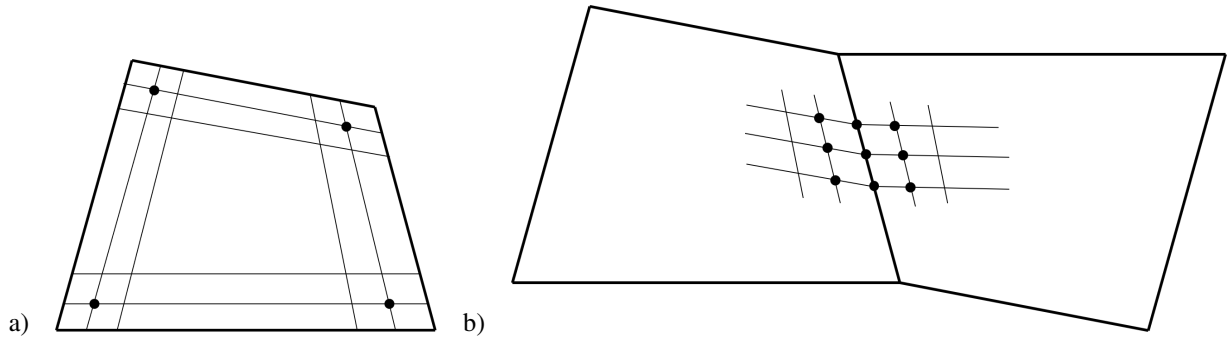


FIGURE 3. Locations for control function evaluation (left). Stencil for the evaluation of equations 1 and 3 near a block boundary (right)

performing local refinement operations or by splitting awkwardly shaped blocks. Finally a mesh is created and smoothed to improve quality and to enforce grid spacing near selected boundaries and boundary orthogonality. The procedure can be repeated any number of times on an already decorated layout to introduce additional layers of detail. Subsections 2.1, 2.2 and 2.3 describe the layout construction, some template layouts for common film geometries and the smoothing operations, respectively.

2.1 Layout generation by template insertion

The main challenge turbine cooling geometries present to the generation of the block layout is the large number of complex geometric features of different scales. Some features, as an example the films, are repeated numerous times with relatively few variations (e.g. setting angle).

Almost all film cooling geometries can be idealised as trunk-and-branch configurations on account of the small size of the cooling films (the branches) compared to the overall dimension of the blade (the trunk). Trunk-and-branch geometries can be meshed effectively by the sweeping and grafting algorithm introduced by Jankovich [**?**] and applied to turbomachinery configurations by Wang [64].

In a large number of cases the film size is not very different from the size of a single block of the trunk grid. Application of Janckovich's [?] grafting algorithm therefore identifies grafting loops containing a very small

 Copyright © 2020 by Rolls-Royce plc.

number of boundary faces. Since the internal flow of the film still requires to be resolved and may need itself an arrangement of blocks, it is more efficient to create a film layout encompassing the film volume and a small transition piece overlapping with the hot-stream or the cooling duct volume. The transition volume attached to the film is constructed in such a way that its faces correspond to the faces of a Cartesian array of blocks (step *i*) in Figure 1). The layouts for the film and the hot-stream (or the cooling duct) are merged by forming a Cartesian cavity in the trunk (step *ii*)) in and connecting the vertices of the cavity thus formed to the vertices of the transition piece on the film layout (steps *iii*) and *iv*)).

2.2 Film templates

The template insertion method described above reduces the problem of generating complex layouts for film cooling geometries to the problem of 1) generating trunk grids for the hot stream and the internal cooling passages and 2) generating a number of suitable layouts for the films. Layouts for different film styles can be created once and for all as templates. The most appropriate template for each film can be selected automatically during the grid generation process based on the film design parameters. Such an approach was advocated by Ross [65] for templating families of configurations with similar geometries.

Different templates are chosen for films inclined at different angles to guarantee that a similar density of blocks is achieved at the film exit, on account of the fact that films inserted at a shallower angle to the surface generate a larger interface than films of similar cross-section inserted orthogonally to the surface. Similar considerations call for different layouts for films with flared exit sections. A selection of viable film templates with transition pieces is shown in Figure 2.

The templates are parameterised with respect to the film axis orientation, film length, average diameter and position of the intersection between the film and the blade (or cooling duct) surface. When the templates are first inserted in the grid layout they do not match the definition of the film geometry. Conformity to the exact definition of the film is enforced during the smoothing step, as explained in the following subsection. The templates normally span half of the length of the film. To create layouts for films passing through walls, two half-films are added separately to the hot-stream and cooling passage domain and these are then joined together.

 Copyright © 2020 by Rolls-Royce plc.

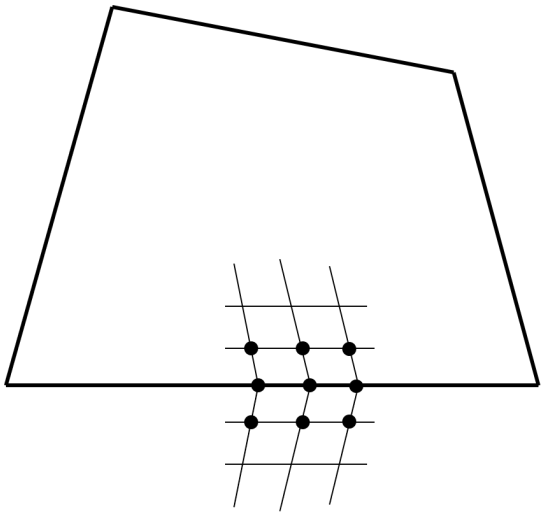


FIGURE 4. Stencil near boundary surfaces

Template insertion is arguably the most important operation to perform on the layout of a multiblock grid in order to represent features such as cooling films, but it is by no means the only one. Additional modifications may be needed to accommodate local refinement, splitting of blocks, or collapse of blocks. The effect of such operations will be shown in the results and examples section 3 but a detailed description of the algorithms and data structures involved falls beyond the scope of this paper.

2.3 Smoothing and size control

Once a layout is generated, the hexahedral grid must be generated. Previous multiblock strategies have mainly relied on interpolation [65], [66], [67], [68], which gives a large degree of control over element size distributions. The success of these methods, however, relies on the block boundaries being in optimal locations, which is difficult to guarantee if a template is used for many different geometries. The distorted grids shown by Charbonnier [50], Kusterer [51] and Gräf [52] were the result of un-optimized placement of block boundaries.

In the present paper, smoothing on the boundary surfaces as well as inside the blocks and at the block boundaries is used to modify the geometry of the block layout and to move the block boundaries in locations where grid distortions can be minimised. The movement of grid points on the boundary surfaces is an important part

 Copyright © 2020 by Rolls-Royce plc.

Algorithm 1 Adding cooling decorations to a multiblock layout.

```
1: procedure TEMPLATE INSERTION WITH SMOOTHING
2: feature:
3: local refinement:
4:     if localfeaturesize < blocksize then
5:         refine locally
6:         goto local refinement
7: template insertion:
8:     Form cavity
9:     Insert templated feature
10:    Create joining elements
11: smooth:
12:    if |dr| > tol then
13:        Update control functions
14:        Smooth elliptically
15:        goto smooth
16:    Optional postprocessing (e.g. block split)
17:    goto feature
18:    end;
```

of the algorithm presented in this paper: see Yao and Stillmann [69] for examples for grid folding caused by the application of smoothing operators with fixed boundary grid distribution.

The overall smoothing strategy is based on Thompson's Poisson system [70]. The Poisson system determines the positions $\mathbf{r}$ of the grid nodes by writing a set of differential equations. In absence of control functions, these equations state the transformed coordinates ξ,η,ζ are harmonic functions of $\mathbf{r}$. Control functions are then introduced to control mesh spacing and the angle formed by grid lines with boundary surfaces - in this case orthogonality is enforced - and are determined iteratively. The control functions are also used in the present work to enforce near wall resolution constraints.

 Copyright © 2020 by Rolls-Royce plc.

The elliptic grid generation PDEs used to smooth the algebraic mesh in three dimensions are:

$$\begin{aligned} R(u) = {} & g_{00}\left(\frac{\partial^2 u}{\partial \xi^2} + P_\xi(\xi,\eta,\zeta)\frac{\partial u}{\partial \xi}\right) + \\ & g_{11}\left(\frac{\partial^2 u}{\partial \eta^2} + P_\eta(\xi,\eta,\zeta)\frac{\partial u}{\partial \eta}\right) + \\ & g_{22}\left(\frac{\partial^2 u}{\partial \zeta^2} + P_\zeta(\xi,\eta,\zeta)\frac{\partial u}{\partial \zeta}\right) + \\ & 2g_{10}\frac{\partial^2 u}{\partial \xi \partial \eta} + \\ & 2g_{20}\frac{\partial^2 u}{\partial \xi \partial \zeta} + \\ & 2g_{21}\frac{\partial^2 u}{\partial \eta \partial \zeta}, \quad u \in (x,y,z) \end{aligned} \tag{1}$$

The determination of the control functions in this paper differs from the technique in [70] because the control functions are only evaluated directly at the vertices of the control volume, whereas Thompson [70] evaluates the control functions over the whole boundary surface. If control functions P_ξ, P_η and P_ζ are known, then the Equations 1 can be used to update x, y, z. Assume now that at a point $\xi = i$, $\eta = j$, $\zeta = k$ only provisional values are known for x, y, z, P_ξ, P_η and P_ζ, but three target grid spacings Δ_ξ, Δ_η and Δ_ζ are given. Then a set of residuals S_μ can be defined representing the deviation of the current grid distribution from the desired grid spacing:

$$S_\mu = \left|\frac{\partial \mathbf{r}}{\partial \mu}\right| - \Delta_\mu \quad \mu \in (\xi,\eta,\zeta) \tag{2}$$

In this case Equations 1 and 2 can provide six equations in the six unknown updates dx, dy, dz, dP_ξ, dP_η and dP_ζ. In order to do so, the equations of the Poisson system can be cast in semi-linearised form, as customary in the

 Copyright © 2020 by Rolls-Royce plc.

iterative solution of elliptic smoothing equations:

$$-2gdu_{ijk} + g_{00}\frac{\partial u}{\partial \xi}dP_{\xi,ijk} + g_{11}\frac{\partial u}{\partial \eta}dP_{\eta,ijk} + g_{22}\frac{\partial u}{\partial \zeta}dP_{\zeta,ijk} = -R(u)$$
$$u \in (x,y,z) \tag{3}$$

Equation 2 can be linearised with respect to perturbations in the coordinates $x_{i,j,k}$, $y_{i,j,k}$, $z_{i,j,k}$ and ignoring perturbation in the position of neighboring grid points to yield:

$$\frac{\partial x}{\partial \mu}dx_{ijk} + \frac{\partial y}{\partial \mu}dy_{ijk} + \frac{\partial z}{\partial \mu}dz_{ijk} = -S_\mu \left|\frac{\partial \mathbf{r}}{\partial \mu}\right| \quad \mu \in (\xi,\eta,\zeta) \tag{4}$$

Equations 3 and 4 now form a system of six linear independent equations in the six unknonws dx, dy, dz, dP_ξ, dP_η and dP_ζ. For the purpose of updating the control functions P_ξ, P_η, P_ζ, Equations 3 and 4 are solved at the corners of the blocks and the corrections for the control functions thus determined are interpolated over the interior of the domain using trilinear interpolation (see Figure 3 a)). If one of the desired grid spacings $\Delta_\mu$is not available because no control is desired over the grid spacing in the direction μ at a block corner, the corresponding entry in the set of Equations 4 is suppressed and replaced by the ansatz $dP_\mu = 0$. Similarly if only one of the Δ_μ spacings is available, then two control function updates are set to nought, and the remaining update is evaluated from the surviving equations in the system 3-4.

The full set of Equations 1-3 can be applied at block boundaries as well as inside the blocks, as long as locally cartesian arrangements of grid lines can be reconstructed. This is always the case for grid nodes at the interface between two blocks but not placed on the block vertices in 2D or on the block edges in 3D (see Figure 3 b)).

When smoothing is performed on the boundaries, Equation 1 is formed with the help of ghost points placed in

 Copyright © 2020 by Rolls-Royce plc.

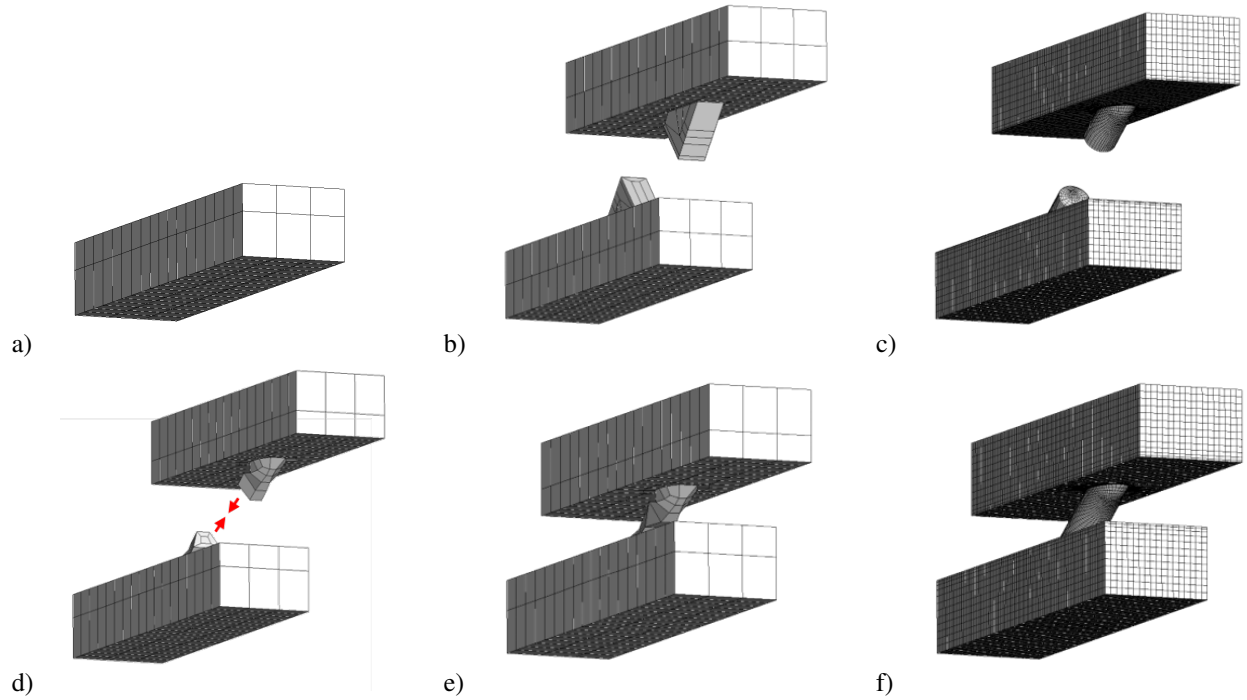


FIGURE 5. Assembly of film layouts starting from clean trunks and joining of film stubs.

such a way as to enforce orthogonality of grid lines to the boundary surface. The corrections dx, dy, dz obtained from Equation 3 are projected onto the surface and transformed into corresponding changes into the parametric coordinates of the point with respect to the surface representation (see Figure 4). The normal component of the displacement vector for each boundary node is modified in order to force the node to reside on the corresponding geometric surface. In this way, the algorithm can be started from a grid that does not conform to the geometric definition of the boundaries. This is always the case when the film templates are first inserted. Smoothing iterations are performed until the 2-norm of the grids displacements are reduced below a given tolerance, which is normally specified as a small fraction of the near wall grid spacing. The method is described in pseudo-code form in Algorithm 1.

The smoothing step modifies the shape of the blocks. As a result the final size, position shape of certain blocks may be considerably different from the initial arrangement of the layout. Because of this feature of the algorithm,

 Copyright © 2020 by Rolls-Royce plc.

the most appropriate layout for each configuration is selected based on its final arrangement after smoothing.

3 Results and examples

Examples of four types of operations are presented in this section: 1) insertion of a film template in an undecorated layout 2) modification of a layout with decorations by repeated splitting operations; 3) modification of a layout by local refinement in the jet region; 4) decoration of a turbine blade with a large number of films. A final example is also shown, illustrating the current method applied to the generation of a cooled turbine section with internal passages.

Figure 5 shows the main steps in the generation of a passing cylindrical film layout and grid. The process starts from a clean layout for the hot stream (a). A template for inclined cylindrical film is inserted on the bottom surface and a similar template is inserted on the top surface of the plenum layout. At this stage the film consists of two separate stubs with rectangular cross section (b). The two half domains are meshed and smoothed to match their real geometry (c). The block layouts for the two domains are updated to reflect the effect of smoothing. The two film stubs have the correct sections and they are capped by a conveniently located interface surface (d). The two halves are now ready to be joined (e). The exit surface of the two stubs is removed and upon smoothing, the grid is redistributed along the length of the film to satisfy near wall distance constraints and orthogonality (f).

Figure 6 shows grid distributions obtained as a result of the operations shown in 5 for a fan-shaped (a) and a cylindrical film (b). The grids conform to the geometry, to a set of specified normal grid spacings and show no distortions or poorly shaped elements.

Figure 7 shows how successive splitting operations can be applied to an existing layout to reduce distortions around singular points, in this case the corners of the annular set of blocks surrounding the film lip. After splitting, the layout is meshed and smoothed. As a consequence the layout geometry - but not its topology - is modified, as shown in part g) of the figure.

Figure 8 shows how local refinement can be applied to the jet region of the cylindrical and fan-shaped film templates shown in Figures 5 and 6, respectively. The refinement is applied to the layout by three-refinement. The operation leaves a dome-shaped layer of blocks enclosing the jet area of the film and causes the spanwise

 Copyright © 2020 by Rolls-Royce plc.

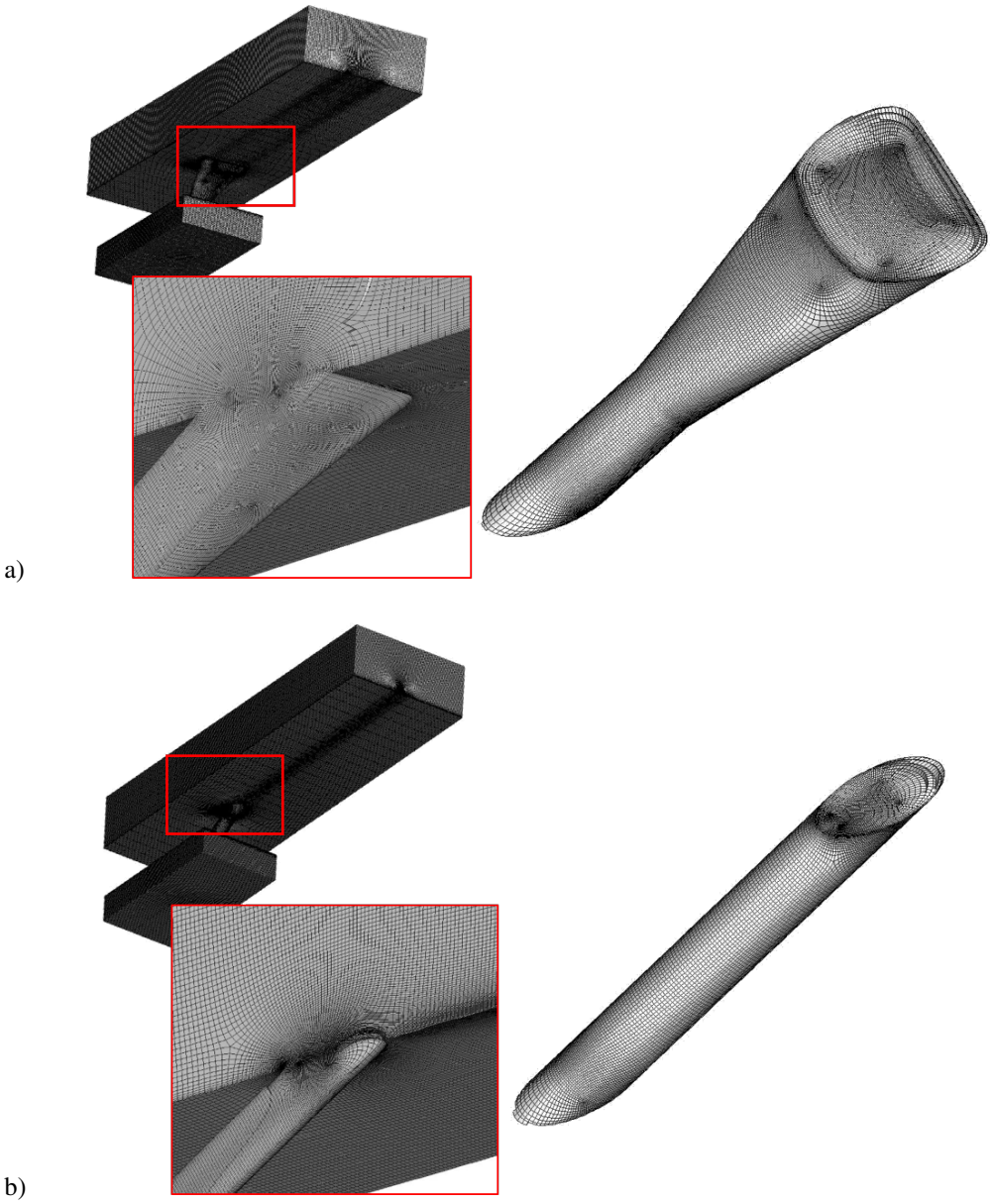


FIGURE 6. Typical appearance of the smoothed layout and final grid for a fan-shaped a) and cylindrical film b).

Copyright © 2020 by Rolls-Royce plc.

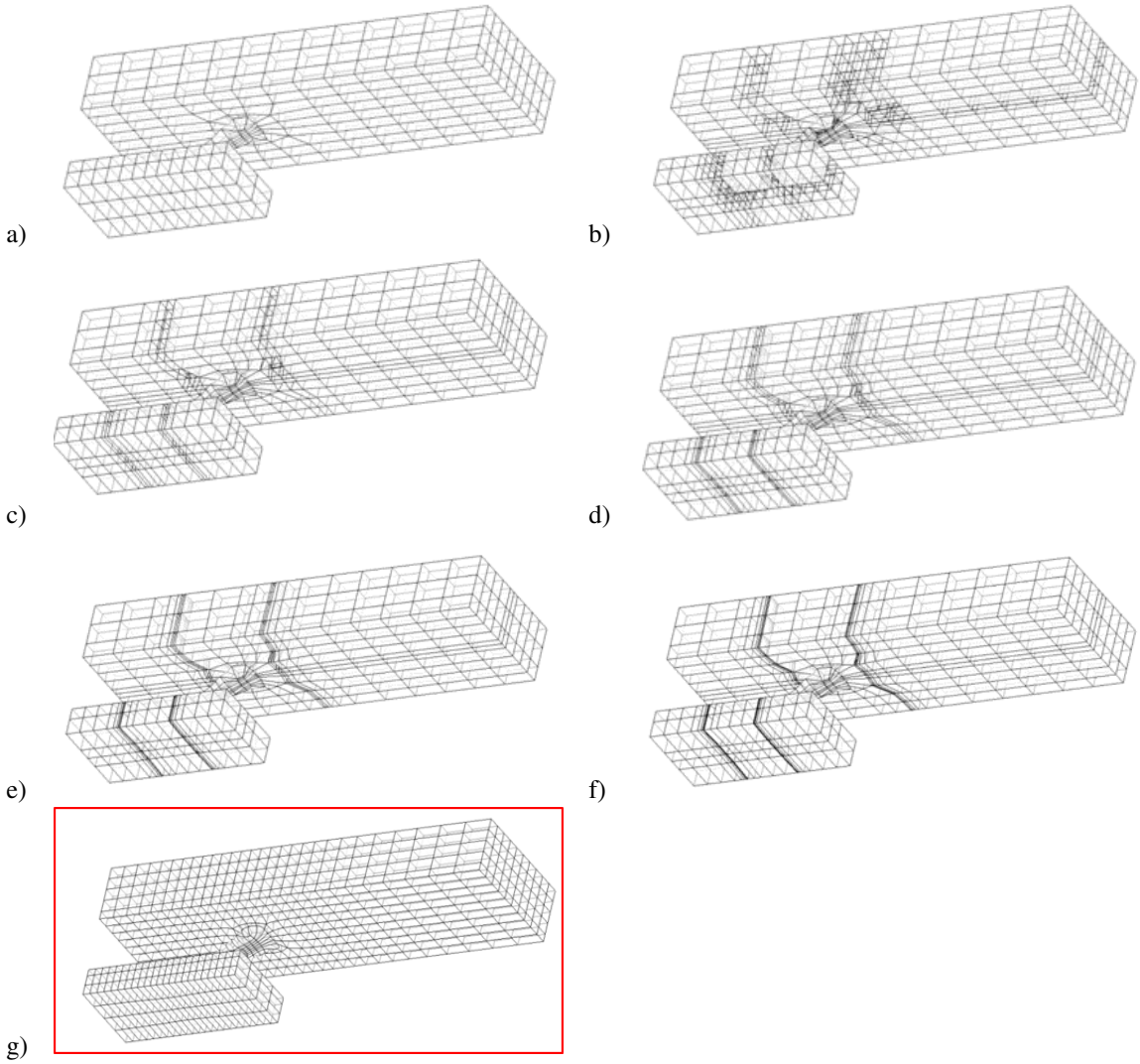


FIGURE 7. Improvement by successive splitting operations (a-f) and final smoothing (g) of a fan-shape film layout.

resolution downstream of the film to be higher than the resolution upstream of it. Additionally, the curvature of the grid lines of the dome-shape layer causes the elliptic smoothing operator to cluster the grid lines in the jet area, even though no attraction is applied there.

Figure 9 shows the sequence of steps followed to add a large array of films to the surfaces of an un-decorated

 Copyright © 2020 by Rolls-Royce plc.

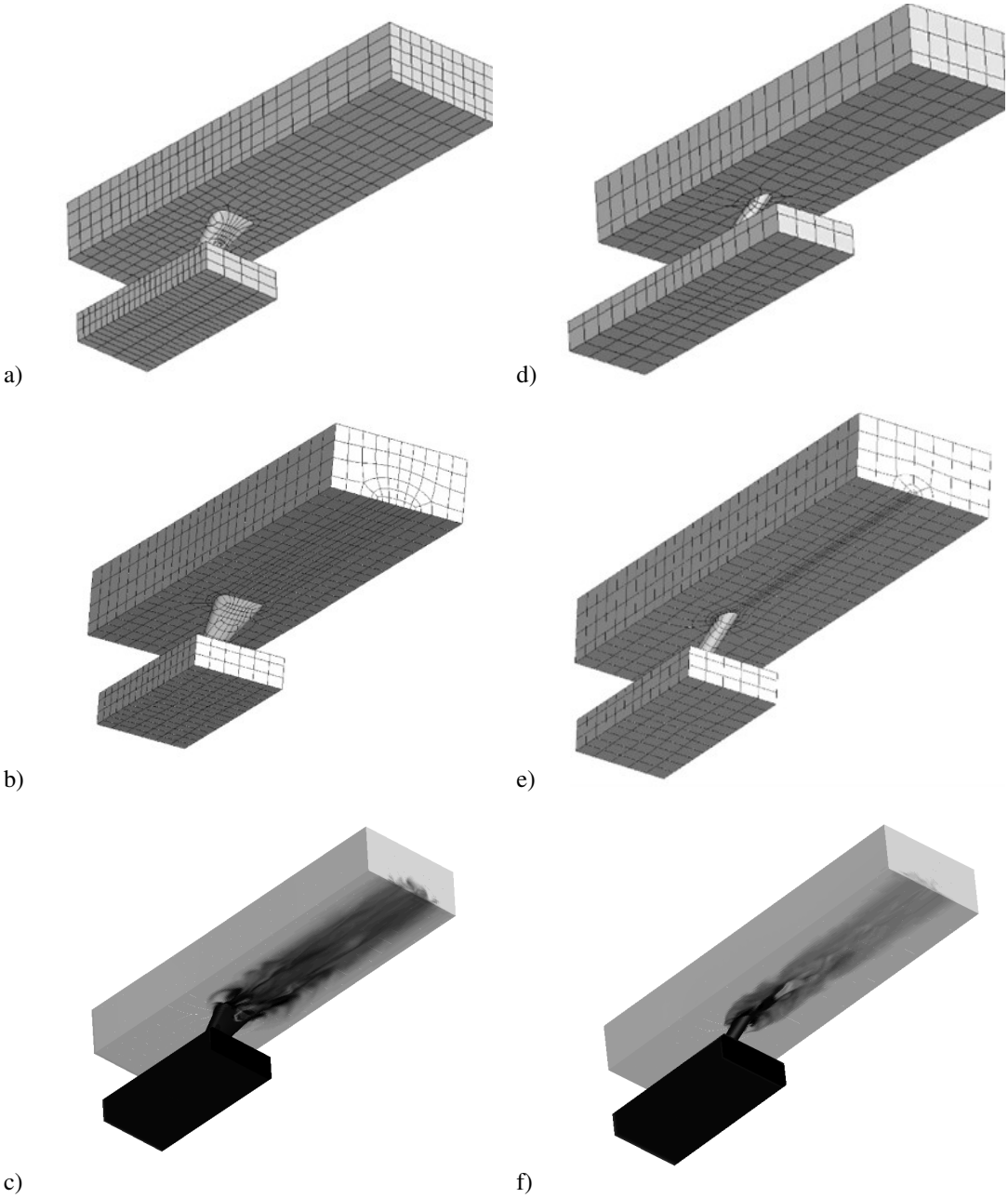


FIGURE 8. Improvement by local refinement in the jet region of a fan shape (a-b) and cylindrical (d-e) film. The contours in c) and f) show nondimensional temperature contours for LES simulations running on the same grids at blow ratio M=1.0.

 Copyright © 2020 by Rolls-Royce plc.

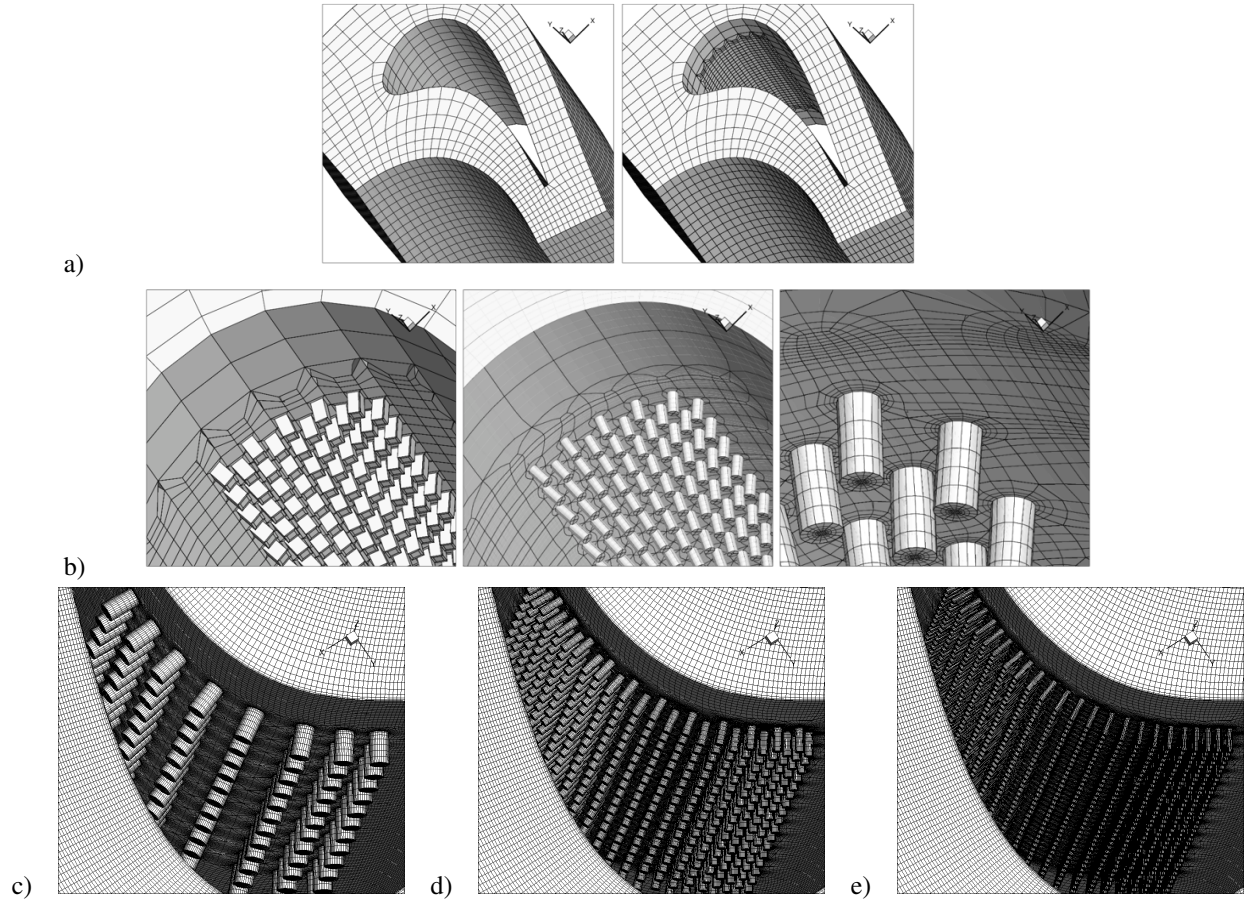


FIGURE 9. Decoration of a turbine blade surface with a large array of cooling films: a) starting layout, 3-refinement and application of the film layouts; b) surface mapping and elliptically smoothed grid; (c-e) similar layout with 96, 432 and 864 films.

turbine blade grid. The initial layout features blocks larger than the individual films to be added. Therefore three-refinement is first applied to the patch that needs to be decorated (Figure 9 a). The refined patch is then decorated by inserting an orthogonal film layout in alternate faces to create an effusion-cooled patch with diamond film arrangement. At this stage the film surfaces are not mapped and the films resemble small prismatic stubs. The layout is now ready to receive a grid and to be smoothed. Boundary conformity is enforced during the smoothing step, which turns the prismatic stub films into correctly shaped cylindrical films. Parts c), d) and e) show the

 Copyright © 2020 by Rolls-Royce plc.

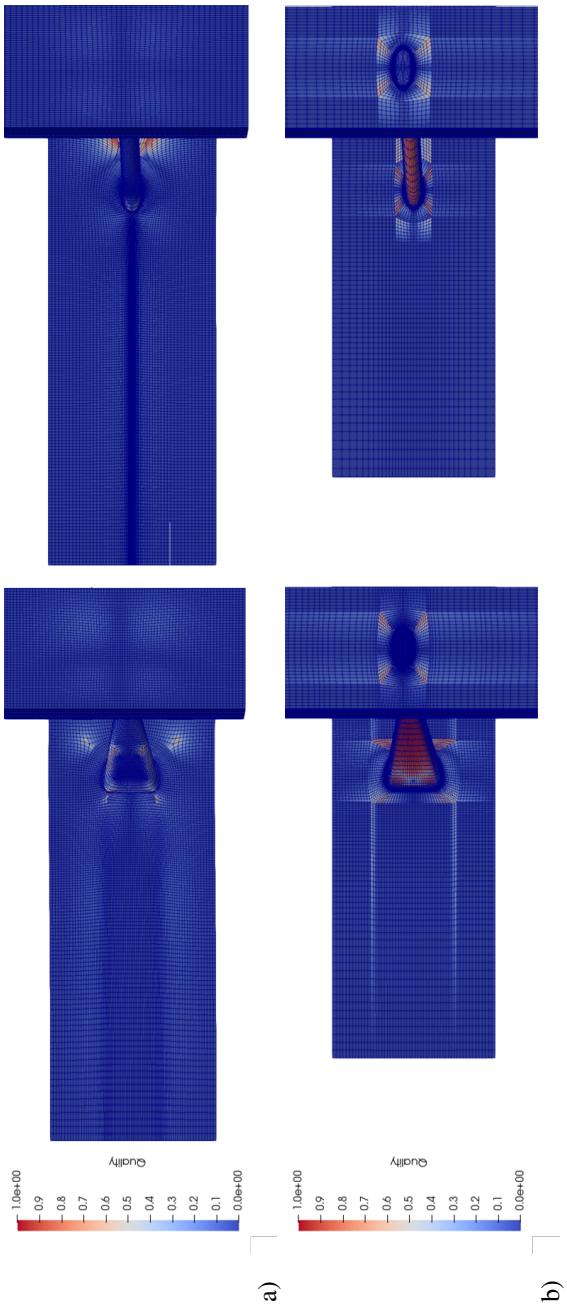


FIGURE 10. Comparison of grid skewness for a fan-shaped and a cylindrical film by a) current method b) commercial package, data from Jiang *et al.* [23].

Copyright © 2020 by Rolls-Royce plc.

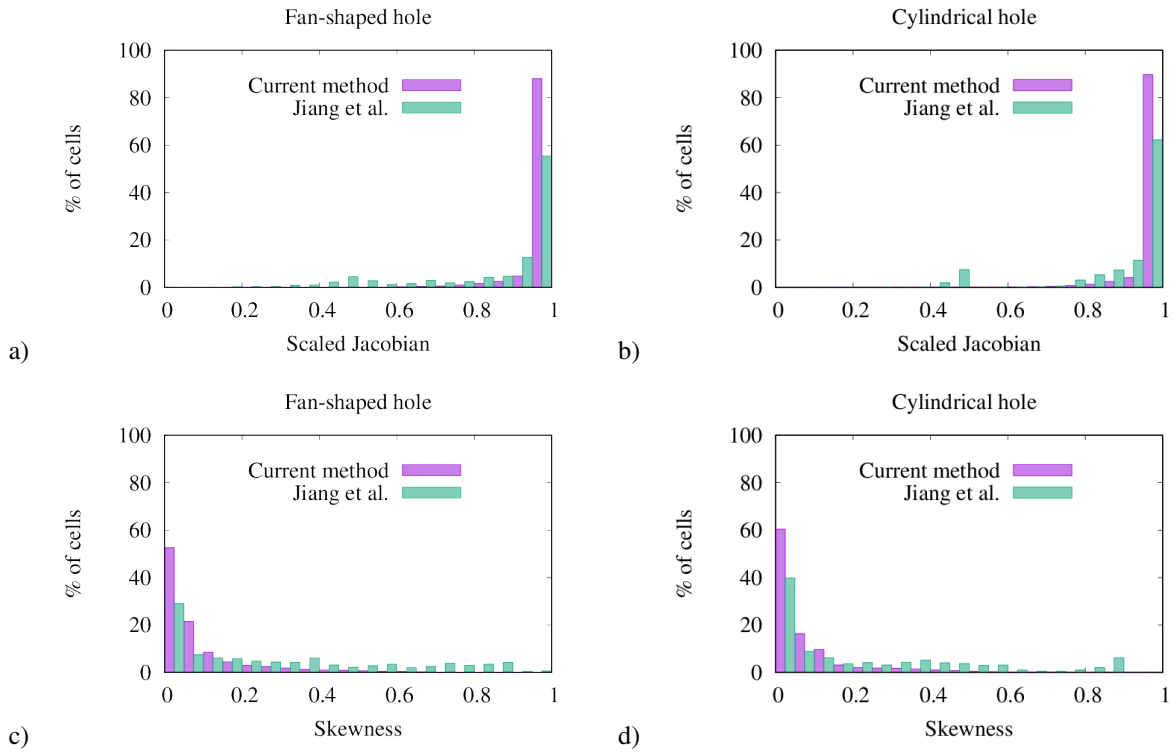


FIGURE 11. Histograms of scaled jacobian (a,b) and skewness (c,d) distribution for cylindrical (a,c) and fan-shaped films (b,d).

result of a similar procedure applied to the pressure side of the same turbine covering a patch spanning 25% of the surface with 96, 432 and 864 films. The total area of the films is kept constant.

Figure 10 shows skewness distributions and Figure 11 shows scaled jacobian and skewness histograms. The quantities are computed for cylindrical and fan-shaped films and comparisons are drawn between grids generated following the authors' method and grids generated by an expert user operating a commercial package and published in Jiang *et al.* [23]. All grids resolve the films with 30 hexahedra across the film diameter in the metering section and have the same near-wall spacing and expansion ratio. All grids introduced a refined region in the jet area to capture the behavior of the coolant downstream of the film exit and its mixing with the main flow. The grids generated by the proposed method contain 453168 and 455328 cells for the cylindrical and fan-shape film

 Copyright © 2020 by Rolls-Royce plc.

respectively, whereas the grids generated by commercial software contain 527651 and 1468048 cells, respectively.

The method proposed by the authors gives scaled Jacobian more concentrated around 1, and skewness more concentrated on 0. For both geometries, the proposed method creates better quality quads around the film exit, including in the jet area and around junction points, compared to those generated by the commercial package. Only a small area upstream of the film inlet in the coolant plenum exhibits normally higher skewness. This area is however far from the film inlet and the flow behaviour there is of little interest. Finally, for fan-shaped films, the proposed method saves almost two thirds of the grid cells while presenting better grid quality due to local refinement and smoothing techniques. Computing time required is therefore largely reduced, and the computation for the whole engine with multiple films will benefit more. Furthermore, the local refinement technique adopted in the area enclosing the jet and inside the hole largely automates the grid generation operations, thus saving the meshing time.

4 Conclusions

The efficient generation of good quality multiblock grids for cooled turbine configurations is a task fraught with difficulties, expecially if a large number of films need to be added to the surface of a blade or a cooling duct. This capability is critical in view of modern trends in cooling devices featuring very large numbers of films and pillars imposing even more demands on the mesh generation system. An efficient method for the generation of good quality grids for such configurations is therefore called for.

This paper proposes a method based on a combination of templated layouts and elliptic smoothing with boundary movement and attraction. The insertion of templates is performed efficiently by exploiting the relative size of the passage and cooling ducts and cooling films. The method is based on general methods for trunk-and branch geometries and it makes use of the small size of film cooling features with respect to the overall turbine geometry. This allows the branches to be connected to relatively small, Cartesian patches on the surface of an existing layout. The film cooling features are applied as templated decorations to existing layouts. Local modifications to the block layout are introduced both prior to the insertion and afterwards to improve grid quality or to generate

 Copyright © 2020 by Rolls-Royce plc.

regions with higher resolution. The smoothing step is based on a novel update method for the control function and on the ability to perform surface smoothing, which is unique to the proposed method. The normal wall spacing is controlled during the attraction step. It was found that the template needs to be suitable to the arrangement of the layout after smoothing, as the smoothing itself can modify the positions of the block vertices in a considerable manner. The results shown in the paper illustrate the better quality achievable with the present method compared to existing methods.

Acknowledgments

The authors gratefully acknowledge Rolls-Royce plc for supporting this work and for granting permission for its publication. The authors thank Dr Yuewen Jiang of the Oxford Thermofluids Institute for providing the grids displayed in figures 10 and 11.

REFERENCES

[1] Patankar, S., Rastogi, A., and Whitelaw, J., 1973. "The effectiveness of three-dimensional film-cooling slots - ii. predictions". *International Journal of Heat and Mass Transfer,* ***16***(9), pp. 1673 – 1681.

[2] Patankar, S. V., Basu, D. K., and Alpay, S. A., 1977. "Prediction of the Three-Dimensional Velocity Field of a Deflected Turbulent Jet". *Journal of Fluids Engineering,* ***99***(4), 12, pp. 758–762.

[3] Bergeles, G., Gosman, A. D., and Launder, B. E., 1978. "The turbulent jet in a cross stream at low injection rates: A three-dimensional numerical treatment". *Numerical Heat Transfer,* ***1***(2), pp. 217–242.

[4] Bergeles, G., Gosman, A. D., and Launder, B. E., 1980. "Double-Row Discrete-Hole Cooling: an Experimental and Numerical Study". *Journal of Engineering for Power,* ***102***(2), 04, pp. 498–503.

[5] Demuren, A., 1983. "Numerical calculations of steady three-dimensional turbulent jets in cross flow". *Computer Methods in Applied Mechanics and Engineering,* ***37***(3), pp. 309 – 328.

[6] Demuren, A. O., Rodi, W., and Sch onung, B., 1986. "Systematic Study of Film Cooling With a Three-Dimensional Calculation Procedure". *Journal of Turbomachinery,* ***108***(1), 07, pp. 124–130.

[7] Bergeles, G., 1976. "Three-dimensional discrete-hole cooling processes : an experimental and theoretical

 Copyright © 2020 by Rolls-Royce plc.

study".

[8] Choi, D., 1993. "A navier-stokes analysis of film cooling in a turbine blade". In 31st Aerospace Sciences Meeting, American Institute of Aeronautics and Astronautics.

[9] Fougères, J. M., and Helder, R., 1994. "Three-Dimensional Navier-Stokes Prediction of Heat Transfer With Film Cooling". Turbo Expo: Power for Land, Sea, and Air.

[10] Hall, E., Topp, D., and Delaney, R. *Aerodynamic/heat transfer analysis of discrete site film-cooled turbine airfoils*.

[11] Lapworth, B., Rose, M., and Nedar, R., 1996. "Calculation of flow and heat transfer near the entrance to film-cooling holes using three-dimensional mesh embedding with solution adaptation". *International Journal of Heat and Fluid Flow,* ***17***(2), pp. 155 – 166.

[12] Tartinville, B., and Hirsch, C., 2008. "Modelling of Film Cooling for Turbine Blade Design". Turbo Expo: Power for Land, Sea, and Air, pp. 2219–2228.

[13] Takahashi, T., Watanabe, K., Fujii, T., and Fujioka, T., 2008. "Numerical Analysis of Temperature Distribution of a Film-Cooled and TBC Coated Blade". Turbo Expo: Power for Land, Sea, and Air, pp. 691–702.

[14] Yamane, T., and Yamamoto, K., 2009. "Introduction of Combined Usage of Overset Grid Method in Conjugate Heat Transfer Simulation". Turbo Expo: Power for Land, Sea, and Air, pp. 737–746.

[15] Castillon, L., Billonnet, G., Riou, J., Péron, S., and Benoit, C., 2014. "A Technological Effect Modeling on Complex Turbomachinery Applications With an Overset Grid Numerical Method". *Journal of Turbomachinery,* ***136***(10), 07. 101005.

[16] Peet, Y. V., and Lele, S. K., 2008. "Near Field of Film Cooling Jet Issued Into a Flat Plate Boundary Layer: LES Study". Turbo Expo: Power for Land, Sea, and Air, pp. 409–418.

[17] Shih, T., 2002. "Overset grids: Fundamental and practical issues". In 20th AIAA Applied Aerodynamics Conference, American Institute of Aeronautics and Astronautics.

[18] Yavuzkurt, S., and Habte, M., 2008. "Effect of Computational Grid on Performance of Two-Equation Models of Turbulence for Film Cooling Applications". Turbo Expo: Power for Land, Sea, and Air, pp. 133–143.

[19] Lad, B., He, L., and Romero, E., 2012. "Validation of the Immersed Mesh Block (IMB) Approach Against

 Copyright © 2020 by Rolls-Royce plc.

a Cooled Transonic Turbine Stage". Turbo Expo: Power for Land, Sea, and Air, pp. 1431–1443.

[20] Lad, B., and He, L., 2012. "Use of an Immersed Mesh for High Resolution Modeling of Film Cooling Flows". *Journal of Turbomachinery,* ***135***(1), 10. 011022.

[21] Lad, B., and He, L., 2013. "An Immersed Mesh Block (IMB) Approach for Conjugate Heat Transfer Predictions". Turbo Expo: Power for Land, Sea, and Air. V03BT11A007.

[22] Jiang, Y., He, L., Capone, L., and Romero, E., 2016. "Investigation of Steady and Unsteady Film-Cooling Using Immersed Mesh Blocks With New Conservative Interface Scheme". Turbo Expo: Power for Land, Sea, and Air.

[23] Jiang, Y., Capone, L., Ireland, P., and Romero, E., 2018. "A Detailed Study of the Interaction Between Two Rows of Cooling Holes". *Journal of Turbomachinery,* ***140***(4), 02. 041008.

[24] Oliver, T. A., Bogard, D. G., and Moser, R. D., 2019. "Large eddy simulation of compressible, shaped-hole film cooling". *International Journal of Heat and Mass Transfer,* ***140***, pp. 498 – 517.

[25] Zhou, J.-m., Salcudean, M., and Gartshore, I. S., 1993. "Prediction of Film Cooling by Discrete-Hole Injection". Turbo Expo: Power for Land, Sea, and Air.

[26] He, P., Salcudean, M., and Gartshore, I. S., 1995. "Computations of film cooling for the leading edge region of a turbine blade model". In ASME 1995 International Gas Turbine and Aeroengine Congress and Exposition, American Society of Mechanical Engineers Digital Collection.

[27] He, P., Licu, D., Salcudean, M., and Gartshore, I. S., 1996. "Leading Edge Film Cooling: Computations and Experiments Including Density Effects". Turbo Expo: Power for Land, Sea, and Air.

[28] Thakur, S., Wright, J., and Shyy, W., 1999. "Convective film cooling over a representative turbine blade leading-edge". *International Journal of Heat and Mass Transfer,* ***42***(12), pp. 2269 – 2285.

[29] Lakehal, D., Theodoridis, G., and Rodi, W., 1998. "Computation of film cooling of a flat plate by lateral injection from a row of holes". *International Journal of Heat and Fluid Flow,* ***19***(5), pp. 418 – 430.

[30] Azzi, A., Abidat, M., Jubran, B. A., and Theodoridis, G. S., 2001. "Film cooling predictions of simple and compound angle injection from one and two staggered rows". *Numerical Heat Transfer, Part A: Applications,* ***40***(3), pp. 273–294.

 Copyright © 2020 by Rolls-Royce plc.

[31] Azzi, A., and Jubran, B., 2003. "Numerical modeling of film cooling from short length stream-wise injection holes". *Heat and Mass Transfer,* ***39***(4), Apr, pp. 345–353.

[32] Vogel, D. T., 1996. "Navier-Stokes Simulation of the Flow Around a Leading Edge Film-Cooled Turbine Blade Including the Interior Cooling System and Comparison With Experimental Data". Turbo Expo: Power for Land, Sea, and Air.

[33] Bohn, D., Kusterer, K., and Sch onenborn, H., 1996. "3-D Numerical Simulation of the Flow Through a Turbine Blade Cascade With Cooling Injection at the Leading Edge". Turbo Expo: Power for Land, Sea, and Air.

[34] Bohn, D. E., Becker, V. J., and Kusterer, K. A., 1997. "3-D Conjugate Flow and Heat Transfer Calculations of a Film-Cooled Turbine Guide Vane at Different Operation Conditions". Turbo Expo: Power for Land, Sea, and Air.

[35] Vogel, D. T., 1998. "Numerical Investigation of the Influence of Specific Vortex Generation on the Mixing Process of Film Cooling Jets". Turbo Expo: Power for Land, Sea, and Air.

[36] Bohn, D. E., Becker, V. J., Kusterer, K. A., and Rungen, A. U., 1998. "Experimental and Numerical Conjugate Investigation of the Blowing-Ratio Influence on the Showerhead Cooling Efficiency". Turbo Expo: Power for Land, Sea, and Air.

[37] Theodoridis, G., Lakehal, D., and Rodi, W., 2001. "Three-dimensional calculations of the flow field around a turbine blade with film cooling injection near the leading edge". *Flow, Turbulence and Combustion,* ***66***(1), Jan, pp. 57–83.

[38] Heidmann, J. D., Rigby, D. L., and Ameri, A. A., 1999. "A Three-Dimensional Coupled Internal/External Simulation of a Film-Cooled Turbine Vane ". *Journal of Turbomachinery,* ***122***(2), 02, pp. 348–359.

[39] Heidmann, J., Ameri, A., Garg, V., and Rigby, D. "Improved modeling capabilities in glenn-ht–the nasa glenn research center general multi-block navier-stokes heat transfer code".

[40] Rigby, D. L., 2003. "Topmaker: A technique for automatic multi-block topology generation using the medial axis".

[41] Garg, V. K., 2000. "Heat transfer on a film-cooled rotating blade". *International Journal of Heat and Fluid*

 Copyright © 2020 by Rolls-Royce plc.

Flow, ***21***(2), pp. 134–145.

[42] Garg, V. K., 2001. "Modeling film-coolant flow characteristics at the exit of shower-head holes". *International Journal of Heat and Fluid Flow,* ***22***(2), pp. 134 – 142.

[43] Gaugler, R. E., and Lee, C.-M., 2001. "Glenn-ht: The nasa glenn research center general multi-block navier-stokes heat transfer code".

[44] Garg, V. K., 2002. "Heat transfer research on gas turbine airfoils at nasa grc". *International Journal of Heat and Fluid Flow,* ***23***(2), pp. 109 – 136.

[45] Medic, G., and Durbin, P. A., 2002. "Toward improved film cooling prediction". *Journal of turbomachinery,* ***124***(2), pp. 193–199.

[46] Goormans-Francke, C., Carabin, G., and Hirsch, C., 2008. "Mesh Generation for Conjugate Heat Transfer Analysis of a Cooled High Pressure Turbine Stage". Turbo Expo: Power for Land, Sea, and Air, pp. 615–625.

[47] Rozati, A., and Tafti, D. K., 2008. "Large-eddy simulations of leading edge film cooling: Analysis of flow structures, effectiveness, and heat transfer coefficient". *International Journal of Heat and Fluid Flow,* ***29***(1), pp. 1 – 17.

[48] Ziefle, J., and Kleiser, L., 2008. "Assessment of a film-cooling flow structure by large-eddy simulation". *Journal of Turbulence,* ***9***, p. N29.

[49] Renze, P., Schr ader, W., and Meinke, M., 2008. "Large-eddy simulation of film cooling flows at density gradients". *International Journal of Heat and Fluid Flow,* ***29***(1), pp. 18 – 34.

[50] Charbonnier, D., Ott, P., Jonsson, M., Cottier, F., and Kobke, T., 2009. "Experimental and Numerical Study of the Thermal Performance of a Film Cooled Turbine Platform". Turbo Expo: Power for Land, Sea, and Air, pp. 1027–1038.

[51] Kusterer, K., Elyas, A., Bohn, D., Sugimoto, T., Tanaka, R., and Kazari, M., 2009. "A Parametric Study on the Influence of the Lateral Ejection Angle of Double-Jet Holes on the Film Cooling Effectiveness for High Blowing Ratios". Turbo Expo: Power for Land, Sea, and Air, pp. 199–211.

[52] Gräf, L., and Kleiser, L., 2011. "Large-eddy simulation of double-row compound-angle film cooling: Setup and validation". *Computers & Fluids,* ***43***(1), pp. 58 – 67. Symposium on High Accuracy Flow Simulations.

 Copyright © 2020 by Rolls-Royce plc.

Special Issue Dedicated to Prof. Michel Deville.

[53] Bell, C., Clarkson, P. J., and Dawes, W. N., 2008. "Improving the Turbine Cooling Conceptual Design Process". Turbo Expo: Power for Land, Sea, and Air, pp. 2631–2640.

[54] Walters, D. K., and Leylek, J. H., 1996. "A Systematic Computational Methodology Applied to a Three-Dimensional Film-Cooling Flowfield". Turbo Expo: Power for Land, Sea, and Air.

[55] McGovern, K. T., and Leylek, J. H., 1997. "A Detailed Analysis of Film Cooling Physics: Part II - Compound-Angle Injection With Cylindrical Holes ". *Journal of Turbomachinery,* ***122***(1), 02, pp. 113–121.

[56] Hyams, D. G., McGovern, K. T., and Leylek, J. H., 1996. "Effects of Geometry on Slot-Jet Film Cooling Performance". Turbo Expo: Power for Land, Sea, and Air.

[57] Hyams, D. G., and Leylek, J. H., 1997. "A Detailed Analysis of Film Cooling Physics: Part III – Streamwise Injection With Shaped Holes ". *Journal of Turbomachinery,* ***122***(1), 02, pp. 122–132.

[58] York, W. D., and Leylek, J. H., 1999. "Numerical Prediction of Mainstream Pressure Gradient Effects in Film Cooling". Turbo Expo: Power for Land, Sea, and Air.

[59] York, W. D., and Leylek, J. H., 2003. "Leading-Edge Film-Cooling Physics – Part III: Diffused Hole Effectiveness ". *Journal of Turbomachinery,* ***125***(2), 04, pp. 252–259.

[60] Dawes, W. N., 2005. "Rapid Prototyping Design Optimisation Using Flow Sculpting". Turbo Expo: Power for Land, Sea, and Air, pp. 991–1000.

[61] Dawes, W., Harvey, S., Fellows, S., Eccles, N., Jaeggi, D., and Kellar, W., 2009. "A practical demonstration of scalable, parallel mesh generation". *47th AIAA Aerospace Sciences Meeting including the New Horizons Forum and Aerospace Exposition*, 01.

[62] Milli, A., and Shahpar, S., 2012. "Padram: Parametric design and rapid meshing system for complex turbomachinery configurations". *ASME Paper No. GT2012-69030*.

[63] Hadade, I., and di Mare, L., 2016. "Modern multicore and manycore architectures: Modelling, optimisation and benchmarking a multiblock cfd code". *Computer Physics Communications,* ***205***, pp. 32 – 47.

[64] Wang, F., and di Mare, L., 2013. "Automated hex meshing for turbomachinery secondary air system". In

 Copyright © 2020 by Rolls-Royce plc.

4.3 | Interpolation of the control function

Control functions are introduced in Technical Paper 1 to control mesh spacing and the angle formed by grid lines with boundary surfaces - in this case orthogonality is enforced - and are determined iteratively. The control functions are also used in the present work to enforce near-wall resolution constraints. Interpolation of the control functions with given spacing distributions is correspondingly proposed. Since the boundary grid positions are not known as a priori, Thompson's interpolation cannot be applied.

The purpose of this part of the work is to build a method for constructing control functions with given normal grid spacing distribution near a set of boundary surfaces. An observation is that the control function for the direction orthogonal to a surface does not affect the position of the nodes on that surface. The problem can be therefore considered as building the control function distribution starting from the knowledge of the control functions at least on the corners of a block.

Interpolation is performed along each direction in turn, shown in Figure 4.1. Figure 4.1 shows six different situations of control function interpolation inside a block (the grey region) in three dimensions ξ, *eta*, and ζ. The three control functions P, Q and R correspond to these three directions ξ, *eta*, and ζ. In each situation, there are three slices on which the specific control function is evaluated (shown in the red region), while in the rest region of this block control functions are interpolated from those evaluation points. Control functions in each direction are first obtained on the opposite near-boundary sections normal to such direction based on which corner points are assigned grid distribution. Assume that nodes in a block

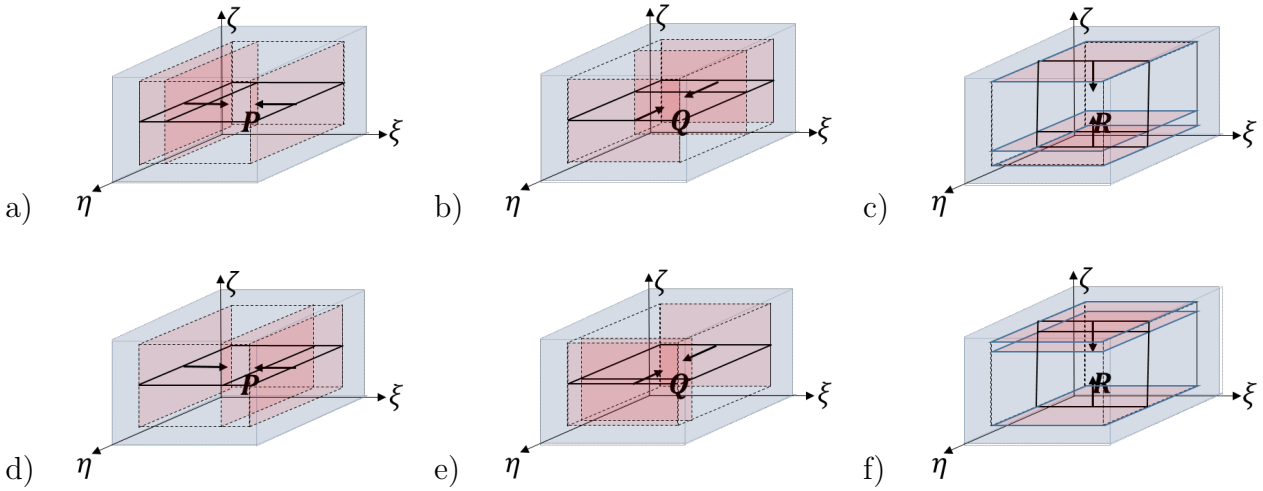


Figure 4.1: Interpolation in three dimensions

are numbered in three directions as $\xi = 0, 1, ..., n$; $\eta = 0, 1, ..., n$; $\zeta = 0, 1, ..., n$. Taking control functions in the ξ direction as an example, sections of $\xi_1 = 1$, $\xi_2 = 2$, $\xi_{n-2} = n - 2$, $\xi_{n-1} = n - 1$ are first located.

Note that the 'corner point' denotes the node one cell away from the block boundaries in those coordinate directions other than the direction in which the control functions are to be evaluated or interpolated, rather than the interaction node between boundaries. The layer on which this algorithm is interpolating the control function is shown in Fig. 4.2. The 'corner points' on the section $\xi_i = i$, for example, are $(i, 1, 1)$, $(i, 1, n-1)$, $(i, n-1, 1)$, $(i, n-1, n-1)$. If a corner point on the first layer near the block boundary is to be assigned a normal space, the proximity corner point on the second layer is to be assigned a normal space scaled with an expansion ratio. The reason why these corner points are one step away from the boundary is that in this way corner points can be effectively positioned by modifying the control function.

On each section to be first assigned, there are generally three situations.

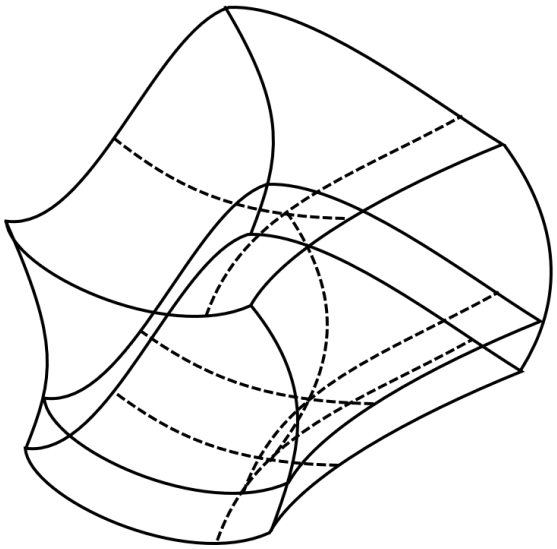


Figure 4.2: Construction of the control function on mesh surfaces and interpolation.

- Situation one: only one of the four corner points is assigned. The control function is evaluated only at the assigned corner point but interpolated at other points in this section by bilinear interpolation.

- Situation two: two corner points in proximity to the same edge are assigned. The control function is evaluated at points along the edge with assigned corner points, whereas control functions in the interior area are linearly interpolated between this assigned edge and the opposite non-controlled edge.

- Situation three: four corner points are all assigned. Control functions are evaluated at every point in this section.

Note that it is impossible to have only three corner points to be assigned for the control functions in the direction normal to their section.

After obtaining control functions throughout four near-boundary sections (two sections on each side), control functions of the interior of the domain are then

interpolated in the direction normal to these sections. Control functions in the ξ direction on interior points $\xi = 3, 4, ..., n-2$, $\eta = 1, 2, ..., n$, $\zeta = 1, 2, ..., n$, that is $P_{\xi,\eta,\zeta}$, are interpolated from $P_{1,\eta,\zeta}$, $P_{2,\eta,\zeta}$, $P_{n-1,\eta,\zeta}$, $P_{n,\eta,\zeta}$. The interpolation in other directions is likewise and omitted in the following description as well. Three options for interior interpolation are given: quadratic interpolation, linear interpolation, and exponential interpolation.

4.3.1 | Quadratic interpolation

Assuming x is the index of the node in the array along which control functions are interpolated, $x = 0, 1, ..., n$, we define the quadratic polynomial $f(x) = ax^2 + bx + c$ as the control function at the x^{th} node in the $n + 1$ array. The distribution of the node control can be categorized as (a) control from the lower x side, and (b) control from the higher x side or no control from either side.

Three known nodes are needed to find the coefficients of the quadratic formula. For (a) condition, the given equations to find solutions are: f(1) equals the control function evaluated on the 1^{st} node by the normal space, f(2) equals the control function evaluated on the 2^{nd} node by the normal space scaled with expansion ratio and f(n-1) equals to the zero control function as the $(n-1)^{th}$ node is not controlled. For (b) condition, the given equations to find solutions are: f(n-1) equals the control function evaluated on the $(n-1)^{th}$ node by the normal space, f(n-2) equals the control function evaluated on the $(n-2)^{th}$ node by the normal space scaled with expansion ratio and f(1) equals to the zero control function as the 1^{st} node is not controlled.

Take the interpolation of the P control function as an example:

$$\begin{cases} f(\xi) = P_{\xi,\eta,\zeta} & \xi = 1, 2, (n-1) \quad \text{Control from lower x} \\ f(\xi) = P_{\xi,\eta,\zeta} & \xi = 1, (n-2), (n-1) \quad \text{Otherwise} \end{cases} \tag{4.1}$$

Writing above in matrix,

if (a)

$$\begin{bmatrix} 1 & 1 & 1 \\ 4 & 1 & 1 \\ (n-1)^2 & n-1 & 1 \end{bmatrix} \begin{bmatrix} a \\ b \\ c \end{bmatrix} = \begin{bmatrix} P_{1,\eta,\zeta} \\ P_{2,\eta,\zeta} \\ P_{n-1,\eta,\zeta} \end{bmatrix} \tag{4.2}$$

if (b),

$$P_{\xi,\eta,\zeta} = a\xi^2 + b\xi + c \quad (\xi = 3, 4, ..., n-2) \tag{4.3}$$

$$\begin{bmatrix} 1 & 1 & 1 \\ (n-2)^2 & n-2 & 1 \\ (n-1)^2 & n-1 & 1 \end{bmatrix} \begin{bmatrix} a \\ b \\ c \end{bmatrix} = \begin{bmatrix} P_{1,\eta,\zeta} \\ P_{n-2,\eta,\zeta} \\ P_{n-1,\eta,\zeta} \end{bmatrix} \tag{4.4}$$

$$P_{\xi,\eta,\zeta} = a\xi^2 + b\xi + c \quad (\xi = 2, 3, ..., n-3) \tag{4.5}$$

The Q and R control function are interpolated likewise.

4.3.2 | Linear interpolation

Assuming x is the index of node in the array along which control functions are interpolated, $x = 0, 1, ..., n$, we define the linear polynomial $f(x) = ax + b$ as the control function at the x^{th} node in the $n + 1$ array. The distribution of the node control can be categorized as (a) control from the lower x side, and (b) control from

the higher x side or no control from either side.

Two known nodes are needed to find the coefficients of the quadratic formula. For (a) condition, f(1) equals the control function evaluated on the 1^{st} node by the normal space, while control functions are linearly interpolated from the 2^{nd} node to the $(n-1)^{th}$ node. Thus, in this case, the given equations to find linear coefficients are: f(2) equals to the control function evaluated on the 2^{nd} node by the normal space scaled with expansion ratio and f(n-1) equals to the zero control function as the $(n-1)^{th}$ node is not controlled. For (b) condition, f(n-1) equals the control function evaluated on the $(n-1)^{th}$ node by the normal space, while control functions are linearly interpolated from the 2^{nd} node to the $(n-2)^{th}$ node. Thus, in this case, the given equations to find linear coefficients are: f(n-2) equals the control function evaluated on the $(n-2)^{th}$ node by the normal space scaled with expansion ratio and f(1) equals to the zero control function as the 1^{st} node is not controlled.

Take the interpolation of the P control function as an example:

$$\begin{cases} f(\xi) = P_{\xi,\eta,\zeta} & \xi = 2, (n-1) \quad \text{Control from lower x} \\ f(\xi) = P_{\xi,\eta,\zeta} & \xi = 1, (n-2) \qquad\quad \text{Otherwise} \end{cases} \tag{4.6}$$

Writing above in matrix,

if (a)

$$\begin{bmatrix} 2 & 1 \\ n-1 & 1 \end{bmatrix} \begin{bmatrix} a \\ b \end{bmatrix} = \begin{bmatrix} P_{2,\eta,\zeta} \\ P_{n-1,\eta,\zeta} \end{bmatrix} \tag{4.7}$$

$$P_{\xi,\eta,\zeta} = a\xi + b \quad (\xi = 3, 4, ..., n-2) \tag{4.8}$$

if (b)

$$\begin{bmatrix} 1 & 1 \\ n-2 & 1 \end{bmatrix} \begin{bmatrix} a \\ b \end{bmatrix} = \begin{bmatrix} P_{1,\eta,\zeta} \\ P_{n-2,\eta,\zeta} \end{bmatrix} \tag{4.9}$$

$$P_{\xi,\eta,\zeta} = a\xi + b \quad (\xi = 2, 3, ..., n-3) \tag{4.10}$$

The Q and R control functions are interpolated likewise.

4.3.3 | Exponential interpolation

Assuming x is the index of the node in the array along which control functions are interpolated, $x = 0, 1, ..., n$, we define the quadratic polynomial $f(x) = e^{(ax+b)} - 1$ as the control function at the x^{th} node in the $n+1$ array. The distribution of the node control can be categorized as (a) control from the lower x side, and (b) control from the higher x side or no control from either side.

Two known nodes are needed to find the coefficients of the quadratic formula. For (a) condition, f(1) equals the control function evaluated on the 1^{st} node by the normal space, while control functions are linearly interpolated from the 2^{nd} node to the $(n-1)^{th}$ node. Thus, in this case, the given equations to find linear coefficients are: f(2) equals to the control function evaluated on the 2^{nd} node by the normal space scaled with expansion ratio and f(n-1) equals to the zero control function as the $(n-1)^{th}$ node is not controlled. For (b) condition, f(n-1) equals the control function evaluated on the $(n-1)^{th}$ node by the normal space, while control functions are linearly interpolated from the 2^{nd} node to the $(n-2)^{th}$ node. Thus, in this case, the given equations to find linear coefficients are: f(n-2) equals the control function

evaluated on the $(n-2)^{th}$ node by the normal space scaled with expansion ratio and f(1) equals to the zero control function as the 1^{st} node is not controlled.

Take the interpolation of the P control function as an example:

$$\begin{cases} f(\xi) = P_{\xi,\eta,\zeta} & \xi = 2, (n-1) \quad \text{Control from lower x} \\ f(\xi) = P_{\xi,\eta,\zeta} & \xi = 1, (n-2) \qquad\quad \text{Otherwise} \end{cases} \tag{4.11}$$

Writing above in matrix,

if (a)

$$\begin{bmatrix} 2 & 1 \\ n-1 & 1 \end{bmatrix} \begin{bmatrix} a \\ b \end{bmatrix} = \begin{bmatrix} log(P_{2,\eta,\zeta}+1) \\ log(P_{n-1,\eta,\zeta}+1) \end{bmatrix} \tag{4.12}$$

$$P_{\xi,\eta,\zeta} = e^{a\xi+b} - 1 \quad (\xi = 3, 4, ..., n-2) \tag{4.13}$$

if (b)

$$\begin{bmatrix} 1 & 1 \\ n-2 & 1 \end{bmatrix} \begin{bmatrix} a \\ b \end{bmatrix} = \begin{bmatrix} log(P_{1,\eta,\zeta}+1) \\ log(P_{n-2,\eta,\zeta}+1) \end{bmatrix} \tag{4.14}$$

$$P_{\xi,\eta,\zeta} = e^{a\xi+b} - 1 \quad (\xi = 2, 3, ..., n-3) \tag{4.15}$$

The Q and R control functions are interpolated likewise.

4.3.4 | Results

Fig. 4.3 compares the generated mesh on a three-block channel by using different interpolation of smoothing, with an expansion ratio of 1,2, 1.4, and 1.6 used. The top 9 figures in Fig. 4.3 are showing the P control function, whereas the bottom 9

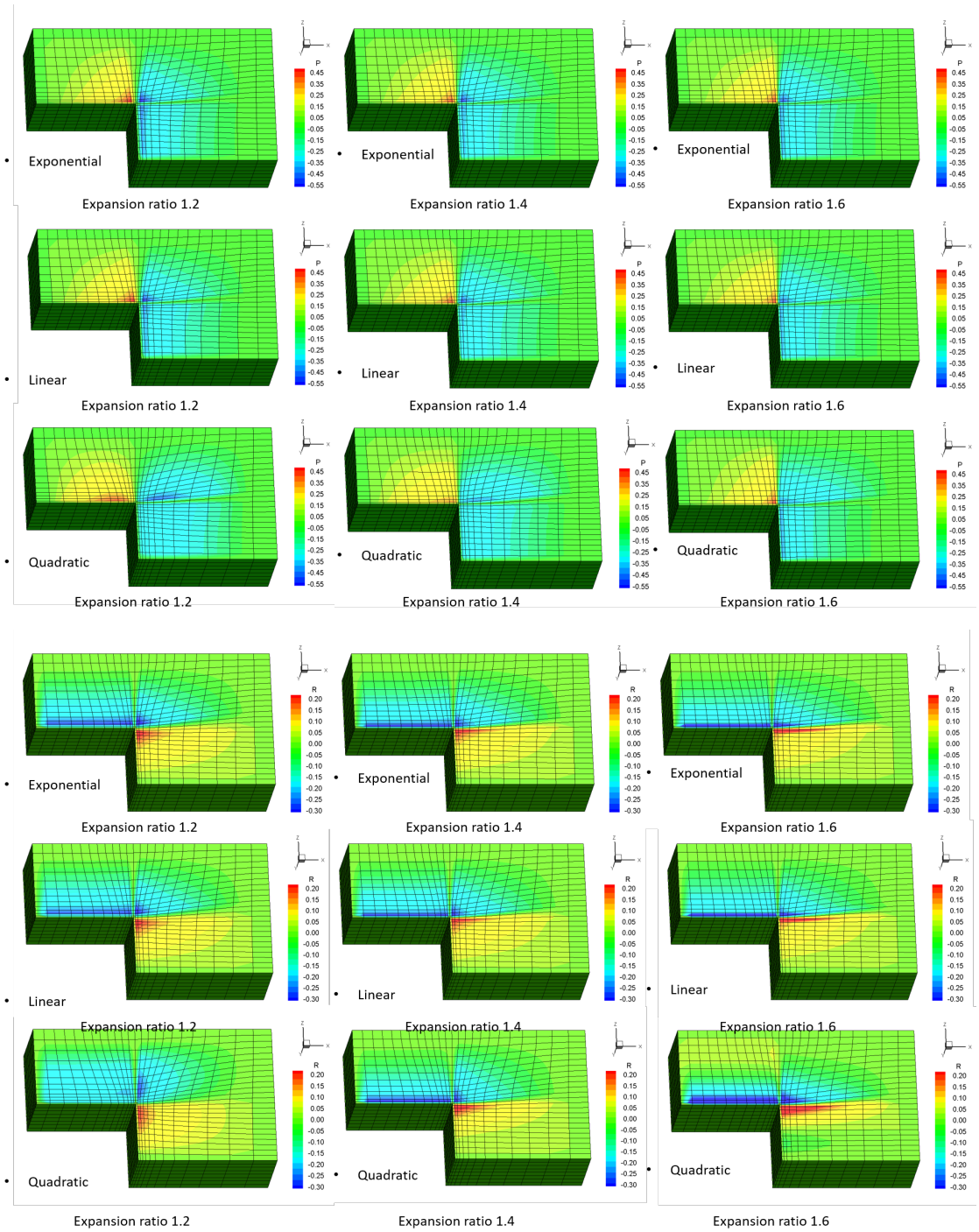


Figure 4.3: Smoothing interpolation for a three-block case

figures are showing the Q control function. Fig. 4.3 shows that when the expansion ratio is larger, the grid lines near the wall are clustered while still maintaining the orthogonality.

Fig. 4.4 compares the generated mesh on a three-block channel by using different interpolations of smoothing. The exponential and quadratic interpolation of smoothing performs better than the linear interpolation in terms of the grid skewness on the left edge intersection between the hole and the trunk. Fig. 4.5 presents the optimal mesh after the quadratic interpolation of smoothing based on the auto-generated hex mesh of the fan-shaped film hole and the cylindrical film hole. Fig. 4.5 a) and Fig. 4.5 b) corresponds to the cutting $y - z$ sections at the inlet center and outlet center in Fig. 6) in Technical Paper 1.

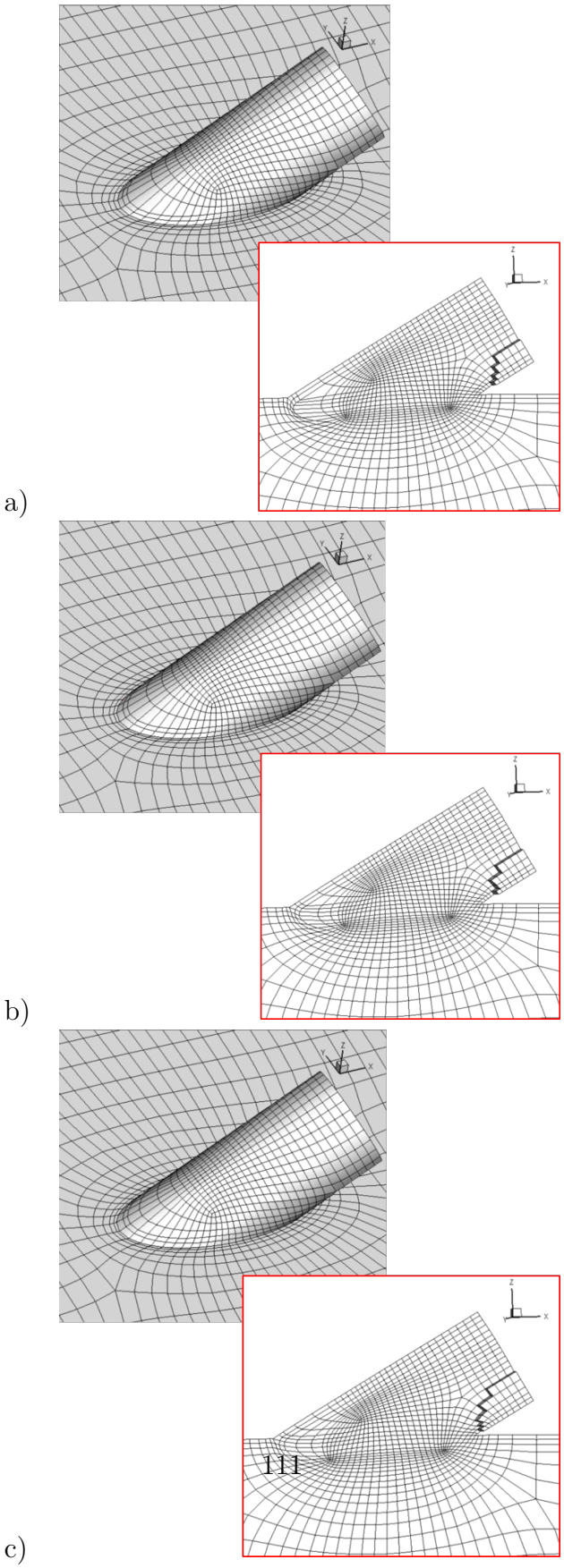


Figure 4.4: Interpolation examples, a)linear interpolation, b)quadratic interpolation, c) exponential interpolation

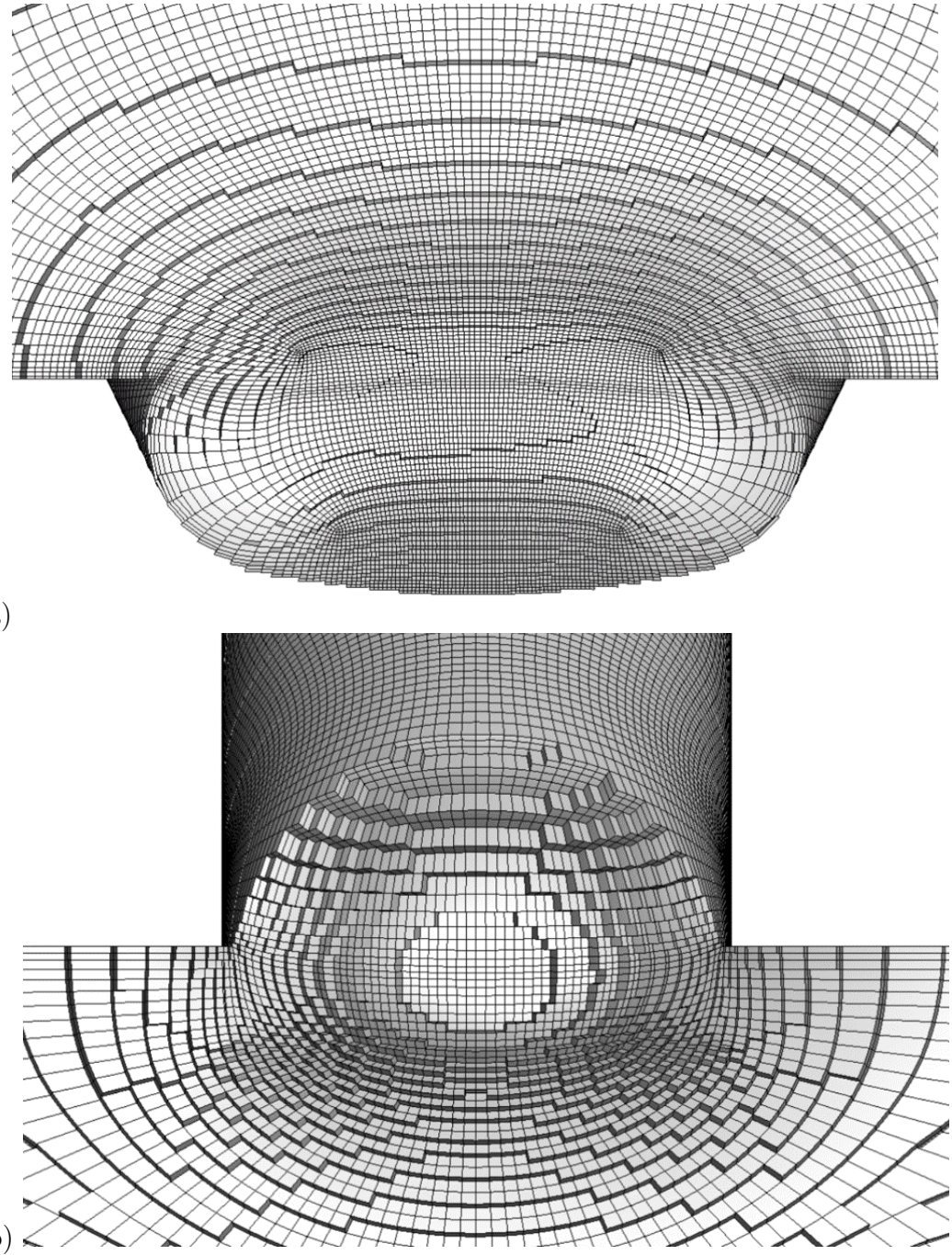


Figure 4.5: cut-off section of grids in a) fan-shaped hole, b) cylindrical hole



5

Generation of correlated fields by Synthetic inflow generator

5.1 | Preface

The third key element for scale resolving of film cooling flows mentioned in Chapter 1 is a turbulence inflow generator. The results of scale-resolving simulations and their capability of resolving turbulent flows depend heavily on accurate boundary conditions, especially for the inflow boundary. At the inlet boundary, a realistic inlet turbulent flow field is necessary. Previous studies have proved the high sensitivity of simulated mean flow and turbulent profiles to the properties of the inlet flow field. An unrealistic inlet flow field might cause the flow to re-laminarize downstream or might cause the boundary layer to readjust over a long section of the domain thereby requiring a longer domain for a given simulation. Therefore, a high-quality time-dependent inflow boundary condition is a needed component for simulating

spatially developing flows.

This study presents a novel synthetic inflow generator capable of producing a random field matching a realistic set of two-point statistics with minimal input.

Section 5.2 contains a published PHYSICS OF FLUIDS Journal paper outlining the mathematical formation of this proposed inflow generator and the detailed explanation of two components of this inflow generator. The first component contains a RANS precursor using EARSM considering its advantage of obtaining anisotropy. The second component is eigenmode decomposition and reconstruction. It also shows a series of simulations validating the proposed inflow generator on LES results of a channel flow and a turbulent boundary flow against DNS data in the literature and the LES result of a reference case with the periodic boundary condition.

Compared with previous synthetic generation methods, the procedure proposed in this study is much more efficient for the following reasons. Results prove that as long as controlling parameters needed are set up reasonably, the proposed synthetic generator can produce turbulence inflow which is more close to realistic compared to other existing inflow generation methods. In addition, general guidance for new users is provided on how to select related parameters for using the proposed synthetic inflow generator. The criteria for setting up the parameters needed are provided. The proposed inflow generator features, cost-effectiveness, robustness, and potential for generalization to complex geometries.

The proposed synthetic inflow generation is used in the following chapters and the other 4 technical papers regarding film cooling.

5.2 | Technical Paper 2

AIP/123-QED, Cite as: Physics of Fluids 34, 115140 (2022)

Generation of turbulent inflow data from realistic approximations of the covariance tensor

Muting Hao (郝苜婷),[1] Joshua Hope-Collins,[1] and Luca di Mare[1]
Oxford Thermo-Fluids Institute, Department of Engineering Science,
University Of Oxford, Oxford OX2 0ES, United Kingdom

(*Electronic mail: correspondence :muting.hao@stcatz.ox.ac.uk)

Abstract

This study presents a novel synthetic inflow generator capable of producing a random field matching a realistic set of two-point statistics with minimal input. The method is based on two main elements. The first element is a procedure to infer realistic two-point covariance tensors from readily available data (e.g. freestream velocity, boundary layer thickness, and turbulence intensity) by a preliminary Reynolds averaged Navier–Stokes (RANS) simulation with an explicit algebraic Reynolds stress model (EARSM) closure. The second element is an efficient eigen-decomposition step of the two-point correlation tensor which determines a set of modes. The modal decomposition guarantees the spatial correlation in transversal directions, while the temporal correlation/streamwise spatial correlation is obtained by digital filters based on longitudinal and transversal spectra of a realistic shape and Taylor's hypothesis. The instantaneous inlet flow field is obtained by a linear combination of the modes via uncorrelated random weights with unit variance. The modes are generated in a computationally inexpensive pre-processing step. Compared to existing inflow generation methods that try to match given two-point statistics, the proposed method relieves the burden of obtaining data from direct numerical simulation (DNS) or experiments, while the complexity of the eigenvalue problem that needs to be solved is reduced. The proposed method is shown to produce a realistic turbulent channel flow and a realistic turbulent boundary layer by the large eddy simulation (LES), which contains statistics that are in good agreement with results from DNS. The proposed inflow generator features, cost-effectiveness, robustness, and potential for generalization to complex geometries.

I. INTRODUCTION

A. Turbulent inflow generation method

The advancement of the computer power has made scale resolving simulation techniques such as direct numerical simulation (DNS)[1,2] or large-eddy simulation (LES)[3–5] applicable to flows of practical interest. The accuracy of these simulations relies on the resolution as well as accurate boundary data. This is especially true for the inflow boundary, where a realistic inlet turbulent flow field is necessary.

Previous studies have proved that simulated mean flow and turbulent profiles are highly sensitive to the properties of the inlet flow field. An unrealistic inlet flow field might cause the flow to relaminarize or might cause the boundary layer to readjust over a long section of the domain thereby requiring a longer domain for a given simulation. Therefore, a high-quality time-dependent inflow boundary condition is a necessary component for simulating spatially developing flows. Similar problems are faced by hybrid RANS-LES methods at the interface between the RANS and the LES domains[6–8].

Generating a turbulent inflow requires a time series containing all the length and time scales resolved by the simulation on the inflow surface. A number of methods have been studied for obtaining fully turbulent inflow data. These methods can be categorized into four groups[9]: (i) transition-inducing methods[10–17], which introduce deliberate perturbations in the flow to trigger transition; (ii) turbulence library-based methods, which extract realistic inflow data from a database of snapshots or an auxiliary simulation; (iii) recycling-rescaling methods[18–20], which generate inflow data by rescaling the flow field at a suitable downstream location. (iv) synthetic inflow generators, which rely on random sequences to generate inflow data. Among these four general methods, (i) is not very practical because of the lack of generality and the need for a large development length - as much as 50 boundary layer thicknesses[17] - to allow for the transitional flow to develop. Method (iii) requires special techniques[21] to handle spurious low-frequency signals induced by the finite distance between the recycling station and the inlet surface[18,21,22]. (ii) and (iv) are preferable and combined in this study.

Library-based methods are superior in terms of reproducing correct phase information as they use a realistic data source. When the data source is close to the target geometry/operating configuration, this method can faithfully generate realistic inflow data.

For complex geometries or industrial applications, it may be difficult to set up auxiliary simulations with periodic boundaries and no source of library data may be available. As a consequence, synthetic inflow generations are the method of choice for general flow configurations.

The earliest example of a synthetic inflow consists in superimposing random disturbances on a laminar profile[23] for a turbulent jet simulation. The main difficulty in constructing synthetic inflow methods is the generation of random sequences that exhibit realistic correlations in both time and space. Different synthetic inflow generators differ in the way they enforce spatial and temporal coherence in the inflow signal.

The temporal correlation was first considered when Hanna et al[24] obtained required time scales along with turbulence intensities in an LES simulation by scaling a base time series. A temporal correlation of exponential shape was enforced. The accuracy of resulting inlet data was still doubtful due to a lack of spatial correlations. Kondo[25] and Lee[26] showed that both spatial and temporal correlations can be preserved when the energy spectrum is prescribed during inverse Fourier transforms(IFT). When being used for recovering realistic turbulence, however, the IFT may need a long development distance, which can be as much as 20 boundary layer thickness as shown in Le et al[27].

Batten[6]'s synthesizing reproduced the imposed length correlation, time correlation, and all second moments, via tensor scaling at the RANS-to-LES interface. In Jarrin et al.'s[7] synthetic-eddy method (SEM) and its variants, the superimposed coherent structures satisfy two-point correlations that are provided in the overlapping zone of the hybrid RANS-LES simulations. However, Batten's method features slow redevelopment, as is shown being more than 20 channel half-heights, indicated in Keating[28]. Jarrin's SEM requires around 2-4 times the boundary layer thickness[29] for the RANS-to-LES transition.

The spectral approaches rely on the properties of Fourier transforms to enforce correlations in space and time. Spectral approaches exploit homogeneous directions and Taylor's hypothesis in order to represent the inflow data as Fourier series in space and time. The Fourier representation of the inflow field makes the introduction of a realistic energy spectrum straightforward. As an example, the random flow generation (RFG) method by Smirnov et al.[30] operates by superimposing harmonic functions with random factors in amplitude and phase. The resulting fluctuations feature the prescribed energy spectrum, turbulence length scales, and time scales. The method requires as input an energy spectrum which is a function of the wave number only.

POD offers a rigorous mathematical framework for the description of spatially and temporally

coherent structures in a turbulence field. POD has been used[31] for synthetic turbulence generation. POD is attractive because of its optimality properties which allow a given flow field to be represented with the smallest number of modes, for a given accuracy[32]. However, since POD necessitates a predetermined dataset e.g. from experiments, DNS or adequately resolving simulations, POD-based methods have not met wide acceptance so far.

The digital filter-based method is a way of generating correlated signals with prescribed length scales. The prescribed value is known from experiments or from heuristic estimates, and the filtering operation imposes these correlated length scales in the originally random noise. Klein's[33] approach to generating a synthetic inflow is filtering an uncorrelated random series with zero mean and unit variance by a set of filter coefficients that are solved by matching different two-point correlation forms. Xie and Castro[34] used an exponential function instead of the Gaussian function assumed by Klein[33] to improve the accuracy of the second correlation function. In terms of generalization to 3D, a cost-effective 2D filtering was promoted[34] instead of the convolution of 1D. These methods assumed a constant time scale as input for the whole inlet. Additional treatment, separating the inlet into zones, was thus required to vary lateral and vertical length scales. More straightforward strategies are needed. Hoepffner[35] tried a novel filtering in the form of an autoregressive linear filter, the coefficients of which are solved from the Yule-Walker equation to ensure the required spatial and temporal correlations. They need to rely on DNS and a long spatial simulation domain for the transition to turbulence to occur or a small amount of noise to extract statistics of the instability of the mixing layer as a reference. However, these methods have shown potential for exploring simpler and more straightforward filtering ways which can vary time scales.

An ideal turbulence boundary condition should satisfy a few requirements: cost-effectiveness, applicability to spatially inhomogeneous flows, lack of spurious signals, and on-the-fly generation of the inflow data. Although most methods mentioned above have attained success in a certain range of applications, they more or less fail to meet all the expectations from an ideal inflow condition. As an example, methods in (i), (ii), (iii), and those synthesizers which have been shown to require relatively long development length can not be used in complex cases of practical interest because of the high computational cost.

An effective synthetic turbulence method can be devised if an inexpensive way of generating two-point correlation tensors can be found and if the information contained in the two-point correlations can be incorporated directly into the inflow data.

Based on these considerations, we propose a turbulence synthesizing method which combines the library-based method, POD, and the digital-filter method. The proposed method is capable of producing a random field matching a realistic set of two-point statistics with minimal input. The method operates in four steps. In the first step, an inexpensive preliminary Reynolds averaged Navier–Stokes (RANS) calculation is used to obtain the mean flow, turbulent kinetic energy (TKE), and Reynolds stress distributions on the inflow surface, together with a length-determining quantity. The RANS simulation operates in a way reminiscent of the precursor simulation in a library-based method, but it can be performed at a negligible computational cost. The RANS simulation is the data source of our proposed synthetic turbulence generator (see Section II A). In the second step, the RANS data are used to construct approximate two-point covariance tensors on the inlet surface (see Section II B). In the third step, a POD is performed on the approximate tensors to obtain an orthonormal basis for the flow quantities on the inflow surface. If the flow has a homogeneous direction, a Fourier representation is used along that direction. The POD and Fourier modes describe the variation of the inflow signal on the inflow surface and are responsible for preserving two-point correlations on that surface (see Section II B). In the fourth and final step, a digital filter is constructed for each POD/Fourier mode and describes the variation of the inflow signal in time. The digital filters are responsible for enforcing two-time correlations (see Section II B). These steps are only performed once prior to the start of the main LES simulation. At each time step of the LES simulation, a new realization of the inflow field is generated by convolution of the previously constructed space-time filters with an uncorrelated random sequence or an interpolation algorithm.

The four steps of the proposed method are presented in detail in the Methodology section II. Section III describes the LES flow solver used for the main simulation and the way of implementing the proposed synthetic inflow generator before and during the LES running. Results and discussions are presented for a channel (see Section IV) and a developing boundary layer (see Section V). Section (IV) presents comparisons with both DNS data and LES results by using the periodic boundary condition. Mean velocity profiles, and Reynolds normal and Reynolds shear stresses are examined for the purpose of validation. The effects of inflow parameters on a developing boundary layer are shown in Section V. Section V presents guidance on the selection of the method parameters for new users who are interested in using the proposed synthetic inflow generator. Finally, conclusions and recommendations for future work are presented in Conclusions.

II. METHODOLOGY

The design of a turbulence generator consists in identifying and reproducing certain statistics.

a. Identifying statistics Statistics are both treated as input and output of the generated turbulence. As for the way to correctly determine the statistics for use, previous studies on synthetic generation have taken into account at least one of the spatial correlations, temporal correlations, and the Reynolds stress tensor.

Early examples of them are utilizing preliminary experimental data. With experimentally determined time series, Bonnet et al.[31,36] defined correlation functions from experiments and built their inflow condition on a mixing layer.

Their success confirmed that introducing correlations using library-based methods is feasible. To get rid of the high cost of experiments, this study expects to find an equivalent numerical precursor that provides information about correlations. In addition, the precursor simulations in all the methods published so far are themselves either DNS or LES. Even though for just the precursor, they use high-fidelity codes to get statistics at the cost of a certain amount of computational resources.

This proposed contribution aims to find a precursor and, via using filtering temporally and spatially, to prepare temporal and spatial correlations which can be incorporated into subsequent inflow synthesizing. We expect the precursor to be realistic approximations from which trustworthy correlations can be extracted. The procedure should be able to set up case-dependent precursor simulations easily with the minimum information required. Computational expenses should be controlled to a minimum while reliable results could be found instantly.

The statistics chosen for turbulence construction in this study is a realistic two-point covariance tensor. It contains information on the magnitudes and the spectrum of different length-scale structures. As the data source in the library-based method, a precursor is proposed to infer a realistic two-point covariance tensor from readily available information (e.g. freestream velocity, boundary layer thickness, and turbulence intensity). The precursor is a preliminary simulation based on RANS incorporated with an explicit algebraic Reynolds stress model (EARSM) closure. Mean velocities are obtained in the meantime.

b. Reconstruction Once a suitable representation of the two-point covariance tensor is obtained from the solution to the identifying statistics, the second step is the generation of the synthetic turbulence.

Different from the synthesizing methods reviewed in Section I, this study will propose an eigenvalue-based synthesizing method. It will combine the advantageous features of the POD, and the filtering-based method reviewed above. The eigenvalue-based method is composed of an efficient eigendecomposition of the two-point correlation tensor, which determines a set of modes and enforces correlation in space. Time filters are applied to individual Fourier modes. Therefore, the final solution is a linear superimposing of time- and space- variance signals through random weights with unit variance. The computational effort will be shown to be modest.

A. Preliminary approximation of two-point statistics

In this section, the preliminary simulation is illustrated. We also show how to build the statistics, i.e. the covariance tensor, which will be decomposed in the next Sec. II A 1, to seek the modes for the following reconstruction.

1. The precursor RANS solver

The preliminary procedure consists of establishing a RANS simulation from which statistics will be extracted and later reproduced using a filter-based reconstruction. The preliminary simulation is designed to take smaller possible computational efforts. The procedure takes a minimal set of input data that allow target flow conditions to be established. The input data includes the free-stream velocity, the temperature, the pressure, the turbulence level, the desired boundary layer thickness, and the viscosity. The parameters needed to be specified for the energy spectrum and the time filtering are chosen according to experience. This study will provide some guidance for the selection of these parameters. The modeling method is a two-equation RANS model with the EARSM closure. The EARSM closure is adopted as it can approximate the anisotropy of the Reynolds stress tensor.

Note that the inflow generation procedure is described for a flow where the inlet section can be generated by a developing turbulent boundary layer, but the method of reconstructing following that can be equally well applied to any inlet configuration as long as RANS data (or higher resolution simulation data) are available.

The configuration of the preliminary simulation depends on the nature of the incoming flow. As an example, if the incoming flow is a developing boundary layer, the preliminary simulation is

based on the parabolized Navier-Stokes equations. In this case, the preliminary simulation takes the shape of a marching procedure that starts from a nominal profile far upstream of the inlet. At the start of the calculation, a one-dimensional mesh is constructed. The grids are orthogonal to the wall and just cover a height of the boundary layer thickness, with the first grid size normal to the wall as $y_0 = 0.5\frac{Nu_0}{u_0}$. The simulation is then marched until the boundary layer thickness matches the desired value. The computational domain is represented at any time during the procedure by only two consecutive streamwise stations where the wall-normal profiles of the flow quantities are computed. At each timestep, the newly generated result overwrites the previous records and is written on the current virtual cell center. In this way, no more than two lines of cells are stored at any timestep, without the cumbersomeness of storing the whole streamwise extent of the precursor domain. The wall-normal grid distribution is updated to adapt to the turbulent boundary layer development until the turbulent boundary layer thickness of δ_{99} or the momentum thickness of θ is satisfied. Fig. 1 shows this computational domain in the two sets of coordinate systems that are used. The coordinate axis 1, 2, and 3 corresponds to the coordinate axis x, y, z, denoting the streamwise, wall-normal, and spanwise directions. The former is used only in Equ. 1 for facilitating the tensor notation, while the latter is used for the rest of the equations.

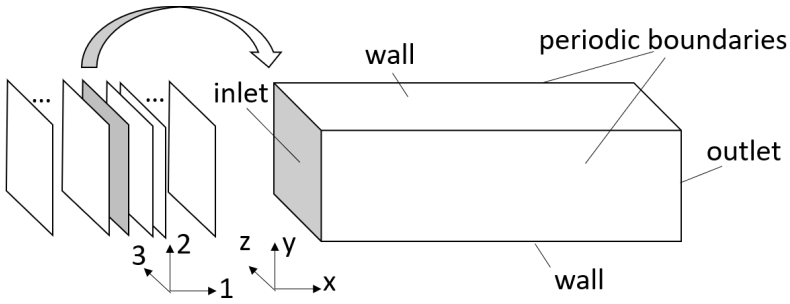


FIG. 1: The computational domain shown in two sets of coordinate systems

Wilcox and Rubesin[37]'s EARSM closure is adopted in the preliminary simulation. The nonlinear constitutive relation for their $k-w^2$ model is

$$\tau_{ij}^0 = -\frac{2}{3}\rho k_e \delta_{ij} + 2\mu_T \left(S_{ij} - \frac{1}{3}\frac{\partial U_k}{\partial X_k}\delta_{ij} \right) + \frac{8}{9}\frac{\rho k_e \left(S_{ik}\Omega_{kj} + S_{jk}\Omega_{ki} \right)}{\beta^* \omega^2 + 2 S_{mn} S_{nm}} \tag{1}$$

This constitutive relationship in Equ. 1 can model Reynolds stresses that do not necessarily align with the mean rates of strain. This prescription for the Reynolds-stress tensor guarantees that the

peak values of

$$\overline{u'^2} : \overline{v'^2} : \overline{w'^2} = 4 : 2 : 3 \tag{2}$$

for the flat-plate boundary layer. Equ. 2 is a good approximation for the log layer and much of the defect layer.

For a parallel shear flow, the individual Reynolds normal stresses are specialized to

$$\overline{u'^2} = \frac{2}{3} k_e \left(1 + \frac{2}{3} \frac{\left(\frac{\partial U_1}{\partial X_2}\right)^2}{\beta^* \omega^2 + \left(\frac{\partial U_1}{\partial X_2}\right)^2} \right) \tag{3}$$

$$\overline{v'^2} = \frac{2}{3} k_e \left(1 - \frac{2}{3} \frac{\left(\frac{\partial U_1}{\partial X_2}\right)^2}{\beta^* \omega^2 + \left(\frac{\partial U_1}{\partial X_2}\right)^2} \right) \tag{4}$$

$$\overline{w'^2} = \frac{2}{3} k_e \tag{5}$$

2. Construction of a covariance tensor from mean profiles

The quick RANS calculation in Section II A 1 estimates mean velocity components (in three directions for 3D cases), Reynolds stresses, and length scales. We now proceed to show the construction of a covariance tensor based on this information. This is done on the inlet slice of the main computation. In general, if the inlet surface contains n grid faces, the correlation tensor contains $3n \times 3n$ entries. If a homogeneous direction is present, then the correlation tensor contains $3n \times 3n$ entries, but n is the number of cells in the wall-normal direction only. A separate correlation tensor must be generated for each Fourier mode.

The shape of the covariance tensor is not very sensitive to Re_τ[38] for a given flow. As an example, in turbulent boundary layers or channel flows, a reasonable covariance tensor can therefore be constructed by assembling the following components:

$$\begin{aligned}
&< u'u' >_\kappa (y_1, y_2) = f_\kappa^0 \sqrt{u'^2(y_1)\, u'^2(y_2)}\, e^{-\alpha \frac{(y_1 - y_2)^2}{\ell(y_1)\ell(y_2)}} \\
&< v'v' >_\kappa (y_1, y_2) = f_\kappa^0 \sqrt{v'^2(y_1)\, v'^2(y_2)}\, e^{-\alpha \frac{(y_1 - y_2)^2}{\ell(y_1)\ell(y_2)}} \\
&< w'w' >_\kappa (y_z, y_2) = f_\kappa^0 \sqrt{w'^2(y_1)\, w'^2(y_2)}\, e^{-\alpha \frac{(y_1 - y_2)^2}{\ell(y_1)\ell(y_2)}} \\
&< u'v' >_\kappa (y_1, y_2) = -f_\kappa^0 \sqrt{u'v'(y_1)\, u'v'(y_2)}\, e^{-\alpha \frac{(y_1 - y_2)^2}{\ell(y_1)\ell(y_2)}}
\end{aligned} \tag{6}$$

where κ is the spanwise Fourier index mode, y_1, y_2 are two wall-normal positions and u', v', w' are turbulent velocities in three directions. In Equ.6, a square root function and a Gaussian shape function are used to ensure that, first, the reconstructed covariance tensor is smooth; second, the Reynolds stresses appear on the main diagonal of the covariance tensor. The entries of the covariance tensor are prescribed from heuristic arguments in the physical space. The covariance tensor is a symmetric matrix. $< u'w' >$, $< v'w' >$ are assigned as zero, because the corresponding Reynolds stresses in the homogeneous directions are zero. Therefore, to build the final combined covariance tensor, only the four sets of components in Equ.6 are needed to know. The covariance tensor is arranged in Equ. 7 and Equ. 8 as below:

$$
\begin{aligned}
R_{uu} &= \begin{bmatrix} u'_1u'_1 & u'_1u'_2 & \cdots & u'_1u'_n \\ u'_2u'_1 & u'_2u'_2 & \cdots & u'_2u'_n \\ \vdots & \vdots & \ddots & \vdots \\ u'_nu'_1 & u'_nu'_2 & \cdots & u'_nu'_n \end{bmatrix} \in \mathbb{R}^{n\times n} \\
R_{ww} &= \begin{bmatrix} w'_1w'_1 & w'_1w'_2 & \cdots & w'_1w'_n \\ w'_2w'_1 & w'_2w'_2 & \cdots & w'_2w'_n \\ \vdots & \vdots & \ddots & \vdots \\ w'_nw'_1 & w'_nw'_2 & \cdots & w'_nw'_n \end{bmatrix} \in \mathbb{R}^{n\times n} \\
R_{vv} &= \begin{bmatrix} v'_1v'_1 & v'_1v'_2 & \cdots & v'_1v'_n \\ v'_2v'_1 & v'_2v'_2 & \cdots & v'_2v'_n \\ \vdots & \vdots & \ddots & \vdots \\ v'_nv'_1 & v'_nv'_2 & \cdots & v'_nv'_n \end{bmatrix} \in \mathbb{R}^{n\times n} \\
R_{uv} &= \begin{bmatrix} u'_1v'_1 & u'_1v'_2 & \cdots & u'_1v'_n \\ u'_2v'_1 & u'_2v'_2 & \cdots & u'_2v'_n \\ \vdots & \vdots & \ddots & \vdots \\ u'_nv'_1 & u'_nv'_2 & \cdots & u'_nv'_n \end{bmatrix} \in \mathbb{R}^{n\times n}
\end{aligned}
\tag{7}
$$

The final covariance tensor is assembled from these individual matrices following the arrangement of $3n \times 3n$ as Equ.8,

$$
M = \begin{bmatrix} R_{uu} & R_{uw} & R_{uv} \\ R_{uw}^\top & R_{ww} & R_{vw} \\ R_{uv}^\top & R_{vw}^\top & R_{vv} \end{bmatrix} \tag{8}
$$

where n is the number of nodes in the wall-normal direction on the inlet slice.

B. Reconstruction by eigenmodes

1. Eigenmode space

The covariance tensor prescribed in the physical space can be interpreted in the eigenmode space. The eigenvectors of the covariance matrix are taken as an alternative basis for the representation of the covariance tensor. The reason why a transformation from the physical space to the eigenmode space is needed can be explained as follows. First, it is easier to generate an uncorrelated signal by a random number generator (shown in Section II B 1 a); the eigenmode space allows an uncorrelated signal to be combined into a known correlation tensor based on the mean flow and the length scales in Equ.6. Second, via transformation, it is possible to make the eigenvalues positive and real, which is essential for a correlation tensor. The current procedure should guarantee that the guessed correlation tensor is hermitian because of the way it is constructed, but the positivity has not been guaranteed for all eigenvalues. In fact, a small number of negative eigenvalues are ordinarily created. These appear in the tail end of the spectrum and represent a small fraction of the whole turbulent kinetic energy. These modes are not realizable, i.e. it is not possible to determine a set of spatial patterns that when combined through a random uncorrelated signal will give correlation patterns associated with these modes. For this reason, they are suppressed by setting the corresponding eigenvalues to zero. Imposing a cut-off in the number of modes is generally sufficient to remove all the unrealizable modes.

a. Reconstruction via a correlated random sequence generator A method of creating a correlated random sequence is shown below. Assuming x_i^* is the output as an uncorrelated random variable which satisfies the property of zero mean and unit variance, i.e. $< x_i^* >= 0$, $< x_i^* x_j^* >= \delta_{ij}$, let

$$y_i^* = p_{ij} x_j^* \tag{9}$$

be a new set of random variables, with the covariance being

$$< y_i^* y_j^* >= p_{ih} p_{jk} < x_h^* x_k^* >= p_{ih} p_{jk} = q_{ij} \tag{10}$$

If q_{ij} is a given covariance tensor, and its symmetric factorization $q_{ij} = s^*_{ih} s^*_{jh}$ is known, the second set of random sequence can be conversely treated as

$$y^*_i = s^*_{ih} x^*_h \tag{11}$$

whose covariance tensor will be q_{ij}. Conversely, a correlated random variable y^*_i can be produced by an uncorrelated random variable x^*_h and the factorization of a prescribed symmetric covariance tensor matrix q_{ij}. In this way, the problem of converting an uncorrelated sequence to a correlated random sequence is reduced to a problem of symmetric factorization. A suitable factorization is the eigenvalue decomposition.

b. Energy cutoff In our case, each eigenvector is $3n$ entries long, with u' components in the first n rows, v' components in the second n rows and w' components in the last n rows. An additional advantage of a decomposition of the correlation tensor in eigenmodes is that not only negative generated eigenmodes can be suppressed, but also few modes are necessary to be retained for most of the turbulent kinetic energy. This modal decomposition property reduces the computational effort required to generate a realistic inlet flow field. A minimum number of eigenvalues are preserved according to the cutoff criteria of total energy. Namely, only leading eigenvalues and their corresponding eigenvectors should be preserved. The total turbulence energy of preserved decomposed eigenmodes hereby should just cover a given large fraction (around 92% is proved to be efficient for our case). No more than one-fifth of eigenmodes are usually needed to recover 92% of the turbulent energy. Assuming the eigenvectors are sorted in descending order, and if m is the number of the retained eigenmodes, Equ. 12 indicates that the total turbulent energy can be approximated by a truncated summation.

$$\sum_{i=0}^{3n-1} k_i \,|_{1\times 3n} = \sum_{i=0}^{3n-1} |\lambda_i| \approx \sum_{i=0}^{m} |\lambda_i| \tag{12}$$

where λ_i is the eigenvalue of the i^{th} eigenmode, and k_i is the kinetic energy retained in the i^{th} eigenmode.

c. The eigenmode reconstruction shown by a test case The velocity on an individual point of the median plane can be constructed by rescaling the retained eigenmodes of the correlation tensor by the square root of their corresponding eigenvalues:

$$\begin{bmatrix} \hat{u}_j(y) \\ \hat{v}_j(y) \\ \hat{w}_j(y) \end{bmatrix} = \begin{bmatrix} g_1^j \\ g_2^j \\ ... \\ g_{3n}^j \end{bmatrix} \sqrt{\lambda_j}, \quad j = 1,2,...,m \quad (m << 3n) \tag{13}$$

where λ_j is the eigenvalue of the j^{th} retained eigenmode, and g_i^j is the i^{th} row of the j^{th} eigenvector.

The reproduced signal will satisfy the prescribed mean flow quantities and length scales. This is proved by a one-dimensional case published by the same group[38] and a two-dimensional case in Fig. 2. Fig. 2 shows that with more eigenmodes, the reconstruction of the covariance tensor can be more accurate. When using 72 eigenmodes, the highest error is within 10% and within an ignorable area. The error between the desired and the obtained covariance is generally below 1%, while there is a 50% reduction in the spectral basis size after construction.

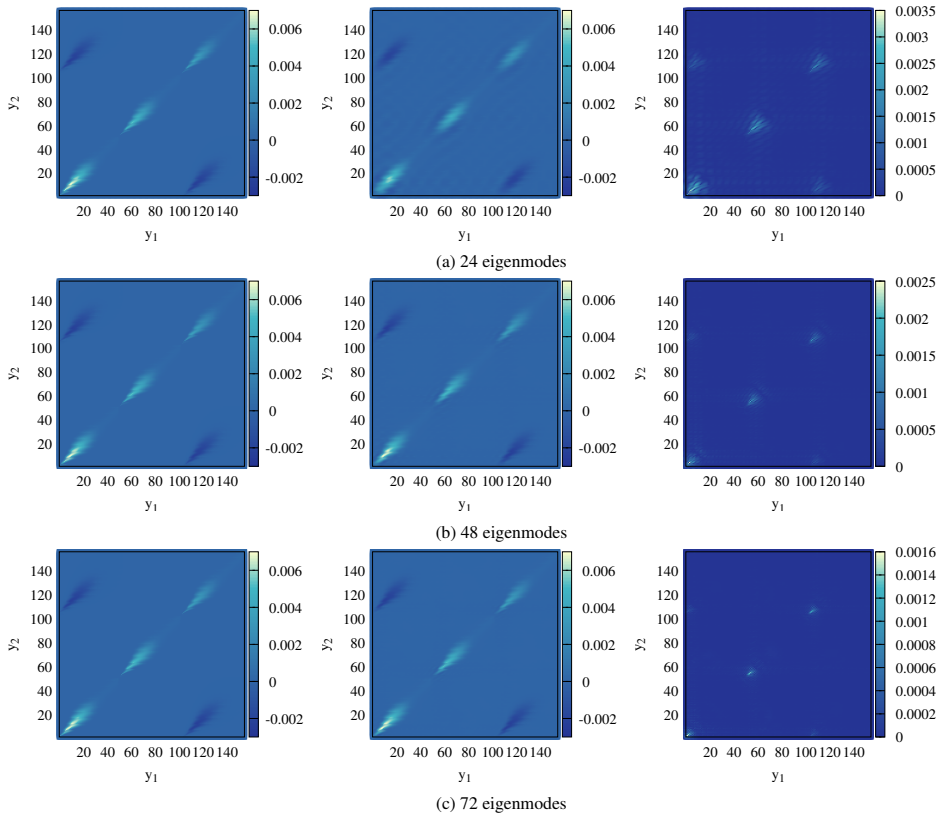
For a three-dimensional domain, the spanwise variation of turbulence should be introduced. In principle, a similar procedure of looking for eigenvectors and eigenvalues can be proceeded in the spanwise direction to generate the genuinely two-dimensional space on each streamwise slice.

2. Fourier space

In fact, the domain of the cases we focus on in this study is symmetric and periodic in the spanwise direction. These features are not specific in many studies of industrial interest. So it's expedient to specialize in the decomposition of this type of computational domain. In such cases, the procedure will be simplified. In the direction where the domain is periodic and the correlation is homogeneous, the eigenvectors are sine and cosine functions, and the eigenvalues are corresponding Fourier amplitudes. We can generate the velocity field in the Fourier space.

Let $\breve{u}_j(y,z)$, $\breve{v}_j(y,z)$,$\breve{w}_j(y,z)$ be the velocity components of the j^{th} scaled eigenvector at the position (y,z). The turbulence intensity in the free stream is indicated in the scaled eigenvectors shown in Equ. 13. The turbulence elements for each wavenumber are taking the form as

$$\begin{bmatrix} \breve{u}_j(y,z) \\ \breve{v}_j(y,z) \\ \breve{w}_j(y,z) \end{bmatrix}_\kappa = \begin{bmatrix} \hat{u}_j(y) \\ \hat{v}_j(y) \\ \hat{w}_j(y) \end{bmatrix} e^{i\frac{2\pi\kappa}{W}z} \tag{14}$$



(a) 24 eigenmodes

(b) 48 eigenmodes

(c) 72 eigenmodes

FIG. 2: Reconstructed statistics in two dimensions (156×156 samples are used, three numbers of eigenmodes are shown in (a), (b), and (c). In each group, the left figure is its initial covariance tensor before decomposition, the middle figure shows the covariance with compression, and the right figure shows the error between original and compressed covariance)

In the end, the actual search of eigenvalues and eigenvectors is only necessary in the non-homogeneous directions. Once the correlation function is known from the preliminary simulation, the 3D reconstruction problem reduces to a 1D eigenvalue problem and a computation of matrix-vector product.

3. Wave number space

The energy spectrum is described by the discrete signal $[\tilde{u}_{j\kappa}(y,z), \tilde{v}_{j\kappa}(y,z), \tilde{w}_{j\kappa}(y,z)]^T$ in the wavenumber space. If energy is equally distributed over the wavenumber range, the turbulence

generated will decay immediately and flow will laminarize because the signal is white noise. A realistic energy spectrum is therefore needed. The spectrum of turbulence is universal.

If the total turbulent energy of the spectrum matches the turbulent energy from the preliminary simulation, the discrete wavenumber amplitude can be distributed with an energy spectrum of a suitable shape. An approximate spectrum is proposed as:

$$f_\kappa = \frac{1}{F}\begin{cases} \left(\frac{\kappa}{N_I}\right)^4, & \kappa \le N_I \\ \left(\frac{\kappa}{N_I}\right)^{-5/3}, & \kappa > N_I \end{cases} \tag{15}$$

$$F = \left(\sum_{\kappa=1,N_I}\left(\frac{\kappa}{N_I}\right)^4 + \sum_{\kappa=N_I+1,N}\left(\frac{\kappa}{N_I}\right)^{-5/3}\right) \tag{16}$$

A more simplified model is reasonable from observations:

$$f_\kappa = \frac{1}{F}\begin{cases} 1, & \kappa \le N_I \\ \left(\frac{\kappa}{N_I}\right)^{-5/3}, & \kappa > N_I \end{cases} \tag{17}$$

$$F = \left(\sum_{\kappa=1,N_I} 1 + \sum_{\kappa=N_I+1,N}\left(\frac{\kappa}{N_I}\right)^{-5/3}\right) \tag{18}$$

The shape of the spectrum above is suggested by the inspection of turbulence spectra in boundary layers reported in the literature (See e.g. Klebanoff[39]). The dividing wavenumber N_I corresponds to the wavelength that is comparable to the momentum thickness, shown in Equ.19. Here a control parameter α_I is introduced to make the shape of the spectrum adjustable, which will be discussed in the results:

$$N_I = \frac{W}{\alpha_I \theta} \tag{19}$$

Thus, for a discrete signal on the point of wall-normal coordinate y and spanwise coordinate z, a two-dimensionally decomposed mode can be constructed as:

$$\begin{bmatrix} \tilde{u}_{j\kappa}(y,z) \\ \tilde{v}_{j\kappa}(y,z) \\ \tilde{w}_{j\kappa}(y,z) \end{bmatrix} = f_\kappa \begin{bmatrix} \hat{u}_j(y) \\ \hat{v}_j(y) \\ \hat{w}_j(y) \end{bmatrix} e^{i\frac{2\pi\kappa z}{W}} \tag{20}$$

, where j is the eigenmode index, which represents the decomposition in the wall-normal direction, and k is the Fourier mode index, which represents the decomposition in the spanwise direction,

4. *Correlated random sequence generation*

In the Sec. II B 3, a signal that displays the desired second-order statistics in space has been constructed. We now introduce a correlated random factor $s_{jk}(t)$ to make

$$\begin{bmatrix} u' \\ v' \\ w' \end{bmatrix} (y,z,t) = s_{j\kappa}(t) \begin{bmatrix} \tilde{u}_{j\kappa} \\ \tilde{v}_{j\kappa} \\ \tilde{w}_{j\kappa} \end{bmatrix} (y,z) \tag{21}$$

a signal that displays the desired second-order statistics in time as well.

Equ. 21 presents a turbulence signal containing the Reynolds stresses information, so there is no need to operate 'decoupling' as in other precursor-synthesizing methods. The term 'decoupling' denotes a linear transformation that takes place after length scales are imposed on individual velocity components. 'Decoupling' takes place via a tensor[30] that makes independent velocity fluctuations to match a desired Reynolds stress tensor. Fathali[40] showed that decoupling causes simulated length scales to deviate from their prescribed values.

5. *The digital time filter*

$s_{jk}(t)$ can be formed from an uncorrelated sequence. This task can be accomplished by a filtering method. The original filter-based[33,4142] signal synthesizing is in nature a linear combination, the linear coefficients of which determine the two-time correlations. These correlations are either constructed from a given Gaussian shape[33], or from a detailed derivation[41]. The resulting velocities can reproduce first- and second-order one-point statistics as well as two-point correlations. These filter-based methods have built synthetically correlated turbulence that matches well with isotropic data.

A signal for a time node by convolution is to be associated with the current time point, the past, and the future. Here a new digital filter is proposed. The digital filter for a mode jk is constructed as

$$\psi_{j\kappa l} = e^{-\left(\frac{l\Delta t}{\tau_{j\kappa}}\right)^2} \tag{22}$$

where $\tau_{j\kappa}$ is a timescale associated with mode $j\kappa$, Δt the time separation that corresponds to two consecutive samples, and l is a time index.

The subscript l varies between $-M_t$ and M_t, where M_t is the time filter support. We thus have

two questions: i.how to define the timescale $\tau_{j\kappa}$? ii. How do we find a reasonable time filter support M_t? The second question is discussed in Section IV B 2.

The first question is solved based on the consideration of a temporal simulation. Taylor's hypothesis is a useful tool for relating spatial and temporal data via a convection velocity. The validity of Talyor's hypothesis has been proved by Lee[26] when the turbulence level is low, viscous forces can be ignored and the mean shear is not large. Wills[43] studied different convection velocities for turbulent fluctuations in the shear layer. In Lee's incompressible condition, the convective velocity has been shown nearly the same as the mean flow velocity except for very small eddies. In this study, these observations are exploited for using Taylor's hypothesis: the timescale of turbulence structures dominated by a certain mode from the inflow slice is transformed from the corresponding spatial scale via the mean freestream velocity (considered reasonable as the convective velocity), for a simplified expression:

$$\tau_{j\kappa} \approx W/U_0\kappa \tag{23}$$

where $\tau_{j\kappa}$ is a time scale associated with mode $j\kappa$, This simplified timescale assigns the same time scale to a mode regardless of wall-normal lengthscales. To avoid this drawback, the variation of velocity along the transverse direction (normal to the wall) should be included. This can be accomplished by the following expression

$$\tau_{j\kappa} = \frac{1}{U_0}\left(\frac{\alpha}{\int_0^{y\max}\left(\frac{du}{dy}\right)_j^2 dy} + \beta\frac{W^2}{\kappa^2}\right)^{1/2} \tag{24}$$

where coefficients α, β are taken as 1. The results shown in this study are all applied with the latter timescale formulation.

Once the $\tau_{j\kappa}$ is obtained, an uncorrelated random sequence $r_{j\kappa l}(t)$ can be built to make the correlated sequence $s_{j\kappa}(t)$. This can be accomplished through the convolution

$$s_{j\kappa}(t) = r_{j\kappa l}(t)\psi_{j\kappa l} \tag{25}$$

Finally, after summing over all possible values of κ and j, a random velocity field will result with the covariance tensor equal to the one we started from.

A random correlated (y-z) velocity field can be generated by

$$\begin{bmatrix} u'(y,z,t) \\ v'(y,z,t) \\ w'(y,z,t) \end{bmatrix} = \sum_{l=-M_t/2}^{M_t/2} \sum_{\kappa=-N,\kappa\neq 0}^{N} \sum_{j=1}^{m} r_{lj\kappa}(t) \begin{bmatrix} \hat{u}_j(y) \\ \hat{v}_j(y) \\ \hat{w}_j(y) \end{bmatrix} f_\kappa e^{i\frac{2\pi\kappa}{W}z} \psi_{j\kappa l} \tag{26}$$

where $r_{j\kappa l}$ is a random complex variable with (* denotes complex conjugate)

$$r_{j\kappa l} = r^*_{j(-\kappa)l} \tag{27}$$

The integer κ goes from $-N$ to N. N is chosen to represent the number of spanwise Fourier harmonics. If there are 128 cells in the spanwise direction, N could be 32.

III. NUMERICAL TECHNIQUE

A. LES flow solver

The LES simulations are performed by solving the Navier-Stokes equations by a home-grown CFD code 'H4X'. The code adopts an implicit LES based on the finite volume approach. The spatial derivatives at the interior points are solved by a third-order scheme that utilizes a non-linear limiter based on a compact three-point stencil. This scheme can well handle discontinuities as well as local extrema while maintaining the diffusion error as low in the smooth region. The mesh is generated by a built-in meshing generator[44]. Different time discretization options are provided according to the application. The implicit dual time stepping method is adopted in low Reynolds number situations, while the explicit runge-kutta method is adopted in medium Reynolds number situations.

B. Inflow generator implementation

As shown in Fig. 3, the whole procedure is separated into the pre-simulation section and the main simulation section. Given the basic information about mean flow, the preprocessing guesses a covariance tensor, builds eigenvectors and digital filters, and interpolates modes onto the target cloud of grid points on the inlet slice of the computational domain. The mean velocity profiles, the modes, and corresponding coefficients on the cell center of the required points are prepared before the LES simulation. The whole preprocessing can be finished within seconds and is needed

only once for one case. The final velocity signal is then reconstructed from those prepared modes weighted by corresponding coefficients according to

$$\begin{bmatrix} u(y,z,t) \\ v(y,z,t) \\ w(y,z,t) \end{bmatrix} = \begin{bmatrix} \overline{u}(y,z) \\ \overline{v}(y,z) \\ \overline{w}(y,z) \end{bmatrix} + \begin{bmatrix} u'(y,z,t) \\ v'(y,z,t) \\ w'(y,z,t) \end{bmatrix} \tag{28}$$

The timescale of the inflow signal might be much larger than the numerical time step. As a result, it is not necessary to generate a new inflow field every numerical time step using Equ. 28. For this purpose, a timescale is introduced dt_{inflow}, which is defined as

$$dt_{\text{inflow}} = \frac{\alpha_t \theta}{uM_t} \tag{29}$$

where α_t is a constant of order 1. Equ. 29 is based on Taylor's hypothesis with θ/u as an integral time scale. The number of simulation timesteps between two consecutive updates of the inflow field is dt_{inflow}/dt. Between two consecutive 'inflow time steps', the inflow field is obtained by linear interpolating from inflow fields at two neighboring 'inflow time steps'.

IV. APPLICATION FOR A CHANNEL

One of the simplest wall-bounded turbulent flows to test is a plane channel. A case with available data published is $Re_\tau = 395$ ($Re_\tau = \delta u_\tau/\mu$). This study shows an LES simulation of the turbulent flow in a three-dimensional channel at $Re_\tau = 395$ by different methods. The LES result is compared with the DNS results from Lee and Moser[45].

The computational domain has the dimensions of $10\pi\delta$, 2δ, and $\pi\delta$ in the streamwise, wall-normal, and spanwise directions where δ is the channel half height. The mesh resolution has $x^+ = 20$, $z^+ = 6$ and $y^+ = 0.15$ at the wall and $y^+ = 6$ further away from the wall. The mesh adopts Pirozzoli and Orlandi[46]'s grid stretching method in the wall-normal direction. This stretching method builds mesh by blending close to constant spacing in the viscous layer and spacing proportional to the kolmogorov lengthscale in the log layer. Their optimal values of a blending parameter and the near-wall grid spacing are employed to maximize the allowed time step. This meshing procedure guarantees the accuracy and efficiency of computational results. Periodic boundaries are applied in the spanwise direction. The dual time stepping is adopted for time advancing in these LES simulations. The physical timestep is set as a quarter of viscous timescale, i.e. $\Delta t = 0.25\mu/(u_\tau^2)$, according to Choi and Moin[47]. The inner iteration of the dual-time scheme

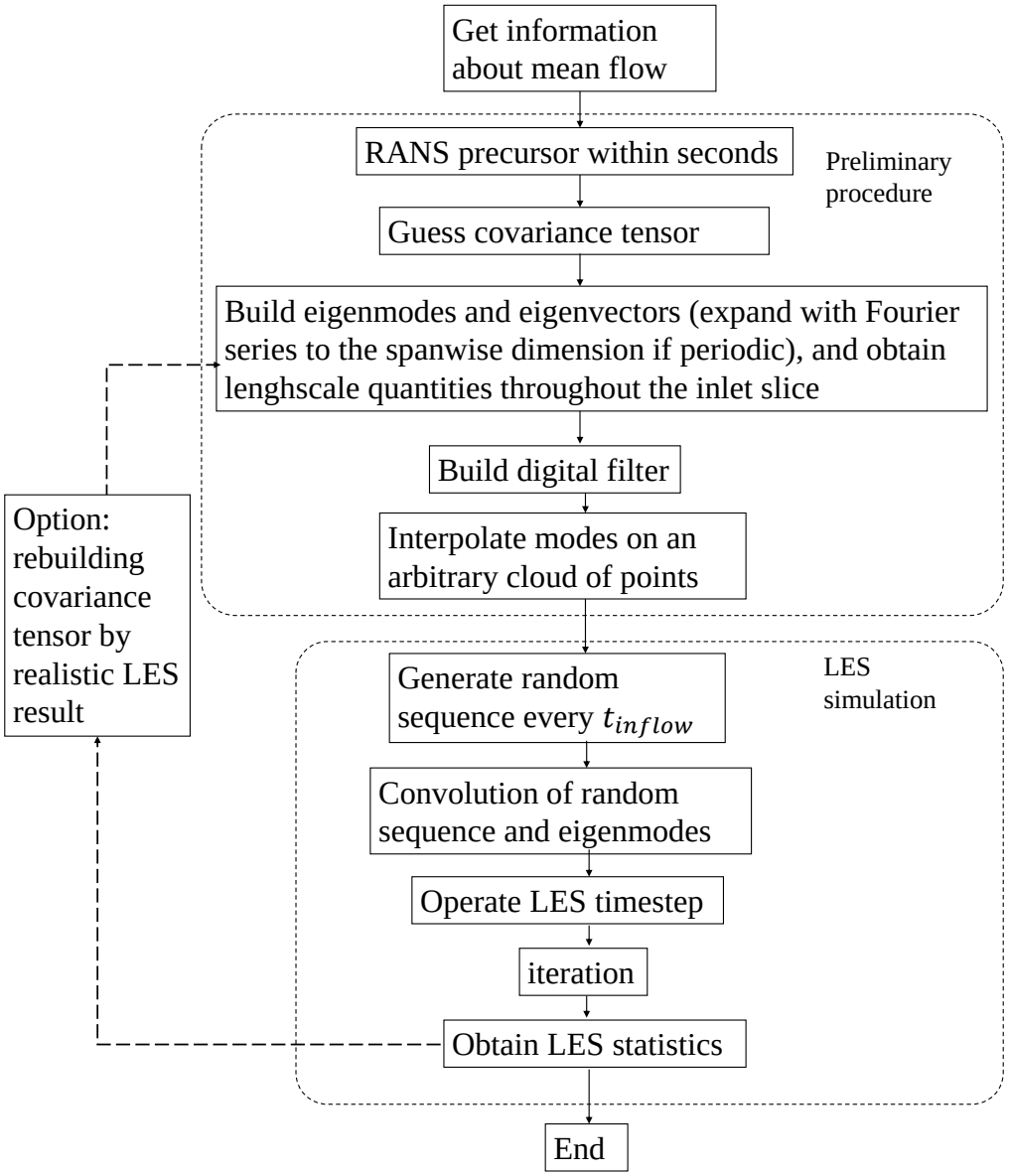


FIG. 3: The whole procedure of an LES simulation with inflow generator

applies a third-order four-stage Runge-Kutta scheme. The simulations were initially run for 10 flow-through times to remove the transient effect. Statistics are collected for 14 flow though times. Both the averaging in the spanwise direction and the mirror averaging along the wall-normal direction are performed at each streamwise position to pursue the convergence of statistics.

A reference simulation (PER0) was performed to compare with all other cases. PER0 is simulated using streamwise periodic boundaries. Its flow is driven by a pressure gradient that is adjusted automatically to maintain a constant mass flux. All the other simulations (INFL0 - INFL7) are using the proposed synthetic inflow generator, with different turbulence parameters specified. All the channel simulations adopt the same mesh and numerical schemes. The configurations of channel simulations are summarised in Table I.

TABLE I: Simulations for turbulent channel flow cases at $Re_\tau = 395$

Cases	**Method**	**Details**
DNS0	DNS, Periodic calculation	Lee and Moser[45]
PER0	LES, Streamwise periodic boundary	—
INFL0	LES, Inflow generator	α_I=0.6, Mt=2048
INFL1	LES, Inflow generator	α_I=0.75, Mt=2048
INFL2	LES, Inflow generator	α_I=1.0, Mt=2048
INFL3	LES, Inflow generator	α_I=2.0, Mt=2048
INFL4	LES, Inflow generator	α_I=0.75, Mt=1024
INFL5	LES, Inflow generator	α_I=0.75, Mt=4096
INFL6	LES, Inflow generator	α_I=0.75, Mt=512
INFL7	LES, Inflow generator	α_I=0.2, Mt=2048

A. Validation

The time-averaged mean velocity profiles in wall units at $x/\delta = 15$ are presented in Fig. 4. The profiles closely agree with the logarithmic law $U^+ = 1/k_l\, log(y^+) + C$ where $k_l = 0.4$ and $C = 5.5$, starting at $y^+ \approx 20$. Compared with the result from the periodic method and the results from the inflow generator method, the inflow generator method case (INFL0) shows a slight advantage over

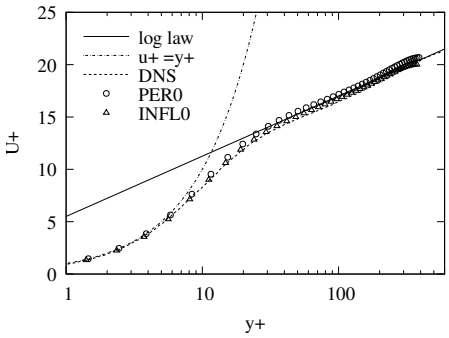


FIG. 4: Mean velocity profiles for a $Re_\tau = 395$ channel at $x/\delta = 15$. Results are compared with the log law $U^+ = 1/k * log(y^+) + C$ and DNS results[45]

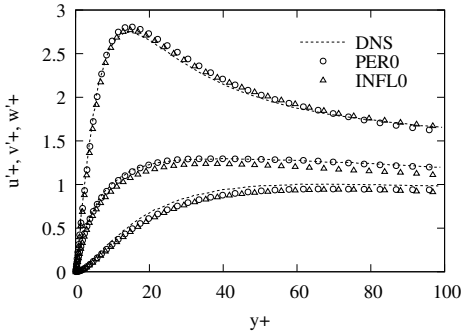


FIG. 5: Rms velocity profiles in wall coordinates for a $Re_\tau = 395$ channel at $x/\delta = 15$. LES results are compared with DNS results[45]. The curves with the amplitudes from high to low are u'^+, w'^+, and v'^+

the case using the periodic method (PER0) in matching the DNS curve in the log-law region. Therefore, the proposed synthetic inflow generator is capable of generating a realistic turbulent velocity profile.

Fig.5 compares the LES result with Lee and Moser's DNS result in terms of the rms of the Reynolds normal stresses ($< u'u' >$,$< v'v' >$ and $< w'w' >$) in wall units. The computed Reynolds normal stresses of both PER0 and INFL0 match well with the DNS result. The slight underpredicting of w'^+ near $y^+ = 40$ is shown in both PER0 and INFL0. This underpredicting is presumably caused by the numerical scheme in the LES code. Both the v'^+ of INFL0 and the v'^+ of PER0 nearly overlap the corresponding DNS curve. The u'^+ of INFL0 becomes overpredicted when

$y^+ > 80$. The u'^+ of INFL0 in the $y^+ < 80$ region and the u'^+ of PER0 throughout all the y^+ regions agree well with the counterpart DNS results. The errors mentioned above are acceptable. The error can be minimized when the energy spectrum, the time filter support, and the t_{inflow} are specified as optimum. The effect of these parameters on the shape of velocities and turbulence intensities will be discussed in the next section.

B. Turbulence parameters

1. The effect of the specified energy spectrum

The shape of the specified energy spectrum is decided by controlling α_I in Equ. 19. A larger α_I means that the inertial region starts from a smaller wavenumber in the approximate spectrum, and leaves a wider inertial region, as indicated by the energy spectrum shown in Fig. 6.

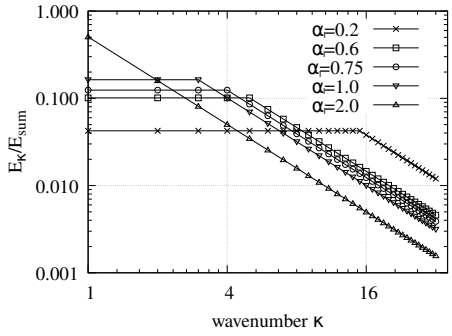


FIG. 6: Energy distribution along wavenumber by different partitions

The prescribed energy spectrum is evaluated by the development of velocity profiles and turbulence intensities downstream of the inlet, shown in Fig. 7 and Fig. 8. The solid line represents the reference case PER0. INFL0, INFL1, INFL2, INFL3 and INFL7 are cases using the inflow generator prescribed with α_I between 0.2 and 2.

Fig. 8 shows the Reynolds normal stresses and the Reynolds shear stress along the streamwise direction. In Fig. 8, INFL3 and INFL7 require the longest development length. This is due to either a too large α_I (INFL3) or a too small α_I (INFL7). INFL3 requires 20δ for the development length of u'^+. Although u'^+ and w'^+ are not very different in INFL3 and in PER0 at 10δ downstream from the inlet, the v'^+ of INFL3 in the near-centerline region maintains a deviation from the PER0

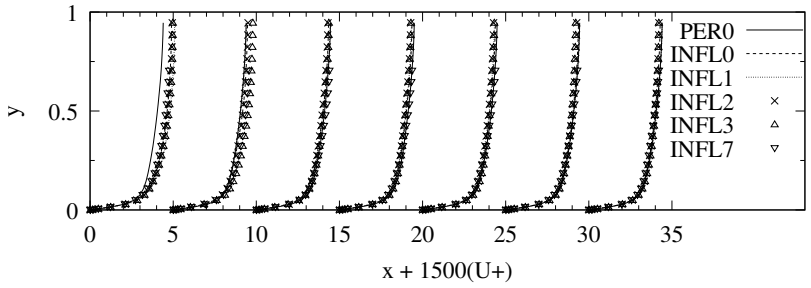


FIG. 7: Downstream development of the velocity profiles downstream the inlet on the bottom half of channel

counterpart till the outlet. In contrast, in INFL0, INFL1 and INFL2, u'^{+}, v'^{+}, w'^{+} and $u'v'^{+}$ collapse onto their contourparts in PER0 from around $x/\delta = 10$.

Above all, INFL2 is the one that collapses onto PER0 most rapidly and that is the closest to PER0. INFL1 and INFL0 are also acceptable. This means that the optimum starting position of the inertial region on the approximate spectrum is when $0.6 < \alpha_I < 1$ ($\alpha_I = 1$ is the best) in this case. The error of INFL3 also indicates that an approximate flat infrared region is needed as a part of the spectrum: ignoring the flat infrared region may result in overpredicted Reynolds normal stresses and Reynolds shear stress. On the contrary, if the wavenumber at the start of the inertial region is set too large, Reynolds normal stresses and the Reynolds shear stress will be underpredicted. This is because when little energy is allocated to lower wavenumbers on the spectrum, small turbulence structures are destroyed immediately.

Fig. 7 shows the development of the velocity profiles downstream from the inlet. It shows that the velocity profiles of all inflow cases collapse onto PER0 downstream from $x/\delta = 10$. Adjusting the intersection point on the energy spectrum doesn't make much difference to the velocity profiles downstream from the end of the inlet development section, which is of 10δ in this channel case.

2. The effect of the specified time filter

In the proposed time filtering method, the shape of the time integration can be decided by adjusting the frequency of time sampling and the total number of physical time samples, namely the time filter control parameter α_t and the time filter support M_t. To guarantee that all energy-containing modes can be presented, inflow time samples should be sufficient and reasonably dis-

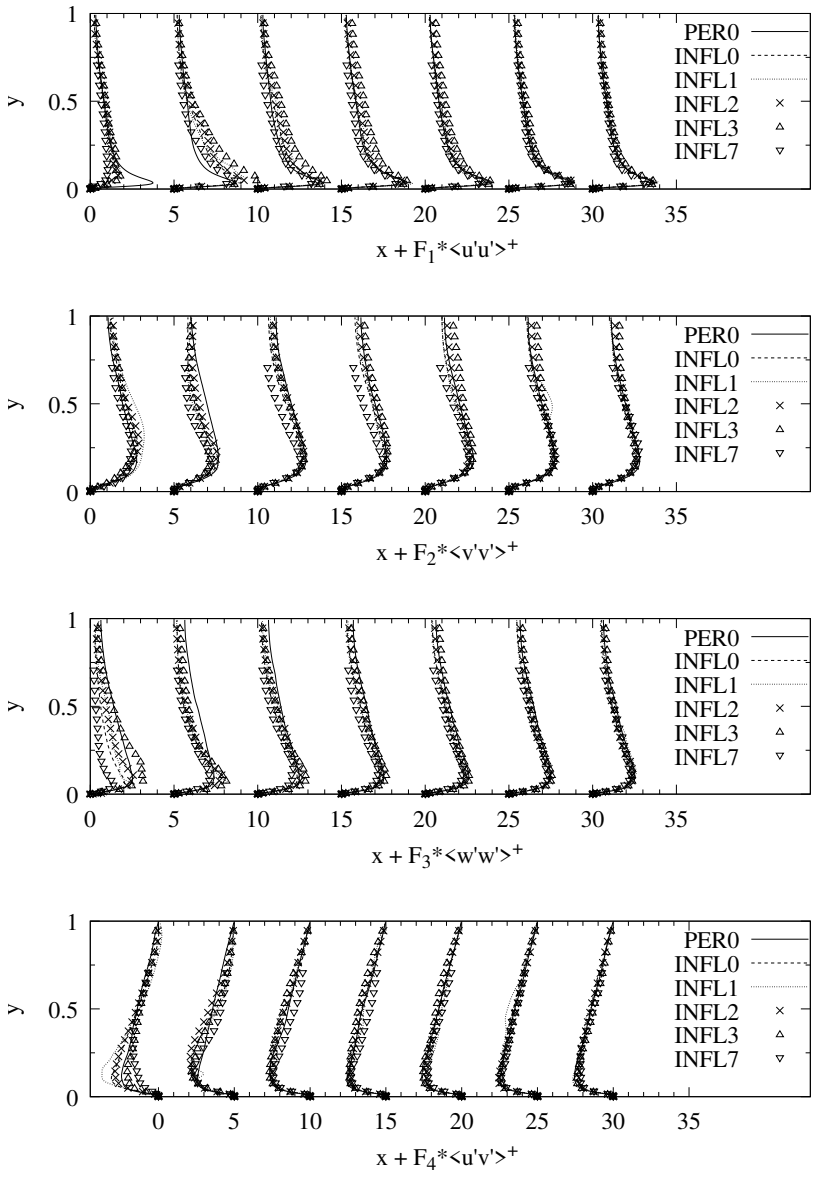


FIG. 8: Downstream development of the normal stress and Reynolds stress downstream the inlet on the bottom half of channel, From top to below are ($x+F_1*u^+$, $x+F_2*w^+$, $x+F_3*v^+$, $x+F_3*uv^+$, where F_1, F_2, F_3 and F_4 are scaling factors)

tributed. For this purpose, an optimum ratio of M_t to α_t is first searched for to select the number of inflow generator time samples. Fixing the ratio of M_t to α_t, the shape of the time filtering is then controlled by only adjusting M_t, as indicated in Equ. 29. Fig.9 shows the time filtering for different combinations of M_t and α_t. Fig.9.(a), Fig.9.(c) and Fig.9.(e) show that when the ratio of M_t to α_I is too large, the time samples of lower index modes may become truncated, thus leading to incomplete total kinetic energy. By contrast, when the ratio of M_t to α_I is too small, there may be not enough sample points to sketch the highest modes. Fig.9.(a), Fig.9.(b), and Fig.9.(f), or Fig.9.(c) and Fig.9.(d) show that when the ratio of M_t to α_I is same, indicating a same inflow time step dt_{inflow}, a larger M_t results in a more concentrated time distribution while the peak amplitude of each corresponding mode is kept the same. For $M_t/\alpha_t = 64$, $M_t = 512$ leads to an incomplete 'Gaussian shape' of the time distribution of the lower index mode, while $M_t = 2048$ leads to an over-concentrated time distribution of all of modes. For $M_t/\alpha_t = 32$, $M_t = 1024$, all of modes are expressed with sufficient sample points when $M_t > 512$. Fig.9.(d), Fig.9.(e) and Fig.9.(f) show that the tightness of the time samples of each mode is dependent on α_t. Given a same $\alpha_t = 32$, $M_t < 1024$ may not provide enough samples for the peak of the highest modes. As a result, 32 is chosen as an optimum ratio of M_t to α_t, and is used in all the cases shown below.

Fig.10 shows the development of the Reynolds normal stresses and the Reynolds shear stress downstream from the inlet. It compares the inflow generator cases by using different time filter supports with the reference case PER0. Since the M_t and α_t that may cause incomplete Gaussian shape of modes have been excluded in advance, the considered values for the time filter support M_t makes little difference to the turbulence intensities. This suggests that $M_t = 1024$ is already sufficient for the simulated case. On the other hand, further increasing the time samples beyond this value will not help fasten the collapse or shorten the inlet development length.

Fig.11 shows the development of the scaled Reynolds shear stress downstream from the inlet. The proposed synthetic inflow generator is compared with Batten's method[6] and Jarrin's Synthetic-Eddy inlet condition(SEM)[7]. INFL4, INFL5, and INFL6 are not shown here as their patterns are similar to INFL1 according to Fig.10.

Among the six situations shown in Fig.11, the Reynolds shear stress prescribed by Batten's method decays most significantly before being regenerated slowly when going downstream from the inlet. It ends up with non-negligible errors localized around the channel mid-height. Jarrin[8] attributed this error to 'an overly large time scale of the inflow data'. On the contrary, the synthetic inflow generator proposed in this study as well as Jarrin's SEM method[8] present Reynolds shear

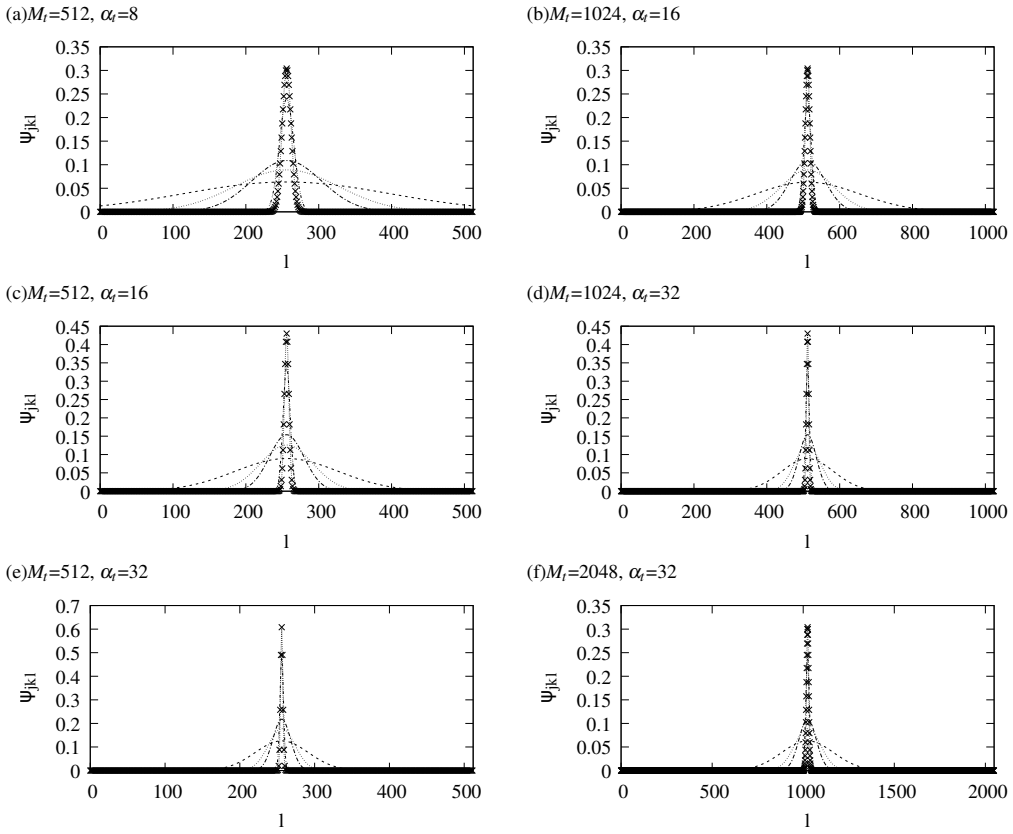


FIG. 9: Time distribution of modes with different Fourier index in the first eigenmode (dash line: 1st Fourier mode, dot line: 2^{nd} Fourier mode, dash dot line: 3^{rd} Fourier mode, dash dot dot line: 16^{th} Fourier mode, dot line with cross symbols: 32^{th} Fourier mode; (a)$M_t = 512$, $\alpha_t = 8$; (b)$M_t = 1024$, $\alpha_t = 16$; (c)$M_t = 512$, $\alpha_t = 16$; (d)$M_t = 1024$, $\alpha_t = 32$; (e)$M_t = 512$, $\alpha_t = 32$; (f)$M_t = 2048$, $\alpha_t = 32$)

stress profiles that rapidly collapse onto the realistic reference (represented by PERO0) profiles after a small transient. Among the considered situations, INFL0 has the smallest 'transient': the levels of Reynolds shear stress agree well with PER0 in the core of the channel and the near-wall region at $x = 5\delta$, while they agree well in the log law region at $x = 10\delta$. INFL1 and INFL2 also have shorter 'transient' than SEM: 5δ in the core of the channel and in the near-wall region; less than 15δ in the log law region. INFL3 has a longer transient than INFL0, INF1, or INFL2 due

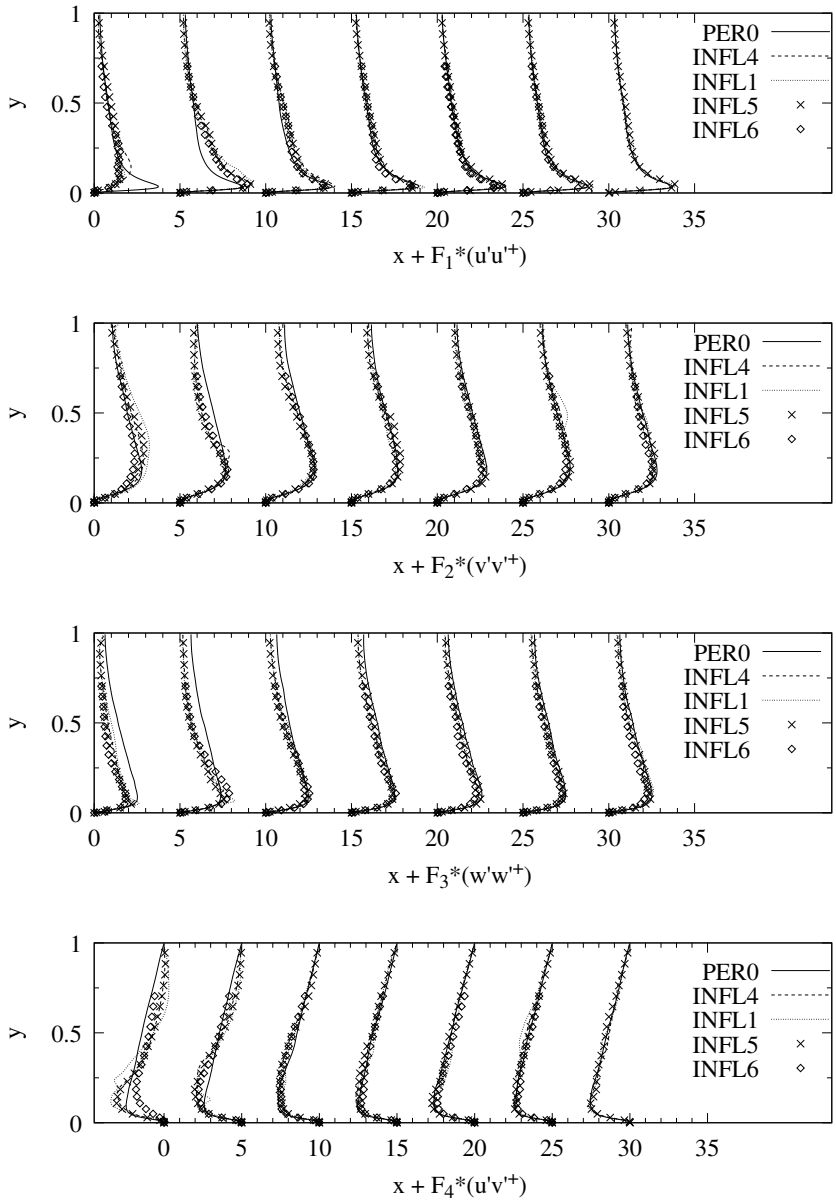


FIG. 10: The development of the normal stress and Reynolds stress downstream from the inlet on the bottom half of channel

to the less realistic energy spectrum of INFL3. This is caused by a too high α_I for INFL3, which leads to a lack of coherence in the turbulent flow. Despite this, the Reynolds stress of INFL3 is on the same level as the SEM result counterparts. This also suggests that if using the synthetic

inflow generator proposed in this study, it is still possible to obtain a realistic turbulent inflow by conveniently adjusting the control parameter for the spectrum shape.

In summary, as long as the parameters (M_t, α_I) are correctly chosen, the regeneration of the Reynolds shear stress can quickly match the reference data. Compared with other methods (including Batten's and SEM), the matching of the proposed inflow generator can be more closed and the 'transient' section from the inlet can be shorter. This is mainly because, rather than using uniform lengthscales for different heights as in other methods, the synthetic inflow generator specifies realistic lengthscales for corresponding heights which are estimated from the preliminary EARSM calculation.

C. Turbulence structures

Fig.12 presents the whole flow field of LES results using the periodic method and the synthetic inflow generator method. These two transient fields present similar turbulence features after a short development length. Similar time scales and lengthscales can be observed in the corresponding heights of the two results. Fig. 13 presents their turbulence structures on the $y^+ = 1$ surface by streamwise velocity fluctuations, respectively. The near-wall turbulent streaks are well reproduced in terms of lengthscales and timescales. Therefore, the proposed synthetic generator has a good capability of reproducing realistic turbulence features in channel flows.

V. APPLICATION FOR A DEVELOPING BOUNDARY LAYER

This section takes a developing boundary layer case as an example to provide general guidance for new users on how to select related parameters for using the proposed synthetic inflow generator. The effect of related controlling parameters on the generated inflow is also discussed.

A. Flow configuration

Sparlart's DNS boundary layer at $Re_\theta = 670$ is targeted. A case of a moderate Reynolds number can be the best test case with a complete log layer and more easily observable turbulent features. The domain size is $100\delta^* \times 20\delta^* \times 25\delta^*$. The grid spacing in x, y, z directions are, in wall units, $\Delta x^+ = 23$, $\Delta y^+ = 0.18$, $\Delta z^+ = 7.8$. The number of points in the y-direction is adjusted to accommodate 10 points within 18 wall units. The numbers of cells are $256 \times 168 \times 192$ in

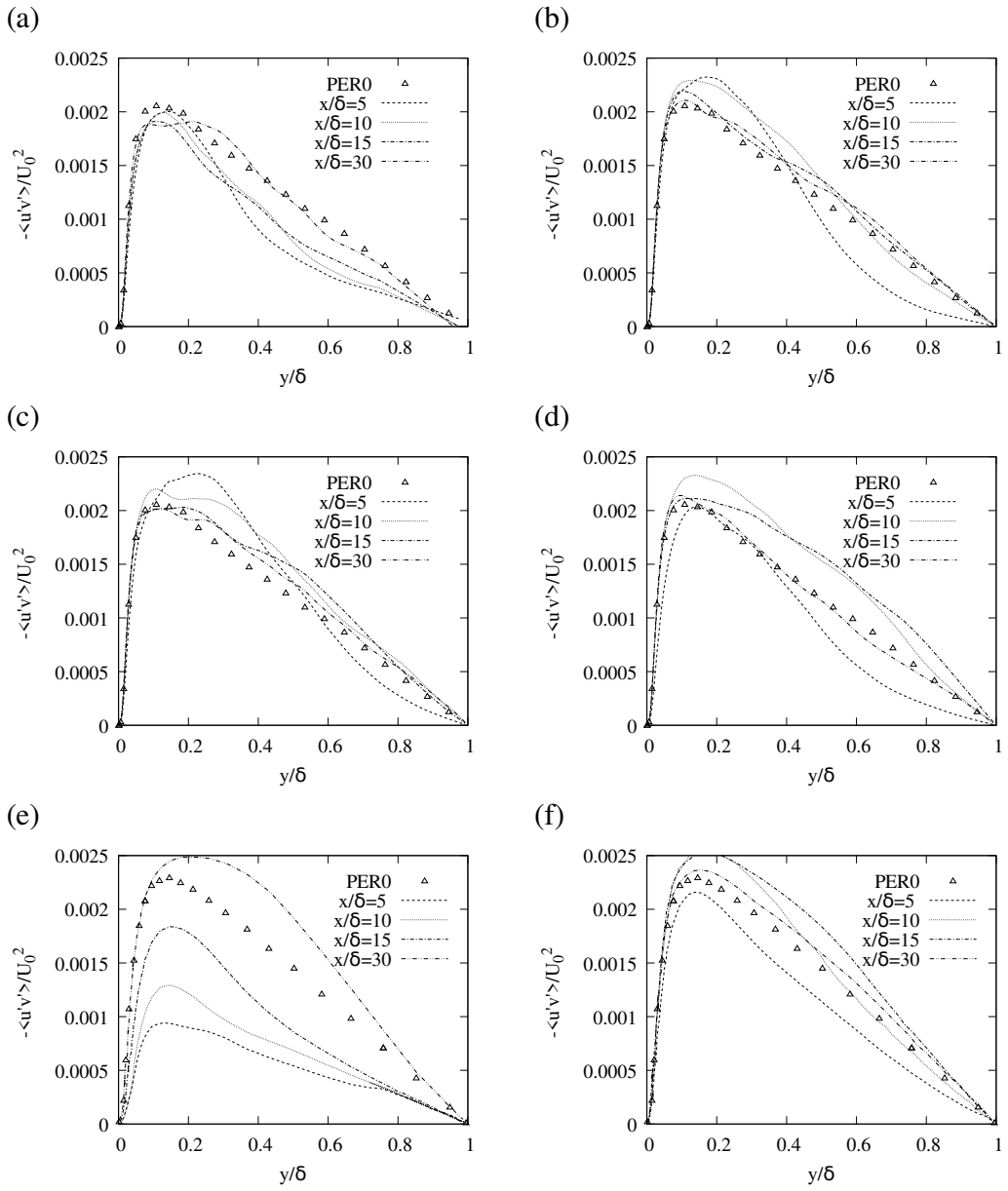


FIG. 11: Profiles of Reynolds shear stress at various streamwise locations in the LES region: (a) INFL7, (b) INFL0, (c) INFL2, (d) INFL3, (e) Batten's method[6], and (f) Synthetic-eddy inflow method[7]. $x/\delta = 5$ (dashed line); $x/\delta = 10$ (dashed line) ; $x/\delta = 15$ (dot-dashed line) ; $x/\delta = 30$ (dot-dashed line); symbols represent periodic LES results. Figures (e) and (f) are reproduced with permission from N. Jarrin et al. Reconstruction of turbulent fluctuations for hybrid RANS/LES simulations using a Synthetic-Eddy Method. 30,3 (2009). Copyright 2009, Elsevier.

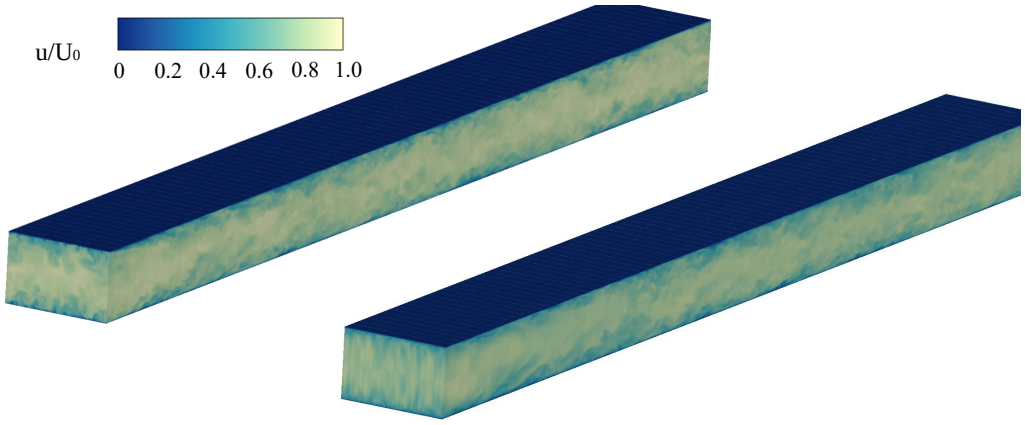


FIG. 12: Downstream development of the velocity profiles downstream from the inlet (3D view , left: PER0, right:INF1)

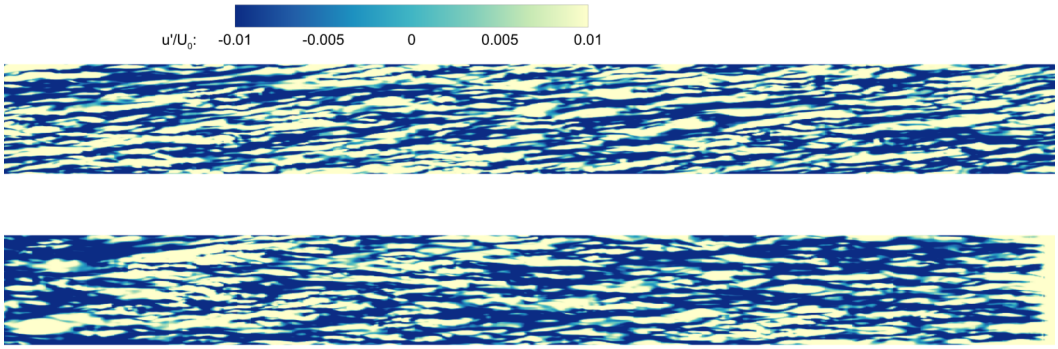


FIG. 13: Downstream development of the velocity profiles downstream from the inlet at the $y^+ = 10$ plane (top: PER0, bottom:INF1)

three dimensions, with 6291456 grids in total. 7 flow through times are run to guarantee that the turbulence reaches a statistically steady state, following that statistics are collected for 10 flow through times. Lateral averaging is performed when analyzing statistics at each streamwise location to guarantee the convergence of statistics.

B. Method parameters

The parameters needed to be set up are the number of Fourier modes specified in the spanwise direction N_f, the number of samples for interpolation in the spanwise direction N_z, the time filter support M_t, the α_I which controls the specified spectrum shape and the retained energy ratio.

1. Spanwise modes

If the flow has a homogenous direction, the spatial variation in the spanwise direction can be described in Fourier modes. The number of modes in the Fourier series is N_f. This section examines the effect of N_f on the property of the flow field. Fig.14 shows turbulent velocities of the generated inflow field on the inlet slice using $N_f = 16, 32, 64$ Fourier modes in the spanwise direction at the same timestep with identical values of all other parameters. As shown in Fig.14, N_f affects the spatial distribution and the strength of turbulent structures.

If the shape of the spectrum is retained, the number of large structures scales approximately with N_f. As an example, approximately 4 large structures are presented when $N_f = 16$ (shown in Fig.14(a)), approximately 8 large structures are presented when $N_f = 32$ (shown in Fig.14(b)), and approximately 16 large structures are presented when $N_f = 32$ (shown in Fig.14(c)). A larger N_f means an increased size of the part of the spectrum obeying the $-5/3$ curve. As a consequence, as N_f increases, more energy is distributed to the higher waves. Given a value of N_f, multiple coherent turbulence structures are generated next to the wall. The size distribution of these structures depends on N_f. The value of N_f is selected as three to four times the number of large structures in the domain.

N_z is the number of the samples used to reconstruct Fourier modes in the spatial domain for the purpose of interpolation onto the inflow surface. Fig.15 shows turbulent velocities of the generated inflow field on the inlet slice using $N_f = 32$ and $N_z = 32, 64, 128, 512$ interpolation samples in the spanwise direction at the same timestep. Using as reference Fig.15(d), no appreciable difference can be discerned among the cases with $N_z = 512$ (in Fig.15(d)), $N_z = 128$ (in Fig.15(c)) and $N_z = 64$ (in Fig.15(b). A loss of resolution can be seen in Fig.15(a) when $N_z = 32$. In general, the minimum number of samples used for the reconstruction should be $N_z \geq 2N_f$.

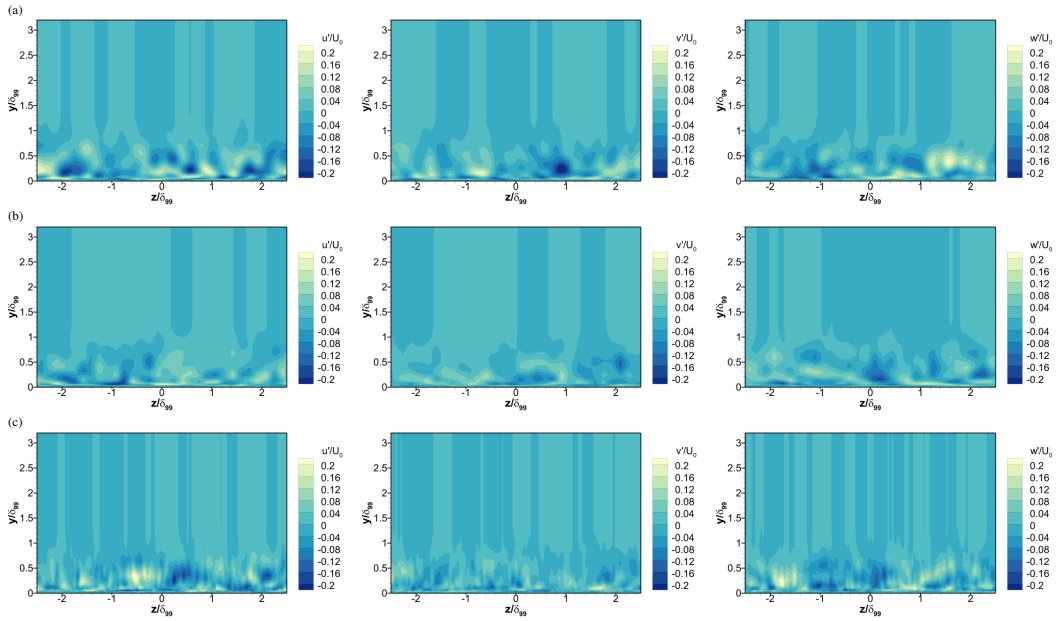


FIG. 14: Turbulence intensities generated at the inflow slice after the same steps: (a) $N_f = 16$, (b) $N_f = 32$, (c) $N_f = 64$

2. *Time filter*

Fig.16 shows the time correlations for the three turbulent velocity components from LES results by using three time filter supports. The correlation coefficient is defined as

$$c(\tau) \equiv \frac{\overline{u_2(t)u_2(t-\tau)}}{\overline{u_2^2}} \tag{30}$$

A larger M_t results in a slower decay of time correlation, whereas a smaller M_t leads to a quicker decay of the time correlation. The integral time scale on a dimensional ground is estimated as proportional to δ/U. The time filter support that results in a decay time longer than the estimated integral length scale is chosen. As a result, $M_t \geq \delta/(U\Delta t)$ is considered sufficient. In this case, $\delta/(U\Delta t) \approx 1024$.

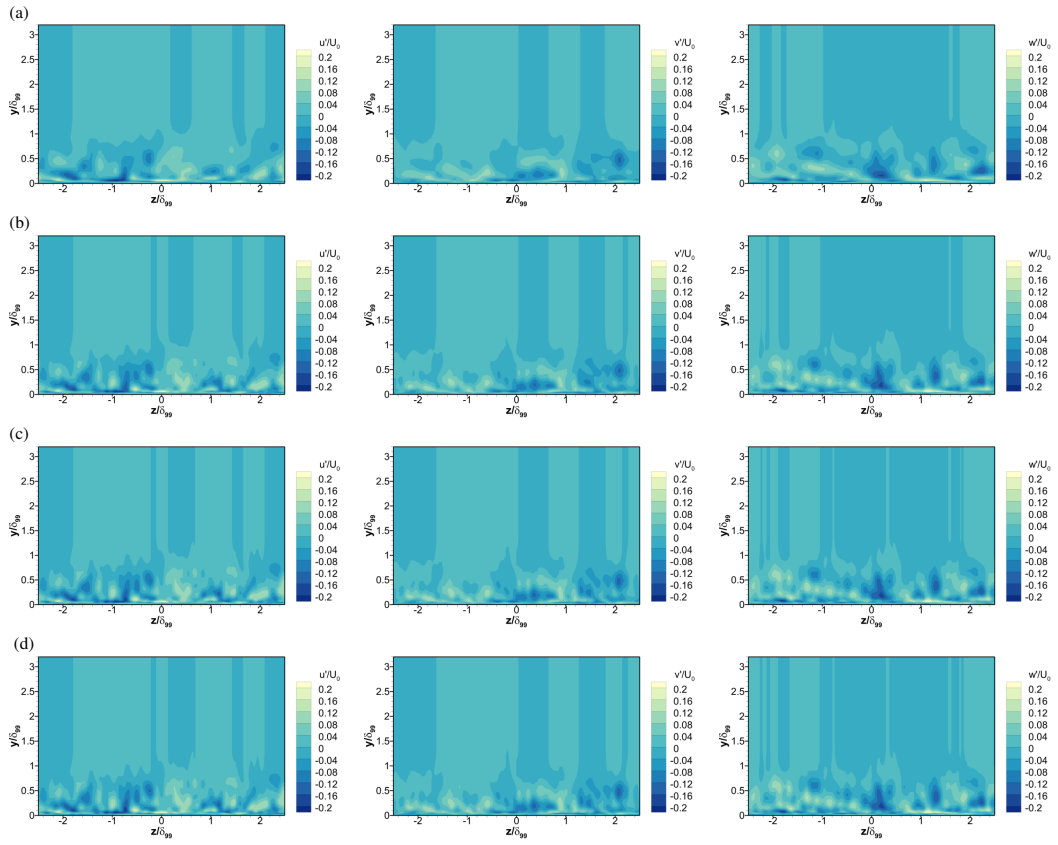


FIG. 15: Turbulence intensities generated at the inflow slice after the same steps: (a) N_z=32, (b) N_z=64, (c) N_z=128, (c) N_z=512

3. Spectrum shape

Two general approaches to spectrum construction are studied, shown in Fig.17(a): firstly, a flat line that represents the infrared region is combined with a $-5/3$ power law curve that represents the inertial region; secondly, a 4 power law curve that represents the infrared region is combined with a $-5/3$ power law curve that represents the inertial region. Once the spectrum construction approach is determined, the shape of the specified energy spectrum is decided by controlling α_I in Equ. 19. A larger α_I means that the inertial region starts from a smaller wavenumber in the approximated spectrum, and leaves a wider inertial region, as shown in Fig.17(a). Four α_I are discussed: 0.5, 1.0, 2.0 and 4.0. As shown in Fig.17(b), $\alpha_I = 4.0$ on both approximated spectrums

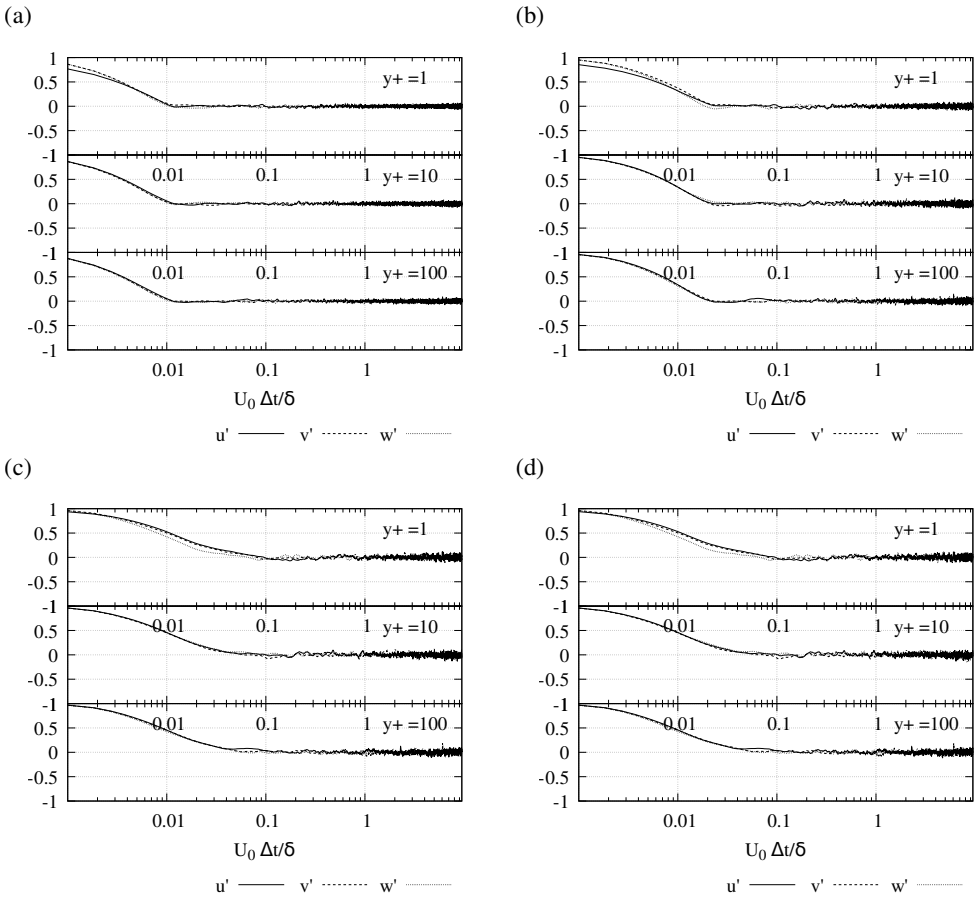


FIG. 16: Time correlations of inflow velocity turbulent components on three y^+ positions, (a)$M_t = 128$, (b)$M_t = 256$, (c)$M_t = 1024$, (d)$M_t = 2048$

can achieve the maximum turbulence intensity roughly as a constant. For those spectrum approximations with much shorter inertial regions, the turbulence intensities decay more severely. This is caused by dissipation, as energy is mostly allocated to large wavenumbers. $\alpha_I = 0.5$ on a 4 power law combined with a $-5/3$ power law spectrum attains the minimum turbulence intensity. The criterion for choosing α_I is that a maximum turbulence kinetic energy can be attained as a constant. When using the optimum α_I, a 4 power law combined with a $-5/3$ power law spectrum approximation can be equivalent to a flat line combined with a $-5/3$ power law spectrum approximation. In this case as an example, the optimal choice is the spectrum constructed by a flat line

and a $-5/3$ power law when $\alpha_I = 4$.

4. Retained energy for retaining modes

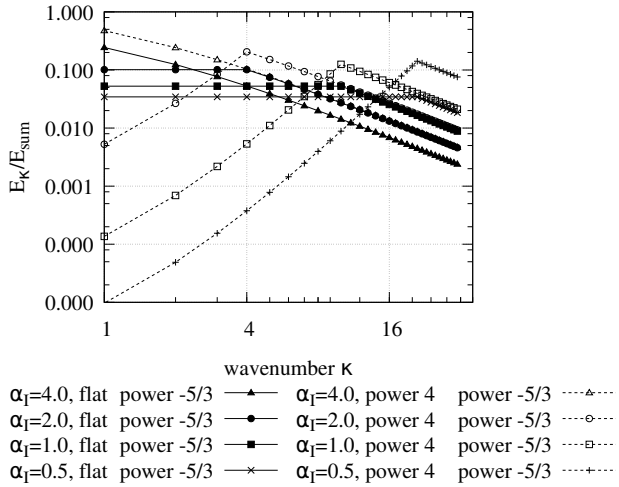
A cutoff criterion based on the total energy is adopted when selecting eigenmodes. It is necessary to retain a sufficient fraction of the total energy of the signal while keeping the least retained eigenmodes. Fig.18 compares two choices of the energy retaining ratio. The method for choosing the retained energy ratio is to choose the smallest number of modes that should be big enough to retain the energy in the Reynolds stresses in the inflow. The criterion is no more 5% difference in turbulent kinetic energy far downstream of the inflow compared to the case where all modes are retained. As an example, Fig.18 shows that retaining 92% energy results in an error of no more than 5% for most parts of turbulence intensity profiles. Meanwhile, no more than one-fifth of eigenmodes are preserved for a fraction of 92%. This helps to save the computational effort during LES simulation as at least four-fifths of eigenmodes are ignored. Therefore, 92% is selected as the energy retaining ratio.

C. Validation

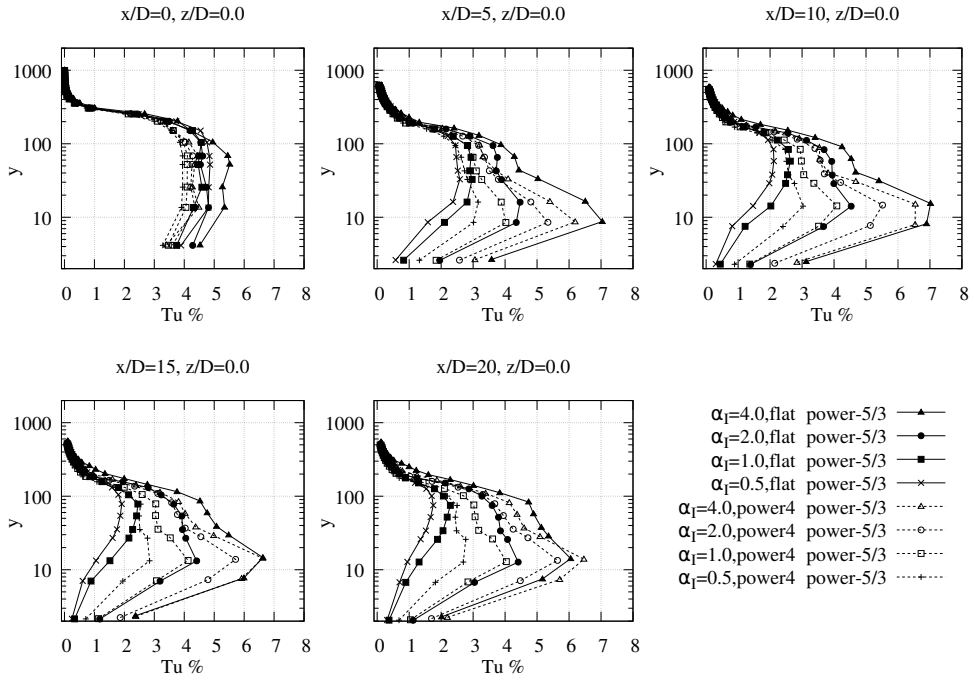
The mean velocity profile in wall units is plotted in Fig.19. The averages are taken in the z direction and in time t. The profile of LES results matches well with the logarithmic law $u^+ = 2.5 * log(y^+) + 5$ from around $y^+ = 30$.

Fig.20 shows the laterally-averaged rms values of Reynolds normal stresses non-dimensionalized by u_τ, vs. y/δ, which are compared with Spalart's DNS result at $Re_\theta = 670$. The LES curves agree well with Spalart's DNS curves reasonably. The LES turbulence intensities in the orthogonal directions v'^+ and w'^+ are slightly offset from the DNS data by a constant distance throughout the wall-normal direction. This might be caused by the dissipation induced by the numerical scheme inherent in the LES code. This good match confirms the validity of the synthetic inflow generator in the boundary layer case of a moderate Reynolds number.

To further visualize qualitative features of the inflow, Fig.21 shows the fluctuation component of the streamwise velocity on the plane near the wall. The synthetic inflow generator is capable of regenerating streaks as in real flow just downstream from the inlet.



(a) Spectrum controlled by α_I



(b) Turbulence intensity of LES results

FIG. 17: The effect of the prescribed spectrum: (a).Spectrum controlled by α_I, (b).Turbulence intensity of LES results

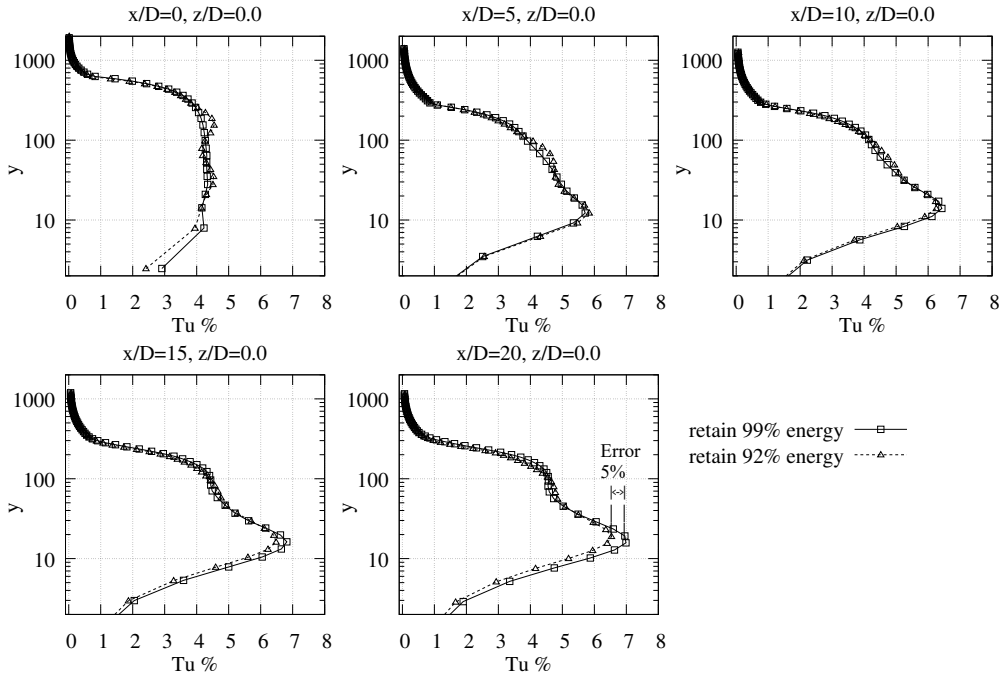


FIG. 18: Turbulence intensity of LES results

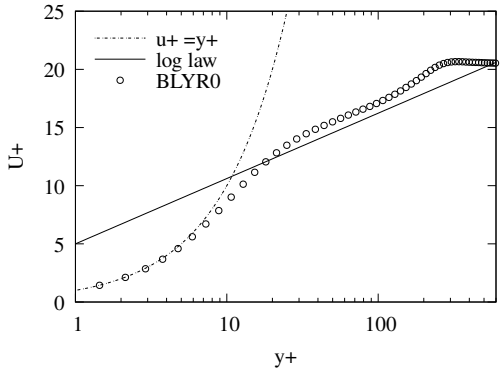


FIG. 19: Laterally-averaged mean velocity profile of Spalart's $Re_\theta = 670$ case at $x/D = 16$

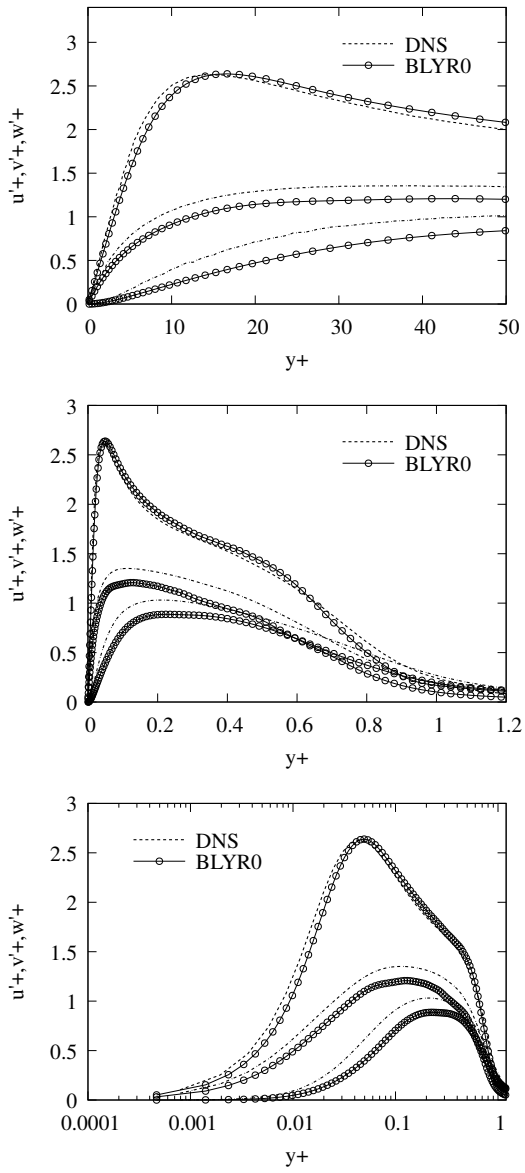


FIG. 20: Turbulence intensities of Spalart's $Re_\theta = 670$ case at $x/D = 16$

D. Computation time

All the filtered coefficients of modes are prepared before the main LES simulation. All the effort for synthesizing the inflow signal, at the stage of the main simulation, is the generation of a random sequence by the random number generator which is only needed once every 'inflow time

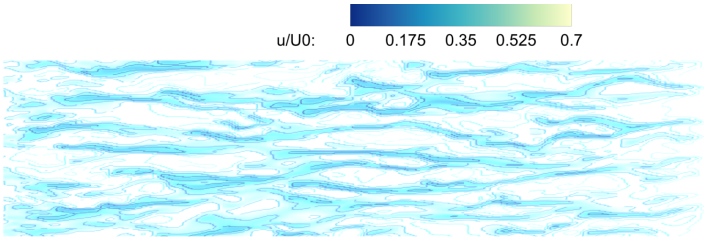


FIG. 21: The instantaneous velocity profiles at $y+ = 15$ of the boundary layer flow

timestep', as well as its following simple linear calculations.

Fig. 22 shows the time needed for the inflow generator. This happens every t_{inflow}.

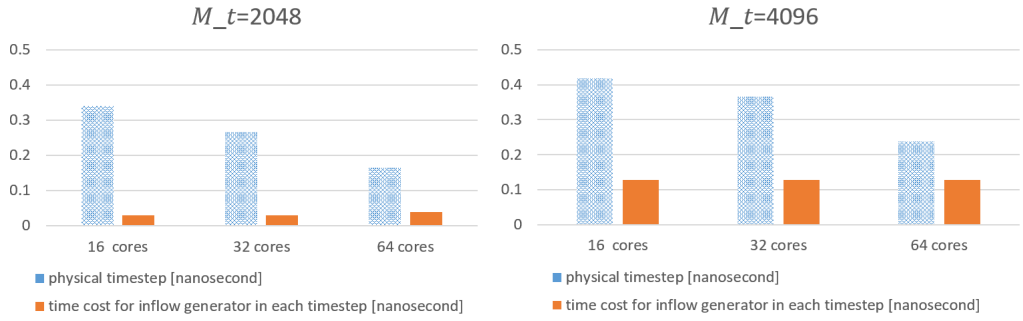


FIG. 22: Wall time for one timestep when random sequence is updated for inflow generation

CONCLUSIONS

This study presents a novel synthetic inflow generator capable of producing a random field matching a realistic set of two-point statistics with minimal input. The method constitutes two main elements, which are the preliminary data generator by RANS and the reconstruction of eigenmodes.

Compared with previous synthetic generation methods, the procedure proposed in this study is much more efficient for the following reasons. First, the preliminary simulation is tiny. A realistic

approximation of correlations for use in the main simulation finishes within seconds. Second, all the efforts required for synthesizing the inflow signal, at the stage of the main simulation, are the random number generator, which does not need to update every timestep, and convolution. All the filtered coefficients of modes are prepared before the main simulation. Third, the synthesizing is operated on a single two-dimensional slice, although 3D data are required. This is enabled by the filtering (the exponential function of the time filter) that correlates the current data with the data from the previous time step. Robustness and accuracy are improved because the proposed method guarantees the prescribed Reynolds stresses, the realistic lengthscales, and two-point and two-time correlations without resorting to a 'decoupling tensor scaling'.

Results prove that as long as controlling parameters needed are set up reasonably, the proposed synthetic generator can produce turbulence inflow which is more close to realistic compared to other existing inflow generation methods. The inflow generator method can show a slight advantage over the periodic method in matching the DNS curve in the log-law region. The computed Reynolds normal stresses can match well with the DNS result, with the error minimized when the energy spectrum, the time filter support, and the t_{inflow} are specified as optimum. Compared with other methods (including Batten's and SEM), the regeneration of the Reynolds shear stress by the proposed inflow generator can collapse onto the reference data more quickly with better matching. This is mainly because, rather than using uniform lengthscales for different heights as in other methods, the proposed synthetic inflow generator specifies realistic lengthscales for corresponding heights which are estimated from the preliminary EARSM calculation.

The general guidance for new users is provided on how to select related parameters for using the proposed synthetic inflow generator. The criteria for setting up the parameters needed are provided. The number of Fourier modes specified in the spanwise direction N_f should be selected as three to four times the number of large structures in the spanwise direction of the domain. The minimum number of samples for interpolation in the spanwise direction N_z should be $N_z \geq 2N_f$. The time filter support M_t should be chosen as a value that results in a decay time longer than the estimated integral length scale. A controlling factor α_I used to control the specified spectrum shape should satisfy the criterion that a maximum turbulence kinetic energy can be attained as a constant. When using the optimum α_I, a 4 power law combined with a $-5/3$ power law spectrum approximation can be equivalent to a flat line combined with a $-5/3$ power law spectrum approximation. The retained energy ratio when selecting eigenmodes should be selected to retain a sufficient fraction of the total energy of the signal while keeping the least retained eigenmodes.

The criterion is no more 5% difference in turbulent kinetic energy far downstream of the inflow compared to the case where all modes are retained.

The synthesized instantaneous inlet flow field is applicable to inhomogeneous (at least in the streamwise and the wall-normal directions) wall-bounded flows.

The proposed inflow generator shows potential for more complex applications, as the mode preparation-and-mode interpolation during the preliminary procedure doesn't limit the shape or the meshing type of the inlet slice. The proposed synthetic inflow generation will be able to make contributions to complex geometries or industrial applications where it may be difficult to set up auxiliary simulations with periodic boundaries or find any source of library data. The authors would recommend applying the proposed inflow generator to a wide range of turbomachinery cases such as film cooling flows.

NOMENCLATURE

U_k mean velocity in tensor notation, $k = 1$: streamwise direction, $k = 2$, wall-normal direction, $k = 3$, spanwise direction

$< u'u' >_\kappa (y_1, y_2)$ convariance component constructed by the u' of y_1 and the u' of y_2

$< u'v' >_\kappa (y_1, y_2)$ the convariance component constructed by the u' of y_1 and the v' of y_2

$< v'v' >_\kappa (y_1, y_2)$ theconvariance component constructed by the v' of y_1 and the v' of y_2

$< w'w' >_\kappa (y_1, y_2)$ theconvariance component constructed by the w' of y_1 and the w' of y_2

α coefficient

α_I the spectrum control parameter

α_t the time filter control parameter

$\bar{u_i}$ mean velocity

$\bar{u}(y,z)$ mean streamwise velocity

$\bar{v}(y,z)$ mean wall-normal velocity

$\bar{w}(y,z)$ mean wall-spanwise velocity

β^* constant

$\check{u}_j(y,z)$ the streamwise velocity component of the j^{th} scaled eigenvector at the position (y,z)

$\check{v}_j(y,z)$ the wall-normal velocity component of the j^{th} scaled eigenvector at the position (y,z)

$\check{w}_j(y,z)$ the spanwise velocity component of the j^{th} scaled eigenvector at the position (y,z)

Δt the time separation that corresponds to two consecutive samples

Δx^+ the grid size in the streamwise direction in wall units

Δy^+ the grid size in the normal-wall direction in wall units

Δz^+ the grid size in the spanwise direction in wall units

$\delta*$ boundary layer displacement thickness

δ channel half height

δ_{99} turbulent boundary layer thickness

δ_{ij} Kronecker delta

$\ell(y_i)$ the lengthscale at the normal-wall position y_i

γ specific-heat ratio, c_p/c_v

$\hat{u}_j(y)$ the constructed velocity on an individual point of the median plane in the streamwise direction

$\hat{v}_j(y)$ the constructed velocity on an individual point of the median plane in the wall-normal direction

$\hat{w}_j(y)$ the constructed velocity on an individual point of the median plane in the spanwise direction

κ the spanwise Fourier mode index

ł the time index

λ_i the eigenvalue of the i^{th} eigenmode

$\mathbb{R}^{n\times n}$ a matrix of n by n

μ_T eddy viscosity

ω specific dissipation rate

Ω_{kj} mean-rotation tensor

$\psi_{j\kappa l}$ the digital filter

ρ density

τ_{ij}^0 specific Reynolds stress tensor

$\tau_{j\kappa}$ a timescale associated with mode $j\kappa$

θ momentum thickness

$\tilde{u}_{j\kappa}(y,z)$ the streamwise velocity component of the uncorrelated constructed signal

$\tilde{v}_{j\kappa}(y,z)$ the wall-normal velocity component of the uncorrelated constructed signal

$\tilde{w}_{j\kappa}(y,z)$ the spanwise velocity component of the uncorrelated constructed signal

$c(\tau)$ correlation coefficient

C constant

dt_{inflow} the 'inflow time step'

F the summation of energy on the approximate spectrum

f_κ^0 correlation coefficient, $f_\kappa^0 = 1$

F_1, F_2, F_3, F_4 scaling factor

f_κ the ratio of discrete signal energy to the energy summation on the approximate spectrum

g_i^j the i^{th} row of the j^{th} eigenvector

i, j, k integer

k_e the kinetic energy of turbulent fluctuations per unit mass

k_i the kinetic energy retained in the i^{th} eigenmode

k_l constant

l_x the streamwise wavenumber

M the assembled covariance tensor

m the number of the retained eigenmodes

M_t time filter support

N the number of spanwise Fourier harmonics

n the number of nodes in the wall-normal direction

N_f the number of Fourier modes specified in the spanwise direction

N_z the number of samples for interpolation in the spanwise direction

N_I the dividing wavenumber

Nu_0 freestream kinematic viscosity

p_{ij} the transformation matrix

q_{ij} the covariance matrix

$r_{j\kappa l(t)}$ a random complex variable

R_{uu} covariance components related with $u'u'$

R_{uv} covariance components related with $u'v'$

R_{vv} covariance components related with $v'v'$

R_{ww} covariance components related with $w'w'$

Re Reynolds number

Re_τ viscous Reynolds number

Re_θ Reynolds number by momentum thickness

s_{ij}^{*} the factorization matrix

S_{ij} mean strain-rate tensor

$s_{j\kappa}(t)$ a correlated random factor

t time

Tu Turbulence intensity

u' turbulent velocity in the streamwise direction

u freestream velocity in the streamwise direction

U^{+} velocity in wall units

u'^{+} turbulent intensity in the streamwise direction in wall units

$u'(y,z)$ A random correlated (y-z) velocity in the streamwise direction

u_0 velocity in the streamwise direction

u_τ friction velocity

v' turbulent velocity in the wall-normal direction

v velocity in the wall-normal direction

v'^{+} turbulent intensity in the wall-normal direction in wall units

$v'(y,z)$ A random correlated (y-z) velocity in the wall-normal direction

w' turbulent velocity in the spanwise direction

W the width of the inlet slice

w velocity in the spanwise direction

w'^{+} turbulent intensity in the spanwise direction in wall units

$w'(y,z)$ A random correlated (y-z) velocity in the spanwise direction

x coordinate/distance in the streamwise direction

x^+ streamwise distance in wall units

x_i^* an uncorrelated random variable

X_k position vector in tensor notation, $k = 1$: streamwise direction, $k = 2$, wall-normal direction, $k = 3$, spanwise direction

y coordinate/distance in the wall-normal direction

y^+ the distance to the wall in wall units

y_0 first grid normal space to the wall

y_1, y_2 wall-normal positions

y_i^* an correlated random variable

z coordinate/distance in the spanwise direction

z^+ spanwise distance in wall units

ACKNOWLEDGMENTS

This work was funded by Rolls-Royce plc. Rolls-Royce plc is gratefully acknowledged for supporting this work and for granting permission for its publication. The authors sincerely thank Aerothermal Specialist Haidong Li in Rolls-Royce plc for helpful suggestions on the paper review. The authors also acknowledge the use of the University of Oxford Advanced Research Computing (ARC) facility in carrying out this work. http://dx.doi.org/10.5281/zenodo.22558. Part of this work was also performed using resources provided by the Cambridge Service for Data Driven Discovery (CSD4) operated by the University of Cambridge Research Computing Service (www.csd3.cam.ac.uk), provided by Dell EMC and Intel using Tier-2 funding from the Engineering and Physical Sciences Research Council (capital grant EP/T022159/1), and DiRAC funding from the Science and Technology Facilities Council (www.dirac.ac.uk).

DATA AVAILABILITY STATEMENT

The data that support the findings of this study are available from the corresponding author upon reasonable request.

REFERENCES

[1]A. Altıntaş, L. Davidson, and S.-H. Peng, "Direct numerical simulation of drag reduction by spanwise oscillating dielectric barrier discharge plasma force," Physics of Fluids **32**, 075101 (2020).

[2]M. E. Nakhchi, S. W. Naung, and M. Rahmati, "Dns of secondary flows over oscillating low-pressure turbine using spectral/hp element method," International Journal of Heat and Fluid Flow **86**, 108684 (2020).

[3]L. Ottolenghi, C. Adduce, F. Roman, and G. la Forgia, "Large eddy simulations of solitons colliding with intrusions," Physics of Fluids **32**, 096606 (2020).

[4]H. Abdulrahman, A. Validi, and F. Jaberi, "Large-eddy simulation/filtered mass density function of non-premixed and premixed colorless distributed combustion," Physics of Fluids **33**, 055118 (2021).

[5]S. Katiyar and S. Sarkar, "Flow transition on the suction surface of a controlled-diffusion compressor blade using a large-eddy simulation," Physics of Fluids (2022).

[6]P. Batten, U. Goldberg, and S. Chakravarthy, "Interfacing statistical turbulence closures with large-eddy simulation," AIAA Journal **42**, 485–492 (2004).

[7]N. Jarrin, S. Benhamadouche, D. Laurence, and R. Prosser, "A synthetic-eddy-method for generating inflow conditions for large-eddy simulations," International Journal of Heat and Fluid Flow **27**, 585–593 (2006).

[8]N. Jarrin, R. Prosser, J.-C. Uribe, S. Benhamadouche, and D. Laurence, "Reconstruction of turbulent fluctuations for hybrid RANS/LES simulations using a synthetic-eddy method," International Journal of Heat and Fluid Flow **30**, 435–442 (2009).

[9]N. S. Dhamankar, G. A. Blaisdell, and A. S. Lyrintzis, "Overview of turbulent inflow boundary conditions for large-eddy simulations," AIAA Journal **56**, 1317–1334 (2018).

[10]H. F. Fasel, U. Rist, and U. Konzelmann, "Numerical investigation of the three-dimensional development in boundary-layer transition," AIAA Journal **28**, 29–37 (1990).

[11]T. Sayadi, C. W. Hamman, and P. Moin, "Direct numerical simulation of complete h-type and k-type transitions with implications for the dynamics of turbulent boundary layers," Journal of Fluid Mechanics **724**, 480–509 (2013).

[12]X. Gloerfelt and J. Berland, "Direct computation of turbulent boundary layer noise," in *15th AIAA/CEAS Aeroacoustics Conference (30th AIAA Aeroacoustics Conference)* (American Insti-

tute of Aeronautics and Astronautics, 2009).

[13]M. L. Shur, P. R. Spalart, M. K. Strelets, and A. K. Travin, "Synthetic turbulence generators for RANS-LES interfaces in zonal simulations of aerodynamic and aeroacoustic problems," Flow, Turbulence and Combustion **93**, 63–92 (2014).

[14]T. Blackmore, W. M. Batten, and A. S. Bahaj, "Inlet grid-generated turbulence for large-eddy simulations," International Journal of Computational Fluid Dynamics **27**, 307–315 (2013).

[15]X. I. A. Yang, J. Sadique, R. Mittal, and C. Meneveau, "Integral wall model for large eddy simulations of wall-bounded turbulent flows," Physics of Fluids **27**, 025112 (2015).

[16]P. Schlatter, R. Örlü, Q. Li, G. Brethouwer, J. H. M. Fransson, A. V. Johansson, P. H. Alfredsson, and D. S. Henningson, "Turbulent boundary layers up to $re_\theta = 2500$ studied through simulation and experiment," Physics of Fluids **21**, 051702 (2009).

[17]N. J. Mullenix, D. V. Gaitonde, and M. R. Visbal, "Spatially developing supersonic turbulent boundary layer with a body-force-based method," AIAA Journal **51**, 1805–1819 (2013).

[18]P. R. Spalart and A. Leonard, "Direct numerical simulation of equilibrium turbulent boundary layers," in *Turbulent Shear Flows 5* (Springer Berlin Heidelberg, 1987) pp. 234–252.

[19]T. S. Lund, X. Wu, and K. D. Squires, "Generation of turbulent inflow data for spatially-developing boundary layer simulations," Journal of Computational Physics **140**, 233–258 (1998).

[20]G. Tabor and M. Baba-Ahmadi, "Inlet conditions for large eddy simulation: A review," Computers & Fluids **39**, 553–567 (2010).

[21]B. Morgan, J. Larsson, S. Kawai, and S. K. Lele, "Improving low-frequency characteristics of recycling/rescaling inflow turbulence generation," AIAA Journal **49**, 582–597 (2011).

[22]L. Duan, M. M. Choudhari, and M. Wu, "Numerical study of acoustic radiation due to a supersonic turbulent boundary layer," Journal of Fluid Mechanics **746**, 165–192 (2014).

[23]M. M. Rai and P. Moin, "Direct numerical simulation of transition and turbulence in a spatially evolving boundary layer," Journal of Computational Physics **109**, 169–192 (1993).

[24]S. Hanna, S. Tehranian, B. Carissimo, R. Macdonald, and R. Lohner, "Comparisons of model simulations with observations of mean flow and turbulence within simple obstacle arrays," Atmospheric Environment **36**, 5067–5079 (2002).

[25]K. Kondo, S. Murakami, and A. Mochida, "Generation of velocity fluctuations for inflow boundary condition of LES," Journal of Wind Engineering and Industrial Aerodynamics **67-68**, 51–64 (1997).

[26]S. Lee, S. K. Lele, and P. Moin, "Simulation of spatially evolving turbulence and the applicability of taylor's hypothesis in compressible flow," Physics of Fluids A: Fluid Dynamics **4**, 1521–1530 (1992).

[27]H. LE, P. MOIN, and J. KIM, "Direct numerical simulation of turbulent flow over a backward-facing step," Journal of Fluid Mechanics **330**, 349–374 (1997).

[28]A. Keating, U. Piomelli, E. Balaras, and H.-J. Kaltenbach, "A priori and a posteriori tests of inflow conditions for large-eddy simulation," Physics of Fluids **16**, 4696–4712 (2004).

[29]B. Roidl, M. Meinke, and W. Schröder, "A reformulated synthetic turbulence generation method for a zonal RANS–LES method and its application to zero-pressure gradient boundary layers," International Journal of Heat and Fluid Flow **44**, 28–40 (2013).

[30]A. Smirnov, S. Shi, and I. Celik, "Random flow generation technique for large eddy simulations and particle-dynamics modeling," Journal of Fluids Engineering **123**, 359–371 (2001).

[31]P. Druault, E. Lamballais, J. Delville, and J.-P. Bonnet, "Development of experiment/simulation interfaces for hybrid turbulent results analysis via the use of dns," in *First Symposium on Turbulence and Shear Flow Phenomena* (Begel House Inc., 1999).

[32]G. Berkooz, P. Holmes, and J. L. Lumley, "The proper orthogonal decomposition in the analysis of turbulent flows," Annual Review of Fluid Mechanics **25**, 539–575 (1993).

[33]M. Klein, A. Sadiki, and J. Janicka, "A digital filter based generation of inflow data for spatially developing direct numerical or large eddy simulations," Journal of Computational Physics **186**, 652–665 (2003).

[34]Z.-T. Xie and I. P. Castro, "Efficient generation of inflow conditions for large eddy simulation of street-scale flows," Flow, Turbulence and Combustion **81**, 449–470 (2008).

[35]J. HŒPFFNER, Y. NAKA, and K. FUKAGATA, "Realizing turbulent statistics," Journal of Fluid Mechanics **676**, 54–80 (2011).

[36]J. P. Bonnet, D. R. Cole, J. Delville, M. N. Glauser, and L. S. Ukeiley, "Stochastic estimation and proper orthogonal decomposition: Complementary techniques for identifying structure," Experiments in Fluids **17**, 307–314 (1994).

[37]D. C. Wilcox and M. W. Rubesin, "Progress in turbulence modeling for complex flow fields including effects of compressibility," NASA STI/Recon Technical Report N **80**, 20527 (1980).

[38]A. Nawab and L. di Mare, "re_τ scaling of POD modes in plane channel flow," Physics of Fluids **30**, 055109 (2018).

[39]P. S. Klebanoff, "Characteristics of turbulence in a boundary layer with zero pressure gradient, naca tn 3178," Tech. Rep. (National Advisory Committee for Aeronautics, 1954).

[40]M. Fathali, M. Klein, T. Broeckhoven, C. Lacor, and M. Baelmans, "Generation of turbulent inflow and initial conditions based on multi-correlated random fields," International journal for numerical methods in fluids **57**, 93–117 (2008).

[41]L. di Mare, M. Klein, W. P. Jones, and J. Janicka, "Synthetic turbulence inflow conditions for large-eddy simulation," Physics of Fluids **18**, 025107 (2006).

[42]A. Kempf, M. Klein, and J. Janicka, "Efficient generation of initial- and inflow-conditions for transient turbulent flows in arbitrary geometries," Flow, Turbulence and Combustion formerly: Applied Scientific Research **74**, 67–84 (2005).

[43]J. A. B. Wills, "On convection velocities in turbulent shear flows," Journal of Fluid Mechanics **20**, 417–432 (1964).

[44]M. Hao, F. Wang, J. Hope-Collins, M. E. Rife, and L. di Mare, "Template-based hexahedral mesh generation for turbine cooling geometries," in *Volume 2C: Turbomachinery* (American Society of Mechanical Engineers, 2020).

[45]M. Lee and R. D. Moser, "Direct numerical simulation of turbulent channel flow up to $re_\tau = 590$," Journal of Fluid Mechanics **774**, 395–415 (2015).

[46]S. Pirozzoli and P. Orlandi, "Natural grid stretching for DNS of wall-bounded flows," Journal of Computational Physics **439**, 110408 (2021).

[47]H. Choi and P. Moin, "Effects of the computational time step on numerical solutions of turbulent flow," Journal of Computational Physics **113**, 1–4 (1994).

[48]M. Pamiès, P.-É. Weiss, E. Garnier, S. Deck, and P. Sagaut, "Generation of synthetic turbulent inflow data for large eddy simulation of spatially evolving wall-bounded flows," Physics of Fluids **21**, 045103 (2009).

[49]R. H. Kraichnan, "Diffusion by a random velocity field," Physics of Fluids **13**, 22 (1970).

[50]L. Davidson, "Hybrid LES-RANS: Inlet boundary conditions for flows with recirculation," in *Notes on Numerical Fluid Mechanics and Multidisciplinary Design* (Springer Berlin Heidelberg, 2008) pp. 55–66.

[51]H. G. Castro and R. R. Paz, "A time and space correlated turbulence synthesis method for large eddy simulations," Journal of Computational Physics **235**, 742–763 (2013).

[52]S. Huang, Q. Li, and J. Wu, "A general inflow turbulence generator for large eddy simulation," Journal of Wind Engineering and Industrial Aerodynamics **98**, 600–617 (2010).

[53]N. Sandham, Y. Yao, and A. Lawal, "Large-eddy simulation of transonic turbulent flow over a bump," International Journal of Heat and Fluid Flow **24**, 584–595 (2003).

[54]J. L. Lumley, "The structure of inhomogeneous turbulent flows," Atmospheric turbulence and radio wave propagation (1967).

[55]A. Spille-Kohoff and H. Kaltenbach, "Generation of turbulent inflow data with a prescribed shear-stress profile," in *DNS/LES Progress and Challenges. Proceedings of the Third AFOSR International Conference on DNS/LES* (2001).

[56]P. R. Spalart, "Direct simulation of a turbulent boundary layer up to $re\theta = 1410$," Journal of Fluid Mechanics **187**, 61–98 (1988).

[57]N. Nikitin, "Spatial periodicity of spatially evolving turbulent flow caused by inflow boundary condition," Physics of Fluids **19**, 091703 (2007).

[58]M. Lygren and H. I. Andersson, "Influence of boundary conditions on the large-scale structures in turbulent plane couette flow," in *TSFP DIGITAL LIBRARY ONLINE* (Begel House Inc., 1999).

[59]E. Sergent, *Vers une methodologie de couplage entre la Simulation des Grandes Echelles et les modeles statistiques*, Ph.D. thesis, Ecully, Ecole centrale de Lyon (2002).

[60]R. Samuel, R. Samtaney, and M. K. Verma, "Large-eddy simulation of rayleigh-b\'enard convection for extreme rayleigh numbers," arXiv preprint arXiv:2204.03697 (2022).



6

Large eddy simulation of film cooling holes

With the key elements: a high-resolution scheme in Chapter 3, an efficient hex mesh generator in Chapter 4, a synthetic inflow generator in Chapter 5 implemented, a homegrown CFD code for LES is ready. Large eddy simulation (LES) is carried out to predict the thermal performance, unsteady flow patterns, and turbulence characteristics of the fan-shaped and cylindrical cooling hole films. Simulations on various operating conditions, including an array of Mach numbers, blowing ratios, and orientation angles, are examined by being compared with classical experimental data.

This chapter contains two journal papers. Technical paper 3 "Scaling laws in three-dimensional wall jets" is under revision in Physics of Fluids. Technical paper 4 "A parametric study of Reynolds stresses and turbulent heat fluxes in fan-shaped and cylindrical film cooling holes" is under revision in International Journal of Heat and Mass Transfer.

In technical paper 3, a theory is proposed explaining the power laws ruling the decay of velocity defect and the growth of the wall jet generated by fan-shaped films and cylindrical films. The theory is based on prime principles and shows that the lateral spread of fan-shaped films is a consequence of the conservation of mechanical energy in the jet, apart from a small loss due to wall friction. The power laws describing the streamwise decay of the Reynolds stresses are shown. An upper bound to the power law describing the downstream evolution of the wall shear stress is also indicated. Estimates for the entrainment rate and power laws describing the wall-normal and transversal velocity scales are obtained. The derivations are based on a small-perturbation expansion for the strength of velocity and density defects.

In technical paper 4, The credibility of the current LES for fan-shaped and cylindrical films is examined first. The discharge characteristics, velocity, and turbulence intensity profiles of the two types of films are compared with published measured data on the same flow configurations. The energy-carrying turbulence structures in and near the cooling holes are illustrated from a standpoint of turbulent Reynolds stresses. Reynolds stresses and turbulent heat fluxes are compared for different blowing ratios and two types of cooling holes in the parametric study. Similarity patterns of velocity profiles, non-dimensional temperature profiles, and Reynolds stresses profiles are discussed.

The findings shown in this paper provide a few useful indications regarding the source of the inaccuracy of RANS simulations. The dataset obtained by using LES allows further budget terms capturing in the transport equations of Reynolds stresses and turbulence heat flux in film cooling cases in Chapter 7, which has never been discussed in the open literature and will be shown in the next chapter.

In addition, a view of hairpin vortices visualized by the iso-surface of Q-criteria colored by scaled streamwise and spanwise components of vorticity is shown in Appendix (in Figure 9.0).

6.1 | Technical Paper 3

AIP/123-QED

Scaling and similarity laws in three-dimensional wall jets

Muting Hao (郝苜婷)[1] and Luca di Mare[1]

Oxford Thermo-Fluids Institute, Department of Engineering Science,

University Of Oxford, Oxford OX2 0ES, United Kingdom

(*Electronic mail: muting.hao@stcatz.ox.ac.uk)

(Dated: 16 January 2023)

Wall jets appear in many situations of technological and scientific interest. In gas turbines, the flows produced by the film as well as impingement cooling devices are three-dimensional wall jets. High-lift devices produce flows that can easily be represented by two-dimensional wall jets. It has been known for a long time that wall jets in both stagnant and moving environments display a layered structure and only partially obey similarity laws. In this paper, we derive scaling laws and obtain self-similar velocity defects, Reynolds stress profiles for the outer part of three-dimensional wall jets in the high-Reynolds-number limit. The scaling laws are derived from prime principles under realistic assumptions about the behavior of the flow. It is shown that the leading term in an expansion of the turbulent kinetic energy (TKE) in powers of the distance from the source must scale like the transversal velocity causing the jet to spread laterally. Only the second term in the TKE expansion is shown to scale like the square of the velocity defect. The scaling laws are tested on numerical and experimental data representing two commonly used film cooling devices.

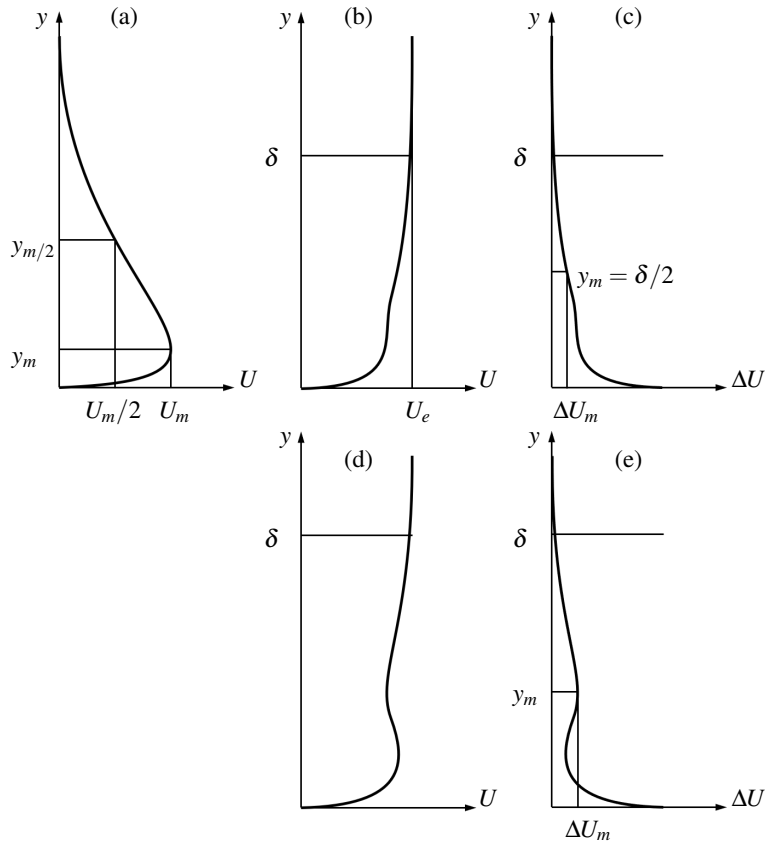


FIG. 1: Wall jet and film cooling jet nomenclature. (a): wall jet; (b) attached cooling film jet velocity profile; (c) attached cooling film jet velocity defect profile; (d) lifted cooling film jet velocity profile; (e) lifted cooling film jet velocity defect profile.

I. INTRODUCTION

Film cooling is a well-established technology to manage the temperature of solid components exposed to very hot streams. Film cooling is indispensable in modern gas turbine engines as it allows the operation of HP turbine blades at gas temperatures far exceeding the melting temperature of the metal. Despite its numerous applications, few theoretical studies exist of the flow field of a film cooling device from a purely fluid mechanic point of view. The closest canonical flow to the flow produced by a film cooling device is a wall jet. A wall jet is a flow produced by a slot or an orifice placed near a solid wall and ejecting fluid in the direction parallel to the wall. Wall jets, as well as film cooling, flows, the display features common to both jets and boundary layers.

The velocity profiles of wall jets are usually parameterized with respect to the maximum velocity U_m and its distance from the wall y_m, see Figure 1 (a). Especially in experimental studies,

it is easier to identify the distance from the wall where the velocity is $U_m/2$. This distance is customarily denoted as $y_{m/2}$ and is commonly used as a length scale for the study of wall jets. In wall-wakes and wall jets produced by film cooling devices, no local maximum of velocity can be identified and the velocity defect with respect to the velocity at the edge of the boundary layer U_e is also monotonic. In this case, the correct scale for the velocity profile is the velocity defect ΔU_m evaluated at $y/\delta_{99} = 1/2$, see Figure 1 (b) and (c). For some film cooling jets, such as those produced by cylindrical films, the jet is lifted off the wall and a maximum velocity defect ΔU_m can be identified, see Figure 1 (d) and (e).

Early interest in film cooling and wall jets arose because of cooling needs in rocket engine combustion chambers[1]. The first set of published wall jet measurements was performed by Förthmann[2], who referred to it as a "partially open jet". Förthmann determined that the velocity profile in his measurements collapsed onto a single curve with the transformation

$$\frac{U}{U_m^p} = f\left(\frac{y}{y_{m/2}}\right) \tag{1}$$

Förthmann also suggested that $p = 1/2$ and $y_{m/2} \approx (x_0 + x)^q$, with $q \approx 1$, based on data on the outer edge of the jet. Föthmann was aware on theoretical grounds that the different scaling may be necessary near the wall and, based on a $1/7$-power law velocity profile, suggested that near the wall

$$\frac{U}{U_m^p} = f\left(\frac{y}{x^q}\right) \tag{2}$$

with $q \approx 0.9$. Förthmann also erroneously identified the location of maximum velocity with the location of zero turbulent shear stress. Liepmann and Laufer[3] showed that the $1/7$ power law is not adequate to describe the velocity profile near the wall and called into question the hypothesis of a constant mixing length for the wall jet.

The wall jet problem was re-examined in the 1950s as the range of possible applications grew from rocket engines to the combustor and turbine cooling, high-lift devices, and de-icing, to name a few. Glauert[4] proved that a laminar wall jet admits self-similar solutions, but that a turbulent wall jet does not obey complete similarity because of the different scaling of the eddy viscosity in the inner and outer parts of the jet. Glauert obtained a self-similar solution by postulating an eddy viscosity consistent with the $1/7$ power law near the wall and a constant eddy viscosity in the outer part of the flow. The two profiles were matched at the location of the maximum velocity, where the stress was assumed to be zero. Glauert's results for a planar wall jet call for a velocity

profile with

$$U_m \approx x^{-1.15} \tag{3}$$

$$y_{m/2} \approx x^{1.015} \tag{4}$$

Glauert's results were partly based on measurements taken by Bakke[5] in a radial wall jet. The numerical constants in the power laws observed by Bakke differed slightly from those predicted by Glauert. Glauert's analysis was also corroborated by Sigalla's data[6],[7] Schwartz and Cosart[8] obtained hot wire measurements of the mean velocity profile in wall jets but not of the Reynolds stresses. They also concluded that the outer part of the velocity profile is self-similar and that the similarity variables are U_m and the jet layer thickness δ. Their analysis showed that U_m must scale with the distance with a power no greater than $-1/2$ and that δ must be linear with respect to distance. Schwarz and Cosart adopted the assumption that the wall layer and the external layer are weakly coupled in their derivation of the similarity parameters and analyzed the wall layer and friction law separately.

Verhoff[9] conducted his analysis based on the assumption that the similarity could be enforced simultaneously in the inner layer and in the outer layer of the wall jet at least over a moderate range of Reynolds numbers. Verhoff also introduced a $1/7$ power law profile as a computational device to derive a universal velocity profile. A similar expression was found in the case of a finite free-stream velocity, but with corrections in the shape of a polynomial expression in the parameter $\zeta = U_\infty/V_j$. Verhoff avoided difficulties with Glauert's assumptions about the eddy viscosity by solving directly for a shear stress profile, which could be expressed in terms of the function f and its integrals. Furthermore, Verhoff showed that there must be a relation between the maximum velocity and the local thickness of the jet layer and that this relation must be of the type

$$U_m \approx (1+M)\delta^{-\lambda} \tag{5}$$

for a suitable constant λ. Similarly, the wall stress must obey a relation of the type

$$u_\tau^2 = -\alpha(1+M)^2 \frac{d}{dx}\delta^{1-\frac{2}{\lambda}} \tag{6}$$

By comparing the kinetic energy of the wall jet with the kinetic energy of a free jet, Verhoff finally showed that the jet thickness must vary exponentially with distance from the orifice:

$$\delta = Ce^{D\left(\frac{2}{\lambda}-1\right)} \tag{7}$$

Kruka and Eskinazi[10] performed measurements and analysis of wall jets in moving streams and found that the maximum velocity U_m, its location y_m and the maximum Reynolds shear stress τ_m are sufficient to collapse mean velocities, turbulence intensities, and Reynolds stress onto universal profiles. They also found that

$$U_m \approx x^{-\alpha} \tag{8}$$

$$u_\tau \approx x^{-2\alpha} \tag{9}$$

Poreh *et al.*[11] studied the axisymmetric wall jet created by a round jet impinging on a wall and attempted to determine universal velocity and turbulent stress profiles based on the local maximum velocity profile and jet thickness. These in turn were found to scale with

$$U_m b/\sqrt{K} = F_m(\sqrt{K}/\nu)(r/b)^m \tag{10}$$

$$\delta/b = F_n(\sqrt{K}nu)(r/b)^{n-1} \tag{11}$$

$$\tau b^2/\rho K = F_\tau(\sqrt{K}nu)(r/b)^{2m+n-1} \tag{12}$$

$$\tag{13}$$

where b is the distance from the geometrical origin of the similarity of the circular jet to the boundary. They noticed that friction data do not corroborate Glauert's assumption that Blasius' friction law holds, nor that the Reynolds stress follows an eddy-viscosity type behavior. Furthermore, Poreh et al found that the turbulence intensities in a wall jet are higher than in the corresponding pipe flow and that the high turbulence intensities are responsible for a modification in the slope and intercept of the velocity profile in the logarithmic region. Poreh's data did not show a complete collapse of the turbulence quantities with the proposed scaling parameters but indicated the scatter in the hot wire data as a possible explanation.

Bradshaw and Gee[12] studied wall jets within the context of boundary layer control and took hot wire measurements of jets flowing along flat and curved walls. They were the first to point out a major flaw in Glauert's solution, namely the non-vanishing shear stress at the location of maximum velocity. They consequently took a stern view on the possibility of formulating numerical predictions for wall jets.

Kacker and Whitelaw[13],[14] produced a detailed survey of wall jets and wall wakes based on hot-wire anemometry and published data on mean velocity profiles, turbulence intensities, Reynolds shear stress, spectra, correlation coefficients and even selected terms in the turbulent kinetic en-

ergy budgets, but did not attempt any form of normalization and did not discuss self-similarity properties exhibited by their results.

Significant contributions to the understanding of the evolution of wall jets at moderate distances from their injection slot were made by Sturgess[15]. Sturgess studied the wall jet produced by cooling slots in combustion chambers with a view to correlating effectiveness data. Sturgess started from the observations that i) most experimental studies are conducted on geometries not closely related to those found in actual devices ii) data from different campaigns cannot be collapsed using commonly applied correlations. Sturgess attributed discrepancies to the existence of a potential core in the wall jet which effectively offsets the start of the self-similar region from the geometric point of injection and produced a model to predict the potential core length. Sturgess[16],[17],[18] later revisited the issue of turbulence generation in cooling slots and correlated the performance of the slot with the extent to which turbulence and flow non-uniformity contribute to mixing in the early history of the jet itself. Turbulence and flow non-uniformity, in turn, was determined by the conditions in the plenum downstream of the metering holes.

Hammond[19] produced a unified velocity profile for the inner and outer region of the wall jet in stagnant surroundings by merging Spalding's universal velocity profile[20] and Coles'[21] law of the wake. Hammond also derived a series of ancillary relations illustrating power laws between the main parameters of the flow, e.g. U_m, y_m, the downstream distance from the slot, and the local friction velocity. Hammond showed that the velocity profiles for a wall jet in inner coordinates do not comply to the same universal logarithmic law of the wall as equilibrium boundary layers.

Launder and Rodi[22] conducted a thorough review of literature on measurements and modeling of wall jets up to 1983. Launder and Rodi summarised the state of understanding of turbulent wall jets up to that year by postulating scaling of the velocity profile with U_m and linear growth of $y_{m/2}$ with distance from the source of the jet.

Wignanski *et al.*[23] studied mean velocity profile and Reynolds shear stress in planar wall jets. Wignaski *et al.* found that the maximum velocity U_m and its position $y_{m/2}$ make the outer part of the velocity profiles collected at different distances from the origin of the jet collapse onto a single line. They introduced the jet momentum flux into their scaling laws and showed from their results

that

$$U_m \approx (x-x_0)^{-0.47} \tag{14}$$

$$y_{m/2} \approx x^{0.88} \tag{15}$$

$$\tau_w \approx x^{-1.07} \tag{16}$$

Wignaski *et al.* also concluded against the possibility of matching velocity profiles to the logarithmic law of the wall. Remarkably, Wignaski *et al.* found it impossible to obtain collapse of their turbulence intensities.

Zhou and Vigatsky[24] focused their analysis on the outer part of velocity profiles of wall jets with a finite free-stream velocity and showed that as long as the ratio of jet velocity to free-stream velocity U_m/U_e is greater than 2, all available data can be made to collapse onto a universal profile of the type

$$\frac{U-U_e}{U_m-U_e} = f\left(\frac{y-y_m}{y_{m/2}-y_m}\right) \tag{17}$$

They also showed that essentially all the macroscopic parameters of the flow could be collapsed onto universal power laws if the momentum thickness was introduced in the analysis.

Eriksson *et al.*[25] reported detailed measurements of mean and turbulent flow quantities and scaling parameters and reported confirmation of the mutual scaling of the maximum velocity and the jet layer thickness, with an exponent close to -1: $\log(U_m) \approx -1.083 - 0.573\log\left(y_{1/2}\right)$. They also found a linear growth rate $y_{1/2}/b = 0.0782\,(x/b) + 0.332$. Eriksson *et al.* also reported normal and shear Reynolds stresses normalized against the local maximum velocity in the wall jet, showing that full similarity is not attained for the Reynolds stresses in external coordinates.

George *et al.*[26] proposed a set of scaling laws based on the friction velocity u^* for the wall layer and the maximum velocity U_m for the outer layer based on the results by Eriksson *et al.* as well as other sources. They showed that the inner and outer layers are not as weakly coupled as initially postulated by Glauert[4] and on the contrary a residual dependence on the length scale ratio $u^* y_{1/2}/\nu$. One of the interesting results obtained by George *et al.* is that the wall-normal Reynolds stress and the Reynolds shear stress scale with different quantities, namely U_m and u^*. They also found that the maximum velocity must scale with an exponent no larger than $-1/2$ with respect to downstream distance.

Barenblatt *et al.*[27] revisited the planar wall jet and showed two separate scaling laws in action

for the inner and outer layer:

$$y/y_m^t \approx x^{0.93} \tag{18}$$

$$y/y_m^w \approx x^{0.68} \tag{19}$$

A recent contribution to the literature on wall jets was made by Gupta *et al.*[28], who derived a universal velocity profile for the buffer layer between the wall and the maximum velocity and showed that the correct coordinate for this part of the flow is rescaled by $\sqrt{Re_\tau}$.

Studies on three-dimensional jets started appearing in literature later than studies on two-dimensional jets. Sforza and Herbst[29]studied three-dimensional wall jets issuing from rectangular orifices. They identified the effect of the jet potential core on the decay rate of the jet and showed the existence of two separate ranges for the spread of a three-dimensional wall jet and determined power laws describing the lateral and vertical growth of the jet, as well as the decay of the maximum velocity. The findings of Sforza and Herbst were reproduced by Kirpatrick and Kenyon[30] a few years later but in the context of wall jets for air conditioning. Newmann *et al.*[31] studied the three-dimensional wall jet issuing from a round hole. They found that the jet has a considerable lateral spread: the jet spreads laterally about seven times faster than it spreads in the direction normal to the wall. The mean velocity components attain self-preserving profiles, but the turbulence intensities do not, even if normalized by a local velocity scale. Swamy *et al*[32] conducted similar investigations. Swamy *et al.* were able to identify not only the power-law spread regime and the radial-like spread regime but also the potential core of their jets. They found that the span-wise and wall-normal spread of the jet requires two separate virtual origins. They otherwise found no collapse of the turbulent quantities. A recent campaign of measurements in a three-dimensional wall jet was conducted by Namgyall and Hall[33], who reported detailed measurements of mean velocity and six Reynolds stresses. Namgyall and Hall also reported estimates of individual TKE production terms and of the overall arrangement of the flow.

In their 1983 review, Launder and Rodi[22] examined the physical mechanism for the fast lateral spread of three-dimensional wall jets and tentatively identified streamline turning and Reynolds stress anisotropy as possible reasons. In a later contribution Craft and Launder[34] examined the question of the lateral spread more in detail by attempting the computation of self-similar two-dimensional solutions based on Reynolds-stress transport models. They concluded that axial vorticity and the lateral spread of the jet are driven by Reynolds stress anisotropy, very much like the secondary flow in a square duct. Craft and Launder produced flow visualizations closely re-

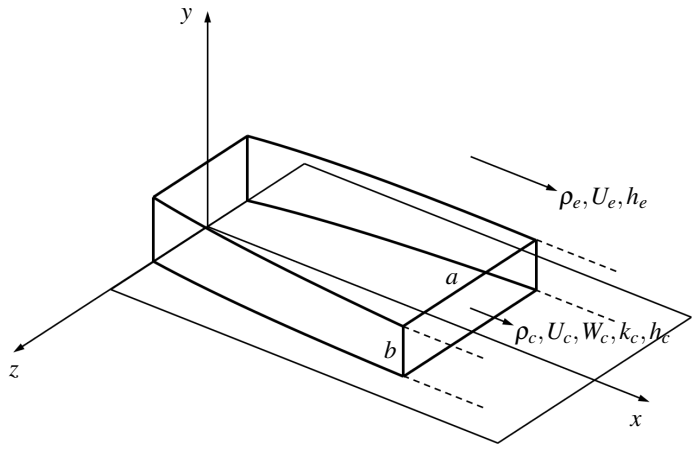


FIG. 2: Downstream development of a film cooling jet.

sembling those produced by Sturgess[16] in his study of turbulence at the exit of combustor cooling slots.

It is clear from this brief review that whereas some consensus exists on the scaling of mean velocity profiles in two- and three-dimensional wall jets, no such agreement exists on the scaling of turbulent quantities with local parameters and with the downstream distance. This paper derives such scaling laws from the first principles, invoking the conservation of fluxes of mass, momentum, and energy for the outer part of the wall jet, neglecting in the first instance the loss of momentum to the wall. The overall conservation equations are stated in II A. A small perturbation theory valid at large distances from the orifice is developed in section II B and estimates of growth rate, entrainment, and transversal velocity scales are derived in section II C. The theory is corroborated by LES data in section III.

II. THEORY

Consider the flow generated by a wall jet, such as a film cooling device. The wall jet is idealized as a rectangular region where the fluid emitted by the film (the coolant) is partially mixed with the hot stream. The jet is surrounded by unperturbed coolant. The flow is developing along a wall and is subject to no imposed pressure gradients. The flow takes place predominantly in the streamwise direction in the hot stream. In the wall jet, the flow has components orthogonal to the free stream

and these are assumed to be comparable in magnitude to the turbulent intensity.

A. Overall conservation equations

The mass, momentum, and total enthalpy fluxes crossing surfaces located at constant streamwise positions are

$$\mathscr{F} = \iint \rho U dydz \tag{20}$$

$$\mathscr{G} = \iint \rho U^2 dydz \tag{21}$$

$$\mathscr{H} = \iint \rho U h^0 dydz \tag{22}$$

The integrals in equations 20-22 can be written as sums of contributions from the wall jet and from the free stream:

$$\mathscr{F} = \iint_S (\rho_c U_c - \rho_e U_e)\, dydz + \iint \rho_e U_e dydz \tag{23}$$

$$\mathscr{G} = \iint_S \left(\rho_c U_c^2 - \rho_e U_e^2\right) dydz + \iint \rho_e U_e^2 dydz \tag{24}$$

$$\mathscr{H} = \iint_S \left(\rho_c U_c h_c^0 - \rho_e U_e h_e^0\right) dydz + \iint \rho_e U_e h_e^0 dydz \tag{25}$$

If the flow properties are uniform within the wall jet and the free stream the integrals are straightforward products:

$$\mathscr{F} = S(\rho_c U_c - \rho_e U_e) + A\rho_e U_e \tag{26}$$

$$\mathscr{G} = S\left(\rho_c U_c^2 - \rho_e U_e^2\right) + A\rho_e U_e^2 \tag{27}$$

$$\mathscr{H} = S\left(\rho_c U_c h_c^0 - \rho_e U_e h_e^0\right) + A\rho_e U_e h_e^0 \tag{28}$$

where the limit $A \to \infty$ is intended and $S = a \cdot b$ is the cross-sectional area of the wall jet. Before processing it is useful to write the total enthalpy in terms of kinetic and static enthalpy contributions:

$$h_c^0 = \frac{\gamma}{\gamma - 1}\frac{p}{\rho_c} + \frac{1}{2}\left(U_c^2 + W_c^2\right) + k_c \tag{29}$$

$$h_e^0 = \frac{\gamma}{\gamma - 1}\frac{p}{\rho_e} + \frac{1}{2}U_e^2 \tag{30}$$

The contribution of the wall-normal component to the kinetic energy of the fluid within the jet is for now neglected: the validity of this approximation will be discussed more in detail in the limit

of large distance from the origin. Conservation laws for mass, momentum, and energy can now be written comparing the fluxes at two nearby streamwise stations to find:

$$\frac{d\mathscr{F}}{dx} = 0 \tag{31}$$
$$\frac{d\mathscr{G}}{dx} = 0 \tag{32}$$
$$\frac{d\mathscr{H}}{dx} = 0 \tag{33}$$

Friction at the wall is neglected in equation 32. Substituting the expressions for the fluxes 26-28 into equations 31-33, and keeping into account that the free stream quantities are constant, one finds

$$\frac{d}{dx}S\rho_c U_c - \rho_e U_e \frac{dS}{dx} = 0 \tag{34}$$
$$\frac{d}{dx}S\rho_c U_c^2 - \rho_e U_e^2 \frac{dS}{dx} = 0 \tag{35}$$
$$\frac{d}{dx}S\rho_c U_c h_c^0 - \rho_e U_e h_e^0 \frac{dS}{dx} = 0 \tag{36}$$

The equations can be further manipulated by substituting the continuity equation 37 into the momentum and energy equations 38 and 39:

$$\frac{d}{dx}\rho_c U_c + (\rho_c U_c - \rho_e U_e)\frac{1}{S}\frac{dS}{dx} = 0 \tag{37}$$
$$\rho_c U_c \frac{dU_c}{dx} + \rho_e U_e (U_c - U_e)\frac{1}{S}\frac{dS}{dx} = 0 \tag{38}$$
$$\rho_c U_c \frac{dh_c^0}{dx} + \rho_e U_e \left(h_c^0 - h_e^0\right)\frac{1}{S}\frac{dS}{dx} = 0 \tag{39}$$

We now introduce the following non-dimensional variables

$$\rho = \rho_c/\rho_e$$
$$U = U_c/U_e$$
$$W = W_c/U_e$$
$$\kappa = k_c/U_e^2$$
$$\xi = x/D$$
$$\zeta = z/D$$
$$\sigma = S/D^2$$

Total enthalpies can be non-dimensionalized thus:

$$\frac{h_e^0}{U_e^2} = \frac{1}{(\gamma-1)M_e^2}+\frac{1}{2} \tag{40}$$

$$\frac{h_c^0}{U_e^2} = \frac{1}{\rho(\gamma-1)M_e^2}+\frac{1}{2}\left(U^2+W^2\right)+\kappa \tag{41}$$

Let

$$\mathscr{M}^2 = (\gamma-1)M_e^2 \tag{42}$$

The non-dimensional form of the conservation equations becomes

$$\frac{d}{d\xi}\rho U+(\rho U-1)\frac{1}{S}\frac{dS}{d\xi} = 0 \tag{43}$$

$$\rho U\frac{dU}{d\xi}+(U-1)\frac{1}{S}\frac{dS}{d\xi} = 0 \tag{44}$$

$$\rho U\frac{d}{d\xi}\left(\frac{1}{\rho\mathscr{M}^2}+\frac{1}{2}\left(U^2+W^2\right)+\kappa\right)+$$
$$\left(\frac{1}{\mathscr{M}^2}\left(\frac{1}{\rho}-1\right)+\frac{1}{2}\left(U^2+W^2-1\right)+\kappa\right)\frac{1}{S}\frac{dS}{d\xi} = 0 \tag{45}$$

B. Small perturbation theory

We now focus on the evolution of the wall jet far downstream of its source. As the jet travels downstream it mixes with its surroundings so that the velocity and temperature of the jet approach the free-stream values. As the jet travels downstream, its effect on the flow becomes weaker and weaker and the non-dimensional quantities describing its behaviour can be represented in terms of negative powers of the distance ξ

$$\rho \approx \rho_1\xi^{-\alpha}+1 \tag{46}$$

$$U \approx U_1\xi^{-\alpha}+1 \tag{47}$$

$$W \approx W_1\xi^{-\beta} \tag{48}$$

$$\kappa \approx \kappa_1\xi^{-\gamma} \tag{49}$$

$$\sigma \approx \sigma_1\xi^{\delta} \tag{50}$$

The velocity defect ΔU is $\Delta U = -U_eU_1\xi^{-\alpha}$. At a large distance from the film, $\xi >> 1$ and for positive α,β,γ the powers of ξ appearing in equations 46-49 are small. This observation will be exploited when obtaining approximate relations from the conservation laws in the limit $\xi >> 1$.

From the ansatz 46-50 the following useful expressions are obtained

$$\frac{1}{S}\frac{dS}{d\xi} = \frac{\delta}{\xi} \tag{51}$$

$$\rho U = 1+\xi^{-\alpha}(\rho_1+U_1)+\xi^{-2\alpha}\rho_1 U_1 \tag{52}$$

Substituting equations 51 and 52 into the continuity equation 43 yields:

$$(\delta-\alpha)\,\xi^{-\alpha-1}(\rho_1+U_1)+\mathscr{O}\left(\xi^{-2\alpha-1}\right)=0 \tag{53}$$

Retaining only terms of order $\mathscr{O}\left(\xi^{-\alpha-1}\right)$ and neglecting terms of order $\mathscr{O}\left(\xi^{-2\alpha-1}\right)$, yields

$$\delta = \alpha \tag{54}$$

The momentum equation is also identically satisfied by the condition in Equ. 54, with an error of order $\mathscr{O}\left(\xi^{-2\alpha-1}\right)$. If wall friction terms are included in the momentum balance for the wall jet, they must also be $\mathscr{O}\left(\xi^{-2\alpha-1}\right)$. In the energy equation, collecting equal powers of ξ we find that the terms containing ρ' as well as first powers of U_1 cancel out. The remaining terms can be rearranged to yield:

$$\left(\frac{\alpha}{2}-\beta\right)\xi^{-2\beta-1}W_1^2+(\alpha-\gamma)\,\xi^{-\gamma-1}\kappa_1-\frac{\alpha}{2}\xi^{-2\alpha-1}U_1^2=0 \tag{55}$$

Requiring

$$\beta = \alpha/2 \tag{56}$$

$$\gamma = \alpha \tag{57}$$

allows the energy equation to be satisfied within an error of order $\mathscr{O}\left(\xi^{-2\alpha-1}\right)$. This estimate will be refined in section II C by using the information on the wall-normal velocities. The conditions 56 and 57 indicate that the contributions from transversal motion and turbulent kinetic energy to the total energy are comparable.

C. Growth and entrainment rate

We now consider the growth rate of the jet in the span-wise and wall-normal direction. For the growth in the span-wise direction we examine the span-wise displacement of the edge of the jet over a short distance $d\xi$:

$$d\zeta = \frac{d\zeta}{d\xi}d\xi = \frac{d\zeta}{d\tau}\left(\frac{d\xi}{d\tau}\right)^{-1}d\xi = \frac{w}{u}d\xi \tag{58}$$

hence

$$\frac{d\zeta}{d\xi} \approx \frac{W_1}{\xi}^{-\alpha/2} \tag{59}$$

Integrating along the streamwise direction, we obtain

$$\frac{a}{D} \approx \xi^{1-\alpha/2} \tag{60}$$

$$\frac{b}{D} \approx \xi^{3\alpha/2-1} \tag{61}$$

Equation 61 allows an estimate to be made for the magnitude of the wall-normal velocities within the jet. Differentiating with respect to ξ and reversing the chain of arguments leading to equation 59 one finds:

$$V \approx \xi^{3\alpha/2-2} \tag{62}$$

Equation 62 confirms the validity of the initial approximation made by neglecting the contribution of the vertical velocity component to the kinetic energy. If the jet is identified as a rectangular area of size S, the mass flow rate carried by jet is

$$\frac{\mathscr{F}}{\rho_e U_e D^2} = \phi = \sigma\rho U = \sigma_1 \xi^{\alpha} + \mathscr{O}\left(\xi^{2\alpha}\right) \tag{63}$$

The entrainment rate is therefore

$$\rho U_e D \frac{d\phi}{d\xi} = \alpha\sigma_1 \xi^{\alpha-1} + \mathscr{O}\left(\xi^{2\alpha-1}\right) \tag{64}$$

III. RESULTS

A. Flow configuration

The theory developed in section II is now tested on a set of numerical results. The results represent a family of well-document film-cooling experiments. The experiments have been described in detail by Wittig *et al.*[35]. The experiments represent single film cooling holes of cylindrical and fan-shaped cross-section with an axis forming an angle of 30^o to the direction of the wall. The ratio of hole length to diameter is $L/D = 6$. The holes discharge into the main channel where a fully developed turbulent flow of hot gas is established. The Mach number in the main channel is $M_e = 0.6$ and the boundary layer thickness upstream of the injection location is $\delta/D = 0.5$. The experiments are conducted with blowing ratios $M = 0.5$, $M = 1.0$, and $M = 1.5$. Further details about the experimental setup are reported in Thole *et al.*[36] and Gritsch *et al.*[37].

B. Numerical Setup

The computations are based on a density-based code. The code is formally third-order accurate in time and space and adopts an implicit LES approach. The space discretization is cell-centered and uses MUSCL variable extrapolation to achieve spatial accuracy. Inviscid numerical fluxes are evaluated using Roe's Riemann solver. Inflow boundary conditions are imposed using a procedure developed by the authors[38] and reproducing realistic estimates of the two-point correlation tensor of the incoming turbulent flow. Full details of the numerical procedure, together with validation data based on the set of experiments by Wittig *et al.*[35] are found in Hao and di Mare[39]. For the purpose of the present calculations, a computational domain comprising the main channel, the hole, and its plenum is formed and discretized with multiblock grids. The grids are constructed using the procedure documented by Hao and di Mare[40]. The domain extends 10D upstream of the injection location and 30D downstream. At the start of each computation, the LES simulation is run for around five flow-through times to eliminate the initial transient effects. Following that, statistics are collected for at least ten flow-through times for each case. The CFL number is 0.8.

C. Downstream evolution of velocity defect and thickness

The downstream evolution of the velocity defect ΔU for the two types of films are shown in figure 3. The exponent α is determined via least square fit for the far-field of the two types of jet and it is found to be $\alpha = -5/6$ for the fan-shaped film and $\alpha = -13/15$ for the cylindrical film. The values obtained from the analysis of the velocity defect data are then used to obtain the exponent of the power law for the jet layer thickness b/D using equation (61). The power laws thus obtained are compared with the variation of b/D obtained directly from the computations. In both cases, the agreement between the observed power law and the predicted power law based on the velocity defect data is excellent.

D. Mean flow quantities

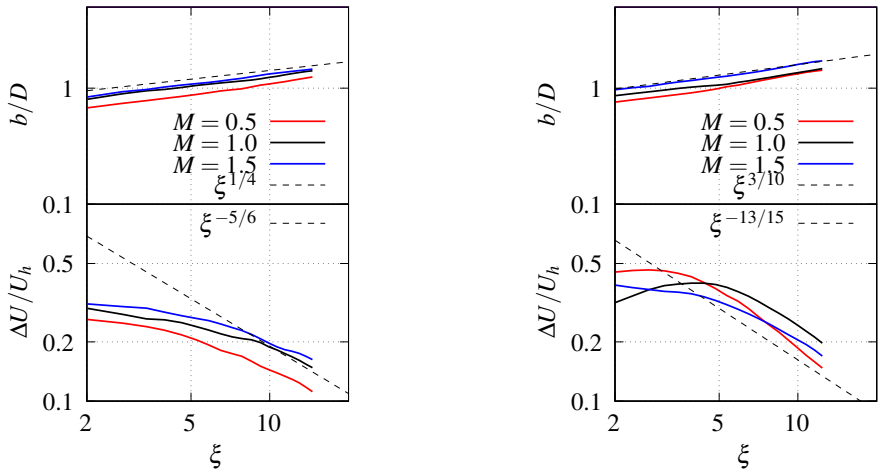
The mean flow profiles are shown for fan-shape and cylindrical films in figure 4. The mean velocity defect profiles for the fan-shaped film show uniformly good collapse of all data between $x/D = 5$ and $x/D = 20$, regardless of the blowing ratio. This finding is consistent with historical evidence on the collapse of wall jet and wall wake velocity profiles both in two- and three dimen-

sions. Similarly, good collapse can be obtained for the cylindrical film data, with the exception that it is now not possible to overlay data from different blowing ratios on a single curve. The data for wall-normal velocity in fan-shaped films corroborate the assumption in equation 29 that the normal velocity is small and therefore its contribution to the kinetic energy of the jet is small. It is also clear that the wall-normal velocity in the wall jet formed by a fan-shaped film is negative: this is a mere consequence of continuity and of the relatively high lateral spreading rate of the jet. In essence, the jet moves fluid from its upper side towards the wall and outwards towards its left and right edges. The collapse of wall-normal velocity data for the fan-shape film in figure 4 also shows that the exponent $2-3\alpha/2$ for the scaling of the vertical velocity is correct. The kinematics of the cylindrical jet is qualitatively different. Here the fluid is drawn upwards, away from the wall, whereas the footprint of the jet on the wall grows narrower as the jet evolves downstream.

E. Reynolds stress

The Reynolds stress profiles are shown for fan-shape and cylindrical films in figure 5. The data in Figure 5 need to be seen in the context of data for Reynolds stress in wall jets. The evidence so far on wall jets shows that the Reynolds stress data do not result in self-similar profiles when normalized with U_m^2. No systematic study exists of the self-similar properties of Reynolds stress profiles in film-cooling wall jets. Equation 57 shows that the Reynolds stress field in the wall jet of a film cooling device does not scale with the velocity defect squared. More precisely, equation 57 shows that when the Reynolds stresses or turbulence intensities are normalized by the velocity defect squared, the quantity obtained scales like $\xi^{-\alpha}$. Some authors in the past have circumvented this difficulty by reporting Reynolds stresses normalized by the maximum value of the turbulent kinetic energy. The data in Figure 5 show that by introducing the additional dependency on ξ predicted by the proposed theory, the collapse of Reynolds stress data can be still obtained for fan-shaped films. The exponent $\beta = \alpha$ is shown to be the correct exponent to rescale turbulence intensity and Reynolds stress. The data reported in 5 also shows that for fan-shaped films the magnitude of the Reynolds stress field can be scaled with the blowing ratio.

The situation for cylindrical films, shown in Figure 5 is slightly more complicated. In this case, no simple power law with respect to the blowing ratio M is suitable to rescale the Reynolds stress profiles. This happens because the different flow regimes - attached or lifted jets - represented in the current data impart different shapes to the Reynolds stress profile. Once the impossibility

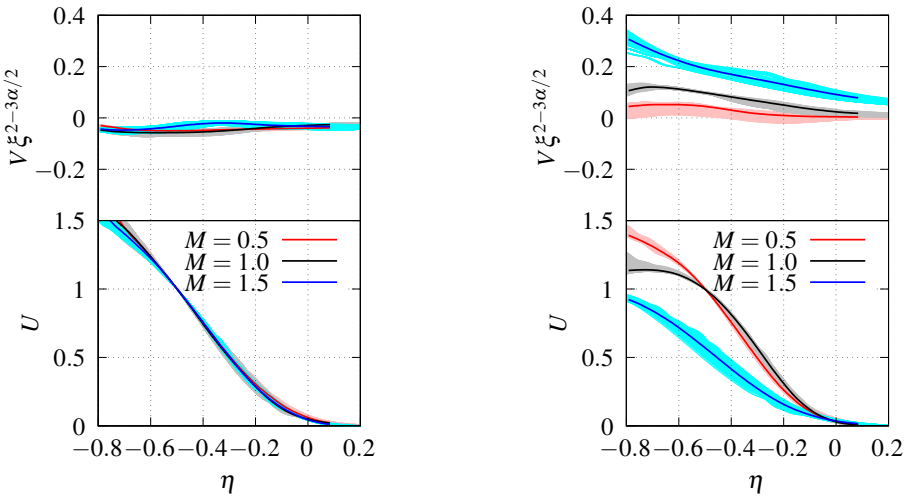


(a) Fan-shaped film

(b) Cylindrical film

FIG. 3: Downstream evolution of velocity defect and jet layer thickness.

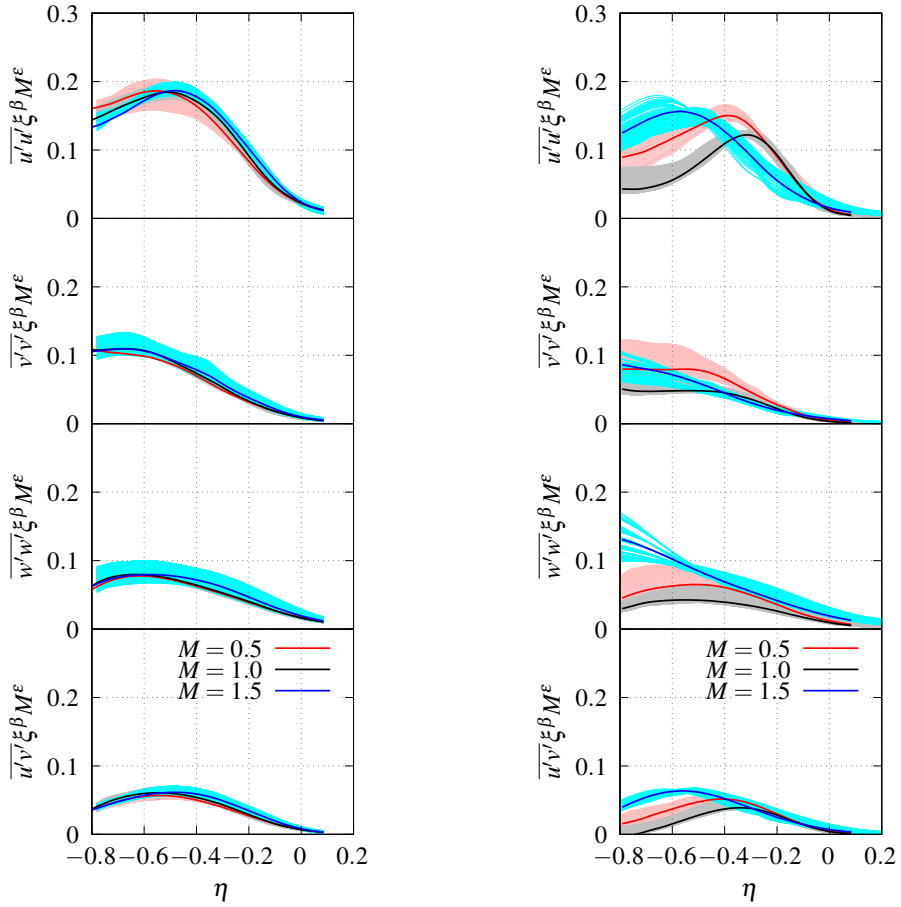
of collapsing curves from different blowing ratios is acknowledged, it is still possible to collapse data for each value of M separately. This is possible because the proposed theory can be applied to each flow condition separately. It is remarkable that, whereas different flow regimes result in different shapes of the Reynolds stress profiles, even for cylindrical films the algebraic relations binding the exponents α and β still hold and the values of this exponent are shown to be fairly insensitive to the blowing ratio.



(a) Fan-shape film.

(b) Cylindrical film.

FIG. 4: Mean velocity defect and wall normal velocities



(a) Fan-shape film.

(b) Cylindrical film.

FIG. 5: Reynolds stresses.

IV. CONCLUSIONS

Historical data on the wall jet show a clear consensus on the universality of mean velocity profiles and the downstream variation of the scaling parameters U_m and $y_{m/2}$. No such consensus exists on the scaling of the turbulent quantities. The authors derive a set of scaling laws for the mean and turbulent flow quantities from prime principles. The first step in derivation is to idealize the area occupied by the jet as a rectangular area. Mass, momentum, and energy fluxes are written in terms of uniform free-stream quantities and mean quantities within the jet. A set of relations is obtained describing the streamwise variation of streamwise velocity defect, density perturbation, spanwise and normal velocity, and turbulence intensity. It is shown that not all these quantities decay with the laws of the same power, but all can be expressed in terms of the exponent α describing the decay of the velocity defect evaluated at a suitably chosen point along the jet layer thickness. One of the consequences of the scaling laws identified is that the correct scale for the turbulence intensity cannot be the velocity deficit squared. Furthermore, the shear stress at the wall is shown to be at most of the order -2α It is also shown that the large difference between spanwise and wall-normal growth rates observed in wall jets is a consequence of the conservation of momentum and energy, and of the initial hypothesis that the wall-normal velocities must be small. Numerical data indicate that the proposed theory is an accurate representation of the jet produced by a fan-shaped cooling film. It is also shown that for this type of device the wall-normal velocity profiles, velocity defects, and Reynolds stress profiles have shapes essentially independent of the blowing ratio M. A power law can also be identified which makes Reynolds stress data at various values of M collapse onto each other.

The jet produced by a cylindrical hole has a different flow arrangement. Nonetheless, power laws for the downstream development of velocity defect, transversal velocity scale, jet layer thickness, and turbulence intensity scale are derived in an identical fashion. The power laws obtained are shown to apply equally well to cylindrical films, albeit with modified exponents for the streamwise decay of the velocity defect and growth of the jet layer thickness. It is seen that the velocity defect, wall-normal velocity, and Reynolds stress profiles have shapes sensitive to the blowing ratio M. As a consequence, it is not possible to identify a power law with respect to M that makes Reynolds stress profiles at various values of M collapse.

V. ACKNOWLEDGMENTS

Rolls-Royce plc is gratefully acknowledged for supporting this work and for granting permission for its publication. The authors sincerely thank Romero Eduardo, Frederic Goenaga, Cristian Orozco Pineiro and Haidong Li from Rolls-Royce plc for helpful discussions. The authors also acknowledge the use of the University of Oxford Advanced Research Computing367 (ARC) facility in carrying out this work. http://dx.doi.org/10.5281/zenodo.22558. Part of this work was also performed using resources provided by the Cambridge Service for Data Driven Discovery (CSD3) operated by the University of Cambridge Research Computing Service (www.csd3.cam.ac.uk), provided by Dell EMC and Intel using Tier-2 funding from the Engineering and Physical Sciences Research Council (capital grant EP/T022159/1), and DiRAC funding from the Science and Technology Facilities Council (www.dirac.ac.uk).

DATA AVAILABILITY STATEMENT

The data that support the findings of this study are available from the corresponding author upon reasonable request.

REFERENCES

[1]D. Singelmann and H. Mueller, "Bmw rocket engine development," Tech. Rep. (AIR MATERIEL COMMAND WRIGHT-PATTERSON AFB OH, 1948).

[2]E. Förthmann, "Über turbulente strahausbreitung," Ingenieur-Archiv **V**, 42–54 (1934), also available as E. Förthmann, Turbulent Jet expansion, NACA TM-789, 1936.

[3]H. W. Liepmann and J. Laufer, "Investigations of free turbulent mixing," Tech. Rep. TN-1257 (NACA, 1947).

[4]M. B. Glauert, "The wall jet," Journal of Fluid Mechanics **1**, 625–643 (1956).

[5]P. Bakke, "An experimental investigation of a wall jet," Journal of Fluid Mechanics **2**, 467–472 (1957).

[6]A. Sigalla, "Measurements of skin friction in a plane turbulent wall jet," The Journal of the Royal Aeronautical Society **62**, 873–877 (1958).

[7]A. Sigalla, "Experimental data on turbulent wall jets: A correlation of existing data," Aircraft Engineering and Aerospace Technology (1958).

[8]W. H. Schwarz and W. P. Cosart, "The two-dimensional turbulent wall-jet," Journal of Fluid Mechanics **10**, 481–495 (1961).

[9]A. Verhoff, "The two-dimensional, turbulent wall jet with and without an external free stream," Tech. Rep. (Princeton Univ NJ, 1963).

[10]V. Kruka and S. Eskinazi, "The wall-jet in a moving stream," Journal of Fluid Mechanics **20**, 555–579 (1964).

[11]M. Poreh, Y. G. Tsuei, and J. E. Cermak, "Investigation of a Turbulent Radial Wall Jet," Journal of Applied Mechanics **34**, 457–463 (1967), https://asmedigitalcollection.asme.org/appliedmechanics/article-pdf/34/2/457/5448397/457_1.pdf.

[12]P. Bradshaw and M. Gee, "Turbulent wall jets with and without an external stream," (1960).

[13]S. C. Kacker and J. H. Whitelaw, "Some properties of the two-dimensional, turbulent wall jet in a moving stream," Journal of Applied Mechanics **35**, 641–651 (1968).

[14]S. C. Kacker and J. H. Whitelaw, "The Turbulence Characteristics of Two-Dimensional Wall-Jet and Wall-Wake Flows," Journal of Applied Mechanics **38**, 239–252 (1971), https://asmedigitalcollection.asme.org/appliedmechanics/article-pdf/38/1/239/5450997/239_1.pdf.

[15]G. J. Sturgess, "Wall cooling by gaseous injection for a high-performance combustion system," (1971).

[16]G. J. Sturgess, "Account of Film Turbulence for Predicting Film Cooling Effectiveness in Gas Turbine Combustors," Journal of Engineering for Power **102**, 524–534 (1980).

[17]G. J. Sturgess, "Design of Combustor Cooling Slots for High Film Effectiveness: Part I—Film General Development," Journal of Engineering for Gas Turbines and Power **108**, 354–360 (1986).

[18]G. J. Sturgess and G. D. Pfeifer, "Design of Combustor Cooling Slots for High Film Effectiveness: Part II—Film Initial Region," Journal of Engineering for Gas Turbines and Power **108**, 361–369 (1986).

[19]G. P. Hammond, "Complete Velocity Profile and "Optimum" Skin Friction Formulas for the Plane Wall-Jet," Journal of Fluids Engineering **104**, 59–65 (1982), https://asmedigitalcollection.asme.org/fluidsengineering/article-pdf/104/1/59/5711578/59_1.pdf.

[20]D. B. Spalding, "A Single Formula for the "Law of the Wall"," Journal of Applied Mechanics **28**, 455–458 (1961), https://asmedigitalcollection.asme.org/appliedmechanics/article-pdf/28/3/455/5444229/455_1.pdf.

[21]D. Coles, "The law of the wake in the turbulent boundary layer," Journal of Fluid Mechanics **1**, 191–226 (1956).

[22]B. Launder and W. Rodi, "The turbulent wall jet measurements and modeling," Annual review of fluid mechanics **15**, 429–459 (1983).

[23]I. Wygnanski, Y. Katz, and E. Horev, "On the applicability of various scaling laws to the turbulent wall jet," Journal of Fluid Mechanics **234**, 669–690 (1992).

[24]M. Zhou and I. Wygnanski, "Parameters governing the turbulent wall jet in an external stream," AIAA journal **31**, 848–853 (1993).

[25]J. G. Eriksson, R. I. Karlsson, and J. Persson, "An experimental study of a two-dimensional plane turbulent wall jet," Experiments in Fluids **25**, 50–60 (1998).

[26]W. K. GEORGE, H. ABRAHAMSSON, J. ERIKSSON, R. I. KARLSSON, L. LÖFDAHL, and M. WOSNIK, "A similarity theory for the turbulent plane wall jet without external stream," Journal of Fluid Mechanics **425**, 367–411 (2000).

[27]G. I. Barenblatt, A. J. Chorin, and V. M. Prostokishin, "The turbulent wall jet: A triple-layered structure and incomplete similarity," Proceedings of the National Academy of Sciences **102**, 8850–8853 (2005), https://www.pnas.org/doi/pdf/10.1073/pnas.0503186102.

[28]A. Gupta, H. Choudhary, A. K. Singh, T. Prabhakaran, and S. A. Dixit, "Scaling mean velocity in two-dimensional turbulent wall jets," Journal of Fluid Mechanics **891**, A11 (2020).

[29]P. M. Sforza and G. Herbst, "A study of three-dimensional, incompressible, turbulent wall jets," AIAA Journal **8**, 276–283 (1970).

[30]A. T. Kirkpatrick and A. E. Kenyon, "Flow characteristics of three-dimensional wall jets," TRANSACTIONS-AMERICAN SOCIETY OF HEATING REFRIGERATING AND AIR CONDITIONING ENGINEERS **104**, 1755–1762 (1998).

[31]B. G. Newman, R. P. Patel, S. B. Savage, and H. K. Tjio, "Three-dimensional wall jet originating from a circular orifice," Aeronautical Quarterly **23**, 188–200 (1972).

[32]N. V. C. Swamy and P. Bandyopadhyay, "Mean and turbulence characteristics of three-dimensional wall jets," Journal of Fluid Mechanics **71**, 541–562 (1975).

[33]L. Namgyal and J. W. Hall, "Reynolds stress distribution and turbulence generated secondary flow in the turbulent three-dimensional wall jet," Journal of Fluid Mechanics **800**, 613–644

(2016).

[34]T. J. CRAFT and B. E. LAUNDER, "On the spreading mechanism of the three-dimensional turbulent wall jet," Journal of Fluid Mechanics **435**, 305–326 (2001).

[35]S. Wittig, A. Schulz, M. Gritsch, and K. A. Thole, "Transonic film-cooling investigations: Effects of hole shapes and orientations," in *Volume 4: Heat Transfer Electric Power Industrial and Cogeneration* (American Society of Mechanical Engineers, 1996).

[36]K. Thole, M. Gritsch, A. Schulz, and S. Wittig, "Flowfield measurements for film-cooling holes with expanded exits," in *Volume 4: Heat Transfer Electric Power Industrial and Cogeneration* (American Society of Mechanical Engineers, 1996).

[37]M. Gritsch, A. Schulz, and S. Wittig, "Adiabatic wall effectiveness measurements of film-cooling holes with expanded exits," in *Volume 3: Heat Transfer Electric Power Industrial and Cogeneration* (American Society of Mechanical Engineers, 1997).

[38]M. Hao, J. Hope-collins, and L. di Mare, "Generation of turbulent inflow data from realistic approximations of the covariance tensor," Physics of Fluids (2022), 10.1063/5.0106664.

[39]L. d. M. Hao, "A parametric study of reynolds stresses and turbulent heat fluxes in fan-shaped and cylindrical film cooling holes," International Journal of Heat and Mass Transfer (2022).

[40]M. Hao, F. Wang, J. Hope-Collins, M. E. Rife, and L. di Mare, "Template-based hexahedral mesh generation for turbine cooling geometries," in *Turbo Expo: Power for Land, Sea, and Air*, Vol. 84089 (American Society of Mechanical Engineers, 2020) p. V02CT35A017.

[41]H. Yadav and A. Agrawal, "Self-similar behavior of turbulent impinging jet based upon outer scaling and dynamics of secondary peak in heat transfer," International Journal of Heat and Fluid Flow **72**, 123–142 (2018).

[42]D. Ahlman, G. Brethouwer, and A. V. Johansson, "Direct numerical simulation of a plane turbulent wall-jet including scalar mixing," Physics of Fluids **19**, 065102 (2007).

[43]A. Dejoan and M. A. Leschziner, "Large eddy simulation of a plane turbulent wall jet," Physics of Fluids **17**, 025102 (2005).

[44]B. Launder and W. Rodi, "The turbulent wall jet," Progress in Aerospace Sciences **19**, 81–128 (1979).

[45]G. D. Catalano, J. Morton, and R. Humphris, "An experimental investigation of a three-dimensional wall jet," AIAA Journal **15**, 1146–1151 (1977).

[46]M. E. Schneider and R. J. Goldstein, "Laser doppler measurement of turbulence parameters in a two-dimensional plane wall jet," Physics of Fluids **6**, 3116–3129 (1994),

6.2 | Technical Paper 4

Reynolds stresses and turbulent heat fluxes in fan-shaped and cylindrical film cooling holes

Muting Hao[a,*,1], Luca di Mare[a,2]

[a]*Oxford Thermofluids Institute, University of Oxford, Southwell Building, Osney Mead, Oxford, OX2 0ES, , United Kingdom*

ARTICLE INFO

Keywords:
Film cooling
Heat transfer
Gas turbines
Large eddy simulation
Reynolds stresses
Turbulent heat fluxes
Shaped holes

ABSTRACT

Large eddy simulation (LES) is carried out to predict the thermal performance, unsteady flow patterns, and turbulence characteristics of the fan-shaped hole and the cylindrical hole cooling films. Velocity fields, Reynolds stresses, and turbulent heat flux distributions are the factors that ultimately determine the film cooling effectiveness by deciding the concentration of coolant and heat near the surface. Accurate prediction of these processes can provide a reliable data set for the design of film cooling systems. It can also help solve difficulties of improving RANS-based simulations in terms of their inaccuracies in matching measured flow rates for a given pressure drop across the film and the mixing process once the coolant is ejected from the film. Credible estimates and modest costs of the current LES originate from the multiblock hexahedra meshing, the turbulence inflow generator, and the numerical schemes implemented. Multiblock hexahedra meshes are adopted and generated by a quasi-automatic mesh generation algorithm utilizing template-based multi-block construction followed by elliptic smoothing. Computational resources are utilized in a way that mesh refinement exists only near cooling decorations of small size and wall boundaries, without the need for associated clustering in the far field which is commonly used in commercial packages. The high orthogonality and continuous smoothness throughout the computational domain are maintained to facilitate turbulence capturing. The synthetic inflow generator produces a random field matching a realistic set of two-point statistics based on eigen-reconstruction in a computationally inexpensive processing step. To prove that the current LES simulations of modest cost can reproduce with high accuracy, the discharge characteristics, velocity, and turbulence intensity profiles of cylindrical and fan-shaped cooling films are compared with published measured data on the same flow configurations. Results reveal that the set of modeling methodologies is valid for calculating film-cooling performance within an acceptable range of accuracy. The energy-carrying turbulence structures in and near the cooling holes are shown and their behaviors are linked to turbulent Reynolds stresses. Reynolds stresses and turbulent heat fluxes are compared for different blowing ratios and two types of cooling holes in the parametric study. Similarity patterns of velocity profiles, non-dimensional temperature profiles, Reynolds stress and turbulent heat flux profiles are discussed.

1. Introduction

Cooling technologies have become key to improving gas turbine engine performance in aircraft propulsion, power generation, and industrial applications alike. Thermodynamic considerations encourage designers to use higher and higher turbine inlet gas temperatures, to improve both efficiency and power output. In order for modern gas turbines to safely operate at turbine inlet temperatures above the metal melting point, several cooling methods have been devised. A successful design for any cooling system uses less cooling air while pursuing lower metal temperatures. This is because whilst essential, turbine cooling comes at a thermodynamic price. Inappropriate amounts of cooling air result in a heavy penalty to thermal efficiency.

Film cooling is a popular method and consists in forming a thin layer of coolant around the component. The coolant is fed through small orifices on the component surface. The design of film cooling systems requires accurate estimates of the film discharge characteristics and of the mixing process of the coolant downstream of the films. This information is needed to formulate accurate predictions of the film effectiveness. Traditionally, this information could be extracted from correlations. Correlation-based tools, however, lack the flexibility required by modern designs and as a result, CFD calculations are deployed more and more often in the design of film cooling systems.

Most film cooling flow predictions are based on the Reynolds-averaged Navier–Stokes (RANS). The RANS method is a popular method due to its efficiency and relatively low computational cost. RANS are currently the predominant choice for simulating cooling applications of industrial interest. Despite continuous improvements in turbulence models in the past 40 years, RANS simulations of film cooling generally suffer from issues such as over-prediction of the penetration distance into the mainstream (see Hoda and Acharya (1999)) and the under-prediction of the coolant jet spreading rate. These inaccuracies originate from the poor performance of RANS model in flows with large density variations and strong streamline curvature. Both these features are present in the flow generated by film cooling devices.

*Corresponding author

Flow in cooling films

To improve RANS modeling, a systematic set of Reynolds stress data are needed. Also, it is these Reynolds stresses that determine how the coolant flows downstream. To solve these problems, Large eddy simulation (LES) can be relied on. Therefore, LES becomes important, not only for its more accurate predictions of heat load and end-wall flow structures but also because the information such as Reynolds stresses that can be provided by LES are crucial in improving turbulence models of RANS simulations.

LES studies on film cooling have become increasingly popular recently. Ziefle and Kleiser (2008) studied the flow structures along a cylindrical cooling hole, which is selected from Sinha, Bogard and Crawford (1991) experiment, by a large-eddy simulation. A deep understanding of the mixing process was provided. However, a simplification of the turbulent boundary layer of inflow to a time-averaged profile prevents them from capturing realistic mixing processes suitably. Oliver, Bogard and Moser (2019a) found the Mach number of coolant flow may be several times higher than the mainstream Mach number, and the resulting compressibility will influence the cooling performance. They gave an explanation of the decomposed mechanisms in the cooling holes in LES results of laterally-expanded holes under two Mach number conditions. Guo, Schröder and Meinke (2006) studied the effect of blowing ratio and incline angle through LES. They observed that the counter-rotating vortex is more downstream in an inclined angle of 30 cases compared to a normal jet case. Renze, Schröder and Meinke (2007) studied the effect of density ratio on the attachment/recirculation by LES of the jet in crossflow. Gräf and Kleiser (2011) carried out an LES study of double-row compound film cooling. Kong, Zhang, Li, Lu, Zhu and Xu (2022) captured the details of flow structures in a film-cooled leading edge model. Chen, Long, Wang, Weng and Luan (2021) simulated the evolution of hairpin vortices and instantaneous flow structures using LES. Wang, Wang, Tao, Zhang, Luo and Cui (2021) combined deep learning with CFD methods to obtain film-cooling effectiveness. These studies focus on capturing the details of instantaneous flow structures by improving part of the numerical tool. However, in these studies, well-resolved profiles of velocity, Reynolds stresses and turbulent heat fluxes and the regularity pattern for them

are barely explored. The requirement for the complete set of well-resolved profiles of these quantities for the design of the film cooling system provides the need for a reliable LES numerical tool that can provide these data of reliable quality.

Moreover, a parametric study of blowing ratios and cooling film hole geometries on the Reynolds stresses is significant. It can provide guidance for designers as it covers a wide range of mixing regimes. Recent RANS-based results (Jiang, Murray, di Mare and Ireland (2022)) show that in most cases RANS predictions contain the correct asymptotic decay of quantities such as effectiveness, but the wrong level. If a parametric study could provide some indications on how the quantities such as Reynolds stress perform under different blowing ratios, modifications on the RANS model might be proposed to give equivalent accuracy of predictions as LES in film cooling.

In this study, LES is carried out to predict the thermal performance, unsteady flow patterns, and turbulence characteristics of the fan-shaped hole and the cylindrical hole cooling films. Simulations on various operating conditions, including an array of Mach numbers, blowing ratios, and orientation angles, are examined by being compared with classical experimental data. Reynolds stresses and turbulent heat fluxes are compared for different blowing ratios and two types of cooling holes in the parametric study. Similarity patterns of velocity profiles, non-dimensional temperature profiles, and Reynolds stresses profiles are discussed.

The structure of this study is arranged as below. Section 2 will introduce the computational details including the configuration, the meshing, the LES platform, and the setting up for simulations. Section 3 will provide validations in terms of meshing independence, the discharge coefficient, the mean profiles, the Reynolds stress, the film cooling effectiveness, and flowfield patterns. Section 4 will present the results and discussion of the flow field and a parametric study of Reynolds stresses and turbulent heat fluxes in film coolings with fan-shaped and cylindrical holes at different blowing ratios. Section 5 will summarize the conclusions.

2. Computational details

2.1. Flow Configuration

The computations are based and validated on experimental data obtained in experiments described by Wittig et al (see Wittig, Schulz, Gritsch and Thole (1996)). The flow conditions and geometries are selected to match those from the experiment by Thole et al (see Thole, Gritsch, Schulz and Wittig (1998)) and (see Gritsch Gritsch, Schulz and Wittig (1998a)). Both fan-shaped and cylindrical film cooling holes are studied. Their geometries are shown in Fig. 1.

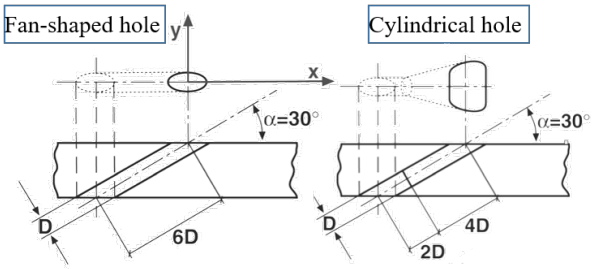


Figure 1: The geometry of film cooling holes: left (a) fan-shaped hole, right (b)cylindrical hole after Thole et al. (1998).

All the studied holes are inclined at 30°, with a hole length-to-diameter ratio of $L/D = 6$. An array of operating conditions with various blowing ratios, mainstream Mach numbers, and orientation angles are simulated. Table 1 shows the considered operating conditions for the current LES study. The availability of experimental data provided in the published references is also listed in Table 1. The data not available from experiments, especially Favre-averaged velocities and Reynolds stresses, can be provided in the current study. This is performed as the current study is attempting to extend the numerical approaches to complement the previously obtained experimental data. Although there are a few LES studies on a similar type of film cooling recently, for example, Zamiri and Chung (2022); Oliver, Bogard and Moser (2019b); Fu, Chao, Tsubokura, Li and Wang (2018); Zamiri, Barigozzi and Chung (2022); Agarwal, Gicquel, Duchaine, Odier and Dombart (2021), a systematic set of Reynolds stress or turbulent heat flux data with well-resolved profiles is still few.

Studies like Kohli and Bogard (2005) are early pioneers that provide Reynolds stress and turbulent heat flux data in film cooling flows from simple holes. A complete set of Reynolds stress and turbulent heat flux data based on more types of cooling holes have not been explored enough.

Table 2 outlines the mesh size and the time consumed for the list of simulations used in Results and Discussions.

2.2. Grid arrangement

Body-fitted, multiblock hexahedral grids are generated by the mesh generator 'H4X' described in Hao, Wang, Hope-Collins, Rife and di Mare (2020). The mesh generator is a quasi-automatic mesh generation algorithm. The algorithm uses templates to construct multiblock grids around complex geometries. The grid is composed of suitably arranged blocks containing identical numbers of cells and joined by conformal interfaces. Because cooling films can be idealized as small-size holes extruded from the main flow passages, they are well suited to templated grid generation using a trunk and branch approach. The grids are smoothed elliptically. The smoothing method is then implemented on the resulting multiblock grids. It uses a modification of Thompson's Poisson system. Elliptic smoothing is performed on the boundaries as well as inside the volume. The position of grid points on the boundary surfaces is not fixed but is determined as a result of the smoothing process. Boundary orthogonality is enforced on all surfaces. Control functions are used to set the wall spacing in the direction orthogonal to the boundary surfaces. A Newton-like update for the control functions of the Poisson systems is relied on for the grid size control. Grid orthogonality and smoothness are guaranteed throughout the computational domains. The block layout can be optimized in such a way that the mesh is refined only near the cooling decorations and the wall boundaries, without the need for clustering extended into the far field which is common when using commercial meshing software.

The meshing procedure 1) starts by generating two trunk layouts for the hot stream channel and the coolant channel. 2) Suitable types of film are added as templated layouts to each block. 3) Once a layout is generated, hexahedral grids are immediately generated by splitting all blocks into the same

Flow in cooling films

Case										Availability			
Geometry	T_{tc}	T_{tc}/T_m	Re_{Dm}	δ_{99}/D	Tu_m	Ma_m	Ma_c	β	M	D_c	η	Mean vel	Reynolds stresses
Fan-shaped	300*K*	1	$\leqslant 5.2 \cdot 10^4$	0.8	$\leqslant 1.5\%$	0.25	0.3	0	1.0	-	-	A	-
Cylindrical	300*K*	1	$\leqslant 5.2 \cdot 10^4$	0.8	$\leqslant 1.5\%$	0.25	0.3	0	1.0	-	-	A,D	A
Fan-shaped	290*K*	0.54	$\leqslant 1.3 \cdot 10^5$	0.5	$\leqslant 2\%$	0.6	0	0	0.5	B, E, F	C	-	-
Fan-shaped	290*K*	0.54	$\leqslant 1.3 \cdot 10^5$	0.5	$\leqslant 2\%$	0.6	0	0	0.5	B, E, F	C, G	-	-
Fan-shaped	290*K*	0.54	$\leqslant 1.3 \cdot 10^5$	0.5	$\leqslant 2\%$	0.6	0	0	0.5	B, E, F	C	-	-
Cylindrical	290*K*	0.54	$\leqslant 1.3 \cdot 10^5$	0.5	$\leqslant 2\%$	0.6	0	0	0.5	B, E, F	C	-	-
Cylindrical	290*K*	0.54	$\leqslant 1.3 \cdot 10^5$	0.5	$\leqslant 2\%$	0.6	0	0	1.0	B, E, F	C, G	-	-
Cylindrical	290*K*	0.54	$\leqslant 1.3 \cdot 10^5$	0.5	$\leqslant 2\%$	0.6	0	0	1.5	B, E, F	C	-	-
Fan-shaped	290*K*	0.54	$\leqslant 1.3 \cdot 10^5$	0.5	$\leqslant 2\%$	0.3	0	0	0.5	B, E, F	H	-	-
Fan-shaped	290*K*	0.54	$\leqslant 1.3 \cdot 10^5$	0.5	$\leqslant 2\%$	0.3	0	0	1.0	B, E, F	-	-	-
Fan-shaped	290*K*	0.54	$\leqslant 1.3 \cdot 10^5$	0.5	$\leqslant 2\%$	0.3	0	0	1.5	B, E, F	H	-	-
Cylindrical	290*K*	0.54	$\leqslant 1.3 \cdot 10^5$	0.5	$\leqslant 2\%$	0.3	0	0	0.5	B, E, F	H	-	-
Cylindrical	290*K*	0.54	$\leqslant 1.3 \cdot 10^5$	0.5	$\leqslant 2\%$	0.3	0	0	1.0	B, E, F	H	-	-
Cylindrical	290*K*	0.54	$\leqslant 1.3 \cdot 10^5$	0.5	$\leqslant 2\%$	0.3	0	0	1.5	B, E, F	H	-	-
Fan-shaped	290*K*	0.54	$\leqslant 1.3 \cdot 10^5$	0.5	$\leqslant 2\%$	0.6	0	90	0.5	E, F	-	-	-
Fan-shaped	290*K*	0.54	$\leqslant 1.3 \cdot 10^5$	0.5	$\leqslant 2\%$	0.6	0	90	1.0	E, F	-	-	-
Fan-shaped	290*K*	0.54	$\leqslant 1.3 \cdot 10^5$	0.5	$\leqslant 2\%$	0.6	0	90	1.5	E, F	-	-	-
Cylindrical	290*K*	0.54	$\leqslant 1.3 \cdot 10^5$	0.5	$\leqslant 2\%$	0.6	0	90	0.5	E, F	-	-	-
Cylindrical	290*K*	0.54	$\leqslant 1.3 \cdot 10^5$	0.5	$\leqslant 2\%$	0.6	0	90	1.0	E, F	-	-	-
Cylindrical	290*K*	0.54	$\leqslant 1.3 \cdot 10^5$	0.5	$\leqslant 2\%$	0.6	0	90	1.5	E, F	-	-	-

* ***A*** is Thole et al. (1998)
* ***B*** is Gritsch, Schulz and Wittig (1998b)
* ***C*** is Gritsch et al. (1998a)
* ***D*** is Thole, Gritsch, Schulz and Wittig (1997)
* ***E*** is Gritsch, Saumweber, Schulz, Wittig and Sharp (1999)
* ***F*** is Gritsch, Schulz and Wittig (2001)
* ***G*** is SAUMWEBER, SCHULZ, WITTIG and GRITSCH (2006)
* ***H*** is Saumweber and Schulz (2012)

Table 1: List of available experimental data in published references

number of cells. 4) The smoothing step maps each separated block onto the cooling hole geometry. 5) Two half-films that have been added separately onto the hot-stream and coolant channels are then

Flow in cooling films

Case						Time	
Geometry	Ma_m	Ma_c	β	M	Mesh Size	Transient	Total
Fan-shaped	0.25	0.3	0	1.0	10534612	7f	191100 chr
Cylindrical	0.25	0.3	0	1.0	10534612	7f	218660 chr
Fan-shaped	0.6	0	0	0.5	10534612	12f	115821 chr
Fan-shaped	0.6	0	0	1.0	10534612	13f	132440 chr
Fan-shaped	0.6	0	0	1.5	10534612	12f	88070 chr
Cylindrical	0.6	0	0	0.5	9674752	11f	156594 chr
Cylindrical	0.6	0	0	1.0	9674752	10f	146950 chr
Cylindrical	0.6	0	0	1.5	9674752	10f	142750 chr
Fan-shaped	0.3	0	0	0.5	1316864	7f	8000 chr
Fan-shaped	0.3	0	0	1.0	1316864	7f	8000 chr
Fan-shaped	0.3	0	0	1.5	1316864	7f	8000 chr
Cylindrical	0.3	0	0	0.5	1209344	7f	9200 chr
Cylindrical	0.3	0	0	1.0	1209344	7f	9200 chr
Cylindrical	0.3	0	0	1.5	1209344	7f	9200 chr
Fan-shaped	0.6	0	90	0.5	1105920	10f	20050 chr
Fan-shaped	0.6	0	90	1.0	1105920	10f	20050 chr
Fan-shaped	0.6	0	90	1.5	1105920	10f	20050 chr
Cylindrical	0.6	0	90	0.5	777216	12f	9200 chr
Cylindrical	0.6	0	90	1.0	777216	12f	9200 chr
Cylindrical	0.6	0	90	1.5	777216	12f	9200 chr

*$1f$ = 1 flow through time, $1chr$ = 1 core hour

Table 2: List of simulations

joined together, with the patches of individual domains merged into the final configuration. 5) The mesh is optimized by operations such as local refinement, splitting, and collapse. 6) A round of smoothing is performed on the final layout to produce the mesh.

Fig. 2 shows the generated layout of the fan-shaped cooling film case with a parallel orientation between the mainstream channel and the coolant channel. The layout presents the block boundaries with every n^{th} point of the mesh. For example, for the most refined mesh used in this study, n is 24 in both types of film cases. As shown in Fig. 2, the layout in the transitional region is unstructured but smoothly transitioned. Fig. 3 shows the meshing used for collecting statistics. Meshing grids in different views corresponding to the sections in Fig. 2a are zoomed in. Fig. 3a which shows

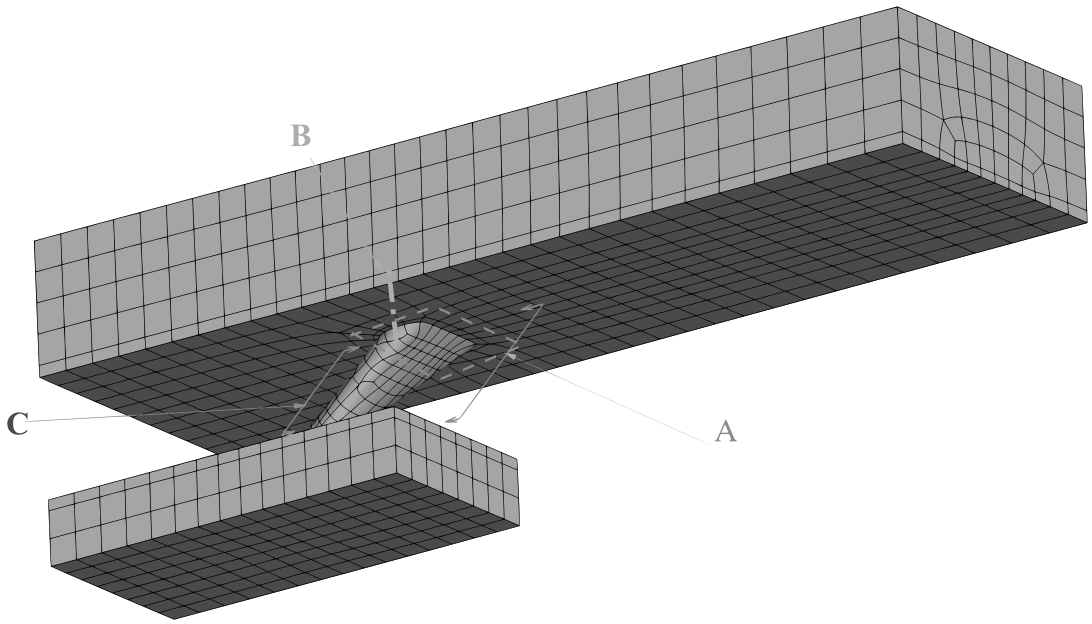
the smoothly allocated grids around the film. Fig. 3b, Fig. 3c, and Fig. 3d show that the grids in the transitional region of the cooling film are seamless, and smoothly distributed in each of the three directions. The mesh is orthogonal to the wall and orthogonal to the junction between the film and the mainstream. The layouts are generated in a way that there are 44 blocks on the connecting intersection across the fan-shaped film hole and 38 blocks on the connecting intersection across the cylindrical film hole. The value of $y+$ is below 1.6, as shown in Fig. 4. $\Delta x^+ \approx 29$. $\Delta z^+ \approx 20$.

A study of grid quality has been examined in Fig. 5 on five grid sizes when the node relocation displacement has arrived at the same residual level after the smoothing operation. Fig. 5 shows that 90 % of grid cells have unit scales of Jacobian for all the considered meshes of both the cylindrical and the fan-shaped holes.

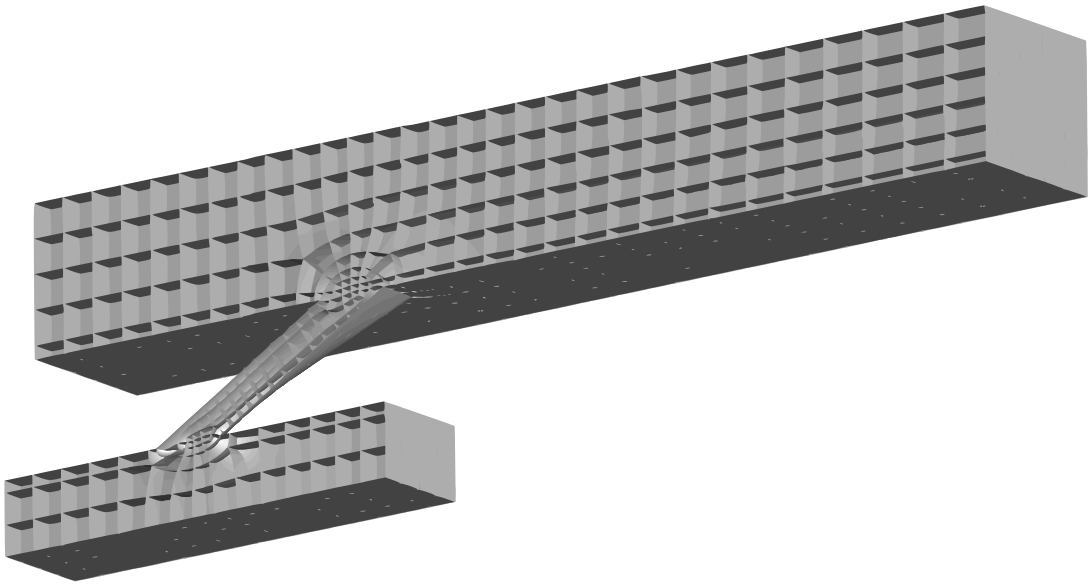
A well-smoothed mesh of $8 \times 8 \times 8$ cells per block can be generally employed for simulations if only a coarse boundary layer resolution is required. So the mesh of 8x8x8 cells per block is chosen for a series of simulations to obtain discharge coefficients (see definition in Gritsch et al. (1998b)). The mesh of $16 \times 16 \times 16$ cells per block is used for obtaining film cooling effectiveness and turbulence statistics (Favre-averaged velocity profiles, Reynolds stresses profiles and turbulent heat flux profiles). It is also used to capture the turbulence structures in the coolant mixing process and the interaction between the coolant and the mainstream. Such task allocations are adopted for the consideration of minimum computational resources and time costs.

2.3. LES platform

A home-grown CFD code 'H4X' is used for LES simulations to solve the Navier-Stokes equations. The governing equations are shown in Equ.1:

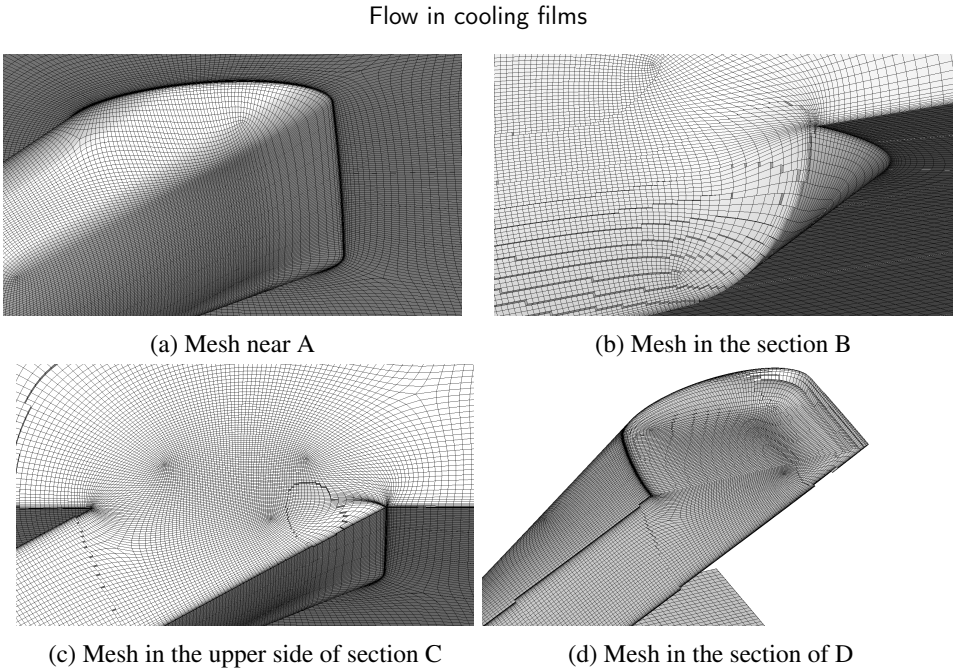


(a) Visualisation from the outside.



(b) Visualisation from the midsection.

Figure 2: The layout of the fan-shaped cooling hole mesh.



(a) Mesh near A (b) Mesh in the section B

(c) Mesh in the upper side of section C (d) Mesh in the section of D

Figure 3: Details of fan-shaped cooling hole mesh.

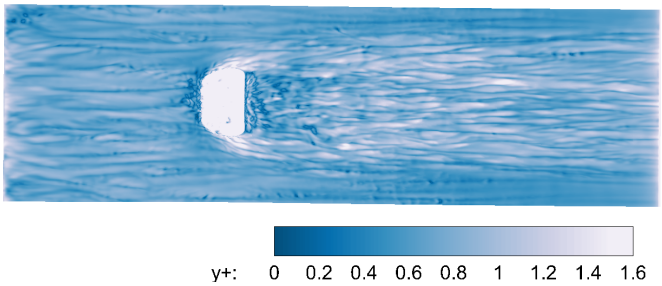
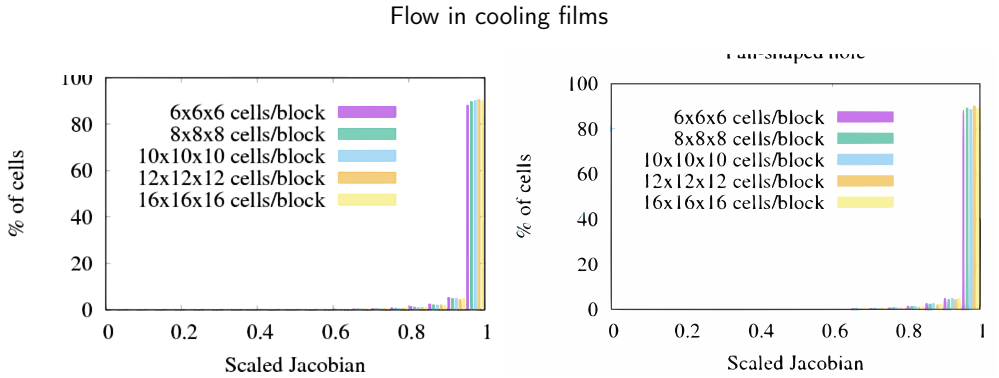


Figure 4: y^+ contour at the flat plat surface of fan-shaped film cooling mesh.

$$\begin{aligned} \frac{\partial \rho}{\partial t} + \frac{\partial \rho u_j}{\partial x_j} &= 0 \\ \frac{\partial \rho u_i}{\partial t} + \frac{\partial \rho u_i u_j}{\partial x_j} + \frac{\partial p}{\partial x_i} &= \frac{\partial \sigma_{ij}}{\partial x_j} \\ \frac{\partial \rho E}{\partial t} + \frac{\partial (\rho E + p) u_j}{\partial x_j} &= \frac{\partial \sigma_{ij} u_i}{\partial x_j} - \frac{\partial}{\partial x_j} q_j \end{aligned} \tag{1}$$



(a) Fan-shaped hole (b) Cylindrical hole

Figure 5: Independence of grid quality on block cell count: (a) fan-shaped hole, (b) cylindrical hole.

The code adopts an implicit LES based on the finite volume approach for the numerical solution of conservation laws. All variables are stored at the cell center. Fluxes are evaluated at cell interfaces. Flow variables are extrapolated to the cell interfaces using the third-order limiter of Čada and Torrilhon (2009). The limiter is applied to the characteristic variables. For the purpose of applying slope limiters, the gradients are obtained using a weighted least squares method. The stencil of the gradients is biased locally by removing contributions from the state of the flow on the opposite side of the interface. The inviscid fluxes are evaluated using Roe's Riemann solver. The resulting scheme has a biased three-point stencil and is formally third-order accurate away from discontinuities and local extrema. The viscous fluxes are evaluated using unbiased least square gradients. The state of the flow used to evaluate transport properties is obtained by linear interpolation between the two cells sharing the interface. The resulting scheme for the viscous fluxes is centered and is formally second-order accurate.

The solution is advanced in time by using a third-order Runge-Kutta scheme. The scheme requires three flux evaluations and four updates for each time step. The CFL limit for the stability of the Runge-Kutta scheme is approximately 0.8, but a lower value is generally adopted during computations.

Flow in cooling films

The three walls attached to the cooling hole (the bottom wall in the main channel, the top wall in the coolant channel, and the wall of the cooling hole) are handled by the non-slip adiabatic wall condition. The adiabatic thermal condition is applied to the temperature of these walls. The on-the-fly inlet boundary is set using a synthetic turbulence inflow generator described in Hao M, et.al Hao, Hope-collins and di Mare (2022). The inflow generator is composed of two elements. One is a preliminary procedure that can infer realistic two-point covariance tensors from readily available data (e.g. freestream velocity, boundary layer thickness, and turbulence intensity). The other is an efficient eigen-decomposition step of the two-point correlation tensor that determines a set of modes. The capability of the inflow generator in retaining realistic spatial and temporal correlations allows for the generation of a realistic turbulent boundary layer for the inlets of film cooling in LES. The boundary layer thickness and turbulent intensity match the experimental data, as these parameters are specified for the inflow generator. The outflows for both external and internal channels are dealt with by the unsteady non-reflecting boundary condition based on Thompson Thompson (1987). Periodic boundary conditions are imposed on the walls in the spanwise direction. The periodicity has already been set during the meshing procedure by matching the corresponding cells on attached boundaries, for which no additional interpolation is needed for data exchange between blocks attached to the same boundary edge. The top wall in the main channel and the bottom wall in the coolant channel are treated as far-field boundaries. The blowing ratio is matched by adjusting the mass flow rate at the inlet of the mainstream and at the inlet of the coolant channel. The multiblock structure facilitates the implementation of MPI for coarse grain parallelism when using domain decomposition, and the implementation of OpenMPI allows for the parallelism among blocks within each MPI rank. The computational simulations are carried out in parallel on 480 processors, and the time run for numerical simulations of each case is shown in Table 2.

At the start of each computation, LES is run for around five flow-through times to eliminate the initial transient effects. Following that, statistics are collected for at least ten flow-through times for

each case. Both integral quantities (running average of the mass flow rates) as well as variations in the profiles of velocity and Reynolds stress are monitored. In the last 10 flow-through times, all cases show below 2% variations. The CFL number is kept as 0.8.

3. Validation

3.1. Discharge coefficients

The discharge coefficient is one of the key parameters during both the design and the analysis of the cooling system. One reason is that the relation between the mass flow rate and the pressure drop of film cooling holes can be represented through the discharge coefficient C_D. This means that for a given coolant flow rate requirement, C_D determines the pressure margin. Another reason is that the discharge coefficient is related to the ratio between the nominal passage area and the area of the *vena contracta*. The definition of C_D is the ratio of the actual mass flow rate to the ideal mass flow rate through the hole. The ideal mass flow rate is obtained with the assumption of a one-dimensional and isentropic expansion from the total pressure in the plenum to the static pressure in the mainstream at the hole exit referring to Gritsch et al. (1998a), as

$$C_D = \frac{\dot{m}_c}{p_{tc}\left(\frac{p_m}{p_{tc}}\right)^{\frac{k+1}{2k}}\sqrt{\frac{2k}{(k-1)RT_{tc}}\left(\left(\frac{p_{tc}}{p_m}\right)^{\frac{k-1}{k}}-1\right)\frac{\pi}{4}D^2}} \tag{2}$$

Fig. 6 compares the C_D result with published experimental data Gritsch et al. (1998a) for the fan-shaped hole and the cylindrical hole. C_D is plotted versus the pressure ratio at three sets of operating conditions in an array of two main channel Mach numbers ($Ma_m = 0.6, 0.3$), one coolant passage Mach number ($Ma_c = 0.0$), and two orientation angels ($\beta = 0, 90°$), The plateau value of $C_D = 0.8$ for the fan-shaped hole and $C_D = 0.75$ for the cylindrical hole are observed in the region of high-pressure ratio, regardless of Ma_m, which matches well the experiment. The numerical results and experimental data of discharge coefficients match very well in the larger pressure ratio region. The small difference between the numerical results and experimental data in the low-pressure ratio

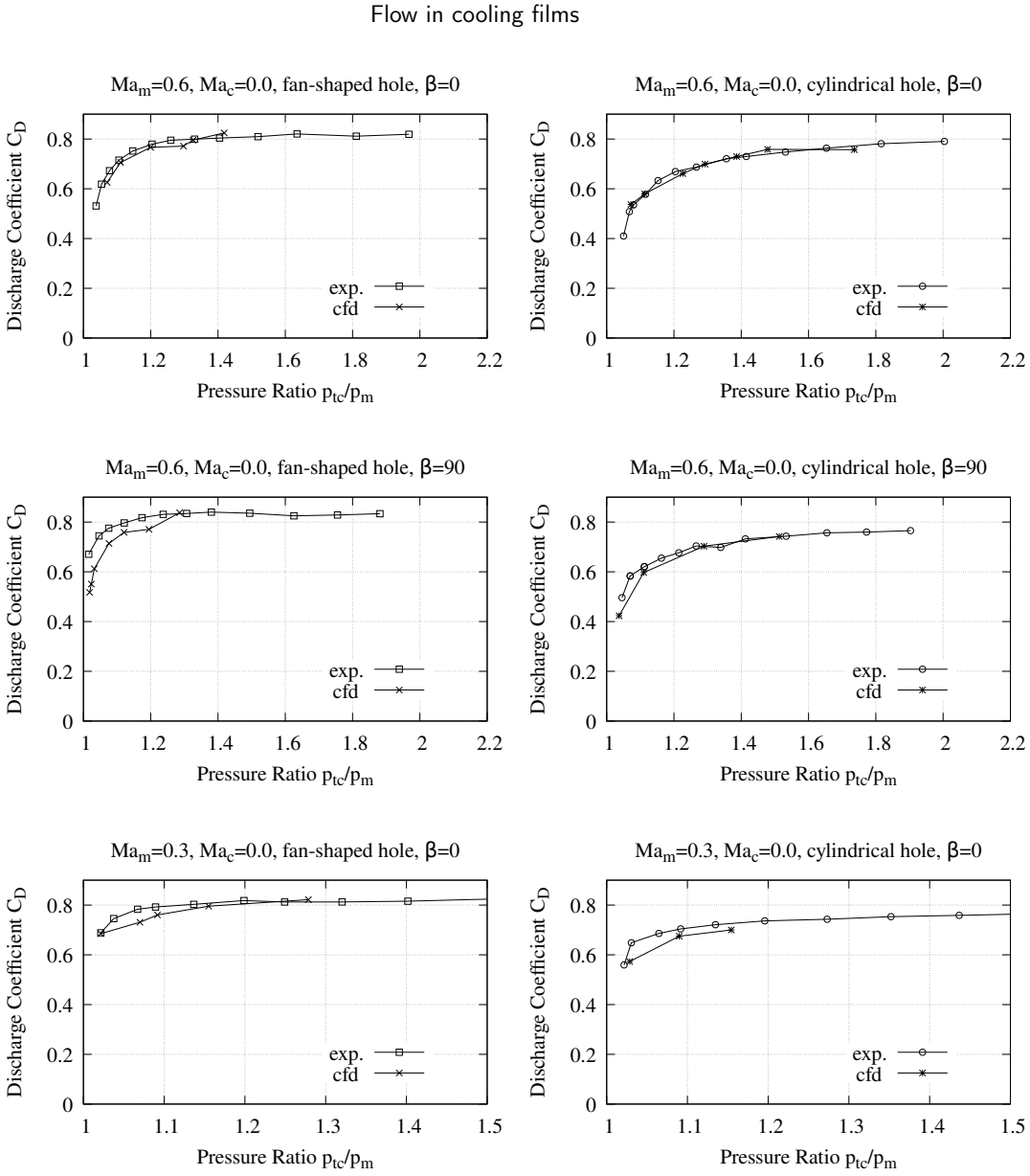


Figure 6: Discharge coefficient for the cylindrical hole and the fan-shaped hole on three sets of operating conditions.

is observed because in LES simulations the Ma_c is not completely adjusted to zero for the purpose of letting the flow go through the coolant channel. This effect is more prominent in lower Ma_m

Flow in cooling films

conditions where the *vena contracta* is more sensitive to the precise configuration of the inflow. In general, the comparison generally shows good agreement with the experimental data.

3.2. Favre-averaged velocity

Fig. 7 compares the streamwise component of the Favre-averaged velocity at three positions at $x/D = 0, 2, 10$. Fig. 9 compares the Favre-averaged streamwise velocity on the slice at $x/D = 4$. It reflects the lateral spreading of the jet velocity. The overall prediction of velocity profiles matches the measured data well.

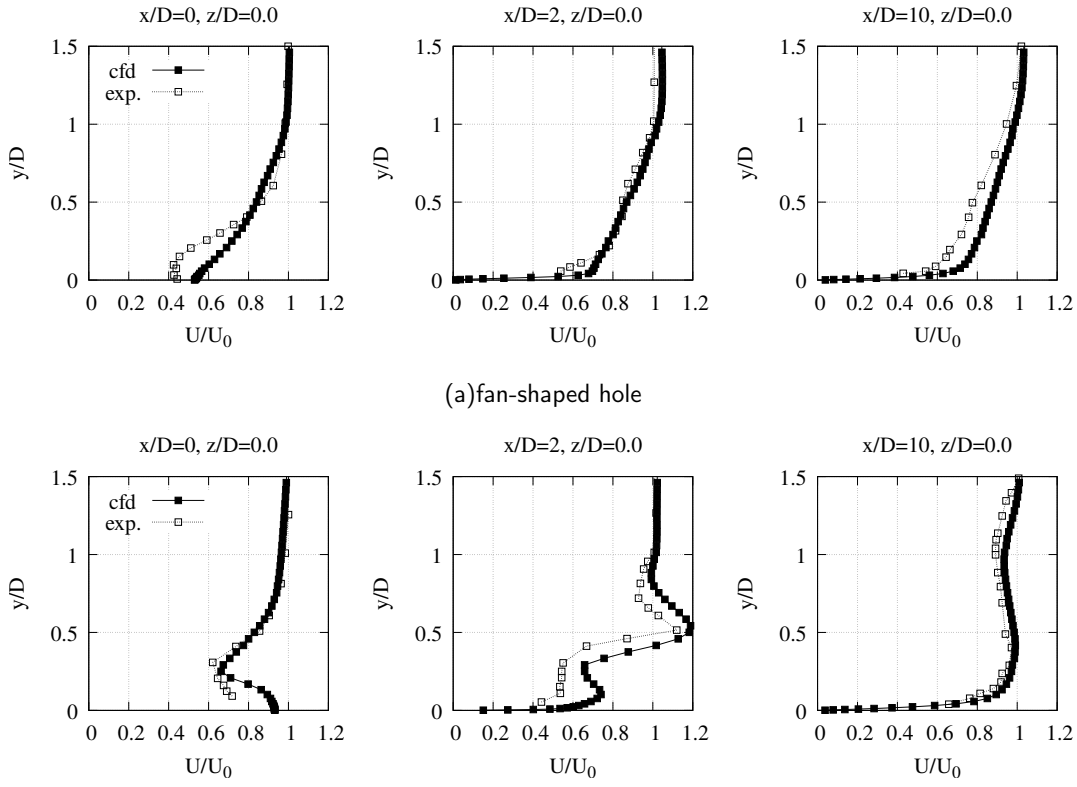


Figure 7: Favre-averaged steamwise velocity profiles at (i)$x/D = 0$, (ii)$x/D = 2$, (iii)$x/D = 10$.

The flow features at $x/D = 4$ are compared: half of the counter-rotating vortex pair (CVP) from the cylindrical hole and the laterally-spreading flow downstream the fan-shaped hole are correctly

captured. Both the shape and position of corresponding contour levels from LES predictions match fairly well with the measured data.

3.3. Turbulence intensities

Fig. 8 shows the turbulence intensity downstream of the cylindrical hole. A good comparison with the experimental profile is shown, with the matching shape of the u_{rms}/U_0 profile and an overprediction of less than 10% at the peaks. Fig. 10 compares the turbulence intensity contours on the slice at $x/D = 4$. It can reflect the lateral spreading of the turbulence of the jet. The overall prediction of the Reynolds stress matches the measured data well. The shape and position of the jet turbulence intensity match the measured data of both cooling holes.

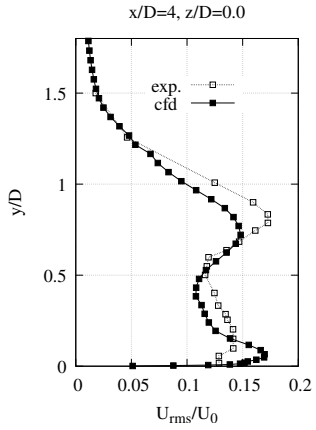
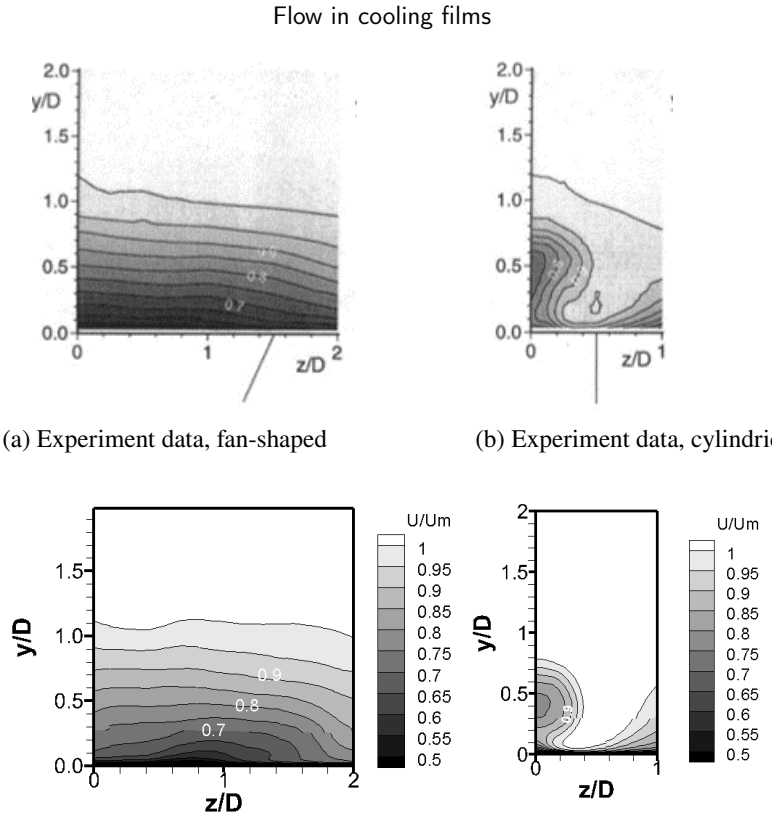


Figure 8: Comparison of u_{rms} at $x/D = 4$ of cylindrical hole with those from experimental data Thole et al. (1998).

3.4. Effectiveness

Fig. 11 shows the comparison of film cooling effectiveness downstream of the hole in the mainstream channel. Both the level and the trend of film cooling effectiveness match well for a range of blowing ratios and for the two studied hole types.



(a) Experiment data, fan-shaped (b) Experiment data, cylindrical

(c) LES result, fan-shaped (d) LES result, cylindrical

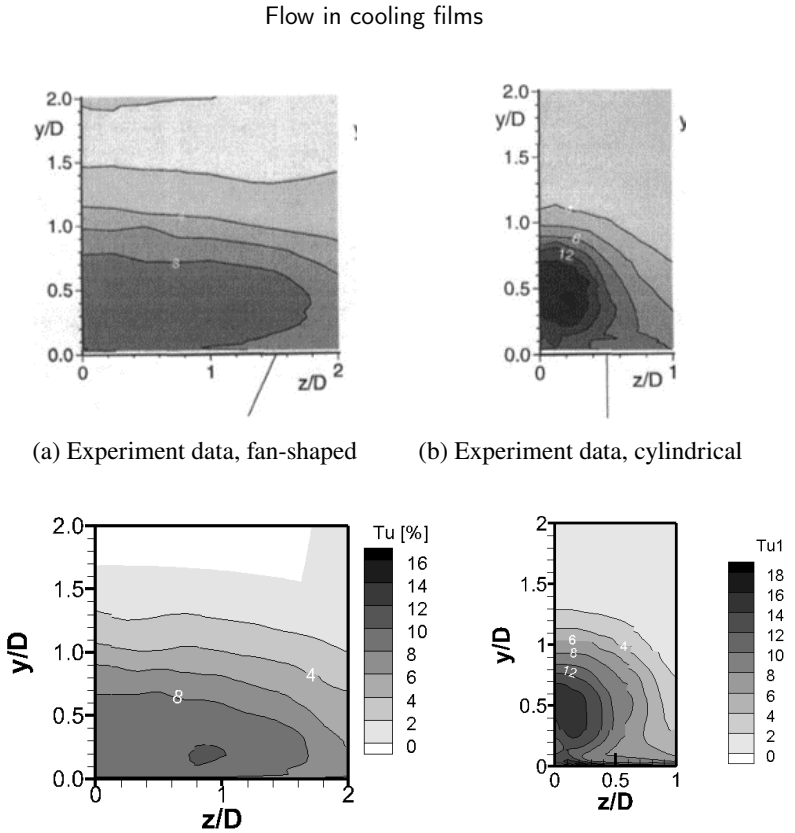
Figure 9: The comparison of time-averaged streamwise velocity contours at $x/D = 4$ between experimental data from Thole et al. (1998) and LES results in the fan-shaped and the cylindrical film.

Overall, the validation has given this study confidence that the simulations in this study can reproduce the main features of experimental flows, in terms of the flow distribution, the coolant distribution, and the structure of turbulence.

4. Results and Discussion

4.1. Favre-averaged velocity

Fig. 12 and Fig. 14 show the normalized Favre-averaged velocity profiles vs y/D downstream of the film cooling hole in the fan-shaped cases and in the cylindrical cases, respectively. The Favre-averaged velocity is normalized by the freestream velocity. In Fig. 12, the trajectory of the jet in the fan-shaped cases can be inferred. The main effect of the blowing ratio is to modify the location and



(a) Experiment data, fan-shaped (b) Experiment data, cylindrical

(c) LES result, fan-shaped (d) LES result, cylindrical

Figure 10: The comparison of turbulence intensity contours at $x/D = 4$ between experimental data from Thole et al. (1998) and LES results in the fan-shaped and cylindrical film cooling.

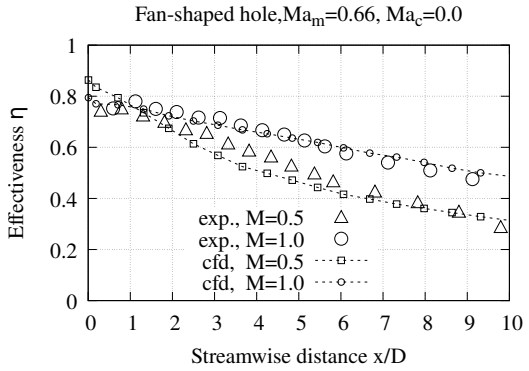


Figure 11: Comparison of the effectiveness of fan-shaped holes with those from experimental data Gritsch et al. (1998a).

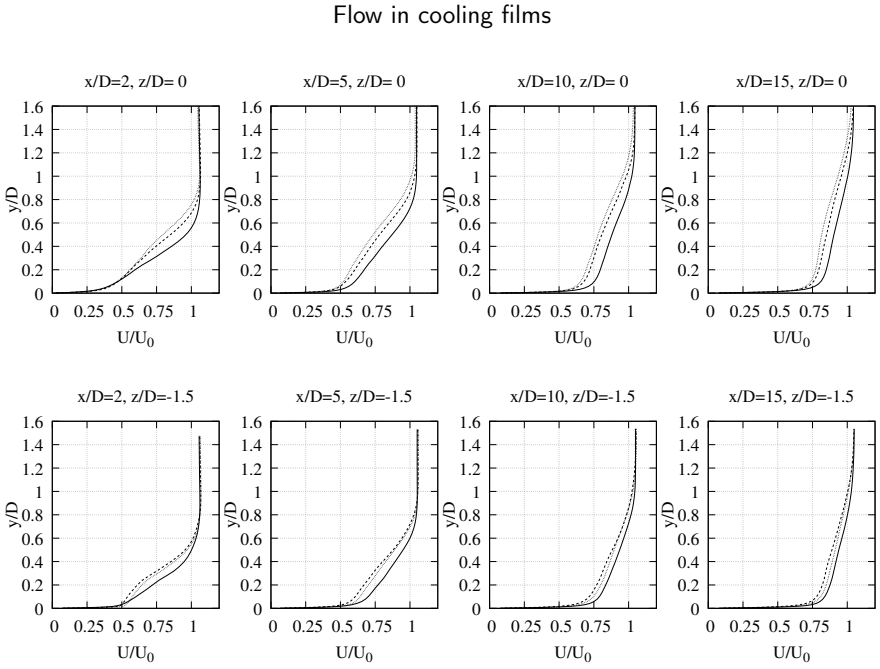


Figure 12: The distribution of Favre-averaged streamwise velocity profiles at different locations downstream of the fan-shaped hole. Solid line: M=0.5; dash line: M=1.0; dot line: M=1.5.

the spreading rate of the jet. In the fan-shaped film, the jet is never lifted off. So the velocity defect caused by the jet is mostly confined below $y/D = 1$. Along the centerline ($z/D = 0$), the edge of the jet starts from between $0.8D$ and $1.0D$ at $x/D = 2$, depending on the blowing ratio, and it gradually grows as the flow evolves downstream. $z/D = 1.5$ is also examined in the fan-shaped hole cases to illustrate the edge of the film. Due to the shape of the jet, $z/D = 1.5$ presents velocity profiles thinner than those at $z/D = 0$. It also shows that the velocity profiles at $x/D = 5, 10, 15$ have the same shape. This suggests that after $x/D = 5$, the jet has become self-similar.

In order to test this hypothesis, Fig. 13 is shown to present the Favre-averaged velocity defect vs y/δ_{99} on the centerline of the fan-shaped hole. The Favre-averaged velocity defect is defined as $1-U/U(\delta_{99})$ where $U(\delta_{99})$ is 99% of the freestream velocity. It is normalized by the velocity defect at the core of the jet H, which is evaluated as the velocity defect at the height of $\delta_{99}/2$ according to Townsend (1956), shown in Equation 3. The idea comes from the fact that δ_{99} is the local boundary layer height and it is modified by the presence of the jet.

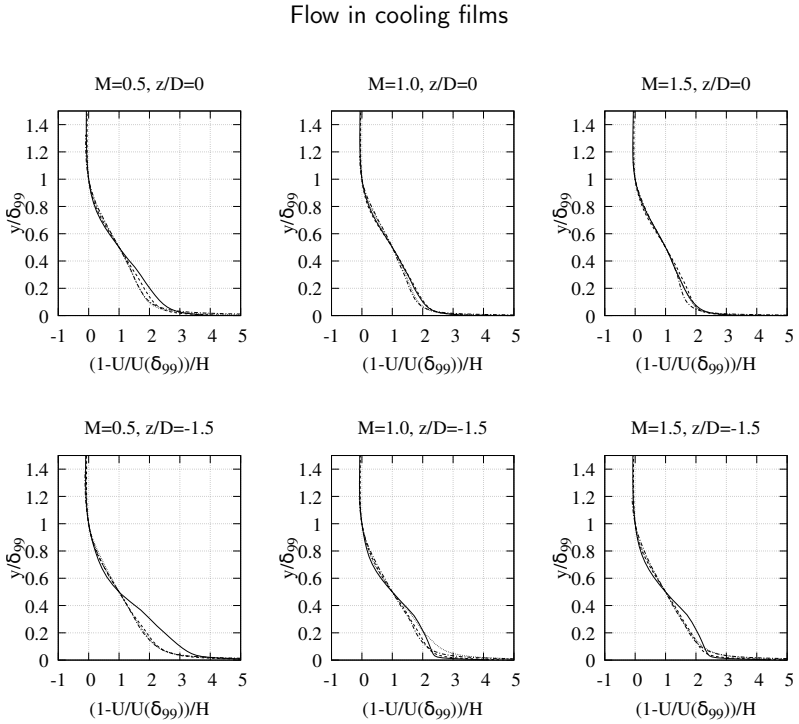


Figure 13: Normalized Favre-averaged velocity defect downstream of the fan-shaped hole. Solid line: $x/D = 2$, dash line: $x/D = 5$, dot line: $x/D = 10$, dash-dot line: $x/D = 15$..

$$H = 1 - \frac{U(\delta_{99}/2)}{U(\delta_{99})} \tag{3}$$

Fig. 14 indicates the trajectory of the jet downstream of the film cooling hole in the cylindrical cases. The centreline profiles are examined on $z/D = 0$, while the profiles on the edge of the film are examined on $z/D = 0.5$. In the cylindrical hole cases: at $M = 0.5$, the coolant is confined within half the diameter of the wall starting from $x/D = 2$ and gradually mixes with the mainstream as it travels downstream; at $M = 1.0$, the freestream flow is entrained between the jet and the wall starting from $x/D = 2$, with the jet centerline approximately located half diameter from the wall; at $M = 1.5$, the jet is lifted off, and the freestream fluid comes as the flow next to the wall.

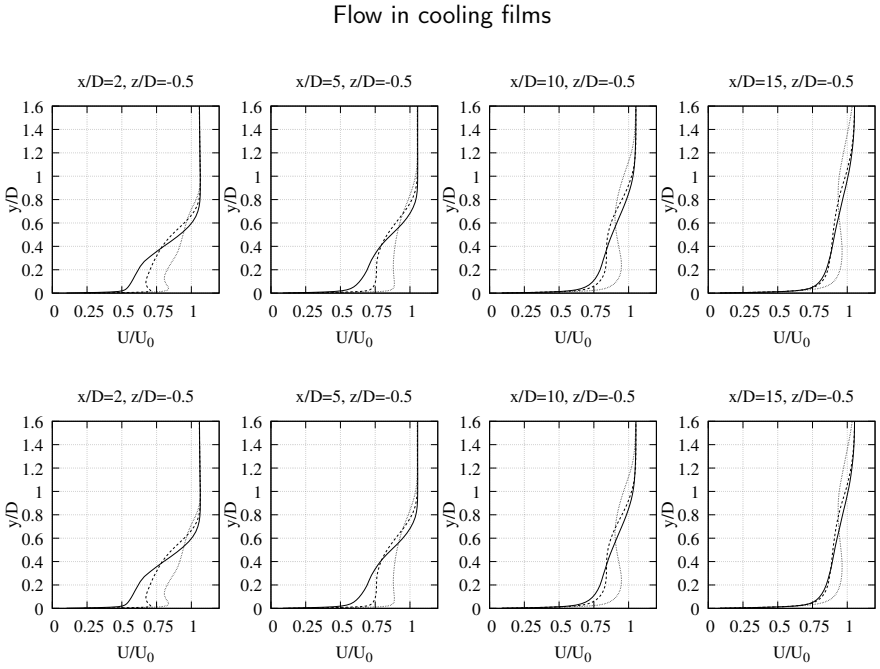


Figure 14: The distribution of Favre-averaged streamwise velocity profiles at different locations downstream of the cylindrical hole. Solid line: M=0.5; dash line: M=1.0; dot line: M=1.5.

Fig. 15 shows the Favre-averaged velocity defect profiles vs y/δ_{99} downstream of the film cooling hole in the cylindrical cases. It uses the same definition and normalization of Favre-averaged velocity defect as Fig. 13. In Fig. 15: at $M = 0.5$, the jet has become self-similar after $x/D = 5$, because the coolant is not lifted off yet; at $M = 1.5$, the jet has become self-similar after $x/D = 5$, because the coolant is mostly lifted off; at $M = 1.0$, the jet doesn't present the self-similarity after $x/D = 5$, because the coolant is partially entrained. $M = 1.0$ is therefore an intermediate blowing ratio.

4.2. Favre-averaged non-dimensional temperature

Fig. 16 shows the non-dimensional profiles of Favre-averaged temperature for the fan-shaped film. In the fan-shaped hole cases (shown in Fig . 16), at the exit of the fan-shaped films ($x/D = 2$), the non-dimensional temperature near the wall has the value corresponding to the coolant stream. Therefore, the flow near the wall at the exit of the hole must be formed by an unmixed coolant. As the

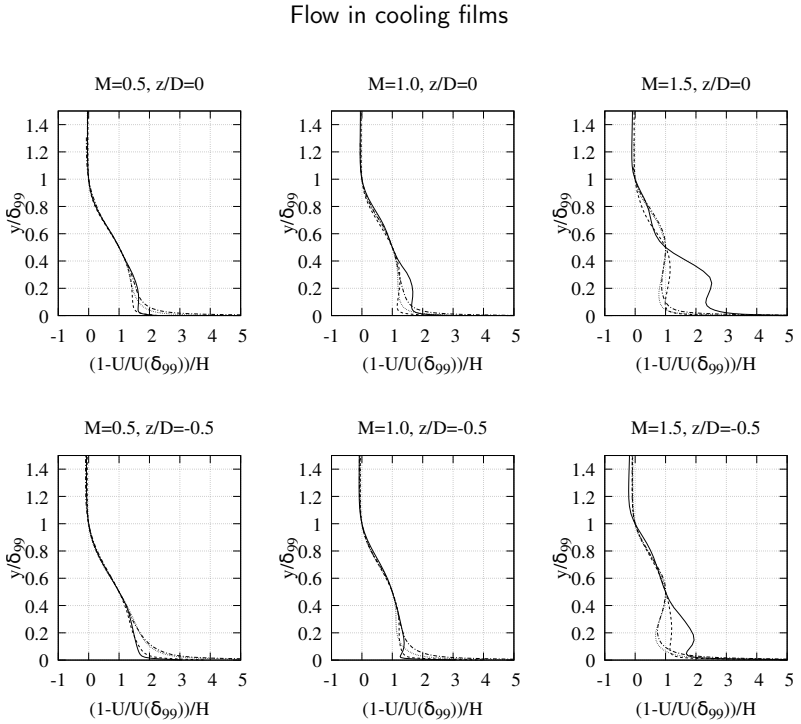


Figure 15: Normalized Favre-averaged velocity defect downstream of the cylindrical hole. Solid line: $x/D = 2$, dash line: $x/D = 5$, dot line: $x/D = 10$, dash-dot line: $x/D = 15$.

		Fan-shaped				Cylindrical			
		$z/D = 0$		$z/D = 1.5$		$z/D = 0$		$z/D = 0.5$	
	x/D	V	T	V	T	V	T	V	T
0.5	2	0.229	0.114	0.137	0.026	0.463	0.316	0.291	0.164
	15	0.100	0.033	0.068	0.010	0.112	0.042	0.94	0.035
1.0	2	0.284	0.204	0.204	0.100	0.386	0.389	0.271	0.301
	15	0.151	0.084	0.093	0.032	0.157	0.097	0.122	0.084
1.5	2	0.304	0.259	0.219	0.145	0.308	0.413	0.117	0.369
	15	0.151	0.084	0.090	0.048	0.135	0.120	0.082	0.094

Table 3: Favre-averaged velocity and temperature defects on the centreline and on the edge of the jet.

coolant fluid moves downstream, it gradually mixes and the non-dimensional temperature near the wall rises. Fig. 17 shows the temperature deficit profiles in fan-shaped films. The non-dimensional temperature deficit vs y/δ_{99} is presented on the centerline and on the film edge. The Favre-averaged

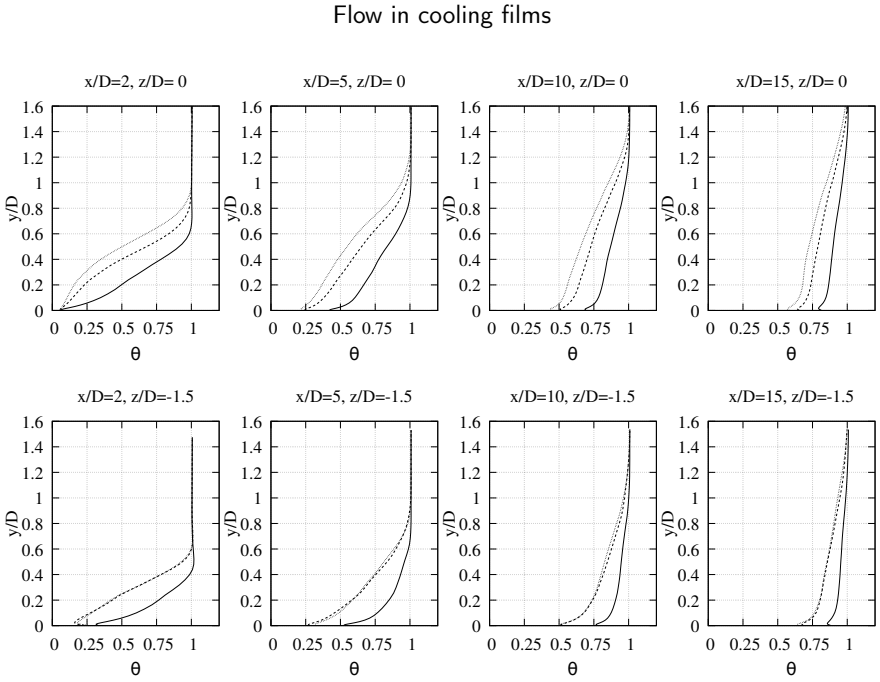


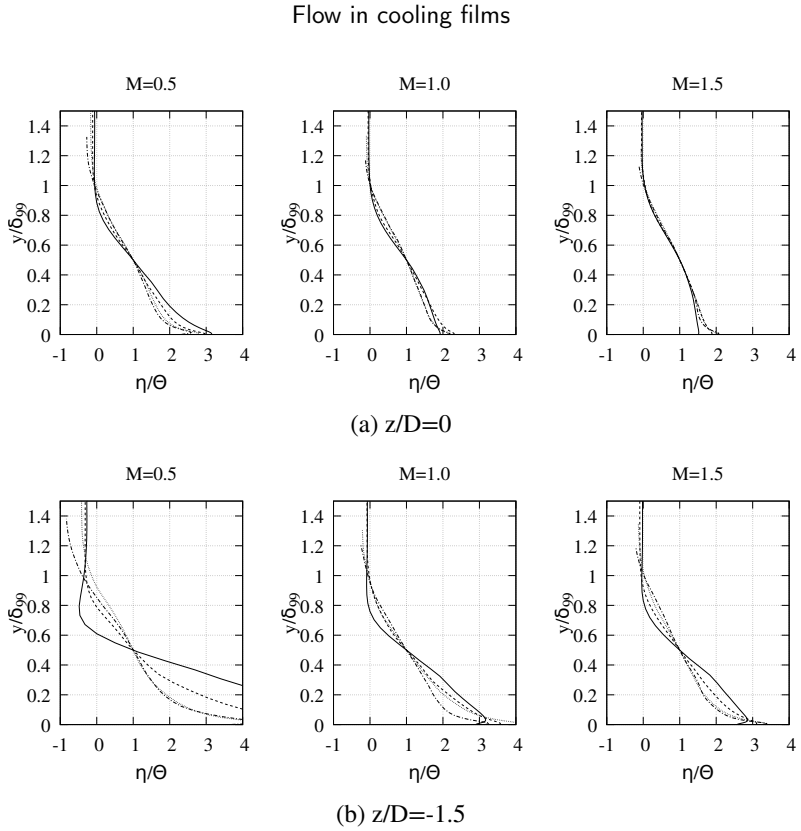
Figure 16: The distribution of Favre-averaged temperature profiles at different locations downstream of the fan-shaped hole. Solid line: M=0.5; dash line: M=1.0; dot line: M=1.5.

temperature deficit (Hoffmeister (1976)) is defined as $1-T/T_{99}$ where T_{99} is the temperature at δ_{99}. It is normalized by the Favre-averaged temperature deficit at the core of the jet Θ,

$$\Theta = \frac{T_m - T(\delta_{99}/2)}{T_m - T_{tc}} \tag{4}$$

which is evaluated as the Favre-averaged temperature deficit at $\delta_{99}/2$. Fig . 17 shows that the temperature deficit profiles are self-similar with the exception of the lowest blow ratio in fan-shaped films. This finding confirms the behavior already observed on the velocity profiles.

Fig. 18 shows the non-dimensional profiles of Favre-averaged temperature for the cylindrical hole. At the lowest and highest blowing ratios, the profiles downstream show similarities, while at $M = 1.0$, the profiles overall do not show similar behaviors. At $M = 1.0$, the top part of the profiles shows similarity, but the lower part never does. The reason for this is that the jet is about to lift off. The similarity patterns are shown in the temperature deficits (in Fig. 19). Fig. 19 shows that the



(a) z/D=0

(b) z/D=-1.5

Figure 17: Non-dimensional Favre-averaged temperature deficit downstream of the fan-shaped hole. Solid line: $x/D = 2$, dash line: $x/D = 5$, dot line: $x/D = 10$, dash-dot line: $x/D = 15$.

temperature deficits at both $M = 0.5$ and $M = 1.5$ collapse from $x/D = 5$ because either they have not lifted off or lifted off too early, while the temperature deficits at $M = 1.5$ do not show a self-similarity pattern below $y/\delta_{99} = 0.5$.

Table 3 shows the values of the temperature deficit at the height of $\delta_{99}/2$, which corresponds to the height of the jet core. Table 3 can be analyzed by taking ratios of velocity defects at $x/D = 2$ to the corresponding values at $x/D = 15$. The same process can be applied to temperature deficits. In this way, estimates of the Favre-averaged decay rates of velocity and temperature deficits can be obtained. The decay rates of quantities such as adiabatic effectiveness downstream of isolated films are fundamental quantities in correlations. The decay rates are direct results of the rates at which momentum and energy are transferred between the jet and the hot stream and within the jet.

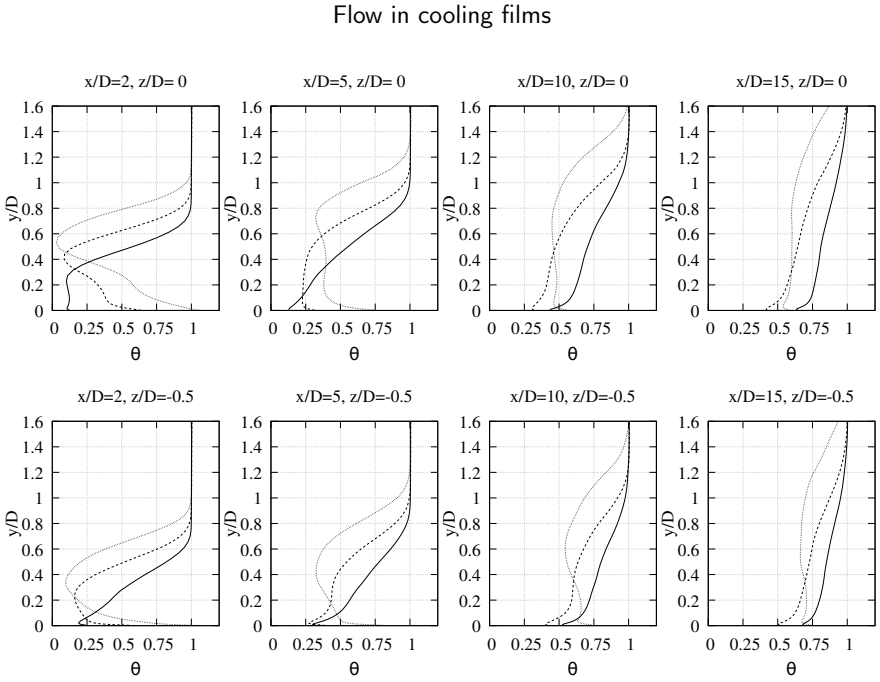
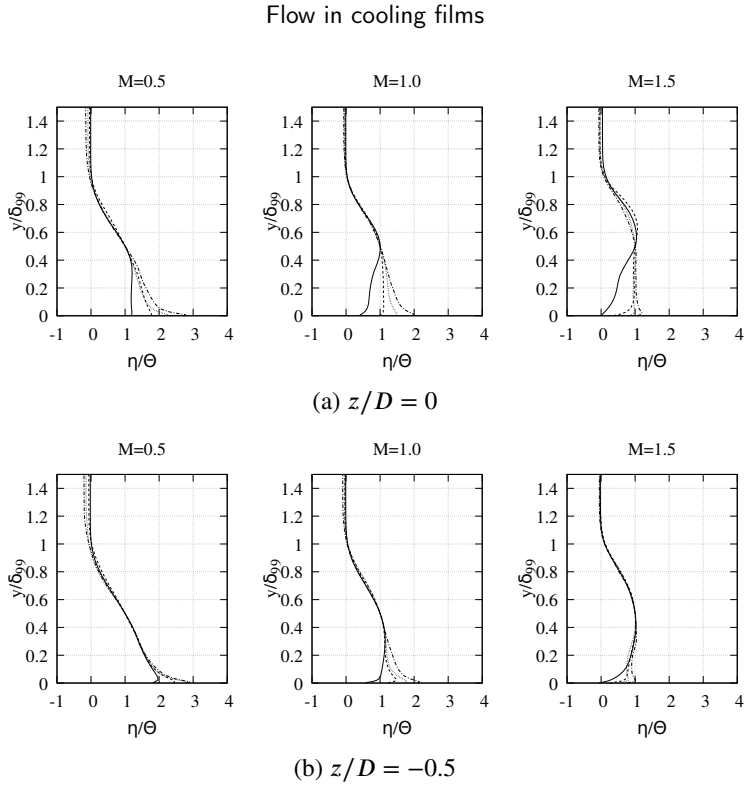


Figure 18: The distribution of Favre-averaged temperature profiles at different locations downstream of the cylindrical hole. Solid line: M=0.5; dash line: M=1.0; dot line: M=1.5.

In the fan-shaped cases, the decay rates of the velocity defects on the centerline are around 2 with the lowest value 1.87 at $M = 1$, while those values on the edge of the jet are 2 at $M = 0.5$ and increase to 2.4 at $M = 1.5$. The decay rates of the temperature deficit on the centerline are around 3 with the lowest value of 2.44 at $M = 1$, while those values on the edge of the jet are around 3 starting from 2.5 at $M = 0.5$. There are two sets of phenomena determining the decay rates. At the centerline the distribution of the coolant evolves under the action of two counter-rotating vortices which draw hot air under the jet and move the cold air into a thinner layer in the top half of the jet; all the while the jet mixes with its surroundings. The quicker decay of the temperature deficit is due partly to the redistribution of the coolant within the jet and partly to turbulent mixing, which progresses at different rates for momentum and energy.

In the cylindrical film, the decay rates of the velocity defects on the centerline decrease from 4 at $M = 0.5$ to 2.3 at $M = 1.5$, while those values on the edge of the jet decrease from 3.1 at $M = 0.5$ to 1.4 at $M = 1.5$. The decay rates of the temperature deficit on the centerline decrease



(a) $z/D = 0$

(b) $z/D = -0.5$

Figure 19: Non-dimensional Favre-averaged temperature deficit downstream of the cylindrical hole. Solid line: $x/D = 2$, dash line: $x/D = 5$, dot line: $x/D = 10$, dash-dot line: $x/D = 15$.

from 7.5 at $M = 0.5$ to 3.4 at $M = 1.5$, while those values on the edge of the jet decrease from 4.7 at $M = 0.5$ to below 4 at $M = 1.0$ and at $M = 1.5$. At the lowest blowing ratio, the coolant jet mixes rapidly with the hot stream, and the velocity defect and temperature deficit decay correspondingly fast. At higher blowing ratios, the jet starts lifting from the wall and mixes at a slower rate with its surroundings, explaining the lower values of the mixing rates. The decay of velocity defects at the edge of the jet becomes slower than that at the centerline, as is the case in isolated turbulent jets Girshovich (1967). The difference in decay rates of the velocity defect and temperature defects is a macroscopic consequence of the turbulent Prandtl number deviating from unity. It is known that the turbulent Prandtl number is in fact a varying quantity throughout boundary layers and shear flows. The variability of the turbulent Prandtl number, together with the way the flow is redistributed within

the film jet, also causes temperature and velocity defects to decay at different rates in different parts of the jet.

4.3. Reynolds stress

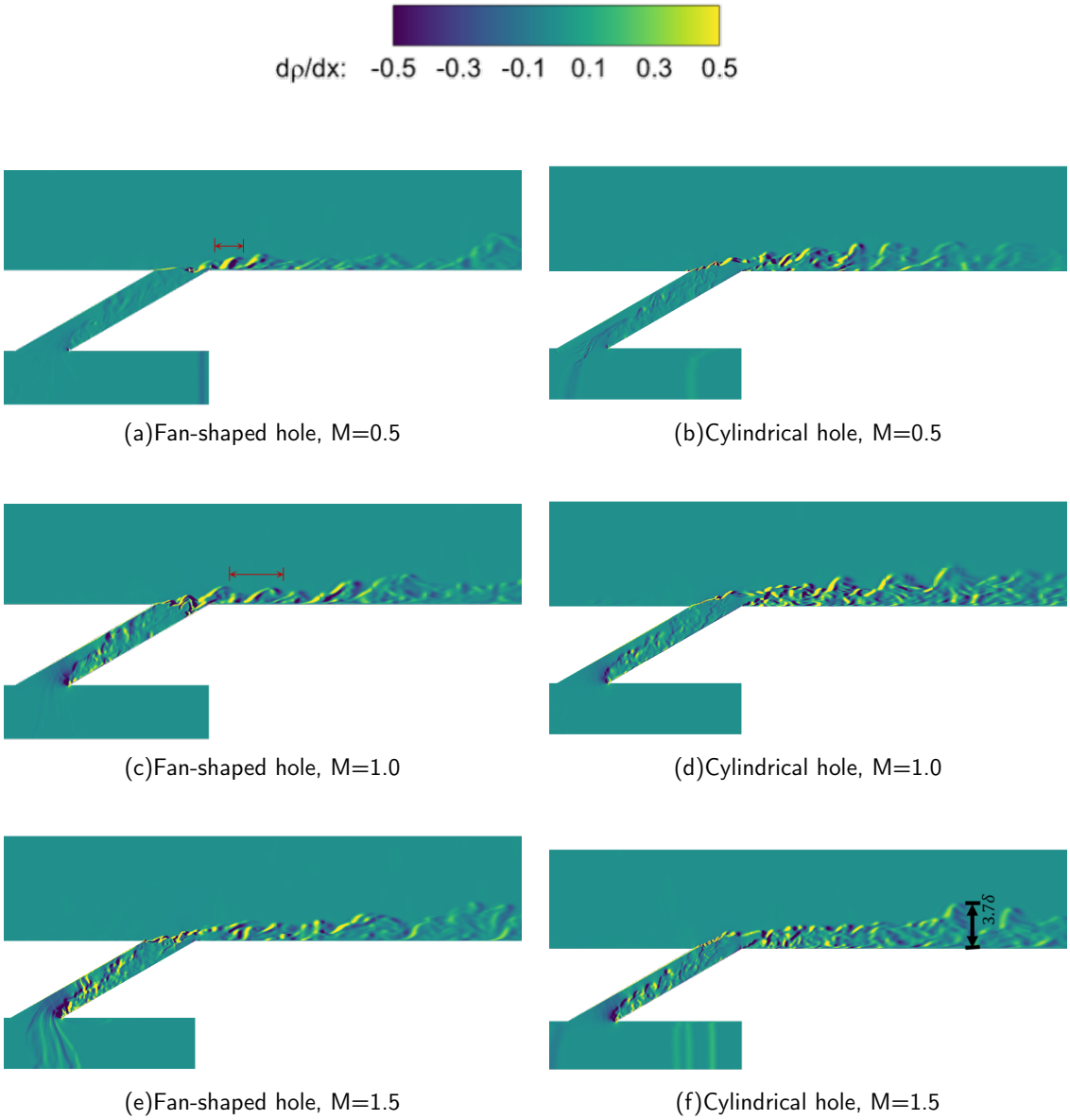
Energy-carrying structures contribute the most to the Reynolds stresses. Therefore, an inspection of these structures can provide indications of the origin and behavior of Reynolds stresses.

Fig. 20 shows the density gradient on the median $x-y$ plane, capturing the size and distribution of energy-carrying structures, which are compared between different blowing ratios. In all cases, the high-density gradient region originates from a Kelvin-Helmholtz instability induced by a shear layer that appears at the windward side of the hole exit.

For the fan-shaped hole at $M = 0.5$ (as seen in Fig. 20(a)) and $M = 1.0$ (as seen in Fig. 20(b)), the shear layer from the windward side of the hole exit falls at the leeward edge of the hole exit, interacts with the boundary layer, and lifts up hairpin vortices from the leeward edge of the hole exit, which evolve into the hairpin packets downstream. The size of hairpin vortices doubles going from $M = 0.5$ to $M = 1.0$, as evidenced by the second hairpin marked in both cases. The vortices are attached to the wall surface in both these two cases. However, at $M = 1.5$ (as seen in Fig. 20(c)) in the fan-shaped case, the shear layer from the windward side of the hole lifts up until it interacts directly with the boundary layer above the mainstream channel surface. This leads to the appearance of hairpin vortices at $x/D = 2.5$. The behavior of the shear layer in the cylindrical cases at all the blowing ratios is correspondingly similar.

The height of vortices arrives at the highest at $x/D = 10$ of the cylindrical hole case at $M = 1.5$, and the height is around 3.7δ. It is also worth mentioning that with the increasing blowing ratio, the number of small-scale turbulent structures increases, giving rise to better cooling film coverage due to an improved vortex shedding frequency. This can be more obvious for the cylindrical cases because the significantly increased vortex shedding inside the cooling hole is a source of turbulence onto the mainstream channel surface, while the interaction between coolant and mainstream dominates the corresponding source in the fan-shaped cases. The size of these hairpin

vortices scales with the thickness of the wall jet. The number of energy-carrying structures that can be accommodated by the jet scales with its width. This could be found in similar instantaneous vortex structures in the $y-z$ plane (not shown here).



(a)Fan-shaped hole, M=0.5 (b)Cylindrical hole, M=0.5

(c)Fan-shaped hole, M=1.0 (d)Cylindrical hole, M=1.0

(e)Fan-shaped hole, M=1.5 (f)Cylindrical hole, M=1.5

Figure 20: Instantaneous snapshot of the density gradient.

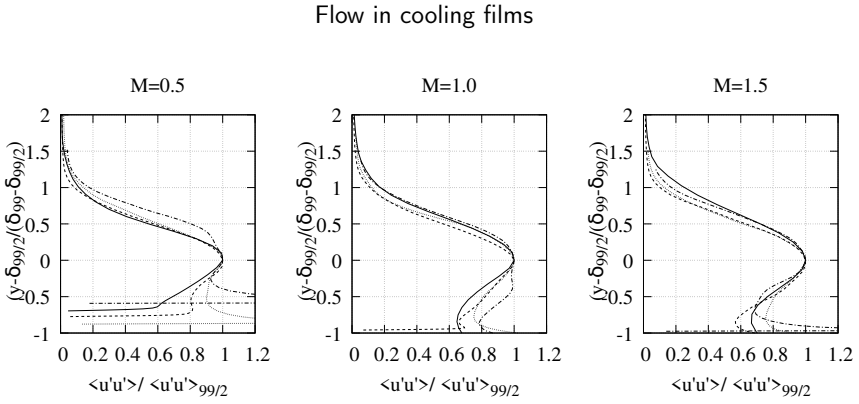
Flow in cooling films

The boundary layer turbulence intensity at the inlet is 1.5%, and the boundary layer thickness is $0.5D$, as shown in Table 2. The turbulence intensity from the film hole varies from 1% at $M = 0.5$ to 4% at $M = 1.5$. The highest value of $< u'u' >$ is located across the mixing layer between the air injected into the flow near the upstream edge of the film and the freestream. This observation holds for both fan-shaped and cylindrical films, as indicated in Fig. 20.

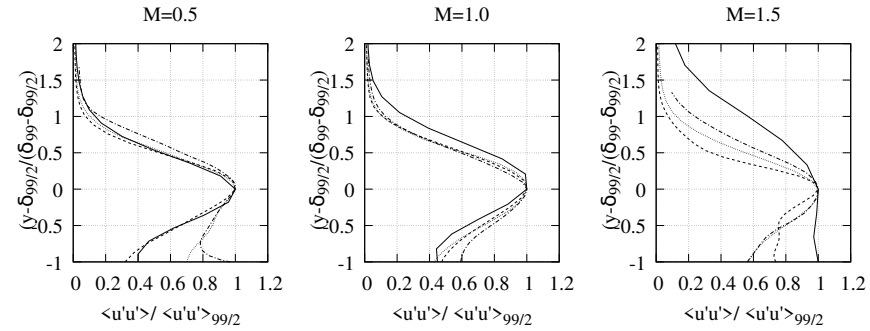
Fig. 21 compares the scaled normal stress along a series of streamwise positions at different blowing ratios. In the fan-shaped film, at $M = 0.5$, the peak of normal stresses is below the edge of the incoming boundary layer, while at $M = 1.0$ and $M = 1.5$, the peak of the normal stresses of the jet is above the edge of the boundary layer. In the cylindrical film, at $M = 0.5$, the jet is fully confined within the boundary layer, while at $M = 1.0$ and $M = 1.5$, part of the jet is located above the boundary layer.

Figures 22, 23, and 24 compare the three components of Reynolds normal stresses. Figures 22a, 23a, and 24a show the fan-shaped film at different blowing ratios, while Figures 22b, 23b, and 24b show the cylindrical film cases at different blowing ratios. In the fan-shaped films, there is a clearly recognizable two-layer structure in the Reynolds normal stresses. The two main components of the flow are a boundary layer in the proximity of the wall and a shear layer in the upper part of the jet. Both layers spread gradually as the flow develops downstream. The part of the flow behaving as a developing boundary layer extends vertically up to approximately $y/D = 0.2$ to $y/D = 0.4$. The normal stresses are relatively flat in this part of the flow. The turbulence in the fan-shaped film is more isotropic in the near-wall region. The anisotropy in the cylindrical cooling film is caused by the hairpin vortices being few and mostly aligned in the direction orthogonal to the flow. By contrast, hairpin vortices are smaller and more numerous in the fan-shaped film.

Fig. 25 shows the distribution of Reynolds shear stresses in two types of films. Fig. 25a compares three fan-shaped hole cases at different blowing ratios. Fig. 25b compares three cylindrical hole cases at different blowing ratios. The comparison in this section is arranged to explain separately



(a) Fan-shaped film

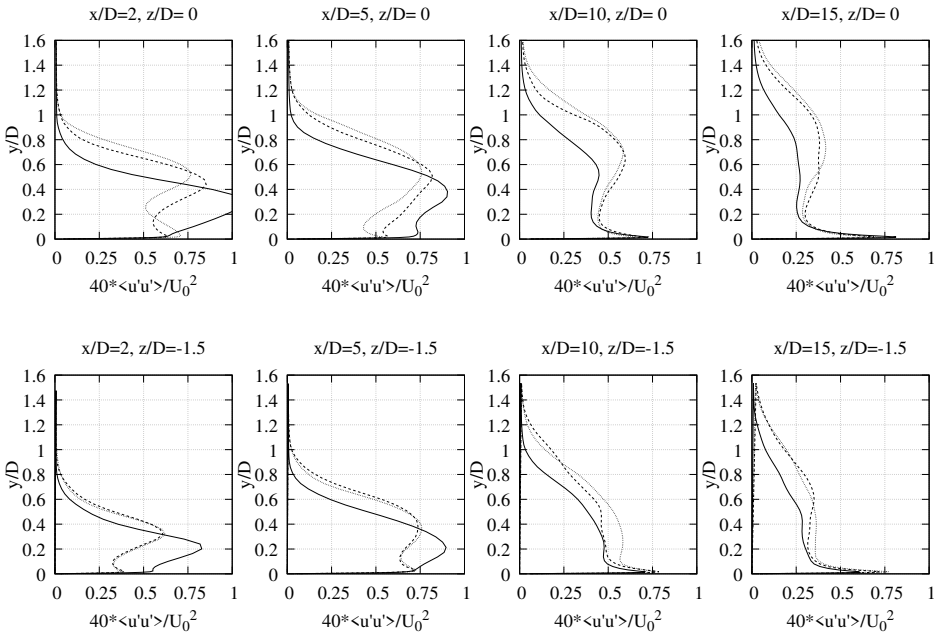


(b) Cylindrical film

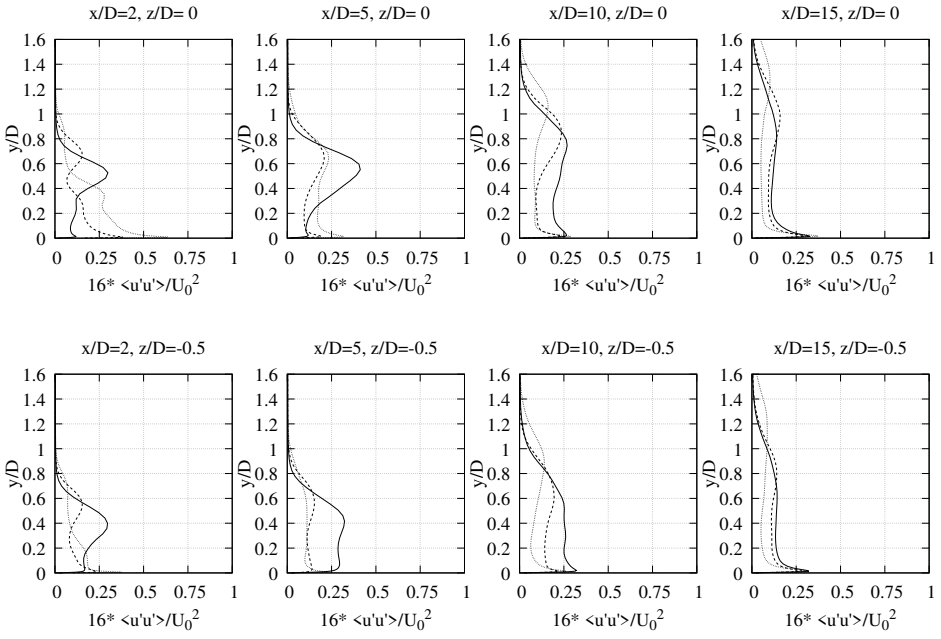
Figure 21: Profiles of the Reynolds normal stress $< u'u' >$ normalized by $< u'u' >$ at the core of the jet $\delta_{99}/2$ Solid line: $x/D = 2$, dashed line: $x/D = 5$, dot line: $x/D = 10$, dash-dotted line: $x/D = 15$.

the behavior of the Reynolds stresses within a short distance from the film (near field) and at a longer distance (far field).

The near-field flow is analyzed at $x/D = 2$ and 5, and it is dominated by the boundary layer in the mainstream channel and by the properties of the turbulence established within the film. In fan-shaped films, at $M = 0.5$, the Reynolds shear stress is negative everywhere as long as it deviates from zero. Momentum is transferred from the freestream to the coolant jet, and from the coolant jet towards the wall (negative peaks at $y/D = 0.1$ and $y/D = 0.6$). At $M = 1.0$ and $M = 1.5$, momentum is transferred from the jet to the wall (negative peaks) and from the freestream to the jet. In cylindrical films, at $M = 0.5$, momentum is transferred from the jet to the freestream

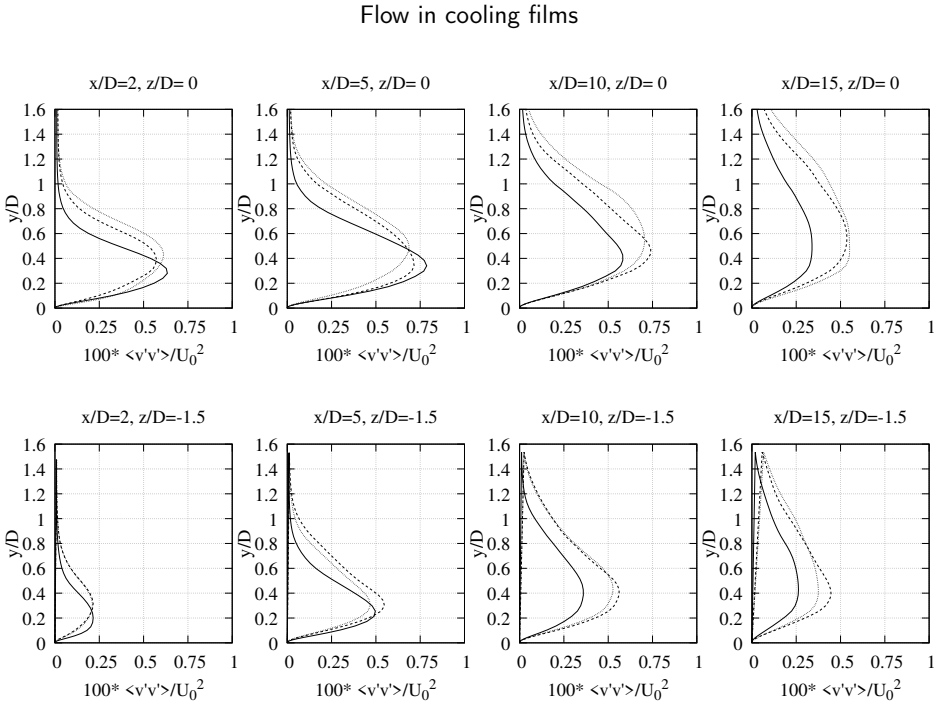


(a) Fan-shaped film

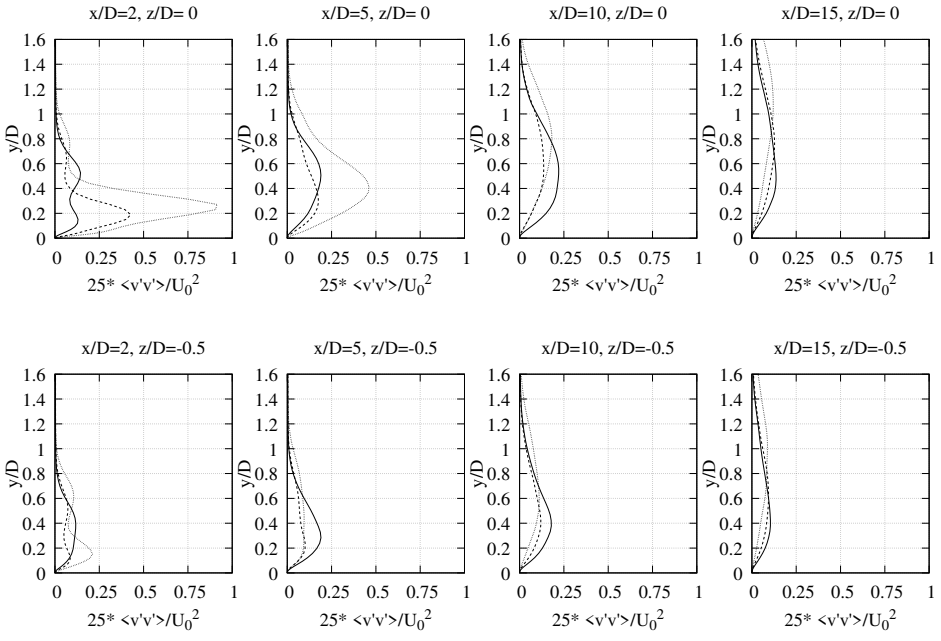


(b) Cylindrical film

Figure 22: The distribution of Reynolds stresses $< u'u' >$ normalized by the freestream velocity squared at different locations downstream of the fan-shaped and cylindrical films. (Solid line: M=0.5; dash line: M=1.0; dot line: M=1.5)

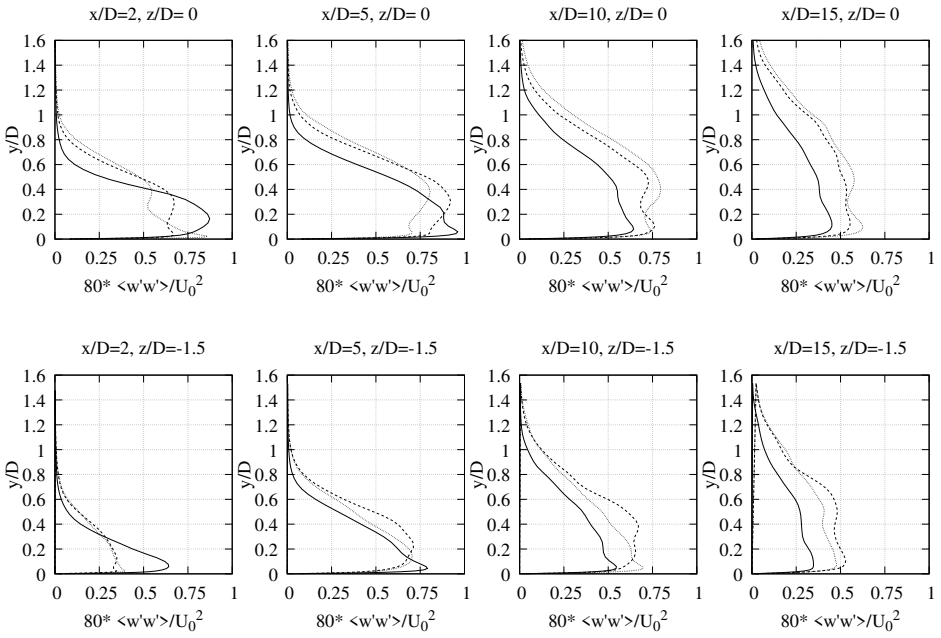


(a) Fan-shaped film

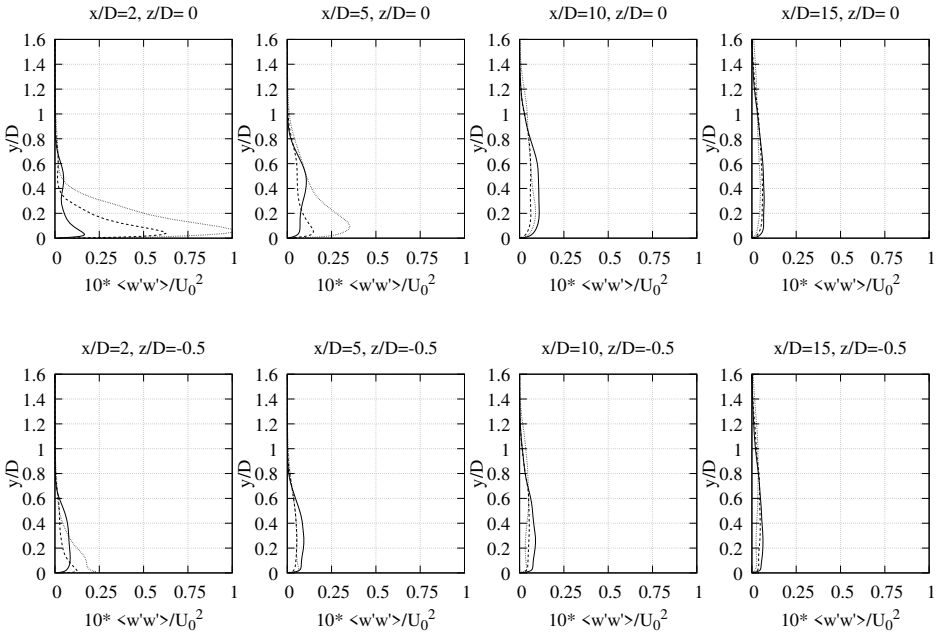


(b) Cylindrical film

Figure 23: The distribution of Reynolds stresses $< v'v' >$ normalized by the freestream velocity squared at different locations downstream of the fan-shaped and cylindrical films. (Solid line: M=0.5; dash line: M=1.0; dot line: M=1.5)



(a) Fan-shaped film



(b) Cylindrical film

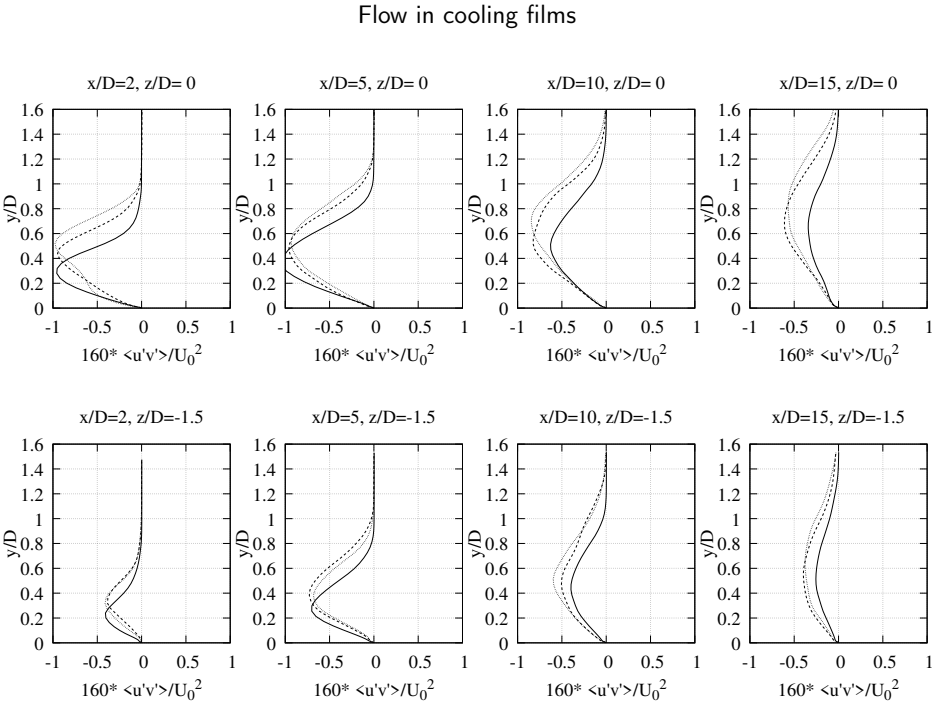
Figure 24: The distribution of Reynolds stresses $< w'w' >$ normalized by the freestream velocity squared at different locations downstream of the fan-shaped and cylindrical films. (Solid line: M=0.5; dash line: M=1.0; dot line: M=1.5)

(positive peak at $y/D = 0.5$) and from the jet to the wall. The level of the Reynolds shear stress for cylindrical cases is low in proximity to the wall. At $M = 1.0$ and $M = 1.5$, momentum transfer in cylindrical films takes place in the same direction as in fan-shaped films. However, in cylindrical cases, the locations where peak stresses are attained are further away from the wall. As an example, for $M = 1.0$, momentum is transferred from the jet to the wall (negative peak at $y/D = 0.3$) and from the jet to the freestream (positive peak at $y/D = 0.8$). At $M = 1.5$, momentum transfer is similar but stronger; momentum is transferred from the jet to the wall (negative peak at $y/D = 0.35$) and from the jet to the freestream (positive peak at $y/D = 0.8$).

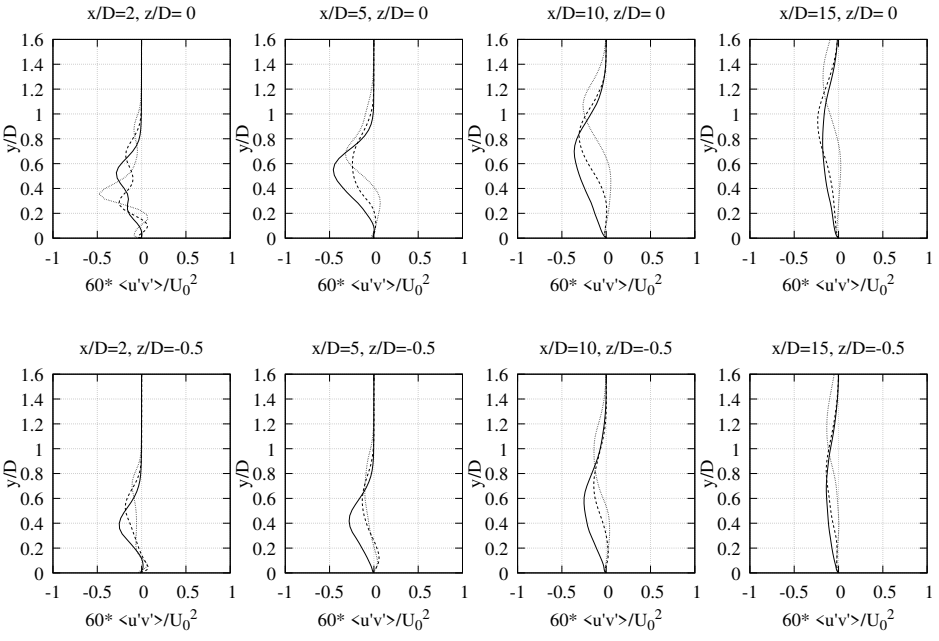
Far-field flow is analyzed at $x/D = 10$ and 15. In the far field, the properties of turbulence are determined by the mixing between the jet and surrounding flow. A peak next to the wall is due to the developing boundary layer, and a relatively flat region that corresponds to the core of the jet. For the fan-shaped films, only at $M = 0.5$, the jet is still confined in the original boundary layer; for the other two blowing ratios, the jet grows to a height larger than the original boundary layer thickness. For the cylindrical films, at $M = 0.5$, the jet is still attached to the wall, whereas at $M = 1.0, 1.5$, the jet is about to be lifted off. Furthermore, the jet produced by the cylindrical films stands at a greater distance from the wall, compared to those produced by the fan-shaped films at the same blowing ratios.

The existence of self-similarity properties in the Favre-averaged velocity and temperature profiles suggests that Reynolds stress profiles may also enjoy similarity properties. Fig. 22a, Fig. 23a and Fig. 24a normalize profiles of the normal Reynolds stress by the freestream velocity squared. Differently from Favre-averaged velocity and temperature profiles, the Reynolds stresses can only be considered to achieve near similarity in the first approximation using this scaling. In the far field ($x/D = 10, 15$), the observations apply to both the cylindrical and fan-shaped films.

At moderate blowing ratios ($M = 0.5, 1.0$), the normal Reynolds stresses in the fan-shaped film, are higher than the Reynolds stresses in the cylindrical film. At the highest blowing ratio, the



(a) Fan-shaped film



(b) Cylindrical film

Figure 25: The distribution of Reynolds shear stresses $< u'v' >$ normalized by the freestream velocity squared at different locations downstream of the fan-shaped and cylindrical films. (Solid line: M=0.5; dash line: M=1.0; dot line: M=1.5)

cylindrical film has higher normalized intensities compared to the other cases. In both fan-shaped and cylindrical films, the normal stresses are nearly uniform throughout the jet.

In the cylindrical hole, the jet is lifted off, so there is turbulence created by the jet that interferes with the wall region. Therefore, no deficit appears in the wall stresses between the wall and the lower edge of the jet. The structure of the flow near the wall is dominated by the boundary layer growing under the jet. In the fan-shaped films, the jet is not lifted off, and the turbulence from the jet is present in the near-wall region. As a result, the shape of the Reynolds normal stress distributions in the far field of fan-shaped and cylindrical films are not very different. The effect of the blowing ratios is to move the peak of the normal stress distributions away from the wall. The higher the blowing ratio is, the further away the jet is from the wall. The part of the jet not influenced by the presence of the wall extends from $y/D = 0.2$ to the height between $y/D = 0.6$ and 0.8 for the fan-shaped hole and the height between $y/D = 1$ and 1.5 for the cylindrical hole. The normal stresses are relatively flat in this domain. The turbulence in the fan-shaped film is very isotropic in the near-wall region. The turbulent flow generated by the cylindrical film is isotropic. The position of the local maximum in the normal stresses shows that the jet produced by the cylindrical film stands downstream further away from the wall compared to the jet produced by a fan-shaped film of similar blowing ratios. However, the locations where peak stresses are attained are further away from the wall.

Fig. 26 and Fig. 27 show the Reynolds stresses scaled by the corresponding Reynolds stress components at the core of the jet vs the wall-normal distance from the core of the jet scaled by the distance between δ_{99} and the core of the jet, that is $(y - \delta_{99})/(\delta_{99} - \delta_{99/2})$. By using this scaling, a better demonstration of the self-similar pattern is discovered in each Reynolds stress component away from the wall in the far-field region. In the fan-shaped cases (in Fig. 26), the scaled $< u'u' >$, $< v'v' >$, $< w'w' >$ and $< u'v' >$ at different blowing ratios collapse well above the core of the jet for the near-field region, and collapse well both above the core of the jet and near the wall for the far-field region. In contrast, for cylindrical cases(in Fig. 27), the scaled Reynolds stress components $< u'u' >$, $< v'v' >$, $< w'w' >$ and $< u'v' >$ exhibit larger differences among different blowing

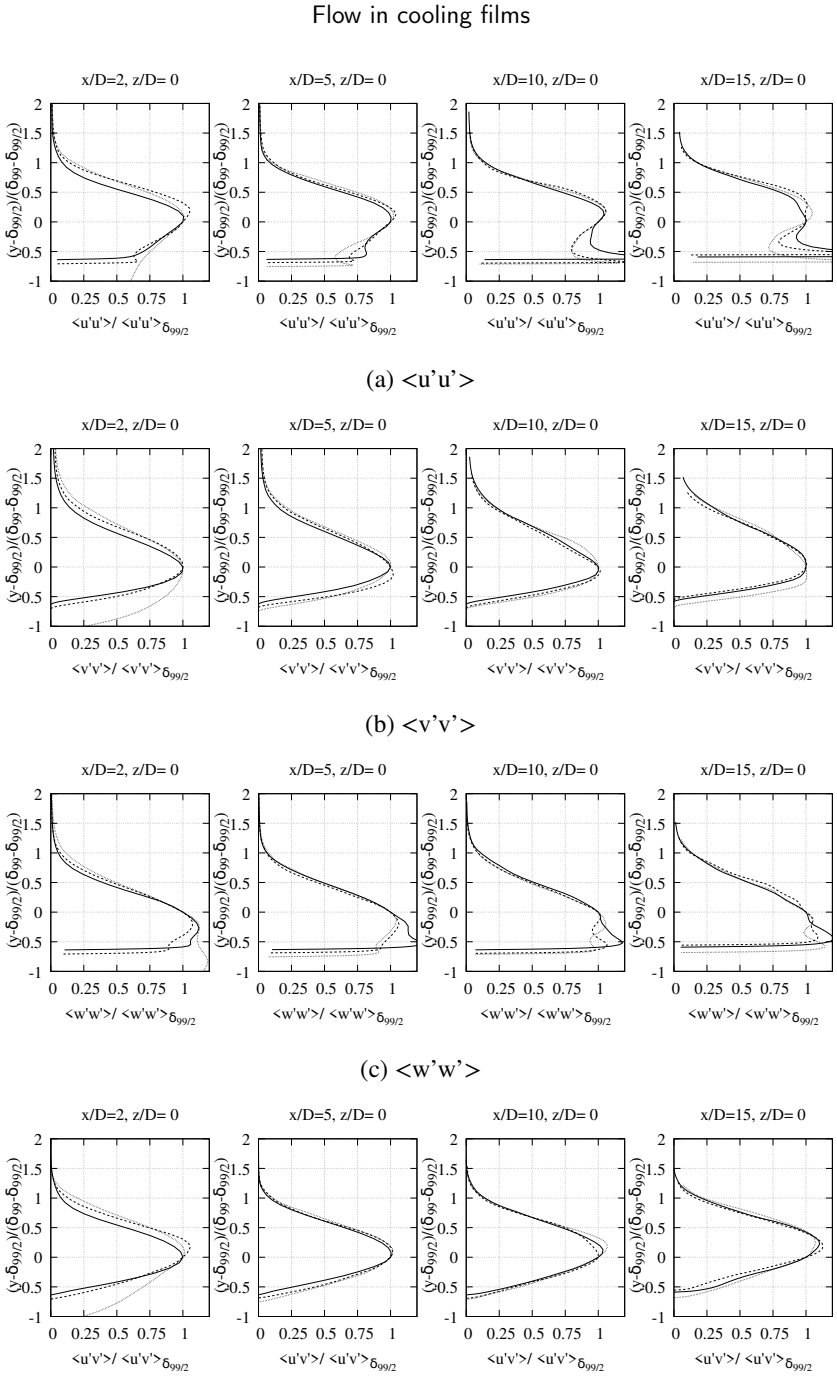


Figure 26: Profiles of the Reynolds stress (a)$< u'u' >$, (a)$< v'v' >$, (a)$< w'w' >$ and (a)$< u'v' >$ normalized by corresponding Reynolds stress component at the core of the jet $\delta_{99}/2$ in the fan-shaped film(Solid line: M=0.5; dash line: M=1.0; dot line: M=1.5)

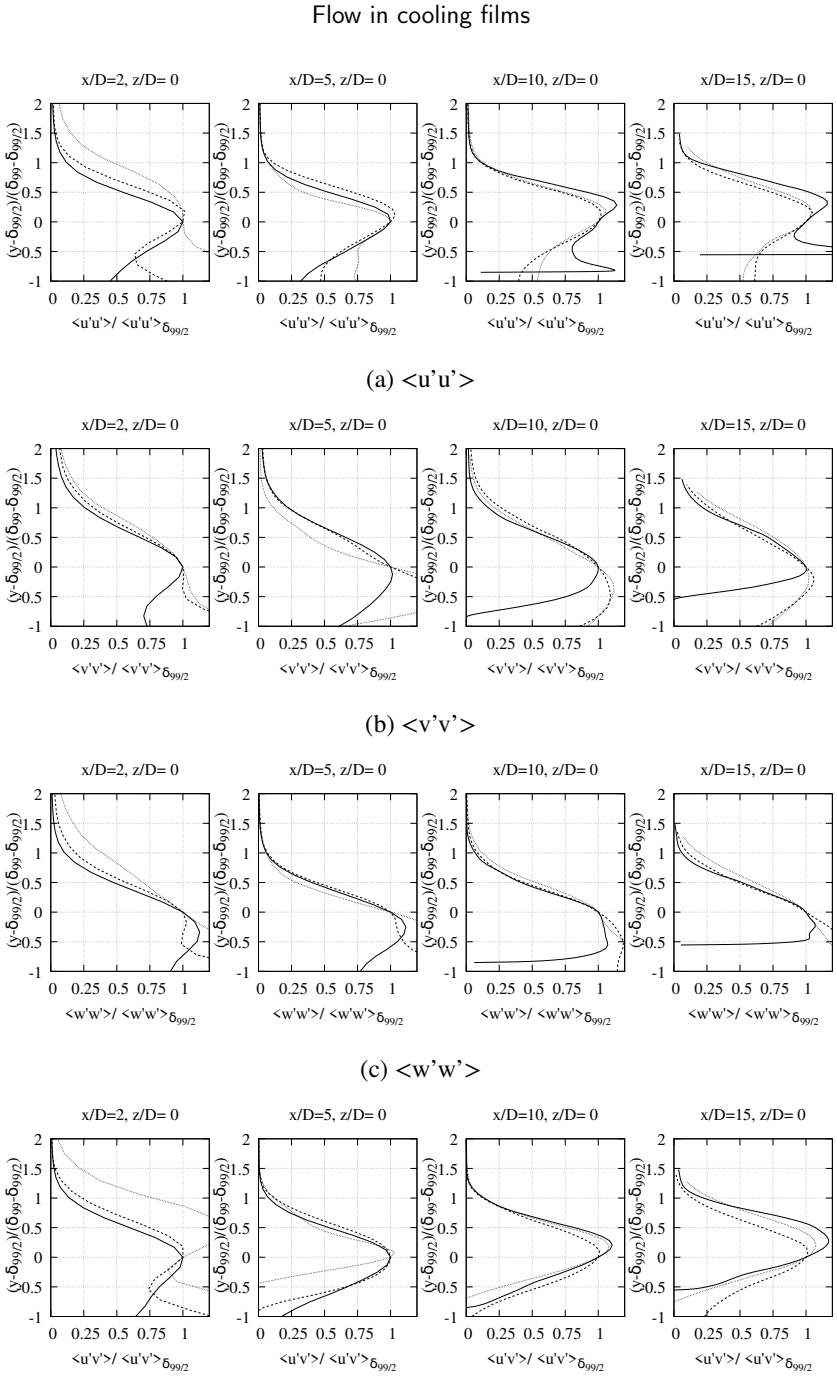


Figure 27: Profiles of the Reynolds stress (a)$< u'u' >$, (a)$< v'v' >$, (a)$< w'w' >$ and (a)$< u'v' >$ normalized by corresponding Reynolds stress component at the core of the jet $\delta_{99}/2$ in the cylindrical film(Solid line: M=0.5; dash line: M=1.0; dot line: M=1.5)

ratios in the near-field region. This is due to the varying flow mechanisms attached to the wall at different blowing ratios, as discussed previously. The scaled Reynolds stress components tend to collapse well above the core of the jet in the far-field region. Overall, the scaling analysis helps to highlight the self-similar nature of Reynolds stresses in the far-field region. However, the behavior of Reynolds stresses in the near-field region is more complex and depends on the blowing ratio and the geometry of the film.

4.4. Turbulent heat flux

Fig. 28 shows the distribution of turbulent heat flux along the wall-normal direction in two types of holes. The turbulent flux is defined as the Favre-averaged product of the velocity fluctuation and the non-dimensional temperature fluctuation. The definition of the non-dimensional temperature is shown below:

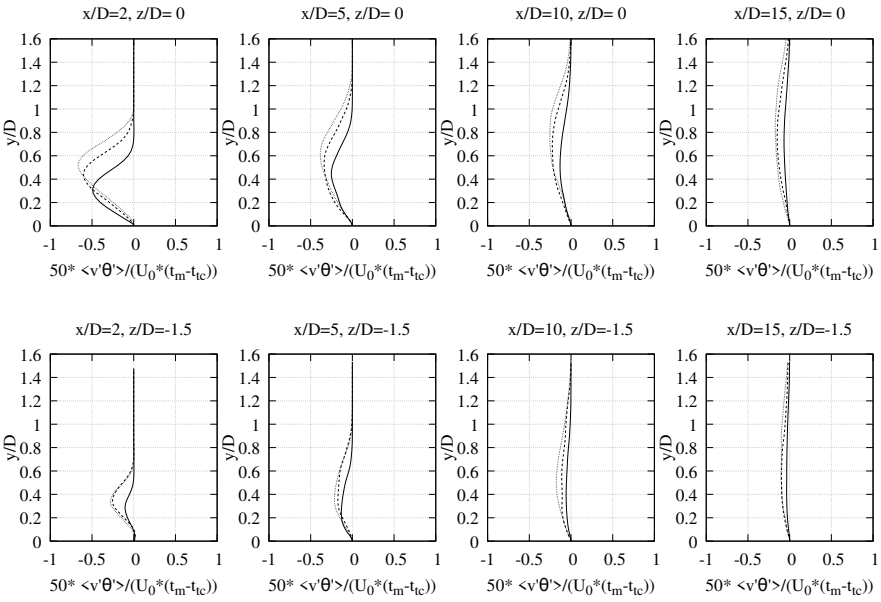
$$\theta = \frac{T - T_c}{T_m - T_{tc}} = 1 - \eta \tag{5}$$

The net heat flux on the wall must be zero due to the adiabatic wall condition, whereas the momentum flux on the wall is not zero because of friction. Therefore, the shape of the turbulent heat flux and the shape of the Reynolds stresses must be different next to the wall. However, away from the wall, the shape of the turbulent heat flux is identical to the shape of the Reynolds shear stresses (shown as in Fig. 25), apart from the sign. Comparing Fig.28 and Fig.25, the positions of the peaks of turbulent heat fluxes and Reynolds shear stress away from the wall are close. This applies to all three blowing ratios.

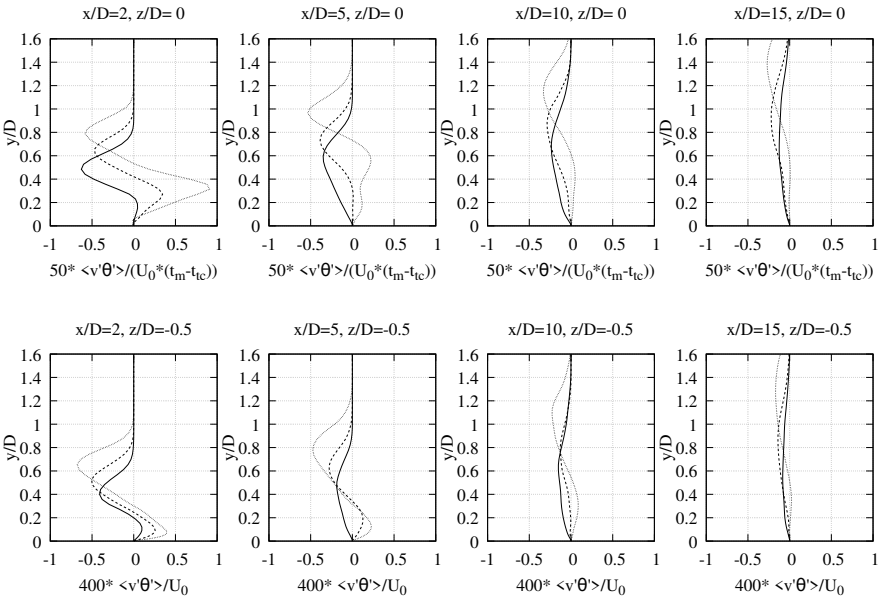
In the fan-shaped film as shown in Fig. 28a, at $M = 0.5$, the peak of turbulent heat flux is everywhere negative. At $x/D = 2$, heat is transferred from the freestream to the coolant jet, with a negative peak located at $y/D = 0.4$ on the centerline. This peak is identified as the upper edge of the jet. The direction of the heat flux at the upper edge of the jet is preserved as the flow develops downstream from $x/D = 5$ to $x/D = 15$. In all cases considered the temperature of the free stream

is higher than the temperature of the coolant. Any mixing at the edge of the jet causes a turbulent heat flux from the free stream to the jet. This explains the negative sign of the turbulent heat flux at the edge of the jet. This situation should be contrasted with the change in the direction of the momentum flux, which is determined by the blowing ratio. The peak of turbulent heat flux is located further away from the wall as the blowing ratio is higher at each streamwise position. As an example, At $x/D = 2$ on the centerline, the peak of turbulent heat flux is located at $y/D = 0.5$ for the $M = 1.0$ case and at $y/D = 0.6$ for the $M = 1.5$ case. Similarly, the negative peak can be identified but with a smaller amplitude on the edge of the jet $z/D = -1.5$ of the fan-shaped film.

In the cylindrical film as shown in Fig. 28b, the negative peak can also be identified throughout the downstream flow domain at each blowing ratio, indicating the upper edge of the jet. As an example at $x/D = 2$ on the centerline of the cylindrical film, heat is transferred from the freestream to the jet with a negative peak at $y/D = 0.5$ for the $M = 0.5$ case, while for the $M = 1.0$ case and the $M = 1.5$ case, heat transfer takes place in the same direction with the negative peak located at $y/D = 0.6$ and $x/D = 0.8$, respectively. In addition, a positive peak of turbulent heat flux is also identified at a position lower than that of the negative peak. At $x/D = 2$ on the centerline, the positive peak is tiny for the $M = 0.5$ case, which is located at $y/D = 2$, but largest for the $M = 1.5$ case, which is located at $y/D = 0.35$. Both the positive and amplitude of the positive peak for the $M = 1.0$ case are in between. The positive peak disappears first in the lowest blowing ratio case till $x/D = 5$, then in the medium blowing ratio case till $x/D = 10$, and retains the longest distance at the highest blowing ratio as the jet goes downstream. This positive peak is identified as the lower side edge of the jet. The sign of the heat flux is determined to a large extent by the relative position of the coolant and the cold jet. The appearance of the positive peak in the cylindrical is because the jet is lifted from the wall and the hot air is drawn under the jet. This results in turbulent fluctuations in the area under the jet moving hot air upwards and cold air downwards, giving a net positive heat flux. Similarly, the patterns of the two peaks can be discovered but with smaller amplitudes on the edge of the jet $z/D = -0.5$ of the cylindrical film.



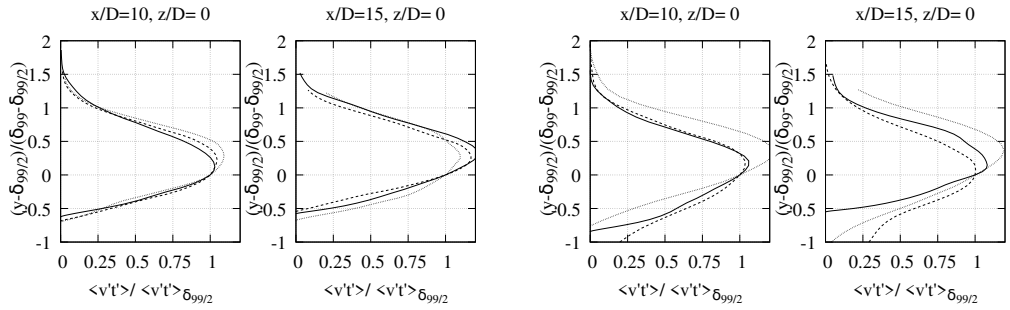
(a) Fan-shaped hole



(b) Cylindrical hole

Figure 28: The distribution of turbulent heat flux in the wall-normal direction in two types of cooling films. Solid line: M=0.5; dash line: M=1.0; dot line: M=1.5.

Fig. 29 shows turbulent heat flux in the wall-normal direction $< v't' >$ scaled by the corresponding turbulent heat flux at the core of the jet, vs the wall-normal distance from the core of the jet scaled by the distance between δ_{99} and the core of the jet, which is $(y - \delta_{99})/(\delta_{99} - \delta_{99/2})$. By using this scaling, a better demonstration of the self-similar pattern can be observed in the wall-normal component of the turbulent heat flux throughout the wall-normal distance for the fan-shaped films. For the cylindrical cases, the turbulent heat flux curves collapse well above the core of the jet, while the curve at the highest blowing ratio deviates. The curves close to the wall lack self-similarity. This shows that even when the flow mechanism is different, the self-similar pattern also exists in turbulent heat flux in the far-field region as long as the suitable scaling method is adopted.



(a) fam-shaped (b) cylindrical

Figure 29: Profiles of turbulent heat flux in the wall-normal direction $< v't' >$ in two types of cooling films. normalized by the corresponding turbulent heat flux at the core of the jet $\delta_{99}/2$ (Solid line: M=0.5; dash line: M=1.0; dot line: M=1.5)

5. Conclusion

A large number of published results focus on quantities of direct interest to the cooling system designer such as the film cooling effectiveness but overlook detailed distributions of the velocity and the Reynolds stress in the flow above the cooled surface. Velocity fields and Reynolds stress distributions are nonetheless the factors that ultimately determine the film cooling effectiveness by deciding the concentration of coolant near the surface.

Flow in cooling films

This study uses LES to investigate the mean flow, Reynolds stress, and turbulent heat flux distributions of a well-documented set of experiments on film cooling. LES simulations are performed on fan-shaped and cylindrical films at blowing ratios of 0.5, 1.0, and 1.5 when the free-stream Mach number is 0.6. The simulations are validated against 1) published discharge characteristics; 2) published velocity and turbulence intensity profiles measured on the same flow configurations.

The results show that:

- LES simulations of modest cost can reproduce with high accuracy the measured discharge characteristics of cylindrical and fan-shaped cooling films.
- The mean velocity and temperature fields produced by a fan-shaped film approach a self-similar flow profile very rapidly downstream of the injection point. The mean velocity and temperature fields produced by a cylindrical film only approach self-similar profiles at low blowing ratios or at high blowing ratios, but not at intermediate blowing ratios (~ 1).
- The similarity variables are the local velocity defect and temperature deficit and the jet layer thickness. These similarity relations only apply to the outer part of the jet.
- The jets acquire a layered structure with a developing boundary layer confined between the jet and the wall, and a free shear layer separating the jet from the mainstream.
- Analysis of the Reynolds stress and turbulent heat flux profiles shows that turbulent quantities do not reach self-similar behavior when scaled with the local velocity defect and jet layer thickness.
- The Reynolds stress and turbulent heat flux profiles show that the section of the jet resembling a free shear layer has essentially uniform and fairly isotropic Reynolds stress and has a distinct behavior from the boundary layer growing between the wall and the jet itself.



7

Reynolds stress budgets and turbulent heat flux budgets in film cooling

7.1 | Preface

With the LES results available in Chapter 6, studies on budgets of Reynolds stresses and turbulent heat fluxes are performed in this Chapter.

The interest in the budgets of Reynolds stresses in realistic industrial applications such as film cooling is stimulated by the motivation for improving the predictive capability of RANS. Although there are gradually accurate predicting tools using LES and DNS available in film cooling studies, RANS methods are still the main choice of simulations by designers when considering their lower computational cost compared with LES and DNS. RANS, however, loses accuracy because they need turbulence models that introduce inaccuracies to the prediction of film cooling performance. Budgets are one of the criteria for assessing the limitations of available

RANS turbulence models. Analyzing related budget terms can also help better understand the physics of turbulence flows. Moreover, examining the budget terms can illuminate fluid physics.

In this chapter, the budgets in the transport equations of Reynolds stresses and turbulence heat flux in film cooling cases are captured using data obtained from LES shown in Chapter 6. The analysis of these budget terms is shown for the first time in the open literature to the author's knowledge.

The following sections contain two journal papers on budgets. Both technical paper 5 and technical paper 6 are under review/revision in Physics of Fluid and International Journal of Heat and Mass Transfer, respectively.

Technical paper 5 "Budgets of Reynolds stress in film cooling with fan-shaped and cylindrical holes" has studied the mechanisms by which energy is extracted from the mean flow and distributed among the normal Reynolds stresses. It shows that the jets of both fan-shaped and cylindrical films can be split into a near field and a far field with different properties. The similarity laws for budgets of the Reynolds stresses are discovered. The exponents in the scaling laws are also studied in terms of the dependence on the film configuration, on the blowing ratio, or on the flow regime.

Technical paper 6 reports a detailed study of "Heat transfer and budgets of turbulent heat flux in film cooling with fan-shaped and cylindrical holes" using LES. A qualitative criterion has been proposed to identify the regions constituting a cylindrical film wall jet based on the relative magnitude of non-dimensional temperature, turbulent heat flux, and temperature fluctuations. Individual terms in the heat flux budgets have been analyzed and the main physical processes

contributing to those budgets have been identified. The turbulent heat flux budgets have also been applied with the scaling and scaling laws proposed in our technical paper 3 on similarity in Chapter 6. The dependence of turbulent heat flux budgets on the downstream position is also searched for.

7.2 | Technical Paper 5

Reynolds stress budgets in fan-shaped and cylindrical film cooling holes

Muting Hao[a,*,1], Luca di Mare[a,2]

[a]*Oxford Thermofluids Institute, University of Oxford, Southwell Building, Osney Mead, Oxford, OX2 0ES, , United Kingdom*

ARTICLE INFO

Keywords:
Film cooling
Self-similarity
Gas turbines
Large eddy simulation
Reynolds stresses
Reynolds stress budgets
Fan-shaped holes

ABSTRACT

The compressible budget terms in the transport equations of Reynolds stresses are examined from the (Large Eddy Simulation) LES result of the film cooling. The capability of LES and the statistical post-processing procedure were first validated. The compressible Reynolds stress budget terms are then analyzed for both fan-shaped and cylindrical cooling films. The balance of all budget terms is shown. The effect of the blowing ratio on each budget term is examined. The mechanisms by which energy is extracted from the mean flow and distributed among the normal Reynolds stresses are highlighted. The sources of anisotropy in the Reynolds stress distributions are examined in detail and their relation to the flow patterns of the mean and instantaneous flow are explored. The downstream development of the Reynolds stress budgets is studied and it is shown that the jets of both fan-shaped and cylindrical films can be split into a near field and a far field with different properties. Far downstream of the cooling films, the Reynolds stress budgets near the wall present similarities with the Reynolds stress budgets in a boundary layer, while the Reynolds stress budgets further away from the wall resemble budgets in a free-shear flow. It is shown that the budgets of the Reynolds stresses in the three-dimensional wall jets object of this study obey approximate similarity laws. These laws are based on easily obtained integral scales but need to be modified by suitable powers of the distance from the orifice producing the jet.

*Corresponding author

Reynols stress budgets in cooling films

1. Introduction

Cooling has become an indispensable tool for the thermal protection of hot gas turbine components as higher and higher operating temperatures are targeted. However, overusing cooling air means that too much thermodynamic cost is introduced by the cooling film. A good cooling design achieves high effectiveness when the optimal amount of cooling air is selected. Accurate predictions of film cooling flows are thus essential for seeking this optimal condition during gas turbine design.

The interest in the budgets of Reynolds stresses in realistic industrial applications such as film cooling is stimulated by the motivation for improving the predictive capability of Reynolds-averaged Navier-Stokes (RANS). Although there are gradually accurate predicting tools using LES and DNS available in film cooling studies, Reynolds-averaged Navier-Stokes (RANS) methods are still the main choice of simulations by designers when considering their lower computational cost compared with LES and DNS. RANS, however, loses accuracy because they need turbulence models that introduce inaccuracies to the prediction of film cooling performance. As an example, the standard $k-\epsilon$ model, even though widely used for film cooing simulations, have issues such as over-prediction of the penetration distance into the mainstream, (see RefHoda and Acharya (1999)) and the under-prediction of the jet spreading (see RefPatankar, Basu and Alpay (1977)). The inaccuracy of turbulence models in RANS partly stems from the base assumption in modeling the Reynolds stress tensor, which is $\overline{\rho}\tau_{ij} = -\overline{\rho u_i'' u_j''}$. One of the most commonly used assumptions for Reynolds stress tensor in RANS is the Boussinesq eddy-viscosity assumption, which determines the Reynolds stress tensor as linearly related with the mean strain-rate tensor ($\bar{S}_{ij}$). Such an assumption is not capable of correctly handling anisotropy and inhomogeneity in flows with rapid variations of mean strain rate and flows with

secondary flows. Budgets are one of the criteria for assessing the limitations of available RANS turbulence models. Analyzing related budget terms can also help better understand the physics of turbulence flows.

In the past years, DNS and LES simulations have been used to provide detailed turbulence statistical quantities including Reynolds stress budgets, turbulent kinetic energy budgets, and other quantities shown in turbulence models. Reynolds stress budgets have been so far studied in flat plate Guarini, Moser, Shariff and Wray (2000), turbulent boundary layers Guarini et al. (2000), channels Huang, Coleman and Bradshaw (1995), pipes Ghosh, Foysi and Friedrich (2010), and interactions between shock waves and turbulent boundary layers Vyas, Yoder and Gaitonde (2019). Nicholson Nicholson, Huang, Duan, Choudhari and Bowersox (2021) compared DNS results with results from RANS simulations based on zero-equation, one-equation, two-equation, and eddy-viscosity models in favorable pressure gradient turbulent boundary layers. They found that the reduction of Reynolds stress can be considerably underpredicted under a stronger pressure gradient by all examined RANS models. They illustrated that the Boussinesq assumption leads to underpredicted wall-normal Reynolds stresses but reasonable Reynolds shear stress. For film cooling, there have been no studies on budgets of the Reynolds stress in the open literature. Only very few studies discussed budgets of turbulent kinetic energy in film cooling. Muldoon and Acharya Muldoon and Acharya (2006) assessed terms of $k-\epsilon$ equations in cooling films by using DNS. They obtained the terms in the $k-\epsilon$ equations directly by using DNS and compared them with the same terms calculated by using the standard $k-\epsilon$ model. They showed that the eddy viscosity of the standard $k-\epsilon$ equations presented a nonnegligible error when simulating film cooling. However, they used incompressible Navier-Stokes equations and they ignored the effect of the compressibility on their budget terms.

Reynols stress budgets in cooling films

Studies on both the LES or DNS of film coolingZhi, Li, Wen, Su and Wang (2023); Zhou, Chen, Liu, Wen and Peng (2018); Zhang, Wu and Wang (2022) and the budgets of stresses or energy Qiao, Mu, Luo and Si (2020); Rogachevskii, Kleeorin and Zilitinkevich (2022); Kleeorin, Rogachevskii and Zilitinkevich (2021) have been increasingly pursued recently, there is so far no study on the Reynolds stress budgets in the film cooling cases.

In a recent turbulence paper by the authors M. Hao (2022), the downstream evolution of Reynolds stress profiles has been discussed. It is shown that the flow cannot attain similarity at all blowing ratios within 5 diameters downstream of the film. This happens because at a high blowing ratio, the direction of momentum transfer between the film and its surroundings is not uniform. Self-similarity of the mean velocity and temperature defect profiles is attained at a larger distance from the film in the outer parts of the wall jets. The similarity variables are the thickness of the film layer and the velocity defect at half of the film layer thickness. However, the Reynolds stress far downstream only obeys similarity in the first approximation.

The target of the present study is to measure the budget terms in the compressible transport equations of Reynolds stresses based on the LES results of film cooling cases. The budget terms for the fan-shaped hole and the cylindrical hole cases are compared. The effect of the blowing ratio on the budget terms is also discussed. The focus on the budget analysis first expects to provide a dynamic balance of statistical correlations. The Reynolds stress budgets are examined in the near field and in the far field, i.e. in the developing section of the jet and in the self-similar section of the jet.

The sources of anisotropy in the Reynolds stress distributions are examined in detail and their relation to the flow patterns of the mean and instantaneous flow is explored. Furthermore, the downstream development of the Reynolds stress budgets is studied and it is

shown that the jets of both fan-shaped and cylindrical films can be split into a near field and a far field with different properties, consistent with the observed properties of the Reynolds stress profiles. It is shown that the budgets of the Reynolds stress in the three-dimensional wall jets object of this study obey approximate similarity laws. These laws are based on easily obtained integral scales but need to be modified by suitable powers of the distance from the orifice producing the jet.

This paper is structured as follows. Section 2 describes the numerical methodology, and the equations of Reynolds stress budgets in the compressible version of the transport equation. Section 4 first recalls some features of the mean and instantaneous flow and then shows the balancing of Reynolds stress budgets; a broad view of the production term of Reynolds stress budgets is studied and its implications for the downstream development of the jets are drawn; self-similarity pattern based on the effect of blowing ratio on Reynolds stress budgets are finally introduced.

2. Methodology

2.1. Flow conditions and numerical methodology

The flow configuration including the geometries of the cooling film, the computational domain, and the flow conditions, is selected to match the experiment presented in Gritsch et al Gritsch, Schulz and Wittig (1998a,b). Based on this, the computations are operated and validated in Hao and di Mare M. Hao (2022).

Figure 1 shows the geometries of the two film cooling holes used in this study: the fan-shaped hole and the cylindrical hole. The two cooling holes are inclined at 30 degree and they have a length-to-diameter ratio of $L/D = 6$ where $D = 0.01$ is the diameter of the hole. As shown in Fig. 1, the coordinate system is built with the origin at the center

Reynols stress budgets in cooling films

of the hole exit plane, the x axis in the streamwise direction, the y axis in the wall-normal direction, and z axis in the spanwise direction.

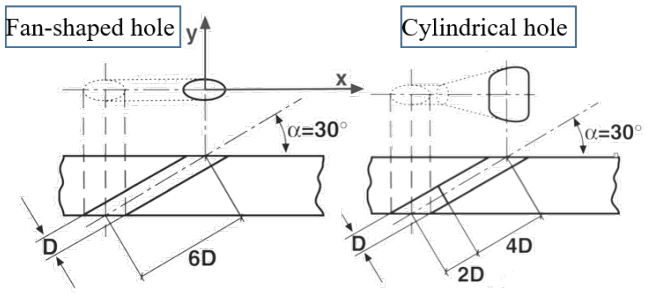


Figure 1: The geometry of film cooling holes: left (a) fan-shaped hole, right: (b)cylindrical hole Gritsch et al. (1998a).

Table 1 lists the operating conditions focused on in the study. Three blowing ratios $BR = 0.5, 1.0, 1.5$ are especially focused on. Figure 2 presents the computational domain for the two types of cooling holes. The computational domain consists of an external mainstream channel, an internal coolant channel, and a cooling hole connecting the two channels. A near-field region is determined for the region between $x/D = 1$ and $x/D = 5$. A far-field region is determined for the region downstream from $x/D = 5$. These two regions are also labeled in Fig. 2 for the following study.

The mesh applied is multiblock hexahedral grids generated by the mesh generator 'H4X' which has been validated in Hao, et alHao and Gorlé (2020). 'H4x' employs a trunk-and-branch template to build the layout of the cooling film, combined with elliptic smoothing with the grid points on the boundary surfaces sliding while control functions are used to enforce the near-wall grid spacing. Such a mesh can greatly satisfy the grid orthogonality near the surface and smoothness throughout the computational domain. These can be reflected in Fig. 3 which shows the mesh for the fan-shaped case an example with

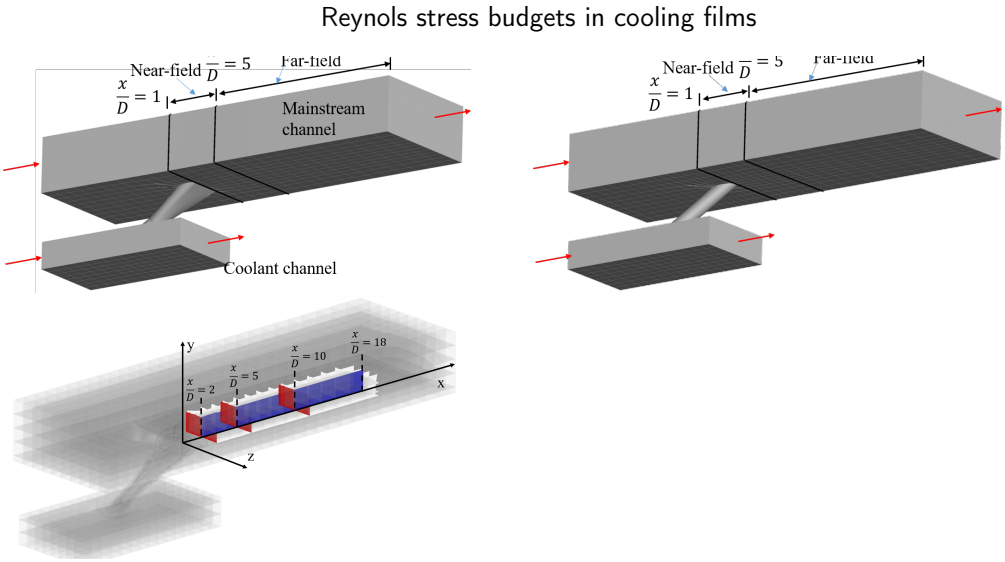


Figure 2: Computational domains: a)fan-shaped hole, b) cylindrical hole

Table 1
Operating conditions of the film-cooling cases

Parameter	Symbol	Value
Internal Temperature	T_{tc}	290K
Blowing ratio	M	0.5, 1.0, 1.5
Pressure ratio	T_{tc}/Ttm	0.54
Internal Mach number	Ma_c	0
External Mach number	Ma_m	0.6
Internal Reynolds number	Re_{Dc}	up to 2.5×10^5
External Reynolds number	Re_{Dm}	up to 1.3×10^5
Boundary layer thickness	δ_{99}/D	0.5
External turbulence level	Tu_m/D	$< 1.5\%$
Internal turbulence level	Tu_c/D	$< 1\%$

the mesh on the cutting median section zoomed in. The number of grids is 9674k for the fan-shaped case, and 1053k for the cylindrical case.

The LES simulations are run by a home-grown CFD code 'H4X'. The governing equations in Eqn.1 are solved. The code is based on an implicit LES using the finite volume method to solve the conservation laws.

Reynols stress budgets in cooling films

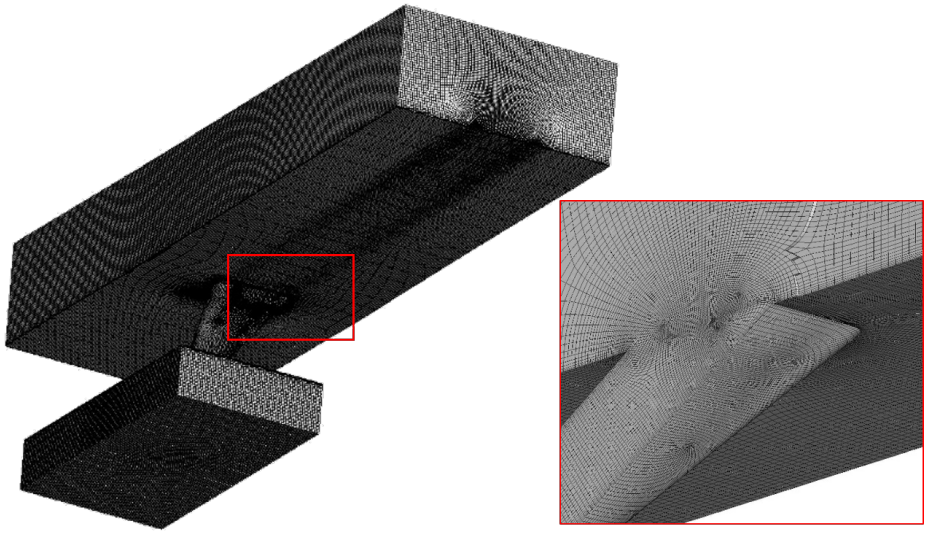


Figure 3: The mesh of the fan-shaped case with the view on the median cutting plane

$$\begin{aligned} \frac{\partial \rho}{\partial t} + \frac{\partial \rho u_j}{\partial x_j} &= 0 \\ \frac{\partial \rho u_i}{\partial t} + \frac{\partial \rho u_i u_j}{\partial x_j} + \frac{\partial p}{\partial x_i} &= \frac{\partial \sigma_{ij}}{\partial x_j} \\ \frac{\partial \rho E}{\partial t} + \frac{\partial (\rho E + p) u_j}{\partial x_j} &= \frac{\partial \sigma_{ij} u_i}{\partial x_j} - \frac{\partial}{\partial x_j} q_j \end{aligned} \tag{1}$$

The cell center is used to store variables. On the cell interface, fluxes are evaluated. Flow characteristic variables are extrapolated to the cell interface by a third-order limiter Čada and Torrilhon (2009). For obtaining slope limiters, a weight least square method is used to obtain the gradients. For the inviscid flux, a method of biased stencil is applied, while the Roe Riemann solver is used to evaluate the flux. This leads to a biased three-point

stencil and then a third-order scheme away from discontinuities and local extrema. For the viscous flux, the unbiased least square method is used to evaluate the gradient. As a result, the viscous flux is centered and has second-order accuracy.

The time advancing applies the third-order Runge-Kutta scheme. The CFL number is chosen as 0.8 as the limit, and lower values are adopted during simulations. The boundary conditions are partly shown in Fig. 2 with red arrows indicating the inlet and outlet. The inlet boundary condition is constructed by a synthetic turbulent inflow generator based on eigenmode decomposition Hao, Hope-collins and di Mare (2022). The outlet boundary condition applies the unsteady non-reflecting boundary proposed by Thompson Thompson (1987). The side wall of the mainstream channel is applied with the periodic boundary condition. The top wall of the mainstream and the bottom wall of the coolant channel are using far-field boundaries. The rest of the walls are treated with non-slip adiabatic wall boundary conditions. MPI and OpenMPI are implemented for the parallelism of running. 480 processors in parallel are used for LES computations. The complete description of the numerical method, the validation of the meshing, and the validations of the numerical method with LES results are shown in Hao and di Mare M. Hao (2022).

The Reynolds averages and Favre averages are obtained from statistics of the last 14 flow through times in the unsteady compressible LES results for each case. Namely, around 8000 instantaneous samples are used for the averaging operations.

2.2. Equations for Reynolds-average, Favre-average, Reynolds stress budgets

The two forms of averaging this study related to are Reynolds averaging and Favre averaging. For a dependent variable f, Reynolds-averaging partitions f into an ensemble

mean and a fluctuation. The Reynolds decomposition takes the form:

$$f(\mathbf{x},t) = \bar{f}(\mathbf{x},t) + f'(\mathbf{x},t) \tag{2}$$

The Favre average is defined as

$$\widetilde{f} = \frac{\overline{\rho f}}{\bar{\rho}} \tag{3}$$

The Favre-averaging procedure partitions f into the Favre average and a fluctuation. The Favre decomposition consequently reads

$$f(\mathbf{x},t) = \tilde{f}(\mathbf{x},t) + f''(\mathbf{x},t) \tag{4}$$

The Favre-averaged Reynolds-stress tensor is

$$\overline{\rho}\tau_{ij} = -\overline{\rho u_i'' u_j''}. \tag{5}$$

The transport equation of the Reynolds-stress tensor in the compressible situation is obtained in a way that the dependent variables take the Favre-averaged form while the equations are in the Reynolds-averaged form. The derivation is achieved by adding two Reynolds-averaged equations, one of which is the product of u_i'' with the fluctuating momentum equation for u_j'', and the other is the product of u_j'' with the fluctuating momentum equation for u_i''. The transport equation of the stress tensor can be written in

the form Gatski and Bonnet (2009):

$$\begin{aligned}\bar{\rho}\frac{\mathrm{D}\tau_{ij}}{\mathrm{D}t} &= \frac{\partial\left(\bar{\rho}\tau_{ij}\right)}{\partial t} + \frac{\partial}{\partial x_k}\left(\widetilde{u}_k\bar{\rho}\tau_{ij}\right) \\ &= \bar{\rho}P_{ij} + \bar{\rho}\Pi_{ij} - \bar{\rho}\epsilon_{ij} + \bar{\rho}M_{ij} + \bar{\rho}D_{ij}\end{aligned} \tag{6}$$

where

Production
$$\bar{\rho}P_{ij} = -\bar{\rho}\left[\tau_{ik}\frac{\partial\widetilde{u}_j}{\partial x_k} + \frac{\partial\widetilde{u}_i}{\partial x_k}\tau_{kj}\right] \tag{7}$$

Redistribution
$$\bar{\rho}\Pi_{ij} = \overline{p'\left(\frac{\partial u_i''}{\partial x_j} + \frac{\partial u_j''}{\partial x_i}\right)} = \overline{p'\left(\frac{\partial u_i'}{\partial x_j} + \frac{\partial u_j'}{\partial x_i}\right)} \tag{8}$$

Dissipation
$$\bar{\rho}\epsilon_{ij} = \overline{\sigma_{ik}''\frac{\partial u_j''}{\partial x_k}} + \overline{\sigma_{jk}''\frac{\partial u_i''}{\partial x_k}} = \overline{\sigma_{ik}'\frac{\partial u_j'}{\partial x_k}} + \overline{\sigma_{jk}'\frac{\partial u_i'}{\partial x_k}} \tag{9}$$

Mass Flux Contribution
$$\begin{aligned}\bar{\rho}M_{ij} &= \overline{\rho' u_i''}\left(\frac{\partial\bar{p}}{\partial x_j} - \frac{\partial\bar{\sigma}_{jk}}{\partial x_k}\right) + \overline{\rho' u_j''}\left(\frac{\partial\bar{p}}{\partial x_i} - \frac{\partial\bar{\sigma}_{ik}}{\partial x_k}\right) \\ &= \overline{\rho' u_i'}\left(\frac{\partial\bar{p}}{\partial x_j} - \frac{\partial\bar{\sigma}_{jk}}{\partial x_k}\right) + \overline{\rho' u_j'}\left(\frac{\partial\bar{p}}{\partial x_i} - \frac{\partial\bar{\sigma}_{ik}}{\partial x_k}\right)\end{aligned} \tag{10}$$

Diffusion
$$\bar{\rho}D_{ij} = \bar{\rho}D_{ij}^{\nu} + \bar{\rho}D_{ij}^{T} + \bar{\rho}D_{ij}^{P} \tag{11}$$

Viscous Diffusion
$$\begin{aligned}\bar{\rho}D_{ij}^{\nu} &= \frac{\partial}{\partial x_k}\left(\overline{\sigma_{ik}''u_j''} + \overline{\sigma_{jk}''u_i''}\right) \\ &= \frac{\partial}{\partial x_k}\left(\overline{\sigma_{ik}'u_j'} + \overline{\sigma_{jk}'u_i'}\right)\end{aligned} \tag{12}$$

Turbulent Diffusion
$$\begin{aligned}\bar{\rho}D_{ij}^{T} &= -\frac{\partial}{\partial x_k}\left[\overline{\rho u_i''u_j''u_k''}\right] \\ &= -\frac{\partial}{\partial x_k}\left[\bar{\rho}\widetilde{u_i''u_j''u_k''}\right]\end{aligned} \tag{13}$$

Pressure Diffusion
$$\begin{aligned}\bar{\rho}D_{ij}^{P} &= -\frac{\partial}{\partial x_k}\left[\delta_{ik}\overline{p'u_j''} + \overline{p'u_i''}\delta_{jk}\right] \\ &= -\frac{\partial}{\partial x_k}\left[\delta_{ik}\overline{p'u_j'} + \overline{p'u_i'}\delta_{jk}\right]\end{aligned} \tag{14}$$

where σ_{ij} is the viscous stress tensor for a Newtonian fluid, with μ as the shear viscosity, and δ_{ij} as the Kronecker delta,

$$\sigma_{ij} = 2\mu \left(S_{ij} - \frac{\delta_{ij}}{3} S_{kk} \right) \tag{15}$$

based on strain-rate tensor S_{kl}, which takes the form:

$$S_{kl} = \frac{1}{2} \left(\frac{\partial u_k}{\partial x_l} + \frac{\partial u_l}{\partial x_k} \right) \tag{16}$$

The transport of the Reynolds stress shown in Equation 6 is balanced among its production term, redistribution (pressure strain) term, dissipation term (resolved viscous dissipation), mass flux contribution, and diffusion terms. Diffusion terms are comprised of viscous diffusion (or molecular diffusion), turbulent diffusion (or turbulent transport), and pressure diffusion. An exhaustive overview of compressible turbulence budget is given in the book by Gatsk, et al. Gatski and Bonnet (2009).

3. Validation

The LES procedure used in this paper has been validated by comparing computed flowfield and heat transfer characteristics with experimental data in a recent paper M. Hao (2022) by the authors. The results in this section focus on the validity of the procedure to compute terms in the Reynolds stress budget.

The correctness of the Reynolds-stress budget algorithm is validated in Spalart's $Re_\tau = 670$ turbulent boundary layer case Spalart (1988). The incompressible version of Reynolds-stress budget terms is used in this case according to SpalartSpalart (1988). The Reynolds

Reynols stress budgets in cooling films

stress budgets computed using the authors' LES code are compared with the results from the DNS data in SpalartSpalart (1988), shown in Fig. 4.

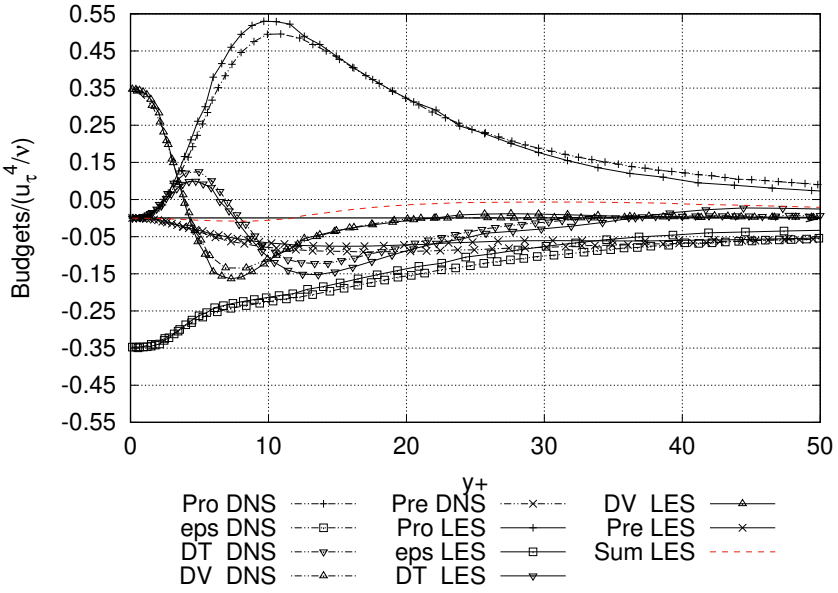


Figure 4: Budget terms of $\widetilde{u'u'}$ for Spalart's turbulent boundary layer Spalart (1988)

Fig. 4 presents the comparison of the production, the turbulent diffusion, the viscous diffusion, the dissipation, and the pressure-velocity correlation budget terms in the incompressible transport equation of the Reynolds stress. The scaling u_τ^4/ν adopted in this case is the same as Spalart's Spalart (1988) paper. An imbalance expressed in Equ. 17 is also shown (in red dashed line) indicating the error in the solution.

$$\text{Imbalance} = \bar{\rho}P_{ij} + \bar{\rho}\Pi_{ij} - \bar{\rho}\epsilon_{ij} + \bar{\rho}M_{ij} + \bar{\rho}D_{ij} - \frac{\partial}{\partial x_k}\left(\widetilde{u}_k\bar{\rho}\tau_{ij}\right) \tag{17}$$

Equ. 17 is obtained by subtracting the left-hand side of Equ.6 and ignoring the time-derivative term. When using LES, the imbalance is a measure of the effect of SGS scales on

the resolved budgets as well as the effect brought by ignoring the time-derivative term. The budget generated from the present LES result matches well with the DNS data in both the viscous layer and log-law region. The maximum imbalance is observed at around $y+ = 25$, with a deviation of less than 0.05 at maximum, which is smaller than the budget error using LES in Vyas'Vyas et al. (2019) study.

Above all, both the cooling film LES results and the procedure generating the Reynolds stress budget terms can be considered trustworthy.

4. Results and discussion

4.1. Structure of the flow mean and instantaneous flow field

Before addressing the structure of the Reynolds stress budgets on the center plane of the flow, it is useful to recall some qualitative features of the mean and instantaneous flow fields. Sections of the flow field at $x/D = 2, 5, 10$ for the fan-shaped film are shown in figure 5a-5e, while the position of these slices are shown in Figure 2(c). The mean flow is shown through contours of the stream-wise velocity component and vectors of the velocities tangential to planes at constant x. The wall jet issuing from the fan-shaped film stays confined in a layer of a modest thickness (comparable to the film diameter) and spreads gradually outwards. As a consequence, the coolant is drawn further towards the wall and outwards as it mixes with the hot stream. The instantaneous contours of streamwise vorticity similarly show a weakly localized set of turbulence structures located in the lower half of the jet and not much stronger than the surrounding boundary layer turbulence.

The development of the wall jet produced by a cylindrical film is shown in Figures 6a-6e. The situation here is considerably different because the jet is confined on the sides

by a pair of counter-rotating vortices. The vortices induce a positive wall-normal velocity on the center plane which lifts coolant away from the wall and favors a rapid mixing of the coolant with the hot stream. Fluid is entrained back into the space between the vortices and the wall on the edge of the jet. Turbulent motion is particularly intense in the area immediately downstream of the film ($x/D = 2$) and gradually dies out further downstream. The area downstream of the film is remarkable because of its anisotropy, as it will be shown in section 4.2. Anisotropy is promoted by the proximity of the wall and of the jet and causes the span-wise velocity fluctuations to be more intense than the other two components.

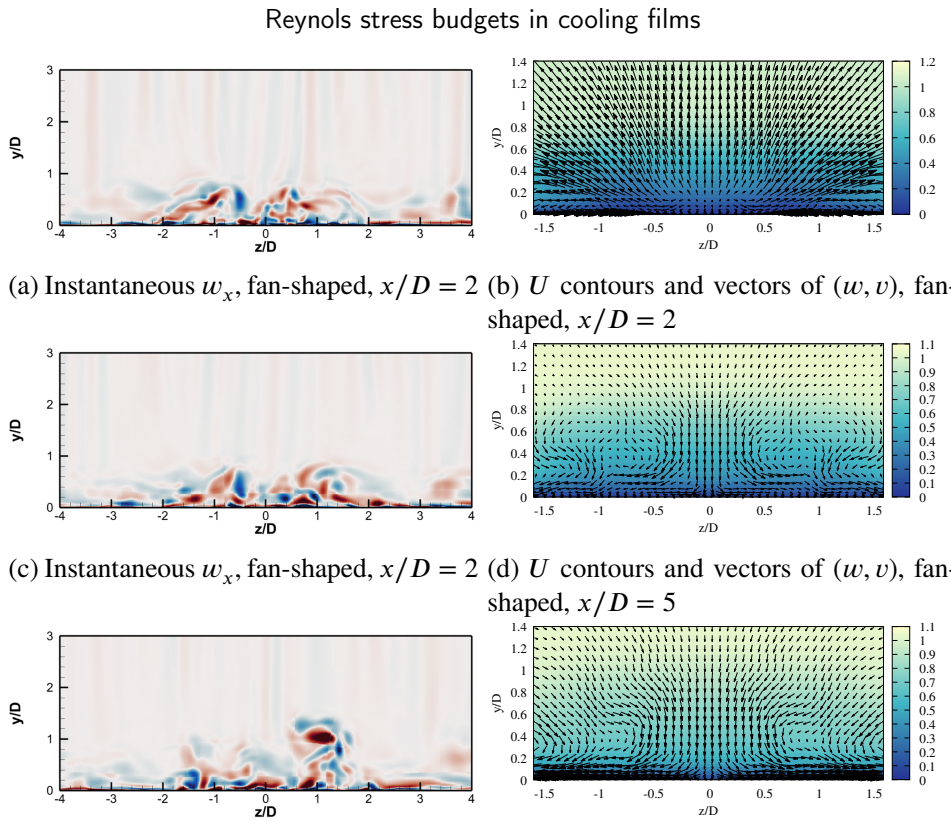
Eddies from the hot mainstream slide under the jet alternatively from the left and the right.

4.2. General balancing of budget terms

The budgets of $\widetilde{u'u'}$, $\widetilde{v'v'}$, $\widetilde{w'w'}$ and $\widetilde{u''v''}$ downstream the film cooling holes of two types are shown in figures 7, 8, 9, 10 respectively, with the position shown as black dash lines in Fig. 2. A two-layer structure in the Reynolds stress budgets is observed which is similar to the one found in the Reynolds stress in Ref. M. Hao (2022). The patterns of Reynolds stresses and corresponding budget terms can be categorized into two regions. One region is near the wall where the general features of the flow resemble a developing boundary layer. Another region is across the jet where the general features of the flow resemble a shear layer.

The budget terms are rescaled using the scaling factor

$$\frac{\Delta u^3}{\delta_{99}} \left(\frac{x}{D}\right)^{-\beta} \tag{18}$$



(a) Instantaneous w_x, fan-shaped, $x/D = 2$

(b) U contours and vectors of (w, v), fan-shaped, $x/D = 2$

(c) Instantaneous w_x, fan-shaped, $x/D = 2$

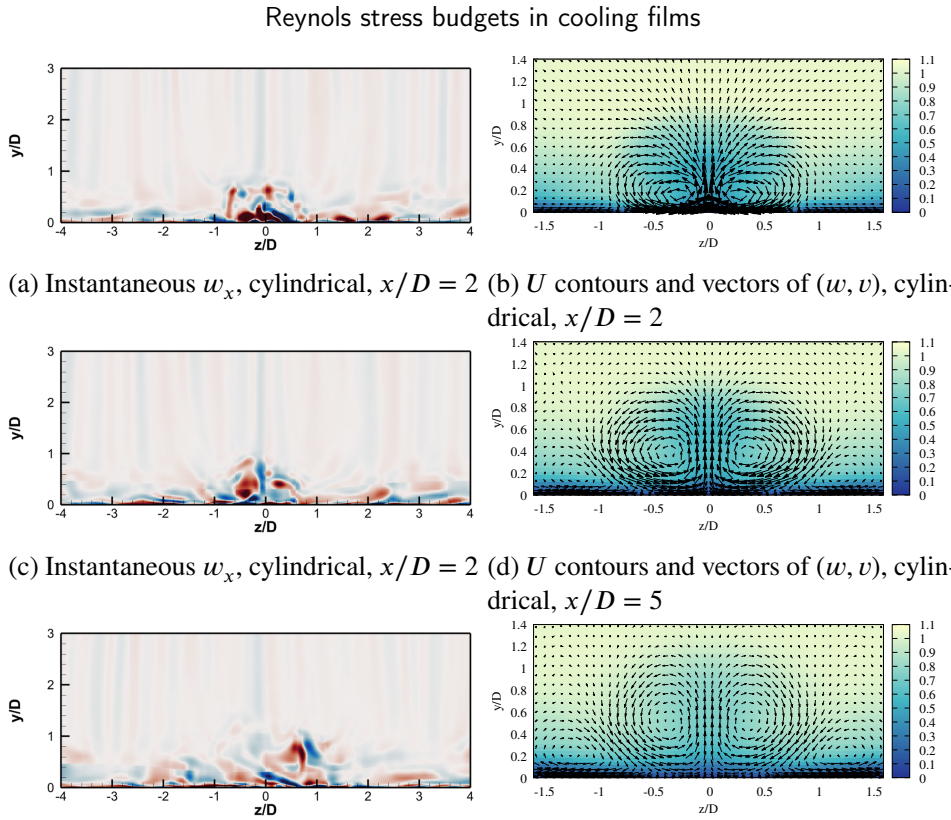
(d) U contours and vectors of (w, v), fan-shaped, $x/D = 5$

(e) Instantaneous w_x, fan-shaped, $x/D = 10$

(f) U contours and vectors of (w, v), fan-shaped, $x/D = 10$

Figure 5: Contours of instantaneous streamwise vorticity(left) and Mean streamwise velocity with mean velocity vectors (right) for fan-shaped films at $x/D = 2$,$x/D = 5$ and $x/D = 10$, at$M = 1.0$

, where, δ_{99} is the height when the velocity arrives at 99% of the freestream velocity, Δu is the the Favre-averaged velocity defect, and β is the exponent factor. The value chosen for β depends on the geometry of the film, but not on the blowing ratios. $\beta = 0.5$ is adopted for the fan-shaped films and $\beta = 0.9$ is adopted for the cylindrical films. The reason for choosing these values is explained in Sec. 5.



(a) Instantaneous w_x, cylindrical, $x/D = 2$

(b) U contours and vectors of (w, v), cylindrical, $x/D = 2$

(c) Instantaneous w_x, cylindrical, $x/D = 2$

(d) U contours and vectors of (w, v), cylindrical, $x/D = 5$

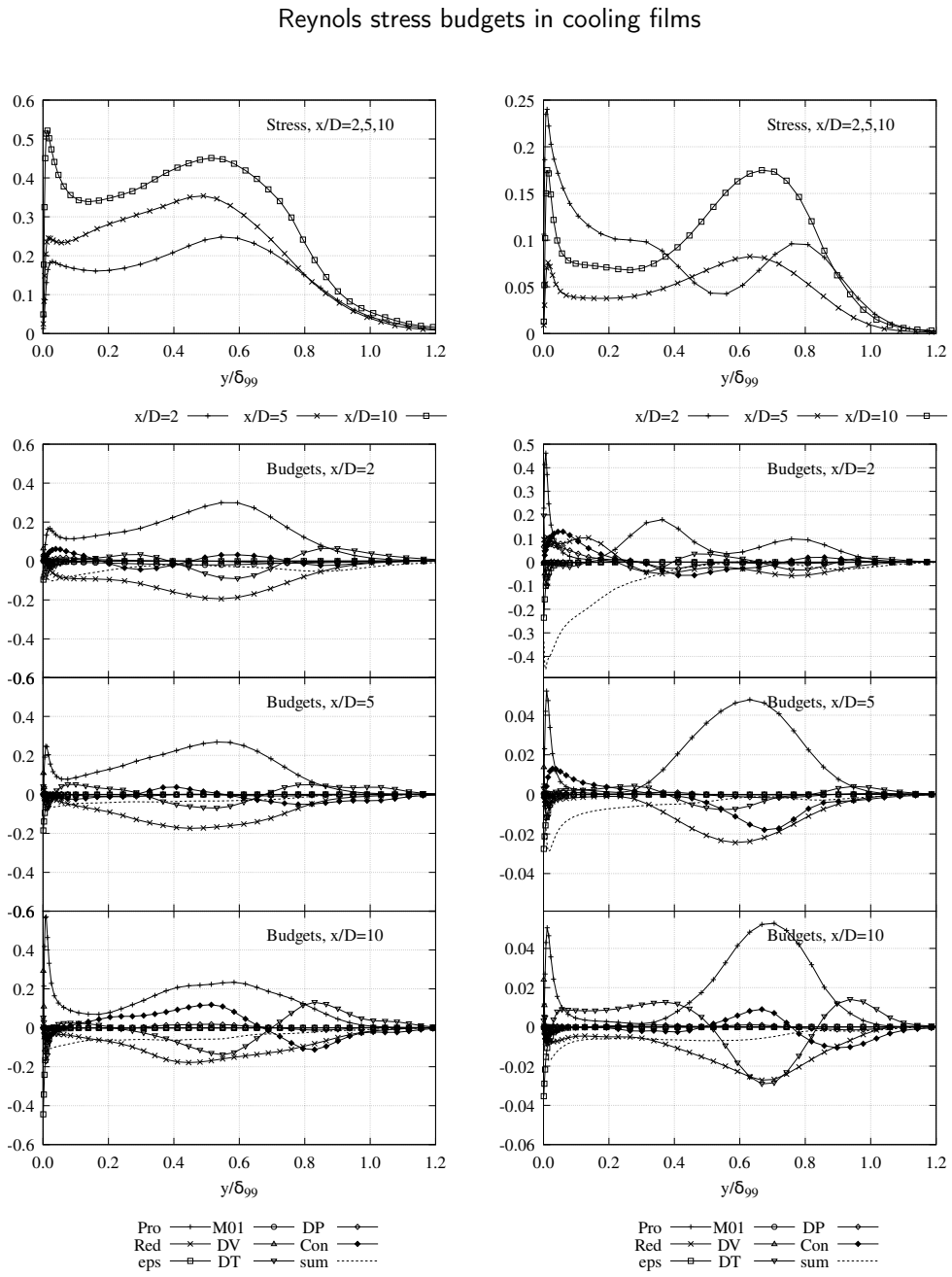
(e) Instantaneous w_x, cylindrical, $x/D = 10$

(f) U contours and vectors of (w, v), cylindrical, $x/D = 10$

Figure 6: Contours of instantaneous streamwise vorticity(left) and Mean streamwise velocity with mean velocity vectors (right) for cylindrical films at $x/D = 2$,$x/D = 5$ and $x/D = 10$, at$M = 1.0$

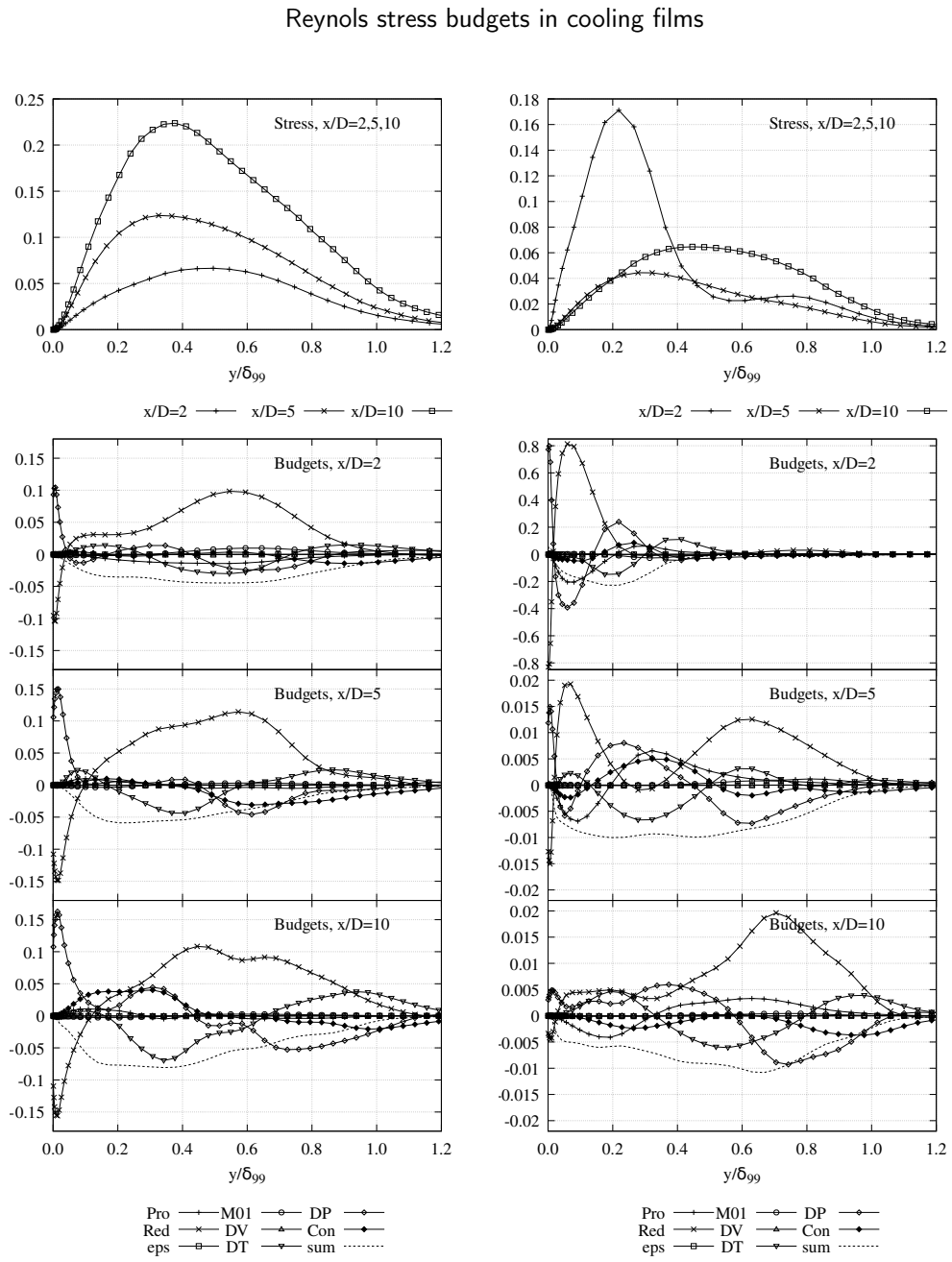
4.2.1. $\widetilde{u''u''}$ budget

In fan-shaped cooling films (shown in Fig. 7b), the main source of $\widetilde{u''u''}$ is the production term (shown in Equation 7) throughout the thickness of the jet layer and the boundary layer. The main sink is the redistribution term 8 away from the wall, whereas near the wall it is the dissipation 9. The convection immediately downstream the film takes energy from the core of the jet to the jet edge and towards the wall. This is because the jet between $y/\delta_{99} = 0, 2 - 0.4$ is diffusing. The convection by the mean flow moves fluid towards the



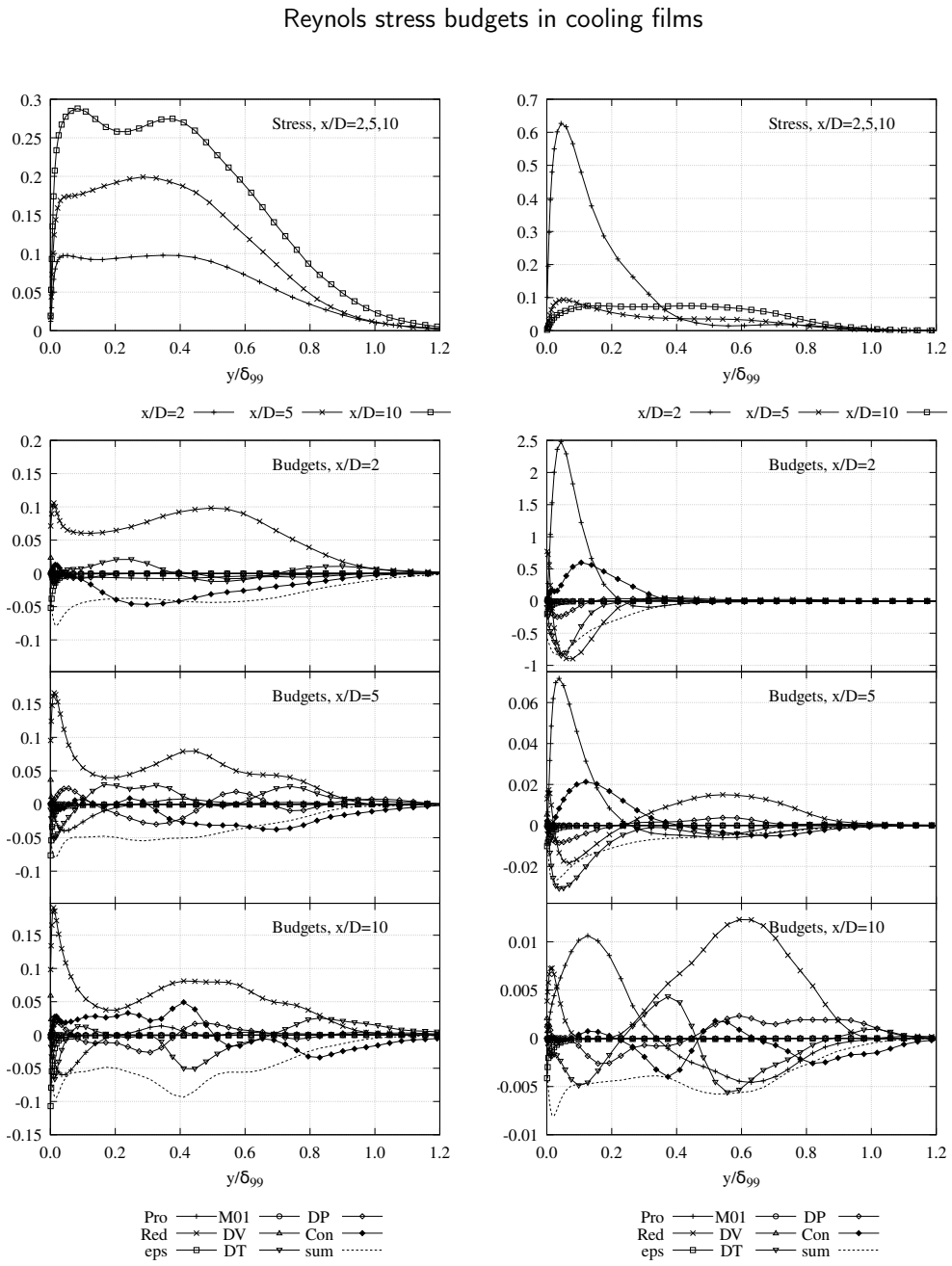
(a) fan-shaped hole (b) cylindrical

Figure 7: Reynolds stress $\widetilde{u''u''}$ and multiple budget terms on $\widetilde{u''u''}$ scaled by $\Delta U^3/\delta_{99}$ for fan-shaped and cylindrical films at $M = 1.0$



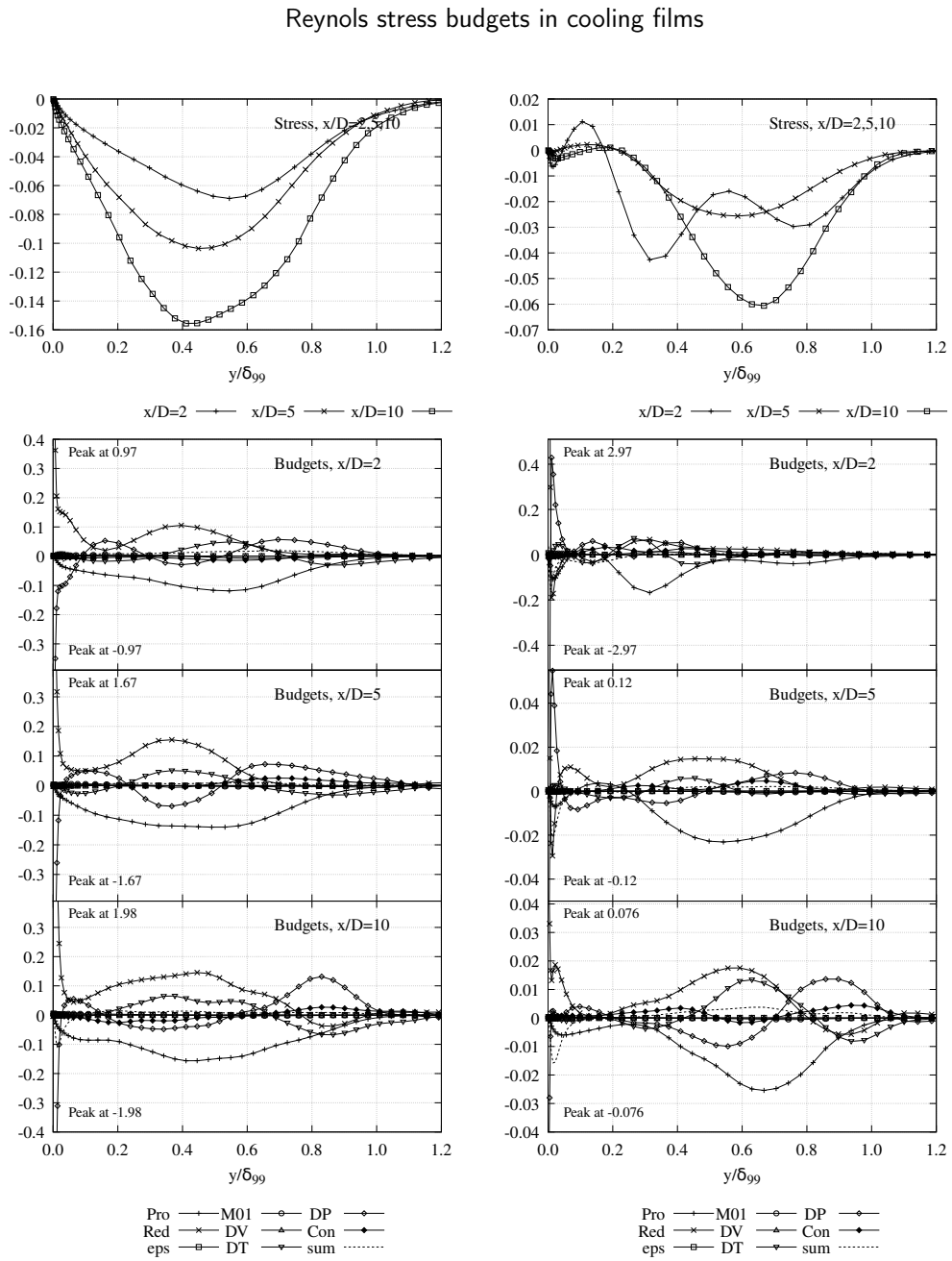
(a) fan-shaped hole (b) cylindrical

Figure 8: Reynolds stress $\widetilde{v''v''}$ and multiple budget terms on $\widetilde{v''v''}$ scaled by $\Delta U^3/\delta_{99}$ for fan-shaped and cylindrical films at $M = 1.0$



(a) fan-shaped hole (b) cylindrical

Figure 9: Reynolds stress $\widetilde{w''w''}$ and multiple budget terms on $\widetilde{w''w''}$ scaled by $\Delta U^3/\delta_{99}$ for fan-shaped and cylindrical films at $M = 1.0$



(a) fan-shaped hole (b) cylindrical

Figure 10: Reynolds stress $\widetilde{u''v''}$ and multiple budget terms on $\widetilde{u''v''}$ scaled by $\Delta U^3/\delta_{99}$ for fan-shaped and cylindrical films at $M = 1.0$

wall and spreads it outwards, as indicated in Sec. 4.1. The turbulent diffusion 13 transfers energy from the local maximum of Reynolds stresses near the wall and near the core of the jet to the edge of the jet and towards the wall, and also towards the region between the core and the wall. The pressure diffusion 14 has two sources, in the proximity of the wall and just below the core of the jet, and two sinks, at the bottom of the Reynolds stress and the top of the jet. The mass flux term 10 is generally very small, except in the proximity of the outlet of the cooling hole. It acts as a sink at the core of the jet.

As the flow travels downstream, the amplitudes of the major sources and sinks away from the wall are preserved by the scaling, shown in Equ. 18. Meanwhile, the amplitudes of the major source and sink terms near the wall grow significantly with the respect to the outer scaling. When the flow arrives $x/D = 10$, the convection and the turbulent diffusion account for a larger proportion of the source and sink far away from the wall. At $y/\delta_{99} = 0.2 - 0.7$, the convection behaves as the source, whereas the turbulent diffusion behaves as the sink. At $y/\delta_{99} = 0.7 - 1.0$, both of these two terms switch their roles as the source and the sink. At $y/\delta_{99} = 0.2 - 1.0$, the production and the redistribution accounted for a smaller proportion of budgets whilst retaining the magnitude of the largest terms. In this sense, the total amplitude of the major sources and sinks far from the wall maintain nearly the same.

Figure. 7b shows the budgets of $\widetilde{u'u'}$ in the cylindrical cooling film. In Figure. 7b, The production is still the major source of $\widetilde{u'u'}$. Compared with the fan-shaped cooling film case, there is a unique feature at $x/D = 2$: apart from the peak in the wall layer, There are two other peaks of production away from the wall, which is an inner peak at $y/\delta = 0.3$ and an outer peak at $y/\delta = 0.8$. This corresponds to the shape of the Reynolds stress $\widetilde{u'u'}$. The

peak at around $y/\delta = 0.3$ is caused by the large flow fluctuations immediately downstream the film described in Sec 4.1. The peak at $y/\delta = 0.7$ is caused by the turbulence at the edge of the jet. The local minimum between these two peaks corresponds to an area of low turbulence intensity in the jet as it emerges from the film. The inner peak of production is balanced by redistribution and turbulent diffusion. For the outer peak, production is balanced in equal measure by convection, dissipation, and redistribution. The level of $\widetilde{u'u'}$ at the local minimum at $y/\delta = 0.5$ between the two peaks is sustained in equal measure by production and turbulent diffusion. The main loss terms are convection and redistribution. There is a region of high turbulent intensity in the proximity of the wall. It is sustained by a sharp peak in the production, balanced by viscous terms of nearly the same amplitude. Between the inner peak and the wall region, turbulence is sustained mainly by convection and redistribution. The budget of $\widetilde{u'u'}$ below $y/\delta_{99} \approx 0.3$ is closed by the viscous terms.

When the jet goes downstream to $x/D = 5$, the outer peak of the production continues to be the main source term around the edge of the jet, while the inner peak disappears. This corresponds to the pattern shown in Fig, 6(a): at $M = 1.0$, there is a region confined in the wall-normal direction by the wall and by the lower side of the jet. This region is also confined in the streamwise direction by the lower side of the jet, see Section 4.1. This is highlighted by the high level of streamwise vorticity fluctuations in Fig. 6(a). At $x/D = 5$, the confinement provided by the jet disappears, because the jet becomes nearly horizontal and gradually mixes with the freestream. Therefore, the Reynolds stresses become more nearly isotropic. This causes the inner peak of the production term of $\widetilde{u'u'}$ to disappear. Both the redistribution and the convection become the major sink terms far away from the wall. The dissipation maintains the sink near the wall.

When it comes to $x/D = 10$, the production maintains the peak of the source. The turbulent diffusion far from the wall becomes the equally major sink together with the redistribution, balancing the peak of the production. The turbulent diffusion at $x/D = 0.1 - 0.4$ grows to the main source, which is balanced by the redistribution and dissipation. The reason why turbulent diffusion behaves as a source below $y/d99 = 0.4$ and as a sink above $y/d99 = 0.4$ is that the flow tries to bring the energy from the peak of Reynolds stress $\widetilde{u'u'}$ at $y/d99 = 0.7$ to around.

4.2.2. $\widetilde{v''v''}$ budget

In Fig. 8a, the main source of $\widetilde{v''v''}$ in the jet layer is the redistribution 8. In the wall layer, $\widetilde{v''v''}$ is sustained mainly by pressure diffusion 14. The main sink of $\widetilde{v''v''}$ is the dissipation 9 in the jet layer, while the main sink of $\widetilde{v''v''}$ near the wall is the pressure redistribution. The convection immediately downstream the hole takes energy from the region around the core of the jet and the top of the jet to the core of the jet and towards the wall. The production immediately downstream of the hole acts as a sink at the core of the jet. Turbulent diffusion transfers energy to the top of the jet and toward the wall. The pressure diffusion has two sources and two sinks. The energy is taken from the region between the near-wall boundary layer and the jet as well as the top edge of the jet towards the jet and to the core of the jet. The mass flux term has one source, at the core of the jet, and one sink, slightly above the wall.

At $x/D = 5$ and $x/D = 10$, the redistribution far from the wall is still the main source. It is balanced by turbulent diffusion, convection, dissipation, and pressure diffusion. Turbulent diffusion behaves as a source beyond the outer edge of the jet.

The main source near the wall is the pressure diffusion, which is balanced by the redistribution term, both of them have a larger amplitude than at $x/D = 2$.

Reynols stress budgets in cooling films

In Fig. 8b, the budget of $\widetilde{v''v''}$ at $x/D = 2$ is dominated by the flow configuration described in the explanation for the budgets of $\widetilde{u''u''}$, see Section 4.1. The flow arrangement results in pronounced peaks in the $\widetilde{v''v''}$ and $\widetilde{w''w''}$ Reynolds stresses immediately below the jet corresponding to a flat area in the $u'u'$ stress. All three Reynolds normal stress terms are depressed in the area corresponding to the core of the jet itself. In this region, the budget of the wall-normal fluctuations is dominated by pressure redistribution, which acts as the main source below $y/\delta_{99} = 0.2$. Here the main loss terms are pressure diffusion and production. Turbulent diffusion acts as usual as a sink in areas of high intensity and as a source in areas of low intensity.

The other main sources of the Reynolds stress $\widetilde{v''v''}$ are the convection, production, and pressure diffusion in the area between $y/\delta_{99} = 0.2$ and $y/\delta_{99} = 0.4$. The main sinks are viscous dissipation and pressure diffusion (in the outer part of the jet). The turbulent diffusion acts to transfer energy away from the peak at $y/\delta_{99} = 0.3$ and towards the wall or towards the edge of the jet. Further downstream after $x/D = 5$ the distribution of $\widetilde{v''v''}$ becomes flatter. The pressure redistribution is still the main source in the outer part of the jet. The arrangement of the flow described in Section 4.1 evolves further and the confinement provided by the jet disappears, partly because of the change in the direction of the jet and partly because of its gradual mixing with the surrounding fluid, as mentioned in the Section 4.1. As a result, the amplitude of the peak in the pressure redistribution below $y/\delta_{99} = 0.2$ is considerably reduced and its amplitude becomes comparable to the magnitude of the largest pressure redistribution in the region at the outer edge of the jet ($y/\delta_{99} \approx 0.6$). Production makes a small contribution to the budget of $\widetilde{v''v''}$ around $y/\delta_{99} \approx 0.4$ at $x/D = 5$, and around $y/\delta_{99} \approx 0.6$ at $x/D = 10$. Away from the wall, pressure redistribution and production are balanced by pressure diffusion, convection, and dissipation. The turbulent

diffusion moves energy away from the broad peak at $y/\delta_{99} = 0.4$ towards the periphery of the jet.

4.2.3. $\widetilde{w''w''}$ budget

In Fig. 9a, The main source of $\widetilde{w''w''}$ both in the jet layer and near the wall is the redistribution and the main sink is dissipation. The convection immediately downstream (at $x/D = 2$) the hole takes energy from the wall to the core of the jet. Away from the hole exit (at $x/D = 5, 10$), energy is taken from the region between the wall and the top of the jet to the core of the jet and towards the wall. The production immediately downstream of the hole has one sink and one source. Energy is transferred to the region beneath the jet towards the wall and to the core of the jet. The turbulent diffusion gradually takes the energy from the core of the jet to its periphery. The pressure diffusion has two sources and two sinks. The energy is taken from the near-wall region and the core of the jet to the region between them and to the edge of the jet. The mass flux term of $\widetilde{w''w''}$ is much smaller and of a lower order of values than the mass flux term of $\widetilde{u''u''}$ and $\widetilde{v''v''}$.

In Fig. 9b, the budgets of $\widetilde{w''w''}$ for the cylindrical film immediately downstream of the film is entirely dominated by the large spanwise fluctuations described in Section 4.1. Closed to the cooling hole, the fluctuations in eddies confined between the jet and the wall give rise to very large production levels below $y/\delta_{99} = 0.2$. These high production levels are the direct result of the unsteady flow pattern and become manifested in the $\widetilde{w''w''}$ budget through the component $\widetilde{w''w''}\frac{\partial \overline{w}}{\partial z}$ of the budget term. The energy transferred to the turbulent motion through the production term of $\widetilde{w''w''}$ is then redistributed to the remaining two Reynolds normal stresses by the pressure redistribution terms, as seen in the previous discussion on budgets of $\widetilde{u''u''}$ and $\widetilde{v''v''}$. The other main contribution to the budget of $\widetilde{w''w''}$ immediately downstream of the cylindrical cooling film is the convection,

which is due to turbulence from the boundary layer and from the front part of the jet being convected towards the rear of the jet itself. These contributions are balanced by pressure redistribution, dissipation, and turbulent diffusion. As the jet evolves downstream to $x/D = 5$, the production is reduced but is still the dominant term below the jet. In the upper part of the jet, pressure redistribution acts as a source for the $\widetilde{w''w''}$ budget, where it contributes energy extracted from the mean flow by the $\widetilde{u''v''}\frac{\partial \overline{u}}{\partial y}$ production term in the $u'u'$ budget. Below $y/\delta_{99} \approx 0.3$, the pressure redistribution acts as a sink for $\widetilde{w''w''}$ and it sustains the $\widetilde{u''u''}$ and $\widetilde{v''v''}$ fluctuations through energy extracted from the mean flow by the $\widetilde{w''w''}\frac{\partial \overline{w}}{\partial z}$ term of production. The remaining sinks for $\widetilde{w''w''}$ below $y/\delta_{99} \approx 0.3$ are the dissipation, turbulent diffusion, and pressure diffusion.

At $x/D = 10$ the production peak at $y/\delta_{99} = 0.2$ is reduced further and has a similar magnitude to the pressure redistribution term further away from the wall. The production of $w'w'$ is composed of three terms: $\widetilde{u''w''}\frac{\partial \overline{w}}{\partial x}$, $\widetilde{v''w''}\frac{\partial \overline{w}}{\partial y}$, $\widetilde{w''w''}\frac{\partial \overline{w}}{\partial z}$. Of these, only $\widetilde{w''w''}\frac{\partial \overline{w}}{\partial z}$ is non-zero on the $z = 0$ plane. The remaining two are zero on the centerline because $\widetilde{u''w''}$, $\widetilde{v''w''}$, $\frac{\partial \overline{w}}{\partial x}$, $\frac{\partial \overline{w}}{\partial y}$ are all zero. The change in sign of production around $y/\delta_{99} = 0.3$ is due to $\frac{\partial \overline{w}}{\partial z}$ changing sign between the part of the flow below and above the cores of the counter-rotating vortex pair. This in turn is due to the mean flow pattern depicted in Figure 6f.

4.2.4. $\widetilde{u''v''}$ budget:

Fig. 10a shows the budgets of the Reynolds shear stress $\widetilde{u''v''}$. Because the Reynolds shear stress $\widetilde{u''v''}$ is negative, the positive terms in this group of figures are the loss, and the negative terms are the gain. At $x/D = 2$ the budget of $\widetilde{u''v''}$ in the jet layer is dominated by the production, which acts as a source, and by the redistribution, which acts as a sink. In the proximity of the wall, the dominant terms are pressure diffusion, which acts as a source,

and redistribution which acts as a sink. The turbulent diffusion acts by transferring the stress from the wall and from the region above the core of the jet to the region between them.

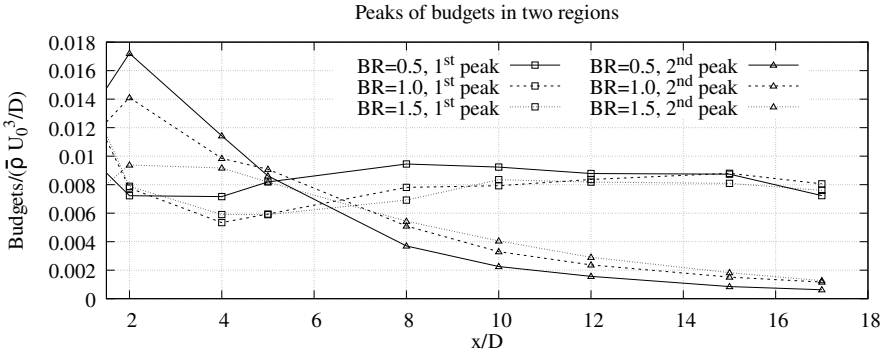
For the fan-shaped film, at $x/D = 5$, the general shape of the amplitudes are similar. Both the production and pressure diffusion grow with respect to their values at $x/D = 2$. They are balanced by the increasing redistribution and the turbulent diffusion below $y/\delta_{99} = 0.6$. Above $y/\delta_{99} = 0.6$, the structure of the budget remains the same, with the pressure diffusion as the sink balancing the production and turbulent diffusion.

At $x/D = 10$, the dominance of the redistribution in the wall-normal direction is extended to $y/\delta_{99} = 0.7$. At $y/\delta_{99} = 0.8$, the pressure diffusion grows to a peak, which is balanced by turbulent diffusion, redistribution, and production.

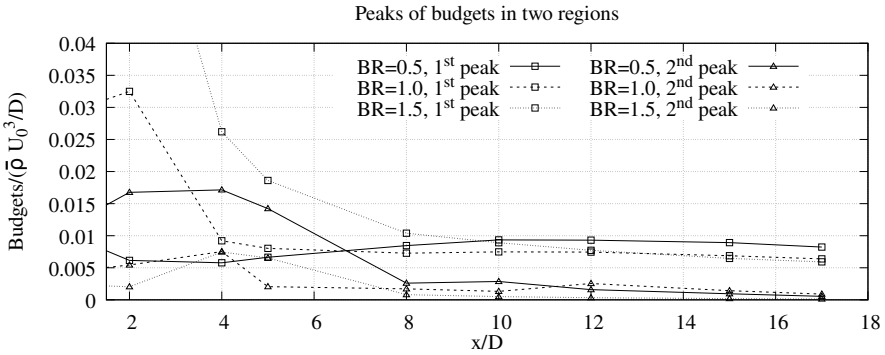
The distribution of the Reynolds stress $\widetilde{u''v''}$ in the cylindrical film case also shows the mark of the area of low turbulence intensities at the core of the jet in the profiles at $x/D = 2$. This area appears as a local dip in the magnitude of $\widetilde{u''v''}$ in the $x/D = 2$ profile around $y/\delta_{99} = 0.5$. The Reynolds stress budget at this location is dominated by the production term, which has local maxima at $y/\delta_{99} \approx 0.3$ and $y/\delta_{99} \approx 0.8$. These locations correspond to the lower and upper edges of the jet, respectively. The budget of $\widetilde{u''v''}$ is balanced by pressure redistribution, pressure diffusion, and turbulent diffusion. In the budgets at $x/D = 5$ and $x/D = 10$, the peculiarities of the flow immediately downstream of the film are somewhat reduced and the budgets display a general structure similar to the one described for the fan-shaped films. The main difference between the cylindrical film and the fan-shape film is that the budgets of the Reynolds stress in the former display reduced magnitudes of all terms in the area between the wall layer and $y/\delta_{99} \approx 0.3$. This is a consequence of the structure of the flow in the cylindrical film which has a region of lower turbulence intensities between the jet and the wall.

Reynols stress budgets in cooling films

4.3. Downstream development



(a) Fan-shaped hole



(b) Cylindrical hole

Figure 11: Streamwise development of the peaks in two regions of Pr_{uu}

During the discussion on the balancing of different budget terms in Section 4.2, there are always at least two peaks in the production term of $\widetilde{u''u''}$. Of these, one is near the wall, the other is near the upper edge of the wall jet[1]. Figure 11 shows the streamwise evolution of these two peaks in the near-wall region (the first peak) and the jet region (the second peak). In the fan-shaped case, the first peak has a nearly constant amplitude downstream of the hole, whereas the second peak decays monotonically. This is because the first peak corresponds

[1] In one cylindrical-film case, a third peak appears but it will not be discussed further in this section.

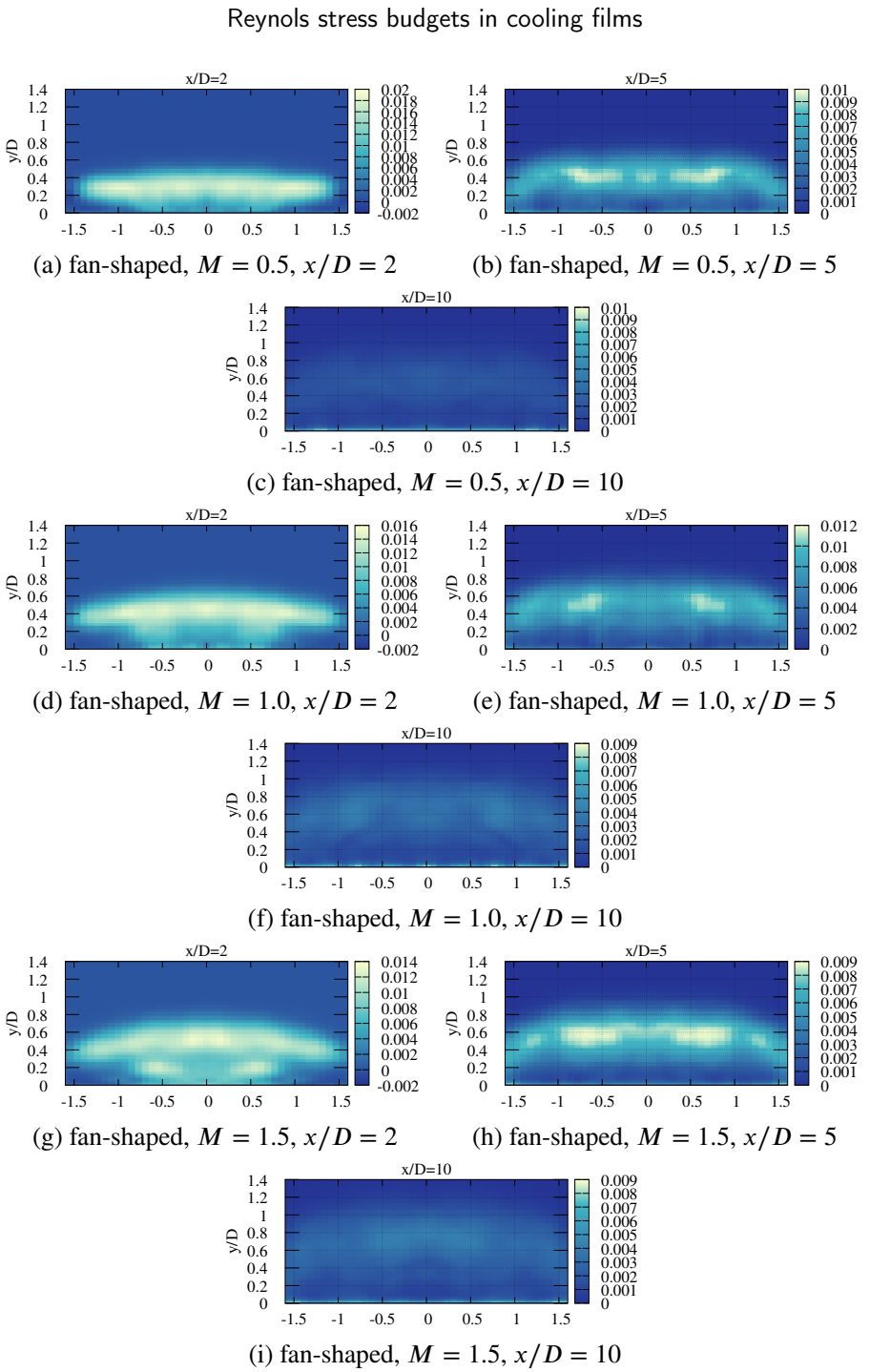
to the largest production in a developing boundary layer, and u_τ changes very little when the jet flows downstream. The second peak corresponds to the largest production in a free-shear layer and scales approximately with the velocity defect ΔU and the distance downstream of the film, as hinted in section 4.2. ΔU decreases as the jet develops downstream and mixes with the mainstream. At a position between $x/D = 5$ and $x/D = 7$, the two peaks overlap. At this position, the production of the $\widetilde{u''u''}$ Reynolds normal stress takes place at the same rate in the inner and outer parts of the wall jets.

In the cylindrical case, the first peak has a nearly constant amplitude only in the far field, but in the near field, from $M = 0.5$ to $M = 1.5$, they decay at a rate related to the blowing ratio. The drop in the near field at M=1.0 and 1.5 is caused by the jet lifting off the wall, while at $M = 0.5$ the jet is still attached and behaves in a way not dissimilar from the jet of a fan-shaped film. The second peaks in the far field of the cylindrical films have similar changes but with a slower rate of change compared to those in the fan-shaped case. By contrast, the second peaks in the near-field of the cylindrical cooling film have different behaviors: they decay monotonically.

The variation of the peak production on the centerline shown in Figure 11 is in reality part of a more complex three-dimensional pattern.

Distributions of production at several streamwise stations and for several blowing ratios are shown for both fan-shaped and cylindrical films in Figures 12 and 13. For the fan-shaped film, it can be seen that the production term is distributed along the upper edge of the jet, which appears as a relatively flat region. Small localized peaks are visible in areas where the jet curves towards the wall at its edges. For cylindrical films, the production is also distributed around the edge of the film, but this is an annular area. Furthermore, whereas the downstream evolution of the production shows activity only around the edge of the jet,

and essentially no production at the core, at $x/D = 2$, the attached cylindrical film cases show two distinct areas of activity. One is located around the outer edge of the jet, the other around the boundary between the jet and an area of high turbulence located on the leeward side of the film.



(a) fan-shaped, $M = 0.5$, $x/D = 2$ (b) fan-shaped, $M = 0.5$, $x/D = 5$

(c) fan-shaped, $M = 0.5$, $x/D = 10$

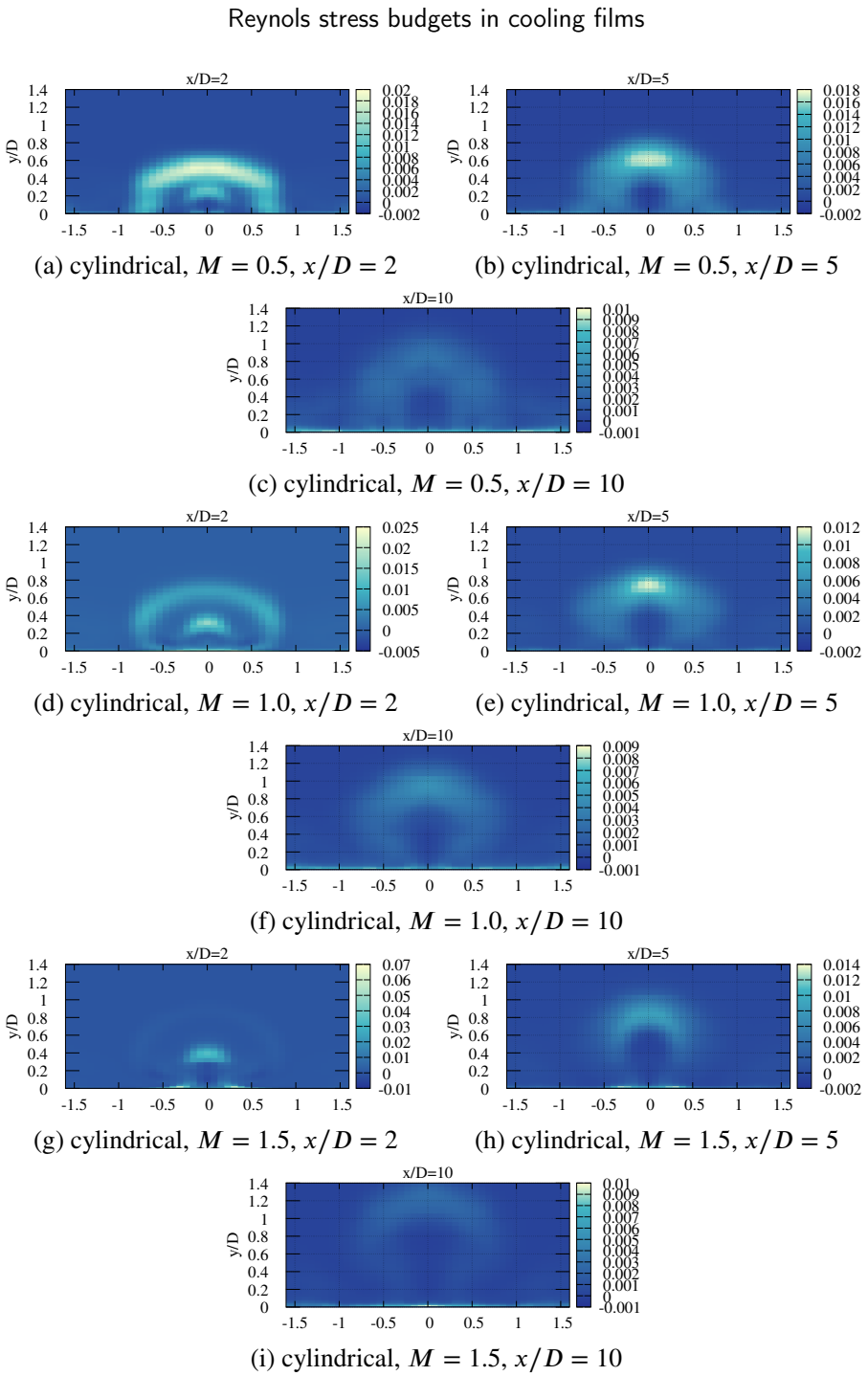
(d) fan-shaped, $M = 1.0$, $x/D = 2$ (e) fan-shaped, $M = 1.0$, $x/D = 5$

(f) fan-shaped, $M = 1.0$, $x/D = 10$

(g) fan-shaped, $M = 1.5$, $x/D = 2$ (h) fan-shaped, $M = 1.5$, $x/D = 5$

(i) fan-shaped, $M = 1.5$, $x/D = 10$

Figure 12: Contours of Pr_{uu} for fan-shaped films at $x/D = 2$,$x/D = 5$ and $x/D = 10$



(a) cylindrical, $M = 0.5$, $x/D = 2$ (b) cylindrical, $M = 0.5$, $x/D = 5$

(c) cylindrical, $M = 0.5$, $x/D = 10$

(d) cylindrical, $M = 1.0$, $x/D = 2$ (e) cylindrical, $M = 1.0$, $x/D = 5$

(f) cylindrical, $M = 1.0$, $x/D = 10$

(g) cylindrical, $M = 1.5$, $x/D = 2$ (h) cylindrical, $M = 1.5$, $x/D = 5$

(i) cylindrical, $M = 1.5$, $x/D = 10$

Figure 13: Contours of Pr_{uu} for cylindrical films at $x/D = 2$,$x/D = 5$ and $x/D = 10$

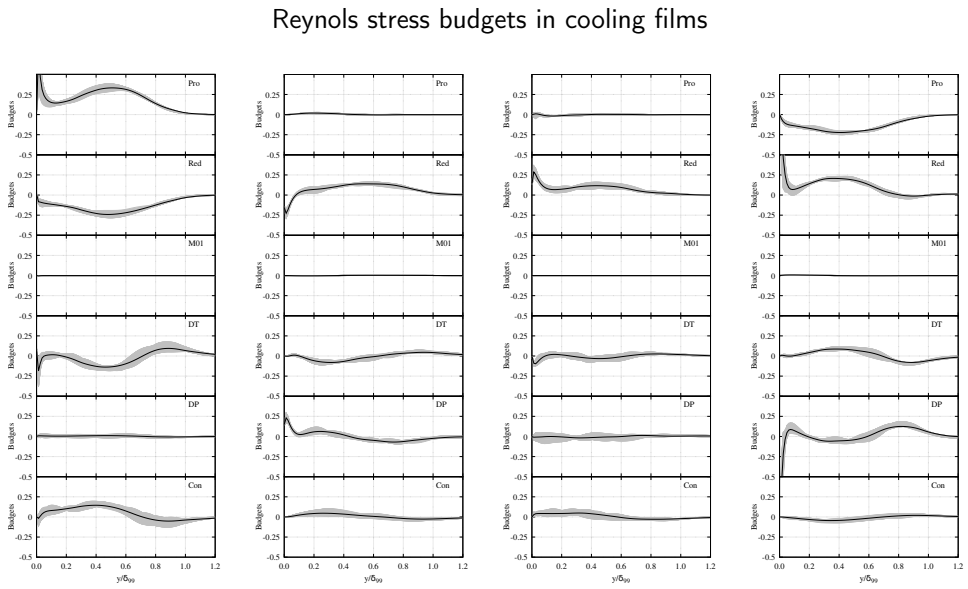


Figure 14: Budget terms scaled by $(\Delta U^3/((x/D)^\beta \delta_{99})$ for fan-shaped film at $M = 0.5$. Grey lines: multiple curves on streamwise positions between $x/D = 5$ and $x/D = 15$, Black lines: Master curve (Average of multiple grey curves). Four columns from left to right are budgets of $\widetilde{u'u'}$, $\widetilde{v'v'}$, $\widetilde{w'w'}$, $\widetilde{u'v'}$. For each column from the top to bottom are corresponding production, redistribution, mass flux term, turbulent diffusion, pressure diffusion, convection.

5. Universal scaling

The self-similarity properties that emerge in the wall-normal profiles of mean quantities and Reynolds stresses are pointed out, as shown by M. Hao (2022). These self-similarity properties cause graphs of quantities such as mean velocities or turbulence intensities taken at different stream-wise positions to collapse onto each other if appropriately rescaled. The scaling quantities are local quantities and are taken as the thickness of the jet layer and the velocity deficit at a suitably defined location across the layer itself. For films with the attached flow, this location is half of the jet layer thickness; the corresponding velocity scale is the velocity defect evaluated at the half-thickness point. For films with the lifted flow, this location is the position of the largest velocity defect in the upper part of the film. In the latter case, the velocity scale is the largest velocity defect in the upper part of the

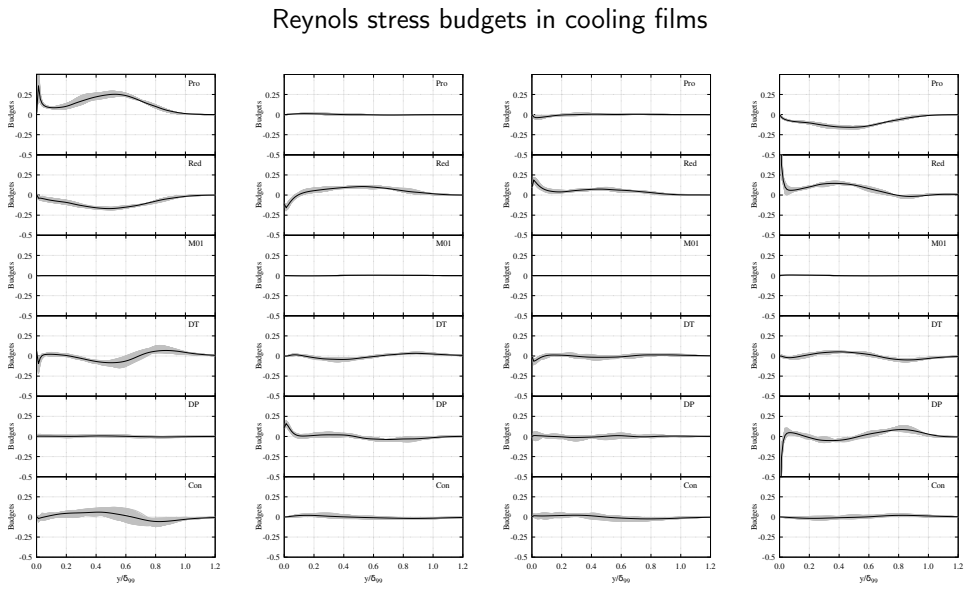


Figure 15: Budget terms scaled by $(\Delta U^3/((x/D)^\beta \delta_{99})$ for fan-shaped film at $M = 1.0$. Grey lines: multiple curves on streamwise positions between $x/D = 5$ and $x/D = 15$, Black lines: Master curve (Average of multiple grey curves). Four columns from left to right are budgets of $\widetilde{u'u'}$, $\widetilde{v'v'}$, $\widetilde{w'w'}$, $\widetilde{u'v'}$. For each column from the top to bottom are corresponding production, redistribution, mass flux term, turbulent diffusion, pressure diffusion, and convection.

film. This scaling, which is based on the integral scales, applies to the outer part of the wall jet, whereas the inner part of the wall jet follows the ordinary wall scaling, albeit with local deviations downstream of the film due to local phenomena like reattachment or adverse pressure gradients.

In this section, it is shown that the external scaling applies not only to the Reynolds stresses but also to their budgets. To this effect, the budget terms taken at locations between x/D=5 and x/D=16 are shown in Figure 14-19. The positions of these lines are indicated by the blue slice as shown in Fig. 2(c). The budget terms are shown for each blowing ratio for the two types of cooling holes. The budget terms are rescaled using the scaling factor $\frac{\Delta u^3}{\delta_{99}} \left(\frac{x}{D}\right)^{-\beta}$ introduced in section 4.2. The wall-normal distances away from the wall are

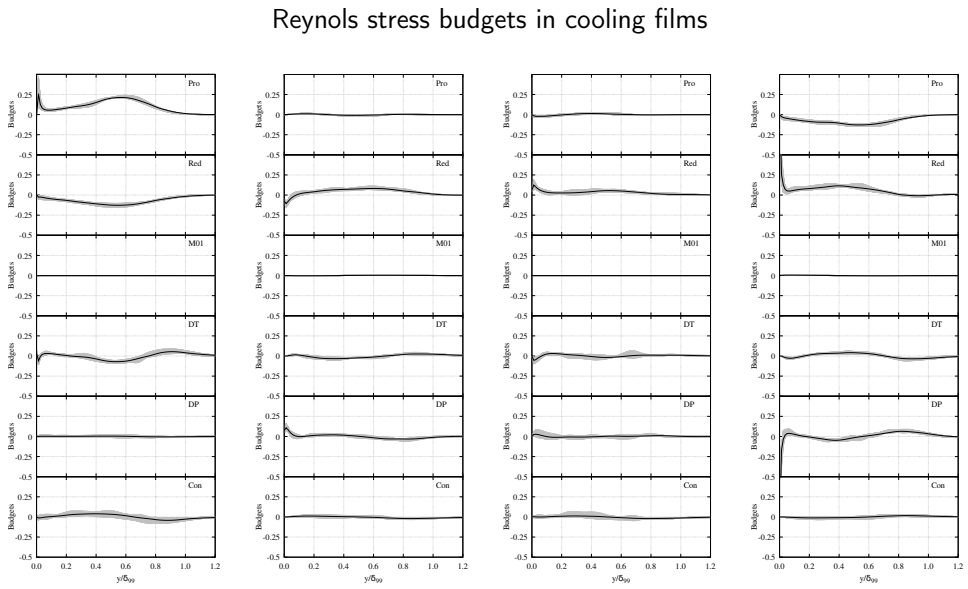


Figure 16: Budget terms scaled by $(\Delta U^3/((x/D)^\beta \delta_{99})$ for fan-shaped film at $M = 1.5$. Grey lines: multiple curves on streamwise positions between $x/D = 5$ and $x/D = 15$, Black lines: Master curve (Average of multiple grey curves). Four columns from left to right are budgets of $\widetilde{u'u'}$, $\widetilde{v'v'}$, $\widetilde{w'w'}$, $\widetilde{u'v'}$. For each column from the top to bottom are corresponding production, redistribution, mass flux term, turbulent diffusion, pressure diffusion, and convection.

scaled by the transformation

$$y \rightarrow \eta = \frac{\delta_{99} - y}{\delta} \tag{19}$$

where δ is δ_{99} for attached cases, or the distance of the maximum velocity defect from the boundary layer edge for lifted cases. All quantities are evaluated on the plane $z = 0$.

It can be seen from the results in Figures 14-19 that the scaling factors above are sufficient to make budget terms collapse into narrow regions. The general trend of the budget terms is easily identified and is shown as master curves in Figures 14- 19. The master curves are obtained by averaging budget terms from all streamwise positions in the wall jet far field *at the same nondimensional distance* η from the wall. The shape of the

7.3 | Technical Paper 6

Heat transfer and turbulent heat flux budgets in cooling films

Muting Hao[a,*,1], Luca di Mare[a,2]

[a]*Oxford Thermofluids Institute, University of Oxford, Southwell Building, Osney Mead, Oxford, OX2 0ES, , United Kingdom*

ARTICLE INFO

Keywords:
Film cooling
Turbulent heat flux
Transport equation
Self-similarity
Gas turbines
Large eddy simulation
Turbulent heat flux budgets
Fan-shaped holes

ABSTRACT

Statistics from large-eddy-simulation (LES) of cooling films with different cooling holes are used to evaluate budgets in the transport equation of turbulent heat flux. The capability of LES has been assessed by comparing simulated results with experimental data, while the correctness of the procedure generating turbulent heat flux budgets has been examined on a turbulent boundary layer. The mechanism of heat transfer has been preliminarily studied throughout the three-dimensional flow field at different blowing ratios using a general outer scaling, to recognize specific regions with corresponding heat transfer patterns. A compressible version of budget terms in the transport equation of turbulent heat flux is then explored to show the thermal behavior of flow downstream from the cooling film holes. Characteristics of each budget term are presented in a defect scaling consistent with the scaling suitable for Reynolds stresses and Reynolds stress budgets. Furthermore, these budget terms are compared among an array of different cooling hole shapes combined with different blowing ratios to explore self-similarity. Results show that the dynamic balance of all budget terms is significantly influenced by the cooling hole shape, while each turbulent heat flux budget term may scale with the velocity defect, temperature deficit, and the normalized streamwise distance to the power of an exponent dependent on the hole shape.

1. Introduction

The high-fidelity of prediction for film cooling has been pursued in recent years when higher and higher operating temperatures are being achieved in hot gas turbine components.

*Corresponding author

The interest in this is warranted because the thermodynamic cost of generating a cooling stream is not monotonic due to the unsteady nature of three-dimensional film jets and a better understanding of flow and heat transfer mechanisms can help film cooling designs. While the accurate prediction of film cooling flows can refer to Large Eddy Simulation (LES) and Direct Numerical Simulation (DNS) that have been developed as increasingly precise simulation tools for film cooling studies, Reynolds-averaged Navier-Stokes (RANS) methods remain the preferred choice for designers due to their lower computational cost. However, the accuracy of RANS for the prediction of film cooling performance is hindered by its turbulence models that introduce inaccuracies in terms of both Reynolds stresses and turbulent heat fluxes. Ellis (2020) presented the RANS results with very little lateral coolant spread and the coolant penetrates further downstream in the streamwise slices. They found a RANS overpredicting the turbulent heat flux as twice the value obtained in LES corresponds to an overprediction of the adiabatic cooling effectiveness of up to 45% on the centerline.

At the early stage, turbulent heat fluxes in the compressible version of transport equations are modeled by the analogy between turbulent momentum and heat transport, which is known as the strong Reynolds analogy, see Morkovin (1962). The easiest subset of these is using the Boussinesq hypothesis via assumptions, for example, of constant turbulent Prandtl numbers. The analogy is not valid in complex flows such as flows with varying pressure gradients, or shock turbulent boundary layer interactions because the turbulent Prandtl numbers cannot be preliminarily prescribed in such flows (Ribault and Friedrich (1997)). This is also the case for film cooling flows. In order to accurately predict turbulent heat fluxes, the transport equation of turbulent heat fluxes should be solved or modeled. The budgets in these transport equations of turbulent heat fluxes should also be studied considering the following reasons.

Heat transfer and Turbulent heat flux budgets in cooling films

First, detailed budgets in the transport equation of turbulent heat flux are critical for developing existing turbulent heat flux models. There have been a few studies regarding the modeling of turbulent heat flux for shear flows. In the 90s, turbulent heat flux models (Ribault and Friedrich (1997)) have been proposed for statistically two-dimensional situations of compressible flows via comparing budgets of transport equations with those of modeled equations. The models developed in this method perform better than algebraic models. Turbulent heat flux models were then developed for three-dimensional situations in the 21^{st} century. Bowersox (2009) proposed an algebraic energy flux model by truncating the compressible turbulent heat flux transport equations. 20 % improvement was shown in the temperature predictions for turbulent boundary layers with moderately cooled walls. The use of Bowersox's AEF model (see Bowersox (2009)) has been extended to higher Mach numbers, see Huang, Nicholson, Duan, Choudhari and Bowersox (2020), and to favorable pressure gradients, see Nicholson, Huang, Duan and Choudhari (2021); Nicholson, Huang, Duan, Choudhari, Morreale and Bowersox (2022).

Second, examining the budget terms can illuminate fluid physics. A few existing modeling assumptions are assessed by Nicholson et al. (2021). They have shown that the Boussinesq assumption results in accurate predictions of the Reynolds shear stress but a loss of accuracy in Reynolds normal stresses. The constant turbulent Prandtl number model leads to reasonable wall-normal turbulent heat flux, but a loss of accuracy in streamwise turbulent heat flux, see Nicholson et al. (2021); Ellis (2020).

For film cooling flows, the analysis of budget terms can provide implications for developing higher-fidelity models, which will finally benefit the understanding of flow mechanisms in film cooling and cooling film designs. However, there has been no literature referring to this area so far to the authors' knowledge. Although Muldoon and Acharya (2006) assessed budget terms

of $k-\epsilon$ equations in cooling films by using DNS, they have not mentioned the characteristics of turbulent heat flux, and they ignored the effect of the compressibility on their budget terms.

In addition, scaling methods are needed for presenting characteristics of turbulent heat flux and turbulent heat flux budgets. These scaling methods are usually designed based on the universal scaling laws for the turbulent velocity turbulent temperature or mean velocity mean temperature. An attempt for a suitable scaling method is then first given among the different methods of such universal scaling laws that have been studied in the context of compressible flows. Considering the wall effect, the simplest method of scaling is the standard wall normalization, with the scaled lengthscale $y+ = y/\delta_v$ and the scaled velocity $\bar{u}^+ = \bar{u}/u_\tau$. Here the viscous lengthscale is $\delta_v = \nu_w/u_\tau$, ν is the kinematic viscosity and $u_\tau = \sqrt{\tau_w/\rho_w}$ is the friction velocity. The standard normalization, however, does not perform well in the log-law region. This is because the use of u^+ includes the assumption $\bar{\rho} = \rho_w$ which is not satisfied in the region beyond the wall. The van Driest density-weighted transformation is widely used in incompressible flows and is a base to be developed for compressible flows. It shows the good collapse of velocity profiles $u^+_{vd} = \int_0^{\bar{u}^+} \left(\bar{\rho}/\rho_w\right)^{1/2} d\bar{u}^+$ of an adiabatic turbulent bounded flow when the compressibility effect is negligible. Foysi, SARKAR and FRIEDRICH (2004) adopted y/h (h is the half-channel height) in the outer scaling region of a supersonic channel flow with isothermal cooled walls. Huang, Coleman and Bradshaw (1995) proposed a semi-local viscous length $\delta_{v^*} = \bar{\mu}/\bar{\rho}u_{\tau^*}$ for a wall-normal non-dimensional definition $y^* = y/\delta_{v^*}$ and a semi-local friction velocity $u_{\tau^*} = \sqrt{\tau_w/\bar{\rho}}$ which collapse better for local rather than wall properties. For an isothermal compressible channel flow, their y^* presents better collapses than yu_τ/ν_w. $yu_\tau/\bar{\nu}$ and $yu_{\tau^*}/\bar{\nu}$. Brun, Boiarciuc, Haberkorn and Comte (2008) devised an integral length $y^+_c = \int_0^{y^+} \left(\frac{\mu_w}{\mu}\right) dy^+$ with a strong near-wall temperature gradient considered. A van Driest transformation $\bar{u}^+_c = \int_0^{\bar{u}^+} \left(\frac{y^+}{y^{c+}}\right)\left(\frac{\mu_w}{\bar{\mu}}\right)\sqrt{\frac{\bar{\rho}}{\rho_w}} d\bar{u}^+$ is also devised to account for

the effect of density and viscosity simultaneously near the wall. This method was proved to help collapse in the viscous sub-layer of isothermal cooled channels for a wide range of Mach numbers. Zhang, Bi, Hussain, Li and She (2012) developed a Mach-invariant scaling $\widetilde{u}^+_{MI} = \int_0^{\widetilde{u}^+} g\left(\frac{\mu_w}{\bar{\mu}}\right) d\widetilde{u}^+$ for compressible turbulent boundary layers via a viscosity-weighted transformation. Compressible turbulent boundary layers of $Ma < 6$ with the adiabatic wall condition were used to validate their scaling method.

Shadloo, Hadjadj and Hussain (2015) expressed the temperature transformation $T^+_{vd} = \int_0^{\bar{T}^+_t} \left(T_w/\bar{T}\right)^{1/2} d\bar{T}^+_t$ by integrating the total temperature distribution through the boundary layer so that it resembles the van Driest velocity profiles $u^+_{vd} = \int_0^{\bar{u}^+} \left(\bar{\rho}/\rho_w\right)^{1/2} d\bar{u}^+$. They showed a good agreement of mean velocity profiles with the incompressible DNS data of Schlatter, Örlü, Li, Brethouwer, Fransson, Johansson, Alfredsson and Henningson (2009) in sub-layer and log-law regions for adiabatic and heating wall cases. However, for cooling isothermal wall boundary layers, both the mean velocity profile and the total temperature profile present deviations, similarly with Duan and Martín (2011). Shadloo et al. (2015) shows that the semi-local length scaling matches better the position of peaks in TKE budgets when comparing turbulent boundary layers with different heated walls, but cannot give a complete collapse of TKE budget terms. Nicholson et al. (2022) presented that the semi-local scaling does not work for collapsing the Reynolds stress and TKE budget terms on hypersonic turbulent boundary layers with zero pressure gradient or favorable pressure gradients. Morkovin (1962)'s hypothesis does not work in such cases. New scaling methods are needed to be devised to collapse and heat flux statistics.

Furthermore, although there are studies on the heat transfer characteristics in turbulent boundary layers (see Vyas, Yoder and Gaitonde (2019); Nicholson et al. (2022); Shadloo, Hadjadj and Hussain (2017); Shadloo et al. (2015)), channels (see Flageul, Benhamadouche,

Lamballais and Laurence (2015)) or applications with practical significance Kawata and Tsukahara (2022),(see Miura, MATSUBARA and SAKURAI (2012), most of them focus on the near-wall flows only. The scaling devised for studying the heat transfer characteristics in their cases is also based on the near-wall flows. For film cooling, Hao and di Mare (2022) has mentioned that the main statistics downstream from the wall is a two-layer structure, composed of a layer close to the turbulent boundary layer in the near-wall region, and a layer in the jet region further away from the wall. For the scaling of the structure in the near-wall region, experience from existing scaling methods for turbulent boundary layer studies can be taken advantage of. However, the definitions for the outer scaling to be used in a range of blowing ratios in film cooling are still an open area when discussing heat transfer downstream from the cooling film.

The objective of this paper is to evaluate the budget terms in the compressible version of transport equations of turbulent heat flux for film cooling cases, based on the database from Hao and di Mare (2022). Two types of cooling holes: the fan-shaped hole and the cylindrical hole are analyzed and compared. There blowing ratios considered in this study are 0.5, 1.0, and 1.5. The main focus is on the development of heat transfer characteristics downstream from the exit of the film cooling hole obtained from the turbulence statistics of flow in the jet region (away from the wall). Particularly, the budgets of turbulent heat fluxes are discussed in a proposed scaling that allows the budget terms in different streamwise positions to collapse onto single curves. The study aims to help disclose the transport mechanisms of heat transfer in film cooling flows.

The following sections are organized as follows: Section 2 introduces the flow configuration, numerical scheme, budget equations of turbulent heat flux, and governing equations. Section 3 provides validation using a turbulent boundary layer to show budgets of the turbulent

heat flux. Section 4 presents the results of the study, with a preliminary viewing of heat transfer in terms of mean temperature, temperature fluctuation, velocity fluctuation, density fluctuation, turbulent heat flux, and temperature variation in cooling films. This section then discusses the balancing of turbulent heat flux budgets in film cooling, with an explanation connected to the heat transfer mechanisms observed from the preliminary viewing. Third, the universal scaling of each budget term is presented.

Overall, this paper provides valuable insights into the transport mechanisms of heat transfer in film cooling flows, which could inform the design of more efficient cooling systems in practical applications.

2. Methodology

2.1. Flow configuration

The flow configuration, including the cooling film geometries, computational domain, and flow conditions, is specifically chosen to match the cooling film experiment described in Gritsch et al's research paper (see Gritsch, Schulz and Wittig (1998)). The computations are then conducted and validated by comparing with the experimental data (from Gritsch et al. (1998)) in Hao and di Mare (2022)'s study.

In this study, two types of cooling holes are studied: the fan-shaped hole and the cylindrical hole. The geometries of these two film cooling holes are shown in Fig. 1. The inclination angle is 30 degree and the ratio of length to diameter is 6, where the diameter of the hole is 0.01. The lateral expansion angle for the fan-shaped hole is 14 deg. Figure 1 also presents the coordinate system used to describe the position of the holes, where the origin is at the center of the hole's exit plane, the x-axis follows the direction of the streamwise flow, the y-axis is perpendicular to the wall, and the z-axis is in the spanwise direction. In Fig. 2, the corresponding computational domains are shown for each with a mainstream channel, a coolant channel, and the cooling hole

included. The near-field and far-field regions are also shown in Fig. 2: the former is defined as the region where x/D is between 1 and 5, while the latter is defined as the region where x/D is greater than 5.

The mesh for the cooling films is generated using a template-based multi-block hexahedral meshing technique by the mesh generator, as described in Hao, Wang, Hope-Collins, Rife and di Mare (2020). Figure 3 displays the fan-shaped mesh on the median cutting plane, along with a view where both the region $z < 0$ and $y > 0$ are blanked out. The $y+$ value is less than 2, indicating an adequate mesh resolution. The quality of the mesh is further validated in Hao et al. (2020).

The boundary condition is set to meet the operating condition: the internal temperature $T_{tc} = 290K$, the pressure ratio $T_{tc}/T_{tm} = 0.54$, the internal Mach number $Ma_c = 0$, the external Mach number $Ma_m = 0.6$, the internal Reynolds number $Re_{Dc} \leq 2.5 \times 10^5$, the external Reynolds number $Re_{Dm} \leq 1.3 \times 10^5$, the boundary layer thickness $\delta_{99}/D = 0.5$, the external turbulence level $Tu_m/D \leq 1.5\%$, and the internal turbulence level $Tu_c/D \leq 1\%$. For each type of cooling hole, three blowing ratios are focused on: $M = 0.5$, $M = 1.0$, and $M = 1.5$. An inflow generator proposed by Hao, Hope-collins and di Mare (2022) is applied to generate the inflow turbulence on the fly. The outflow applied for both external and internal channels is the non-reflecting boundary condition, see Thompson (1987). The bottom wall of the external channel, the top wall of the internal channel, and the wall of the cooling hole are applied with the non-slip wall condition for the velocity and the adiabatic wall condition for the thermal behavior. The top wall of the external channel and the bottom wall of the internal channel is applied with the far-field boundary condition. The sides of the boundaries in both channels are dealt with by the periodic boundary condition.

Heat transfer and Turbulent heat flux budgets in cooling films

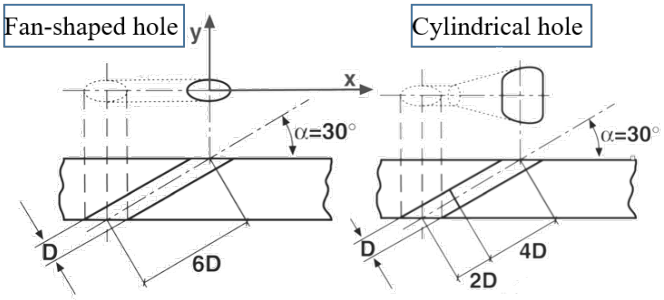


Figure 1: The geometry of film cooling holesGritsch et al. (1998): left (a) fan-shaped hole, right (b)cylindrical hole.

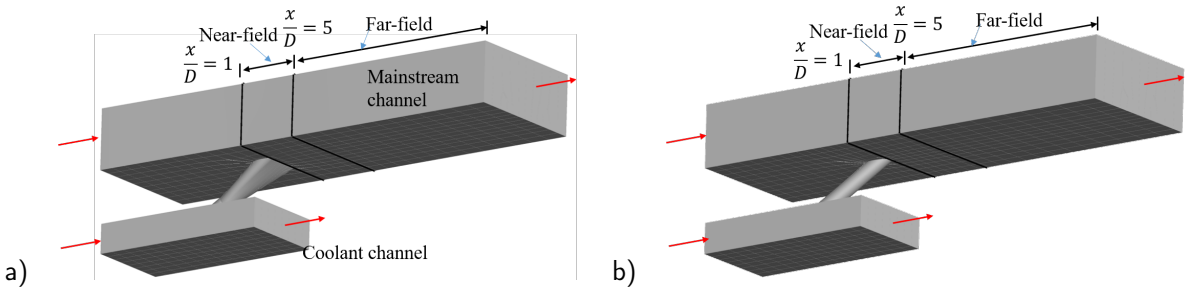


Figure 2: Computational domains: a)fan-shaped hole, b) cylindrical hole

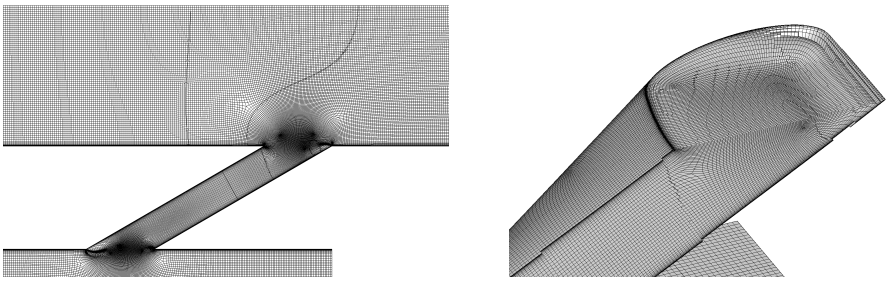


Figure 3: The mesh of the fan-shaped case in the view on the median cutting plane and the view with both the median plane and the horizontal plane blanking

Present simulations are based on an in-house CFD code called 'H4X'. The Navier-Stokes equations are solved by an implicit LES using a finite volume method. Conservative variables are stored at the cell center. Inviscid fluxes are extrapolated at the cell interface by using Roe's

Riemann solver from gradients of the characteristic variables based on a third-order compact scheme Čada and Torrilhon (2009). The scheme employs a limiter based on a three-point stencil. The limiter is applied to locally biased gradients that are obtained by a weighted least square algorithm in neighboring stencils so that only stencils that contribute most to the reconstructed flux are retained. This scheme gets rid of oscillations near discontinuities and local extrema, achieving third-order accuracy away from these regions. Viscous fluxes are reconstructed by least square gradients based on a four-point stencil, achieving a Second-order accuracy. The time advancement is achieved by a third-order Runge-Kutta algorithm, with three evaluations of fluxes and four updates of conservative variables for each time step. The CFL is lower than 0.8. The simulation is parallelized using MPI and OpenMPI, and 480 processors are used for LES computations. Turbulent statistics are collected at the end of simulations to sweep the initial transient solutions. A time series of statistics covering at least 14 flow though times are sampled and then post-processed into Favre-averaged quantities. More details regarding numerical settings and the correctness of LES results of film cooling cases analyzed in this study can be referred to Hao and di Mare (2022).

2.2. Budgets of turbulent heat flux

Compared with incompressible cases where the momentum equation is decoupled from the energy equation, the compressible cases are more complex when handling turbulent heat flux modeling. The compressible transport equations of Reynolds fluxes are obtained by derivations using the mass conservation, the fluctuating momentum equation, and the fluctuating temperature equations. The gas is assumed as a perfect gas. The buoyancy effect is assumed not included.

Heat transfer and Turbulent heat flux budgets in cooling films

The turbulent heat flux vector is $q_T = \overline{\rho u_i'' T''} = \bar{\rho}\widetilde{u_i'' T''}$, where $\widetilde{\ }$ is the Favre averaging whereas — is the Reynolds averaging. For a dependent variable f, the Reynolds decomposition partitions f into an ensemble mean (the Reynolds average) and a fluctuation:

$$f(\mathbf{x}, t) = \bar{f}(\mathbf{x}, t) + f'(\mathbf{x}, t) \tag{1}$$

and the Favre decomposition partitions f into the Favre average and a fluctuation as

$$f(\mathbf{x}, t) = \tilde{f}(\mathbf{x}, t) + f''(\mathbf{x}, t) \tag{2}$$

where the Favre average is defined a

$$\widetilde{f} = \frac{\overline{\rho f}}{\bar{\rho}} \tag{3}$$

The transport equation of the turbulent heat flux is

$$\begin{aligned} \frac{\mathrm{D}\bar{\rho}\widetilde{u_i'' T''}}{\mathrm{D}t} &= \frac{\partial\left(\bar{\rho}\widetilde{u_i'' T''}\right)}{\partial t} + \frac{\partial}{\partial x_k}\left(\widetilde{u}_k \bar{\rho}\widetilde{u_i'' T''}\right) \\ &= \bar{\rho} P_{Ti}^1 + \bar{\rho} P_{Ti}^2 + \bar{\rho}\Phi_{Ti} - \bar{\rho}\varepsilon_{Ti} - \bar{\rho} D_{Ti} + \bar{\rho} C_{Ti} \end{aligned} \tag{4}$$

where the right-hand side is balanced among the production due to the mean velocity and mean temperature $\bar{\rho} P_{Ti}^1$, Production due to the fluctuating strain rate $\bar{\rho} P_{Ti}^2$, the 'Pressure-scrambling'

term $\bar{\rho}\Phi_{Ti}$, the turbulent viscous-thermal dissipation term $\bar{\rho}\epsilon$, the turbulent viscous-thermal transport contribution $\bar{\rho}D_{Ti}$ and compressibility associated terms $\bar{\rho}C_{Ti}$, as shown below:

(1) Production due to the mean velocity and mean temperature

$$\bar{\rho}P^1_{Ti} = -\bar{\rho}\tau_{ik}\frac{\partial\widetilde{T}}{\partial x_k} - \bar{\rho}\widetilde{u''_k T''}\frac{\partial\tilde{u}_i}{\partial x_k} - \bar{\rho}(\gamma-1)\widetilde{u''_i T''}\widetilde{S}_{kk} + \left(\frac{\gamma}{c_p}\right)\overline{u''_i\sigma'_{jk}}\widetilde{S}_{kj} \tag{5}$$

(2) Production due to the fluctuating strain rate

$$\bar{\rho}P^2_{Ti} = \left(\frac{\gamma}{c_p}\right)\left[\overline{u''_i\sigma'_{jk}s''_{kj}} - \overline{u''_i p' s''_{kk}}\right] \tag{6}$$

(3) 'Pressure-scrambling'

$$\bar{\rho}\Phi_{Ti} = -\left[\overline{T''\frac{\partial p}{\partial x_i}}\right] \tag{7}$$

(4) Turbulent viscous-thermal dissipation

$$\begin{aligned}\bar{\rho}\epsilon_{T_i} &= -\left(\frac{\gamma}{c_p}\right)\overline{q'_k\frac{\partial u''_i}{\partial x_k}} + \overline{\sigma'_{ik}\frac{\partial T''}{\partial x_k}} \\ &= \left(\frac{\gamma}{c_p}\right)\left[\bar{k}_T\overline{\frac{\partial u''_i}{\partial x_k}\frac{\partial T'}{\partial x_k}} + \overline{k'_T\frac{\partial u''_i}{\partial x_k}\frac{\partial\bar{T}}{\partial x_k}} + \overline{k'_T\frac{\partial u''_i}{\partial x_k}\frac{\partial T'}{\partial x_k}}\right] + \left[\overline{\sigma'_{ik}\frac{\partial T''}{\partial x_k}}\right]\end{aligned} \tag{8}$$

(5) Turbulent viscous-thermal transport contribution

$$\begin{aligned}\bar{\rho}D_{Ti} &= -\left(\frac{\gamma}{c_p}\right)\frac{\partial}{\partial x_k}\left[\overline{u''_i q'_k}\right] - \frac{\partial}{\partial x_k}\left[\overline{\rho u''_i T'' u''_k} - \overline{\sigma'_{ik}T''}\right] \\ &= \left(\frac{\gamma}{c_p}\right)\frac{\partial}{\partial x_k}\left[\bar{k}_T\overline{u''_i\frac{\partial T'}{\partial x_k}} + \overline{k'_T u''_i}\frac{\partial\bar{T}}{\partial x_k} + \overline{k'_T u''_i\frac{\partial T'}{\partial x_k}}\right] - \frac{\partial}{\partial x_k}\left[\overline{\rho u''_i T'' u''_k} - \overline{\sigma'_{ik}T''}\right]\end{aligned} \tag{9}$$

(6) Compresibility associated terms

$$\bar{\rho}C_{Ti} = \overline{T''}\frac{\partial\bar{\sigma}_{ik}}{\partial x_k} + \left(\frac{\gamma}{c_p}\right)\left[\overline{u''_i}\bar{\sigma}_{jk}\widetilde{S}_{kj} + \overline{u''_i s''_{kj}}\left(\bar{\sigma}_{kj} - \bar{p}\delta_{kj}\right)\right] \tag{10}$$

Heat transfer and Turbulent heat flux budgets in cooling films

2.3. Governing equations

In governing equations, variables are normalized by using the wall-normal distance at 99% of far-field velocity δ_{99}, velocity defect ΔU, temperature deficit ΔT. The governing equations in non-dimensional form can be written as:

$$\begin{aligned} \frac{\partial \rho}{\partial t} + \frac{\partial \rho u_j}{\partial x_j} &= 0 \\ \frac{\partial \rho u_i}{\partial t} + \frac{\partial \rho u_i u_j}{\partial x_j} + \frac{\partial p}{\partial x_i} &= \frac{1}{\partial x_j}\left(\partial \sigma_{ij} + \sigma_{ij}^{(sgs)}\right) \\ \frac{\partial \rho E}{\partial t} + \frac{\partial (\rho E + p) u_j}{\partial x_j} &= \frac{1}{\partial x_j}\left(\partial \sigma_{ij} u_i - \partial q_j + \partial \sigma_{ij}^{(sgs)} u_i - \partial q_j^{(sgs)}\right) \end{aligned} \tag{11}$$

where $u_i (i = 1, 2, 3)$ is the velocity vector, with $(u_i, u_j, u_k) = (u, v, w)$. The directions of $i (i = 1, 2, 3)$ correspond to (x, y, z), which are in the streamwise direction, wall-normal and spanwise direction. Other variables in Equ. 11 include the time t, the pressure p, the density ρ, the temperature T, the total energy $E = e + 0.5 u_i u_j$, the heat flux $q_i = -k_T \frac{\partial T}{\partial x_i}$, the viscous stress tensor σ_{ij} for a Newtonian fluid,

$$\sigma_{ij} = 2\mu \left(S_{ij} - \frac{\delta_{ij}}{3} S_{kk} \right) \tag{12}$$

based on strain-rate tensor S_{kl}, which takes the form:

$$S_{kl} = \frac{1}{2}\left(\frac{\partial u_k}{\partial x_l} + \frac{\partial u_l}{\partial x_k} \right) \tag{13}$$

where μ is the viscosity and δ_{ij} is the Kronecker delta.

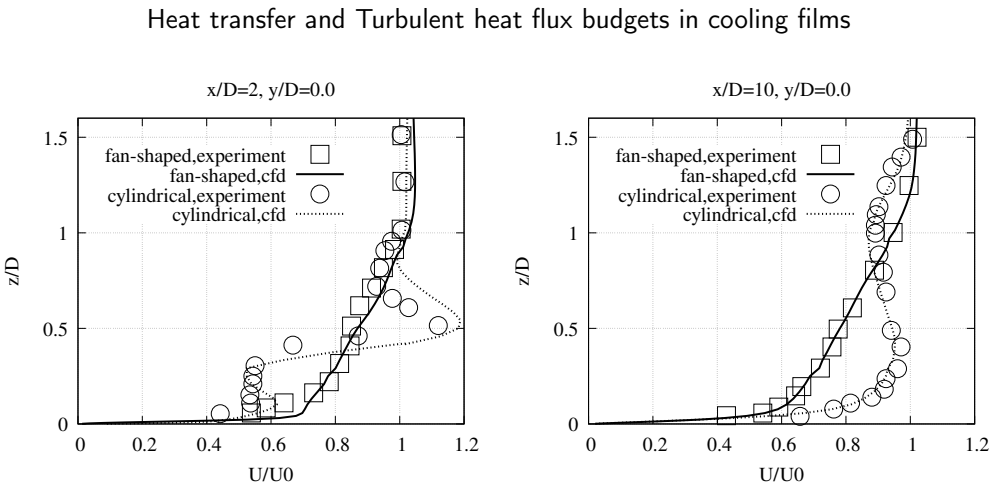


Figure 4: Simulation results versus experimental results from Thole et al. (1998)

3. Validation

Validations include two parts. The first part is to validate the correctness of the LES result of cooling films by comparing the LES result with experimental data. In Fig. 4, the velocity profile is shown as a representative of validation for LES correctness. A good match of the velocity profiles shows that the numerical tool adopted in this study can show reasonably accurate budgets. More validation in terms of the flowfield and heat transfer characteristics can be found in Hao and di Mare (2022).

The second part is to validate the procedure of generating compressible turbulent heat flux budgets. A turbulent boundary layer flow with an adiabatic wall has been conducted. The compressible turbulent heat flux budgets from LES results are compared with the DNS data from Shahab, Lehnasch, Gatski and Comte (2011). Fig. 5 shows the comparison of compressible turbulent heat flux budget terms in the wall-normal direction. A sum of imbalance and a loss of the effect of the sub-grid scale indicated in Equ. 14 is also shown (in red dash line) indicating the aggregate error of the budget terms and a loss of unresolved dissipation. Equation 14 is obtained by subtracting the left-hand side of Equ.4 and ignoring the

Heat transfer and Turbulent heat flux budgets in cooling films

time-derivative term which is based on an assumption of statistically stationary flow. The left-hand side sum includes the imbalance and the effect of SGS (sub-grid scales) on the resolved budgets (represented by f_{sgs}):

$$Imbalance + f_{sgs} = \bar{\rho}P_{Ti}^{1} + \bar{\rho}P_{Ti}^{2} + \bar{\rho}\Phi_{Ti} - \bar{\rho}\epsilon_{Ti} - \bar{\rho}D_{Ti} + \bar{\rho}C_{Ti} - \frac{\partial}{\partial x_k}\left(\widetilde{u}_k\bar{\rho}\widetilde{u_i''T''}\right) \quad (14)$$

The budgets generated from the present LES results match well with the DNS data in the viscous layer and log-law region. The maximum sum of the imbalance and the unresolved dissipation is observed in the lower $y+$ region, with a deviation of 0.05 at maximum, which means the aggregate error of budget terms is even smaller than the result in the budget studyVyas et al. (2019).

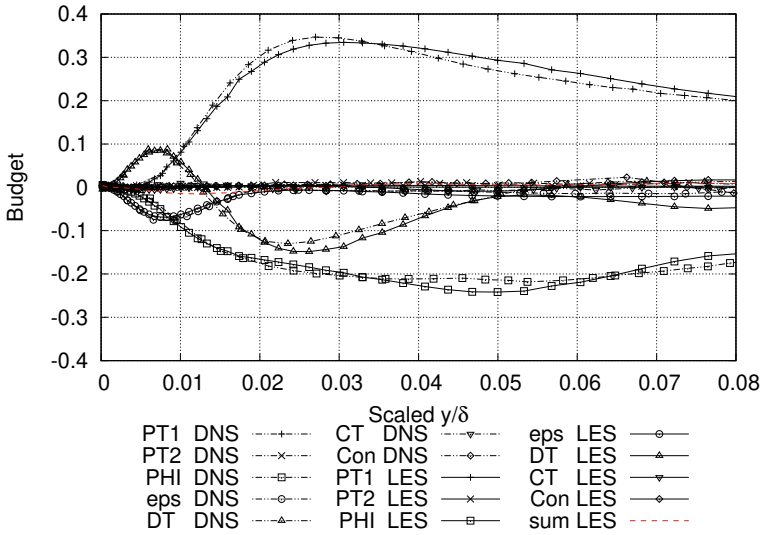


Figure 5: Budget terms of $\widetilde{v''T''}$ for Spalart's turbulent boundary layer Shahab et al. (2011)

Similarly, in the results shown in the Results and discussion of film cooling Section, the imbalance and unresolved viscous terms are lumped together.

4. Results and discussion of film cooling

4.1. A preliminary viewing of heat transfer in film cooling

4.1.1. Fluctuations in the instantaneous flowfield

Fig. 6 shows the turbulent temperature fluctuation T'' scaled by on the median plane of the cases described in Section 2. Grey lines are added at $x/D = 2, 5, 10$ for marking positions. In Fig. 6, the structures of hairpin vortexes near the wall downstream from the film can be identified. The temperature fluctuation indicates that the vortexes develop as the boundary layer thickness grows, which is dependent on the flow configuration. An insight from this is that if a scaling with the local boundary layer thickness δ_{99} is used, all the details in the flow field can be compared based on the same dimension of the boundary layer.

Following this method, Fig.7 shows the scaled turbulent temperature fluctuation T'' contours on the $z-y$ planes at $x/D = 2, 5, 10$ of two types of cooling films. With the scaling using δ_{99} on the wall-normal distance, the coolant distribution and flow patterns within boundary layers in different flow configurations can be more easily compared as they are seen within the same height of the boundary layer thickness. From $x/D = 2$ to $x/D = 10$, in the fan-shaped film, the space occupied by the coolant is shared by a varying number of flow structures. As an example, three hairpin vortexes can be clearly seen in Fig.7e. In the cylindrical film, these structures are even less easy to be identified using other outer or inner scalings. Fig. 7b and Fig. 7d each show evidence of a single hairpin vortex surrounding the coolant jet.

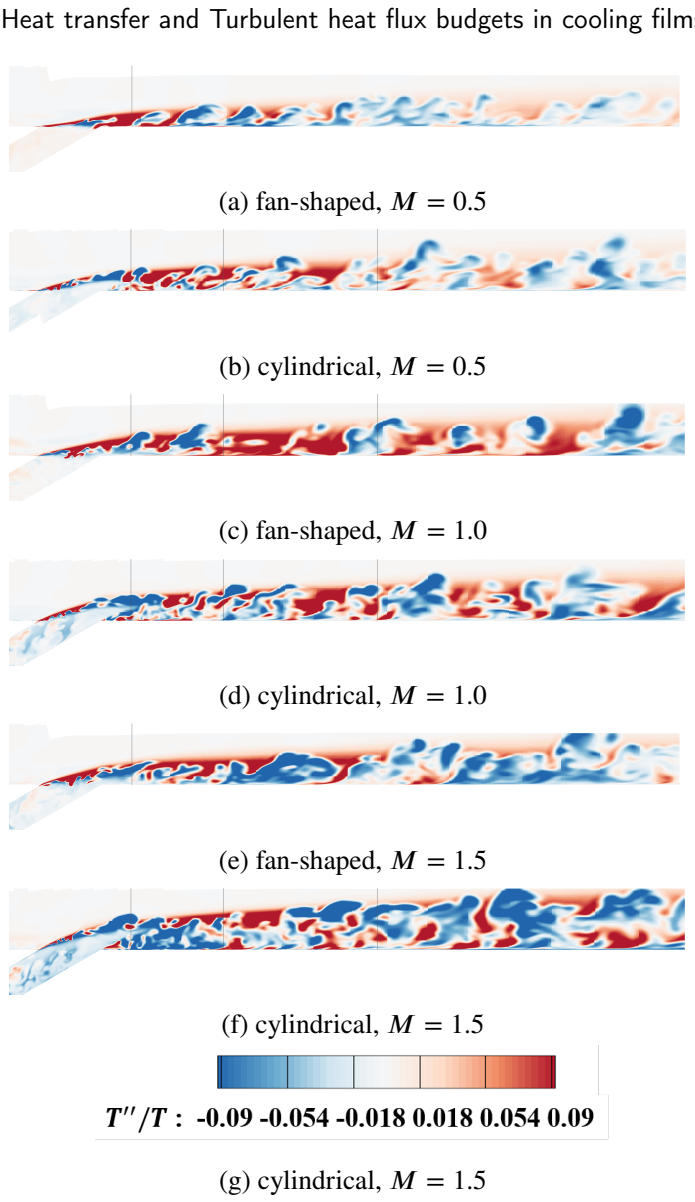
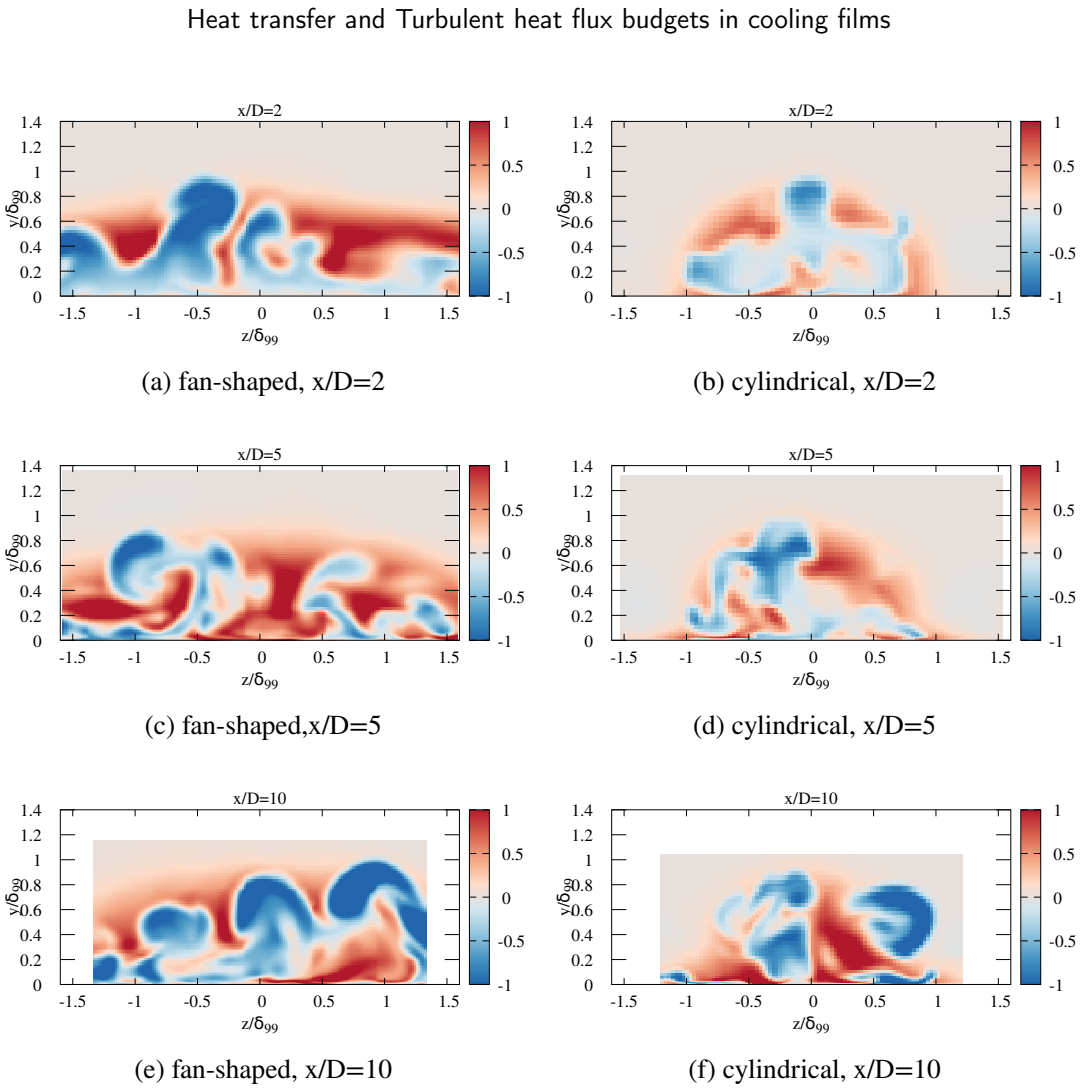


Figure 6: Contours of turbulent temperature fluctuation T'' scaled by T_0 on the median plane for fan-shaped and cylindrical films at $M = 0.5, 1.0, 1.5$

4.1.2. Favre-averaged flowfield

Fig. 8 - Fig. 11 show the Favre-averaged temperature $\widetilde{T}$ non-dimentionalised by T_0, the streamwise component of Favre-averaged turbulent heat flux $\widetilde{u''T''}$ non-dimentionalised by



(a) fan-shaped, x/D=2

(b) cylindrical, x/D=2

(c) fan-shaped,x/D=5

(d) cylindrical, x/D=5

(e) fan-shaped, x/D=10

(f) cylindrical, x/D=10

Figure 7: Contours of the scaled turbulent temperature T'' for fan-shaped and cylindrical films at $M = 1.0$

$U_0(T_m - T_c)$, the wall-normal component of Favre-averaged turbulent heat flux $\widetilde{v''T''}$ non-dimentionalised by $U_0(T_m - T_c)$, and the temperature variance $\widetilde{T''T''}$ non-dimentionalised by $(T_m - T_c)^2$ on the median planes together with $z - y$ slices at $x/D = 2, 5, 10$ of the film cooling cases studied. These contours provide the structure of temperature and heat fluxes in a three-dimensional view. The results show that the jet at different blowing ratios in the

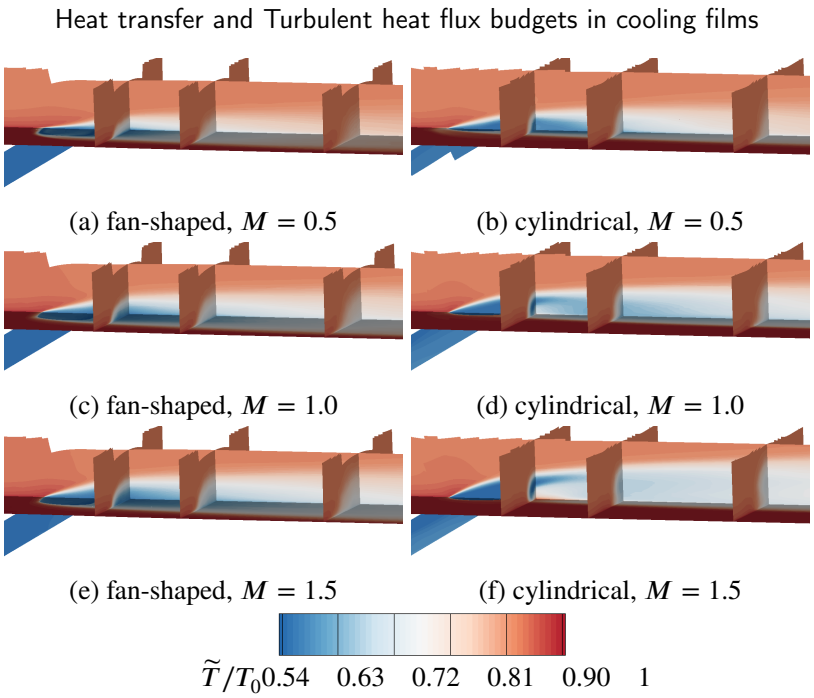


Figure 8: Contours of Favre-averaged temperature $\widetilde{T}$ scaled by T_0 on the median plane for fan-shaped and cylindrical films at $M = 0.5, 1.0, 1.5$

fan-shaped films is attached to the wall. A larger blowing ratio gives rise to a thicker jet layer thickness in the (x, z, y) dimension, which corresponds to the Cartesian streamwise, spanwise, and wall-normal direction. For the cylindrical film, Fig. 8 - Fig. 10 show that the jet at $M = 0.5$ is first detaching and reattaching on the wall after around $x/D = 5$, and the jet at $M = 1.0$ is detaching from the wall, maintaining a roughly parallel flow after $x/D = 2$, and the jet at $M = 1.5$ is lifted off after $x/D = 2$. Fig. 11 shows that in the cylindrical film when $M = 1.0$ and $M = 1.5$, the contour forms a triangle region on the median plane that corresponds to low-temperature variance exiting from the cooling hole in the mainstream. Accordingly, the turbulence intensity generated inside the rear part of the cooing hole quickly decays to zero at the exit of the cooling hole when the jet comes into the mainstream, as shown by the turbulence kinetic energy in Fig. 12, indicating that a potential core exists. This potential core can also

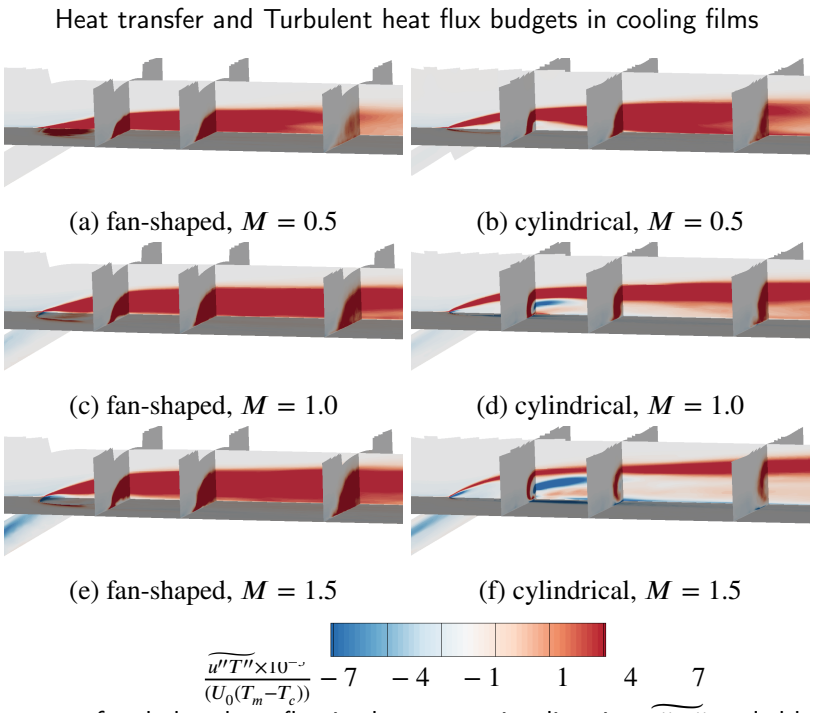


Figure 9: Contours of turbulent heat flux in the streamwise direction $\widetilde{u''T''}$ scaled by $U_0(T_m - T_c)$ on the median plane for fan-shaped and cylindrical films at $M = 0.5, 1.0, 1.5$

be clearly identified by $\widetilde{T}$ (shown in Fig. 8) and $\widetilde{T''T''}$ (shown in Fig. 11). At $M = 1.0$ and $M = 1.5$, the potential core extends up to around $x/D = 3$ (shown in Fig. 17). It can be identified by an area of very low fluctuations of temperature and turbulent heat fluxes. In the fan-shaped film, there is no recognizable potential core.

In addition, in the cylindrical film when $M = 1.0$ and $M = 1.5$, a confined region is observed immediately after the jet enters the mainstream, below the lower side of the jet which is under the potential core, and above the wall, see $x/D = 2$ in Fig. 8 and Fig. 11. A typical confined region is sketched in Fig. 13. The confined region is a result of the confinement from both the wall and the jet. In this confined region, the flow and heat transfer is limited in the streamwise direction and wall-normal direction. In the confined region: temperature $\widetilde{T}$ is close to the minimum when $M = 1.0$ as the jet attached to the wall limits the flow stay

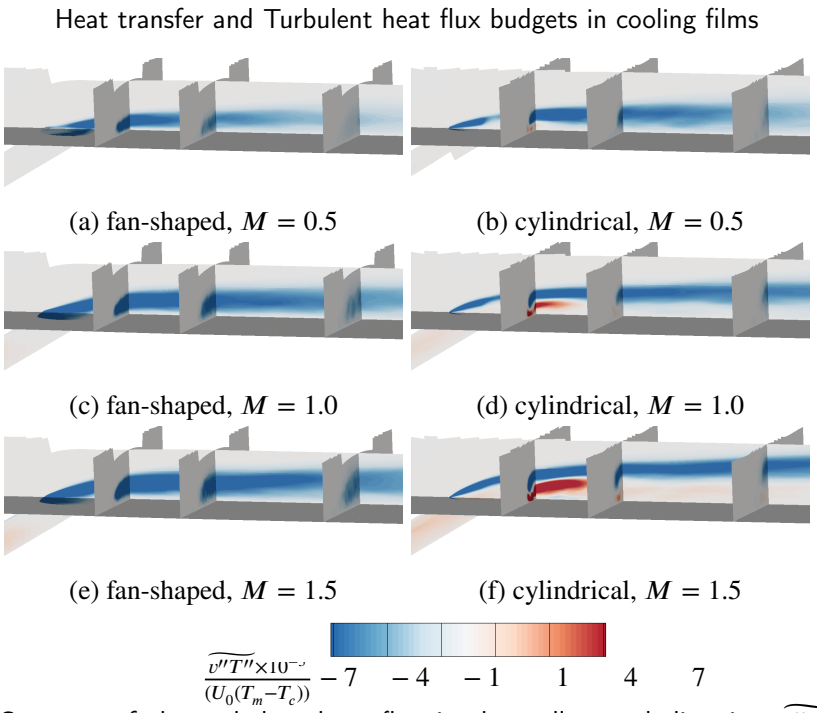


Figure 10: Contours of the turbulent heat flux in the wall-normal direction $\widetilde{v''T''}$ scaled by $U_0(T_m - T_c)$ on the median plane for fan-shaped and cylindrical films at $M = 0.5, 1.0, 1.5$

inside this region, but is high at $M = 1.5$ as the hot stream is entrained. The streamwise and wall-normal turbulent heat flux components, $\widetilde{u''T''}$ and $\widetilde{v''T''}$, and the temperature variance $\widetilde{T''T''}$ are generally weaker than those of the surrounding jet. The confined region disappears around $x/D = 2$ when $M = 1.0$ and disappears around $x/D = 5$ when $M = 1.5$.

The flow for all flow configurations show similarities after $x/D = 10$, which is also concluded in Hao and di Mare (2022). Since the three locations, $x/D = 2, 5, 10$, are representatives of the main processes taking place in the early development of the jet, these locations are focused on in the following discussion.

Fig. 14 - Fig. 17 show the scaled quantities including the Favre-averaged temperature $< T >$, the streamwise component of Favre-averaged turbulent heat flux $< u''T'' >$, the wall-normal component of Favre-averaged turbulent heat flux $< v''T'' >$, the temperature variance

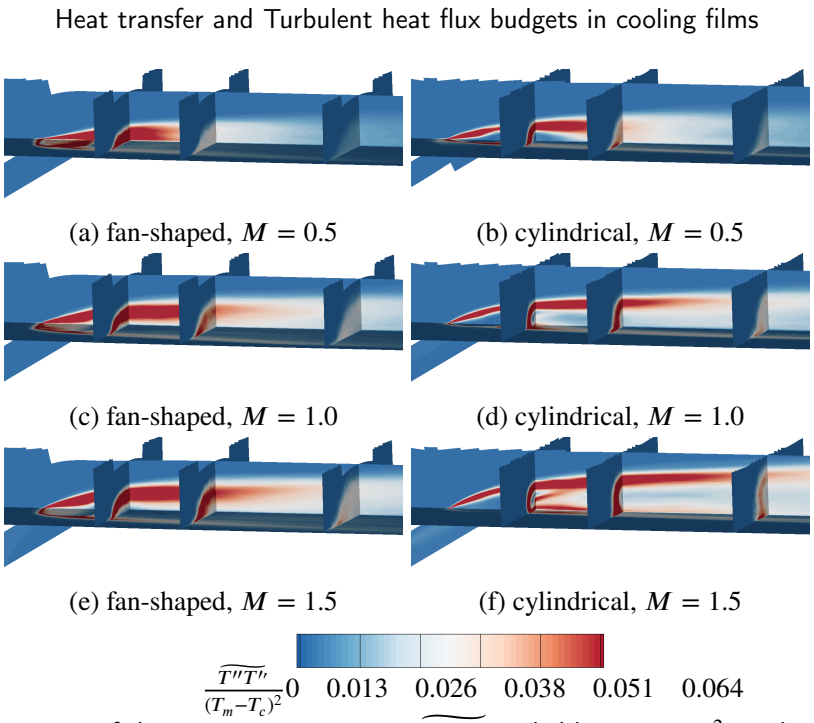


Figure 11: Contours of the temperature variance $\widetilde{T''T''}$ scaled by $(T_m - T_c)^2$ on the median plane for fan-shaped and cylindrical films at $M = 0.5, 1.0, 1.5$

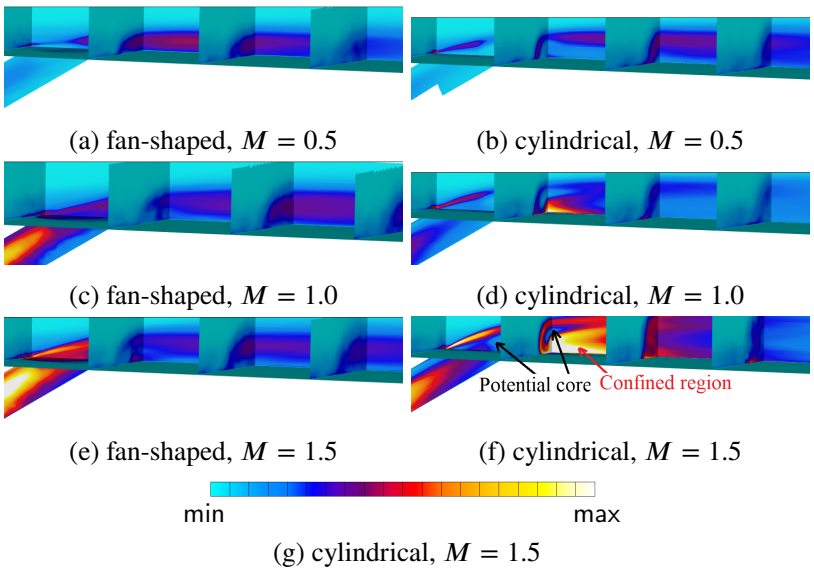


Figure 12: Turbulence kinetic energy contours on the median plane for fan-shaped and cylindrical films at $M = 0.5, 1.0, 1.5$

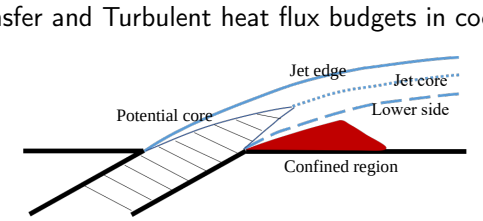


Figure 13: A typical sketch of the confined region

$< T''T'' >$ on $z-y$ slices at $x/D = 2, 5, 10$. <> is used to represent the scaled Favre-averaged quantity. These quantities are first Favre-averaged and then scaled according to the boundary layer thickness δ_{99}, velocity defect ΔU, and temperature deficit ΔT. Specifically,

$$< T >= \widetilde{T}/\Delta T \tag{15}$$

$$< u''T'' >= \widetilde{u''T''}/(\Delta U \Delta T) \tag{16}$$

$$< v''T'' >= \widetilde{v''T''}/(\Delta U \Delta T) \tag{17}$$

$$< T''T'' >= \widetilde{T''T''}/(\Delta T \Delta T) \tag{18}$$

For the fan-shaped cases, the Favre-averaged temperature (shown in 14a, 14c,14e), the variance of temperature (shown in 17a, 17c,17e), and turbulent heat fluxes (shown in 15a, 15c, 15e and 16a, 16c, 16e) are concentrated in a weakly curved layer around $y/\delta_{99} = 0.4 - 0.6$. For the cylindrical film, the blowing ratio controls the strength of the second motion in the $z - y$ plane, and this motion drives the configuration of the jet. At $M = 0.5$, the jet is spread over the range between $z/\delta_{99} = -1$ to 1 in the spanwise direction and below $y/\delta_{99} = 1$ in the wall-normal direction. At $M = 1.0$, the jet is confined in the range from $z/\delta_{99} = -1$ to 1 in the spanwise direction and below $y/\delta_{99} = 1$ in the wall-normal direction. At $M = 1.5$, the jet

is confined in the range from $z/\delta_{99} = -1$ to 1 in the spanwise direction and $y/\delta_{99} = 0.2 - 1$ in the wall-normal direction. Two special regions are concerned:

1) The potential core can be identified from low levels of temperature variance $< T''T'' >$. For example, at $M = 1.0$ (shown in Fig. 17d), the potential core is around $y/\delta_{99} = 0 - 0.6$ in general and around $y/\delta_{99} = 0.4 - 0.6$ on the centreline. At $M = 1.5$ (shown in Fig. 17f), the potential core is around $y/\delta_{99} = 0.2 - 0.6$ in general and around $y/\delta_{99} = 0.4 - 0.6$ on the centreline. It is also noted in Fig. 12g.

2)The confined region can be identified from low levels of wall-normal component of the turbulent heat flux $< v''T'' >$ and it is located below around $y/\delta_{99} = 0.2$ at $M = 1.0$ (shown in Fig. 16d) and $M = 1.5$ (shown in Fig. 16f). It is also noted in Fig. 12g.

Table 1 is shown to give an adjustment of the specific region from the Favre-averaged temperature $< T >$, the variance of temperature $< T''T'' >$, and turbulent heat fluxes $< u''T'' >$ and $< v''T'' >$. '-' represents the negative value, while '+', '++', '+++' represent positive values. '+++' represent a value higher than the value represented by '++' which represented a value even higher than the value represented by '+'. '0' represents a value with an absolute value close to the minimum value of the corresponding quantity. Table 1 summarised that: when $< T >$, $< T''T'' >$, $< v''T'' >$ are positive and $< u''T'' >$ is negative, it identifies the edge of jet; when all these four quantities are close to the minimum, it identifies the potential core; when $< T >$, $< T''T'' >$, $< u''T'' >$ are positive and $< v''T'' >$ is negative, it identifies the lower side of the jet; when only $< T >$ has a high positive value with the rest three quantities close to zero, it identifies the confined region. The table provides a way to identify different specific regions for the downstream flow from a cooling film.

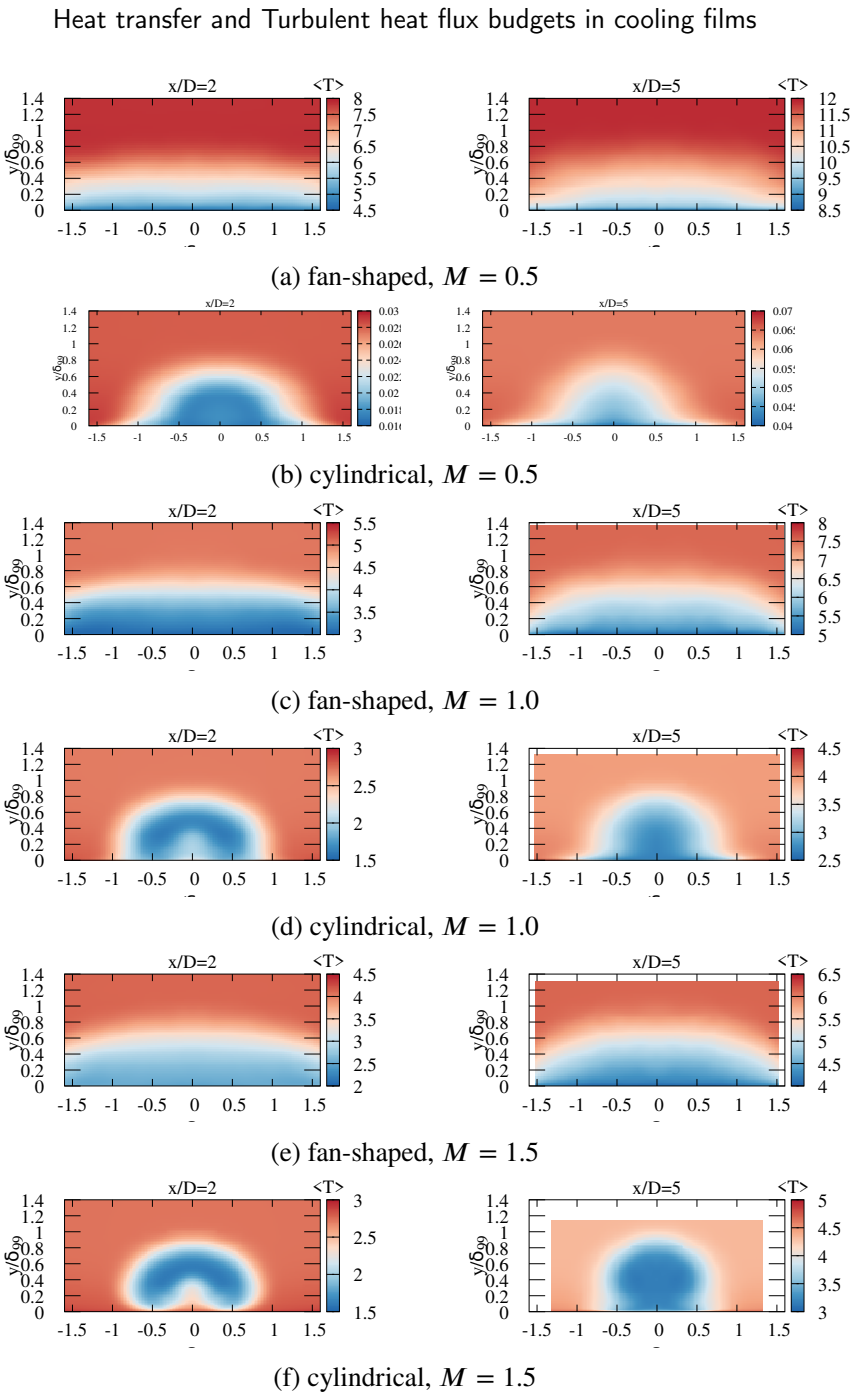
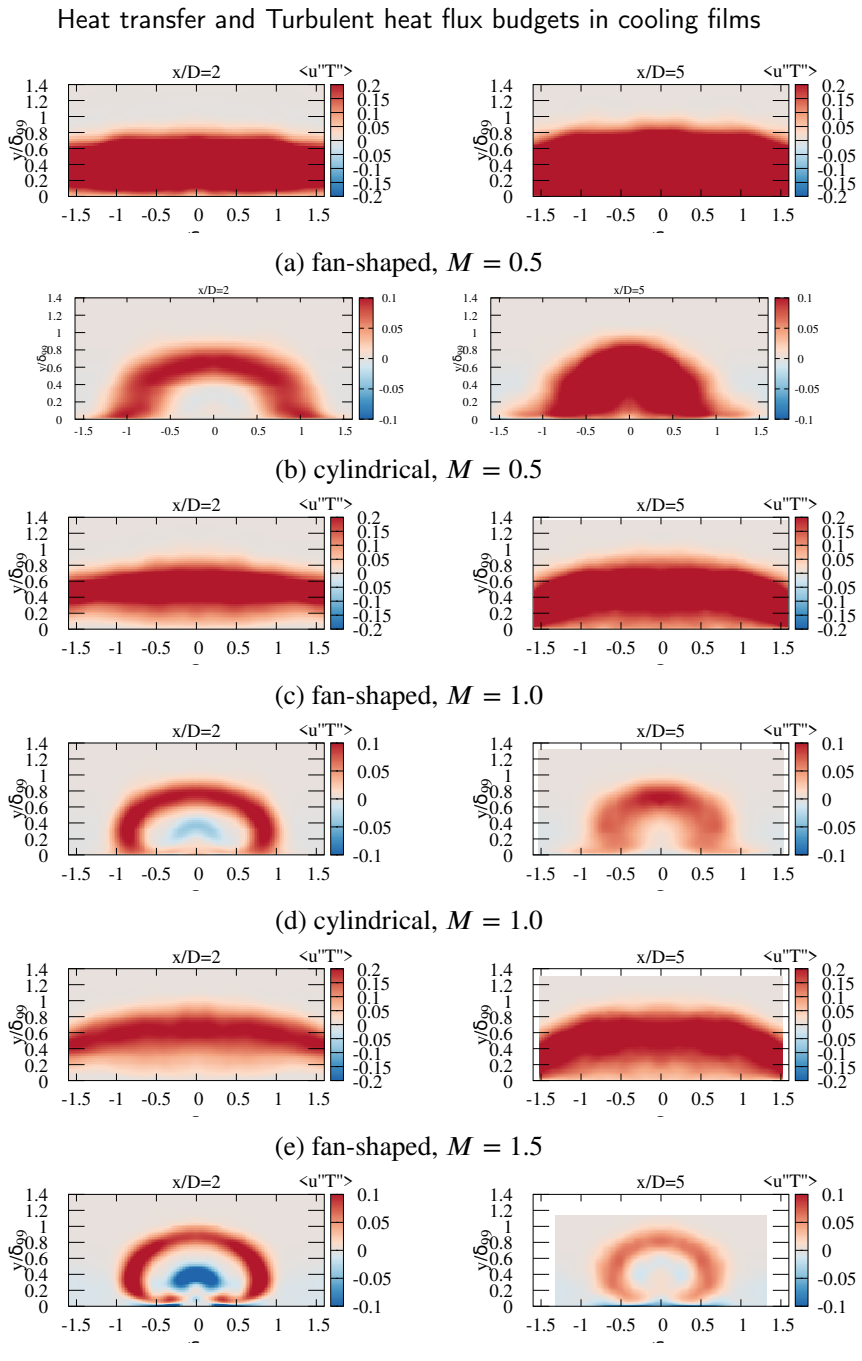


Figure 14: Favre-averaged temperature $\widetilde{T}$ contours on the median plane for fan-shaped and cylindrical films at $M = 0.5, 1.0, 1.5$. Legend (blue:minimum, white:middle, red:maximum)



(a) fan-shaped, $M = 0.5$

(b) cylindrical, $M = 0.5$

(c) fan-shaped, $M = 1.0$

(d) cylindrical, $M = 1.0$

(e) fan-shaped, $M = 1.5$

(f) cylindrical, $M = 1.5$

Figure 15: Turbulent heat flux in the streamwise direction $\widetilde{u''T''}$ contours on the median plane for fan-shaped and cylindrical films at $M = 0.5, 1.0, 1.5$. Legend (blue:minimum, white:zero, red:maximum)

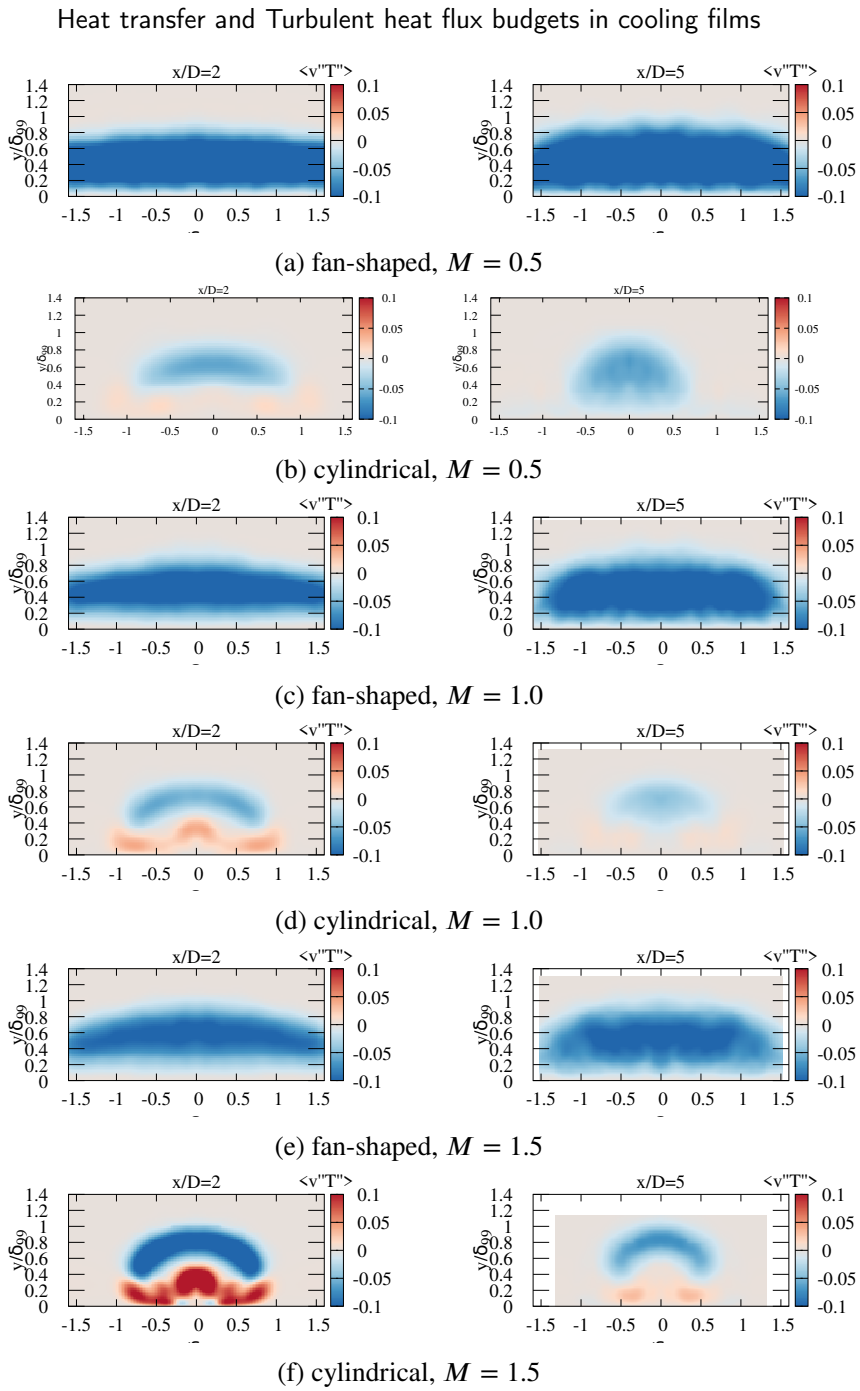


Figure 16: Turbulent heat flux in the wall-normal direction $\widetilde{v''T''}$ contours on the median plane for fan-shaped and cylindrical films at $M = 0.5, 1.0, 1.5$. Legend (blue:minimum, white:zero, red:maximum)

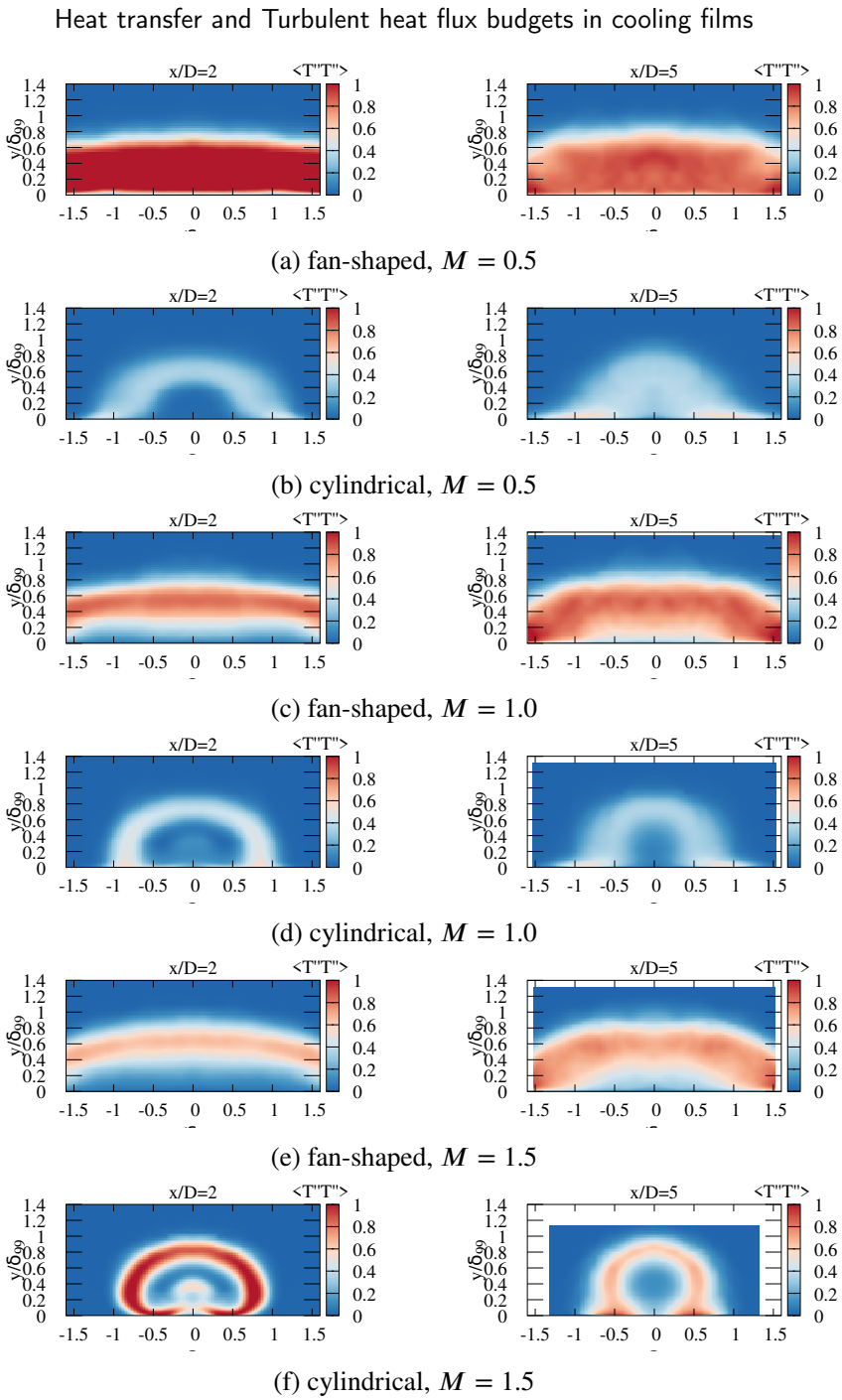
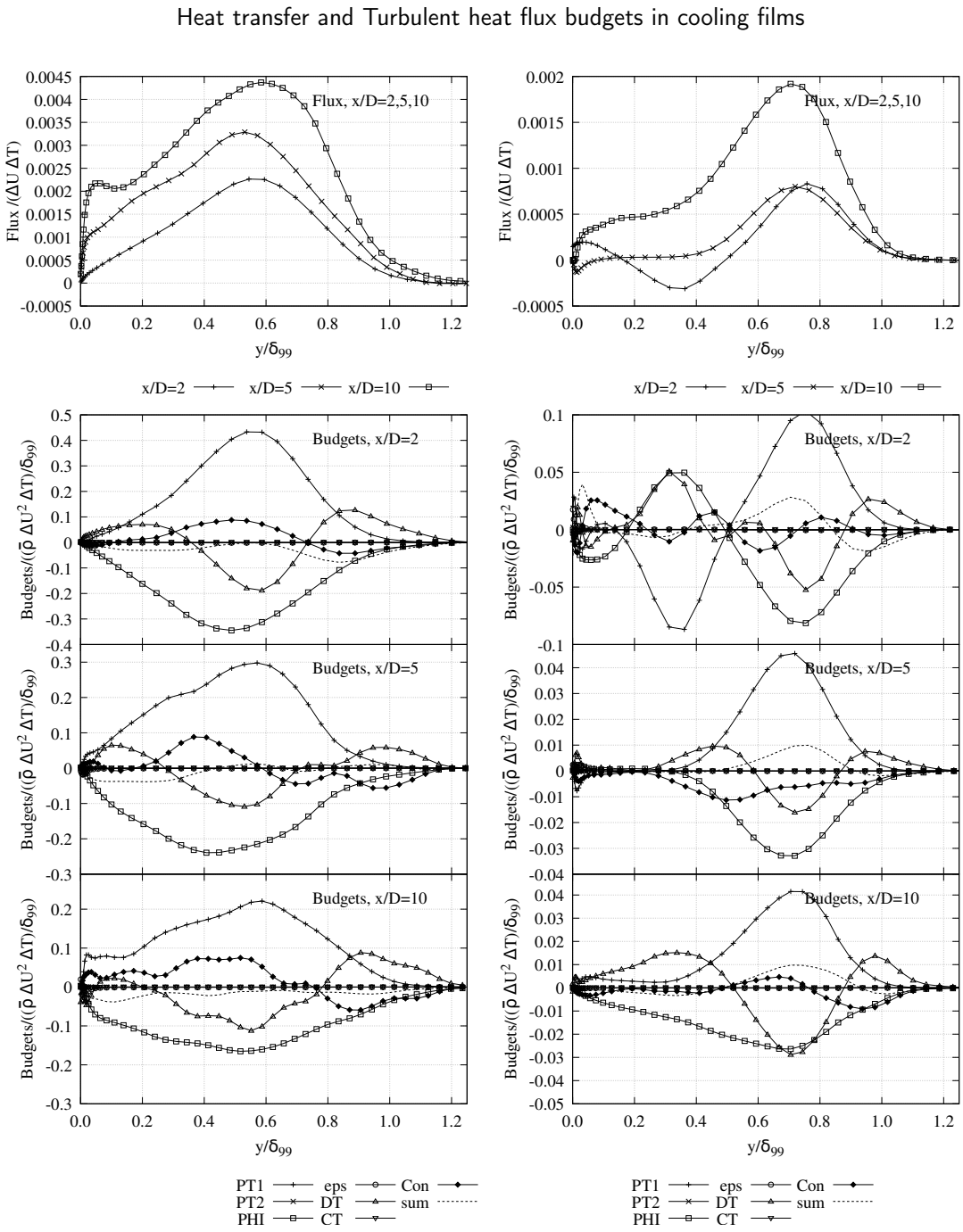
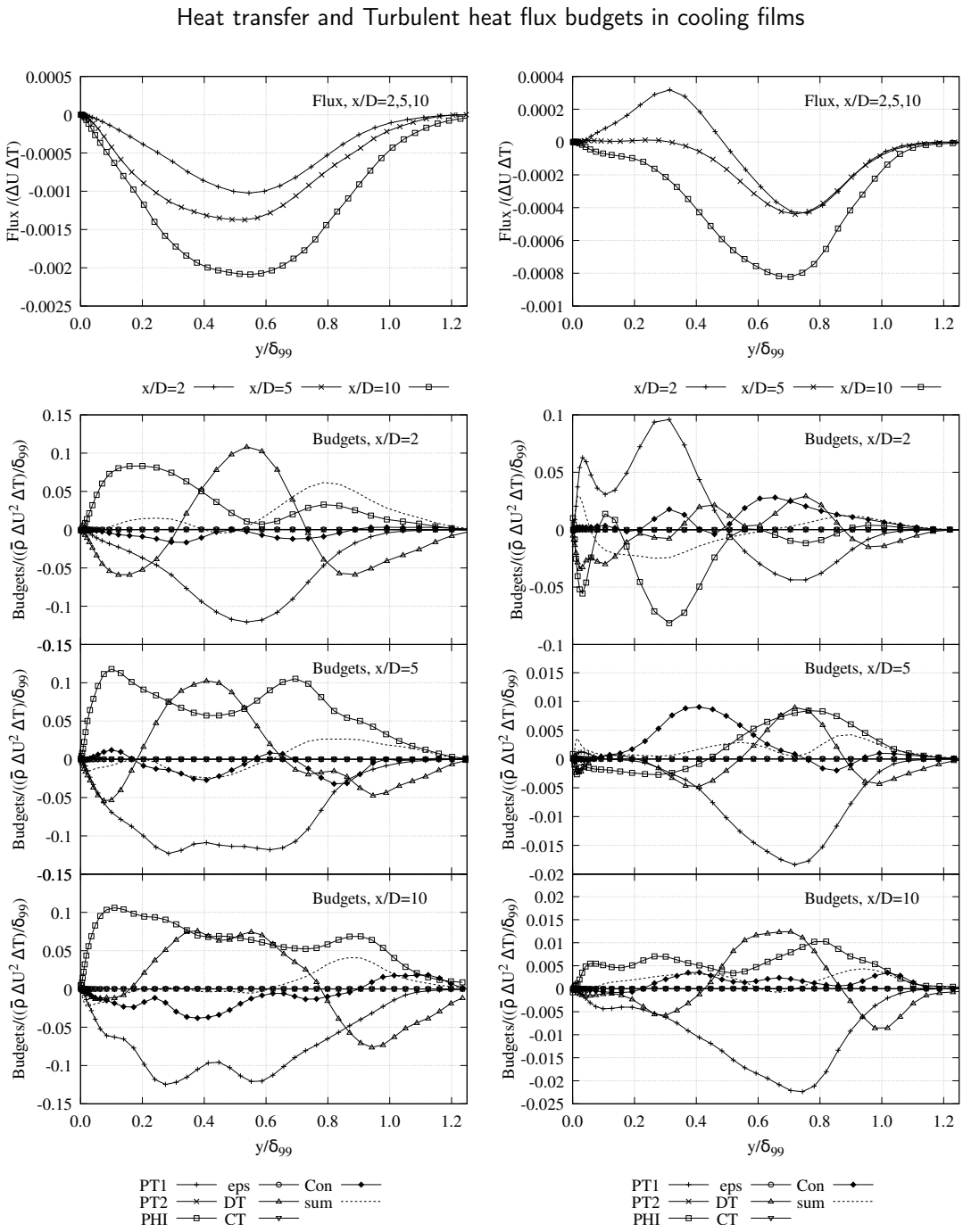


Figure 17: Turbulent temperature fluctuation $\widetilde{T''T''}$ contours on the median plane for fan-shaped and cylindrical films at $M = 0.5, 1.0, 1.5$. Legend (blue:minimum, white:middle, red:maximum)



(a) fan-shaped hole (b) cylindrical

Figure 18: Turbulent heat flux $\widetilde{u''T''}$ scaled by $\Delta U \Delta T$ and Budget terms of $\widetilde{u''T''}$ scaled by $\Delta U^2 \Delta T/\delta_{99}$ for fan-shaped and cylindrical films at $M = 1.0$



(a) fan-shaped hole (b) cylindrical

Figure 19: Turbulent heat flux $\widetilde{v''T''}$ scaled by $\Delta U \Delta T$ and multiple budget terms of $\widetilde{v''T''}$ scaled by $\Delta U^2 \Delta T / \delta_{99}$ for fan-shaped and cylindrical films at $M = 1.0$

Heat transfer and Turbulent heat flux budgets in cooling films

Table 1
Adjustment of regions in film cooling

y/δ_{99}	$< T >$	$< u''T'' >$	$< v''T'' >$	$< T''T'' >$	Mechanism
0.6-0.8	+++	-	++	++	edge of jet
0.4-0.6	0	0	0	0	potential core
0.2-0.4	+	+	-	+	lower side of jet
0.0-0.2	++	0	0	0	confined region

* +: positive, ++: higher positive, +++: highest positive, -: negative.

4.2. The balancing of turbulent heat flux budgets in film cooling

To analyze different budget terms in the transport equation of turbulent heat fluxes according to Equ. 5 -Equ. 10, the defect scaling is adopted using the boundary layer thickness δ_{99}, velocity defect ΔU, temperature deficit ΔT. Together with the turbulent heat flux $\widetilde{u''T''}$ and $\widetilde{v''T''}$ scaled by $\Delta U \Delta T$, budget terms of $\widetilde{u''T''}$ and $\widetilde{u''T''}$ are scaled by $\Delta U^2 \Delta T / \delta_{99}$. Fig. 18 and Fig. 19 show the scaled turbulent heat fluxes and the scaled budget terms of the corresponding turbulent heat flux on the centerline for fan-shaped and cylindrical films at $M = 1.0$.

In Fig. 18 (top row), the variations of the streamwise component of the turbulent heat flux correlations across the jet layer downstream from the cooling hole are shown with the defect scaling. The streamwise flux is larger than the wall-normal turbulent heat flux in both fan-shaped and cylindrical cooling films, as seen when comparing Fig. 18 (top row) and Fig. 19 (top row). There is an increase of around 43% in the streamwise heat flux peak magnitude from $x/D = 2$ to $x/D = 5$ and when $x/D = 10$ the magnitude arrives at 190% of its initial magnitude in the fan-shaped cases, as shown in Fig. 18 (first row, left). The position of the peak corresponds to the edge of the jet. This is why the current deficit scaling using δ_{99} preserves the position of the peak. The outer scaling or semi-local scaling (not shown here) does not preserve the position of this peak. In comparison, the streamwise heat flux in the cylindrical cooling

film, shown in Fig. 18 (first row, right), presents no change from $x/D = 2$ to $x/D = 5$, but an increase of more than twice its magnitude from $x/D = 5$ to $x/D = 10$ on the corresponding peak due to the edge of the jet. It should be noted that the heat flux because of mixing on the edge of the jet is uniformly improved along the streamwise distance downstream from the hole for the fan-shaped film, while for the cylindrical film the improvement of heat flux due to the jet edge mixing happens only from the far field. The location of the peak magnitude for the cylindrical film is at around $y/\delta_{99} = 0.7 - 0.8$ with the defect scaling. It means that the jet layer thickness is higher in the cylindrical film than that in the fan-shaped film.

In addition to the peak present on the edge of the jet, the streamwise component of the heat flux in the cylindrical film presents another peak in the proximity of the wall when the jet just comes out from the hole at $x/D = 2$. Between the two peaks, there is a local minimum with a negative value of flux at around $y/\delta_{99} = 0.35$ where the lower side of the jet appears. The region below $y/\delta_{99} = 0.35$ corresponds to the limited region (or confined region) which is described in the above Section. This can be identified in the high temperate-variance area on the slice of $x/D = 2$ in Fig. 11. This region spans from above the wall to below the lower side of the potential core which locates at around $y/\delta_{99} = 0.5$ where the turbulent heat flux is zero.

The dynamics of the heat flux properties can be assessed by studying the budgets in terms of the streamwise component $\widetilde{u''T''}$ and the wall-normal component $\widetilde{v''T''}$. Fig. 18 (row 2-4, left column) shows the budget terms in the transport equation of the streamwise turbulent heat flux for the fan-shaped film at $M = 1.0$. At $x/D = 2$, through most of the thickness of the wall jet, the main gain in the budgets of $\widetilde{u''T''}$ is the production due to the mean velocity and mean temperature $PT1$. The main loss is pressure scrambling PHI. The peak of these two terms is located at around $y/\delta_{99} = 0.5$, which corresponds to the edge of the jet. The next term in order of magnitude is turbulent viscous-thermal transport contribution DT. This term is responsible

for transporting the $\widetilde{u''T''}$ flux from the edge of the jet ($y/\delta_{99} = 0.5$) to above (approximately $y/\delta_{99} = 0.8$) and towards the wall. The convection acts as the gain at the edge of the jet and the loss above the edge of the jet. These budget terms represent net gain and loss for control volumes drawn around a narrow strip near the center plane. The net loss due to convection beyond the edge of the jet (y/δ_{99}) takes place because the streamwise convective flux of $\widetilde{u''T''}$ grows in the streamwise direction and there is no contribution from the wall-normal velocity V. The net gain due to convection happens around the edge of the jet ($y/\delta_{99} = 0.5$), as high values of $\widetilde{u''T''}$ are convected downwards by the fact that V is negative throughout the entire thickness of the jet. At $x/D = 5$, most budget terms maintain the same shape each with its magnitude slightly reduced. The relative size of each term is also maintained. When the flow comes to $x/D = 10$, most of the budget terms maintain the same shape except for the region in proximity to the wall. In the near-wall region, the balancing of $\widetilde{u''T''}$ budget terms starts to present the pattern of a turbulent boundary layer: the turbulent viscous-thermal transport contribution *eps* is a loss and quickly decays towards the wall while the production due to the mean velocity and mean temperature $PT1$ grows to be the major gain throughout the thickness of the jet layer; they are balanced by the pressure scrambling as the loss. Throughout the inner layer considered in this study, production due to the fluctuating strain rate $PT2$ is negligible.

Fig. 18 (row 2-4, right column) shows the budget terms in the transport equation of the streamwise turbulent heat flux for the cylindrical film at $M = 1.0$. At $x/D = 2$, the budget terms of $\widetilde{u''T''}$ in the jet region between $y/\delta_{99} = 0.5$ and $y/\delta_{99} = 1.2$ of the cylindrical film present similar shapes of corresponding budget terms for the fan-shaped film throughout the whole jet layer thickness of the fan-shaped case. The magnitudes of this part of budget terms for the cylindrical film are around 20% of those for the fan-shaped film. This means that the structure of $\widetilde{u''T''}$ budget terms above the center of the potential core in the cylindrical film

corresponds to the structure of $\widetilde{u''T''}$ budget terms above the wall in the fan-shaped film. For the cylindrical film, between $y/\delta_{99} = 0.1$ and $y/\delta_{99} = 0.5$, the main budget terms reverse sign compared to those in the region above the potential core. The production $PT1$ of $\widetilde{u''T''}$ becomes negative and acts as the loss, which is balanced by the two most prominent gain terms: pressure scrambling PHI and turbulent viscous-thermal transport contribution DT. The patterns of budget terms below the center of potential core between $y/\delta_{99} = 0.1$ and $y/\delta_{99} = 0.5$ can be treated as a mirror image of the patterns of corresponding budget terms above the center of potential core. The center of the potential core behaves as a mirror letting the turbulent heat flux on the upper side and on the lower side be symmetric. Between the wall and $y/\delta_{99} = 0.1$ of the cylindrical film, turbulent viscous-thermal transport contribution DT is the main gain in $\widetilde{u''T''}$, and the pressure scrambling PHI is the main loss. The pair of dissipation *eps* and convection *con* show extremes of opposite sign: the convection *con* acting as the gain and the turbulent viscous-thermal transport contribution DT acting as the loss in the upper part of this region convert their roles when going towards the wall. The complexity in this region is because turbulent heat flux is confined in the streamwise and wall-normal directions in this limited region, as discussed in the section above. When it comes to $x/D = 5$, those peaks in the proximity of the wall shrink, and the structure originating from the flow mechanisms in the confined region at $x/D = 2$ disappears. On the contrary, the region shown above the potential core at $x/D = 2$ is here expanding towards the wall, with generally similar shapes of source terms and sink terms, and magnitudes of their peaks reduced to around half. This happens because at $x/D = 5$, the confined region has already disappeared. At $x/D = 10$, the general shapes of budget terms of $\widetilde{u''T''}$ throughout the studied jet layer thickness except in the near-wall region retain. Production due to the mean velocity and mean temperature $PT1$ is still the major gain. The sink terms are the pressure scrambling PHI and

the turbulent viscous-thermal transport contribution DT with its magnitude increased from upstream to equally large as the magnitude of the pressure scrambling PHI at this position. The increase in the turbulent viscous-thermal transport contribution DT means the diffusion of turbulence from the upper side of the jet to around is more prominent at downstream positions. The influence of the near-wall budget peak becomes minor in terms of both the magnitude and the coverage in the wall-normal direction. This is because the jet and near-wall turbulent boundary layer become detached as the jet goes downstream at this blowing ratio.

In Fig. 19 (top row), the variations of the wall-normal component of the heat flux correlations across the jet layer downstream from the cooling hole are shown in the defect scaling. The vertical component of heat flux correlations in the fan-shaped film acts as the sink throughout the positions downstream from the hole. The peak magnitude is located at the upper side of the jets, which is similar to the pattern shown for the streamwise component of heat flux correlations at corresponding streamwise positions. The increase in the magnitude of the vertical component is uniformly distributed along the streamwise positions. For the cylindrical case, the peak located at the upper side of the jet (at around $y/\delta_{99} = 0.7 - 0.8$ with the defect scaling) maintains magnitude as the same from $x/D = 2$ to $x/D = 5$ but grows its magnitude to a most prominent extreme from $x/D = 5$ to $x/D = 10$. Apart from the peak at the upper side of the jet, a peak of the source at the lower side of the jet appears at around $y/\delta_{99} = 0.35$ when $x/D = 2$. This corresponds to the lower side of the jet. There is a local minimum between $y/\delta_{99} = 0.0$ and $y/\delta_{99} = 0.2$. This corresponds to the confined region. The mechanism behind this peak and the local minimum have been described in detail, see Section 4.1.1. The potential core can be identified at $y/\delta_{99} = 0.5$ where the turbulent heat flux is shown as zero. The sign of the flux curve indicates that below the potential core heat is transferred upwards, while above the potential core the heat is transferred downwards. This

can be explained as the potential core being the cold jet, and the confined region further lower than that holding the hot air entrained. Downstream from $x/D = 2$, the local minimum around $y/\delta_{99} = 0.1$ disappears because the confined region disappears. The heat in the upper side of the jet is also transferred to the jet below.

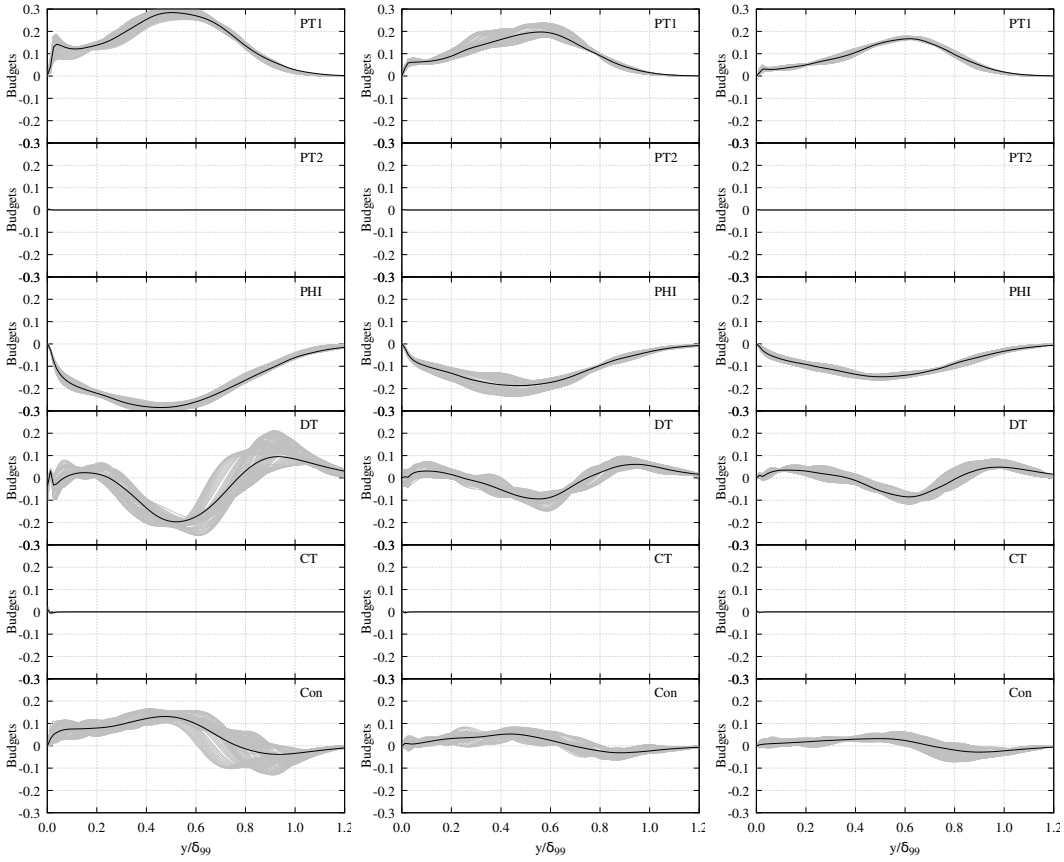
Fig. 19 (row 2-4, left column) shows the budget terms in the transport equation of wall-normal turbulent heat flux $\widetilde{v''T''}$ for the fan-shaped film at $M = 1.0$. At $x/D = 2$, the peak magnitudes of the overall budget terms are located at the extremes of the turbulent viscous-thermal transport contribution DT. At the edge of the jet ($y/\delta_{99} = 0.5$), the gain in the budgets of $\widetilde{v''T''}$ is the turbulent viscous-thermal transport contribution DT, which is balanced by the peak of production due to the mean velocity and mean temperature $PT1$, acting as the loss. In the near-wall region, the gain is the pressure scrambling PHI, balancing the negative extreme of the turbulent viscous-thermal transport contribution DT as well as production due to the mean velocity and mean temperature $PT1$ with a smaller and decreasing magnitude when going towards the wall. At $y/\delta_{99} = 0.9$, the turbulent viscous-thermal transport contribution DT behaves as the loss in $\widetilde{v''T''}$, where the pressure scrambling is the gain. An imbalance appears here due to a non-zero time gradient, which happens possibly because of the large gradient of production due to the mean velocity and the mean temperature $PT1$. When it goes downstream, the general shape of corresponding budget terms maintains the same. Compared with the patterns at $x/D = 2$, the pressure scrambling PHI grows to a more averaged distribution with the highest magnitudes of gain at below $y/\delta_{99} = 0.9$ and around $y/\delta_{99} = 0.1$, respectively, when it arrives $x/D = 10$. Also at $x/D = 10$, the production due to the mean velocity and mean temperature $PT1$ grows to a more averaged distribution, acting as the major loss from the wall to just over $y/\delta_{99} = 0.8$. From $y/\delta_{99} = 0.85$ to above, the turbulent viscous-thermal transport contribution DT becomes the major loss in $\widetilde{v''T''}$. Throughout the near-wall

region and the jet region studied in this section, production due to the fluctuating strain rate $PT2$ downstream from the hole is negligible.

Fig. 19 (row 2-4, right column) shows the budget terms in the transport equation of the wall-normal turbulent heat flux $\widetilde{v''T''}$ for the cylindrical film at $M = 1.0$. At $x/D = 2$, the budget terms of $\widetilde{v''T''}$ in the jet region between $y/\delta_{99} = 0.5$ and $y/\delta_{99} = 1.2$ of the cylindrical film is similar with the structure of budget balancing in the whole jet layer of the fan-shaped film, except that the convection term becomes the gain for the cylindrical film. A lower level of magnitude is shown in this region for the cylindrical film. This means that the properties of $\widetilde{v''T''}$ budget terms above the center of the potential core in the cylindrical film correspond to the properties of $\widetilde{v''T''}$ budget terms above the wall in the fan-shaped film. There are two other groups of budget peaks. One is just below the center of the potential core, which is between $y/\delta_{99} = 0.1$ and $y/\delta_{99} = 0.5$, where production due to the mean velocity and mean temperature $PT1$ is the gain and pressure scrambling PHI is the loss. This region corresponds to the lower side of the jet. The other group of high magnitude is in the proximity to the wall, with the production due to the mean velocity and mean temperature $PT1$ and unresolved dissipation acting as the gain, while pressure scrambling PHI and turbulent viscous-thermal transport contribution DT acting as the loss. The bottom of magnitude between these two groups of peak magnitude corresponds to the confined region, where the production of turbulent heat flux is low. When it goes downstream to $x/D = 5$, the pattern of both the two groups of high magnitude and the bottom shrinks to none as the confined region disappears. At $x/D = 10$, the pressure scrambling PHI becomes the major gain throughout the jet layer thickness, while production due to the mean velocity and mean temperature $PT1$ becomes the major loss throughout this region. Turbulent viscous-thermal dissipation takes the highest peak at

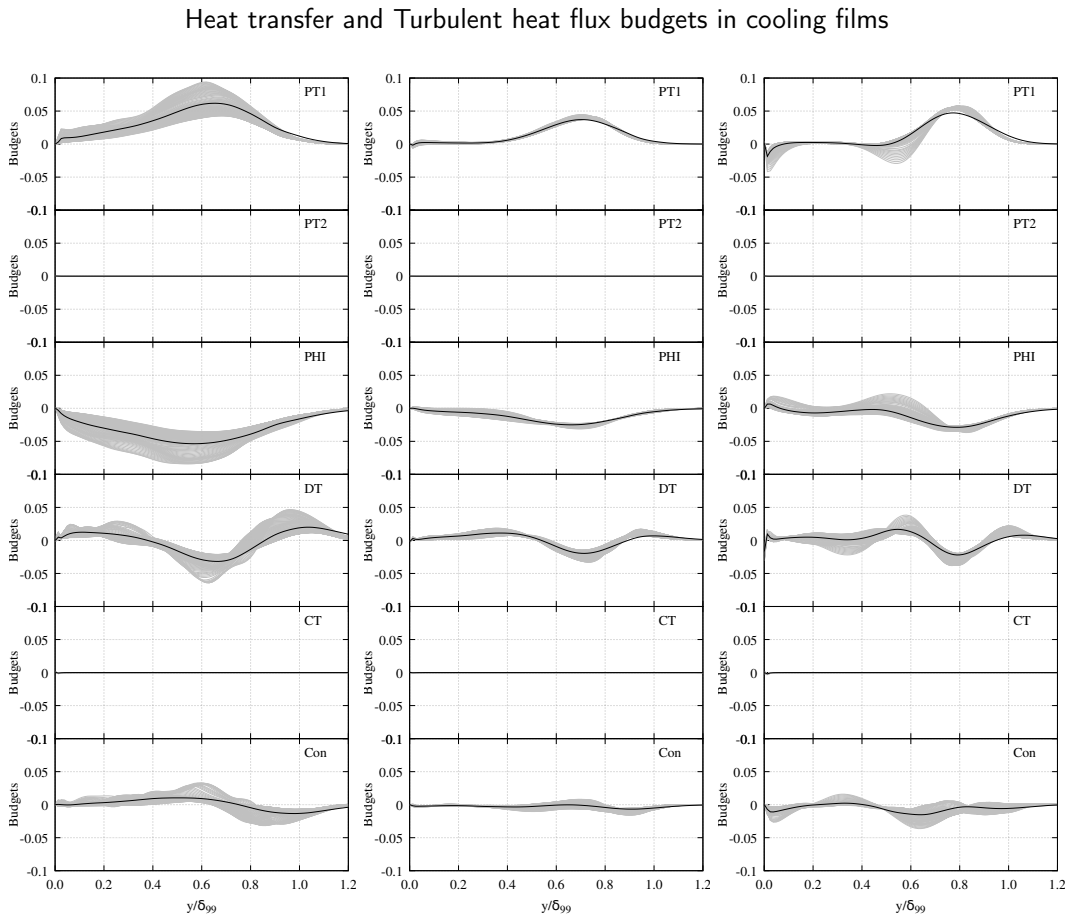
$y/\delta_{99} = 0.7$ as the gain in $\widetilde{v''T''}$, as well as the sink at $y/\delta_{99} = 0.3$ and $y/\delta_{99} = 1.0$ as the loss. This happens because the heat is transferred from the side of the jet to around.

4.3. Universal scaling



(a) $M = 0.5$ (b) $M = 1.0$ (c) $M = 1.5$

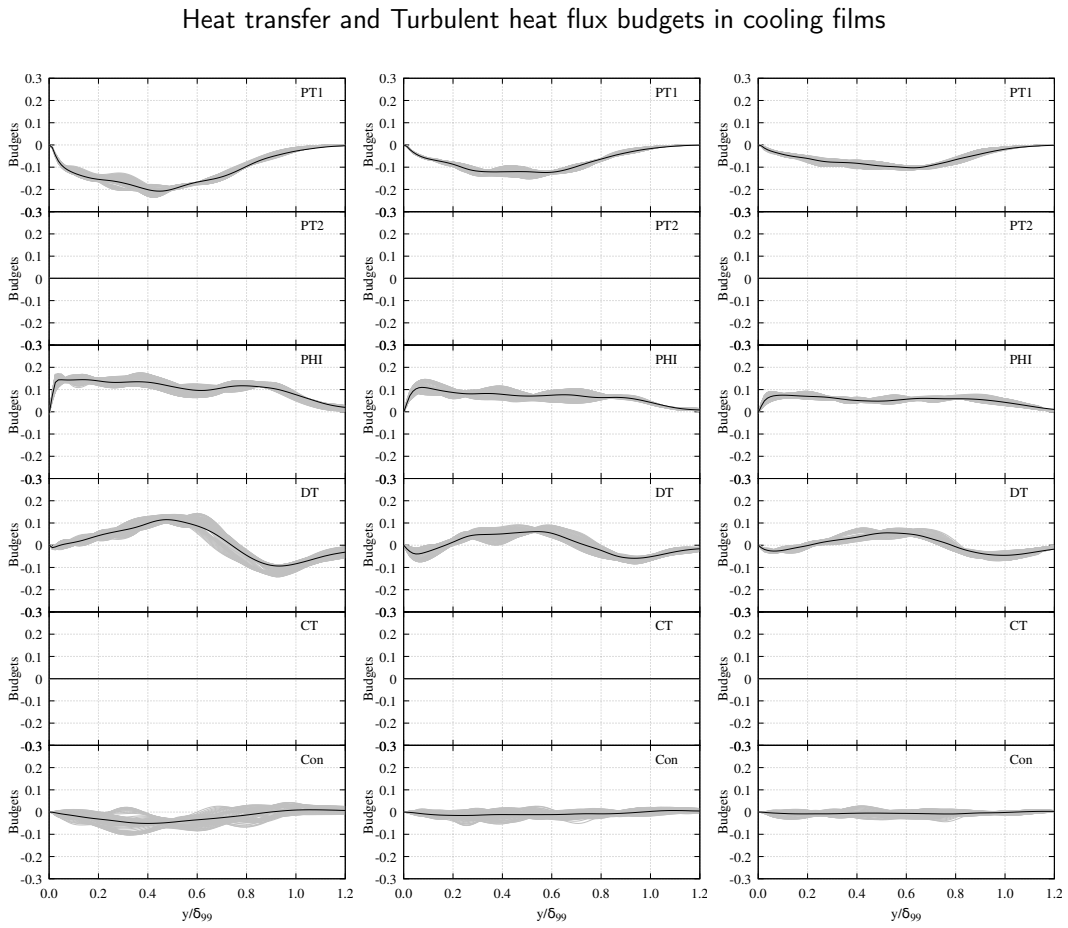
Figure 20: Budget terms of $\widetilde{u''T''}$ scaled by $(\bar{\rho}\Delta U^2 \Delta T (x/D)^{-\beta}/\delta_{99}$ for fan-shaped film at three blowing ratios. Grey lines: multiple curves on streamwise positions between $x/D = 5$ and $x/D = 16$, Black lines: Master curve (Average of multiple grey curves). Three columns from left to right are budgets of $M = 0.5$, $M = 1.0$, $M = 1.5$. For each column from the top to bottom are corresponding production due to the mean velocity and mean temperature $PT1$, Production due to the fluctuating strain rate $PT2$, Pressure-scrambling PHI, Turbulent viscous-thermal transport contribution DT, compressibility associated terms CT, and convection Con.



(a) $M = 0.5$ (b) $M = 1.0$ (c) $M = 1.5$

Figure 21: Budget terms of $\widetilde{u''T''}$ scaled by $(\bar{\rho}\Delta U^2 \Delta T(x/D)^{-\beta}/\delta_{99}$ for cylindrical film at three blowing ratios. Grey lines: multiple curves on streamwise positions between $x/D = 5$ and $x/D = 15$, Black lines: Master curve (Average of multiple grey curves). Three columns from left to right are budgets of $M = 0.5$, $M = 1.0$, $M = 1.5$. For each column from the top to bottom are corresponding production due to the mean velocity and mean temperature $PT1$, Production due to the fluctuating strain rate $PT2$, Pressure-scrambling PHI, Turbulent viscous-thermal transport contribution DT, compressibility associated terms CT, and convection Con.

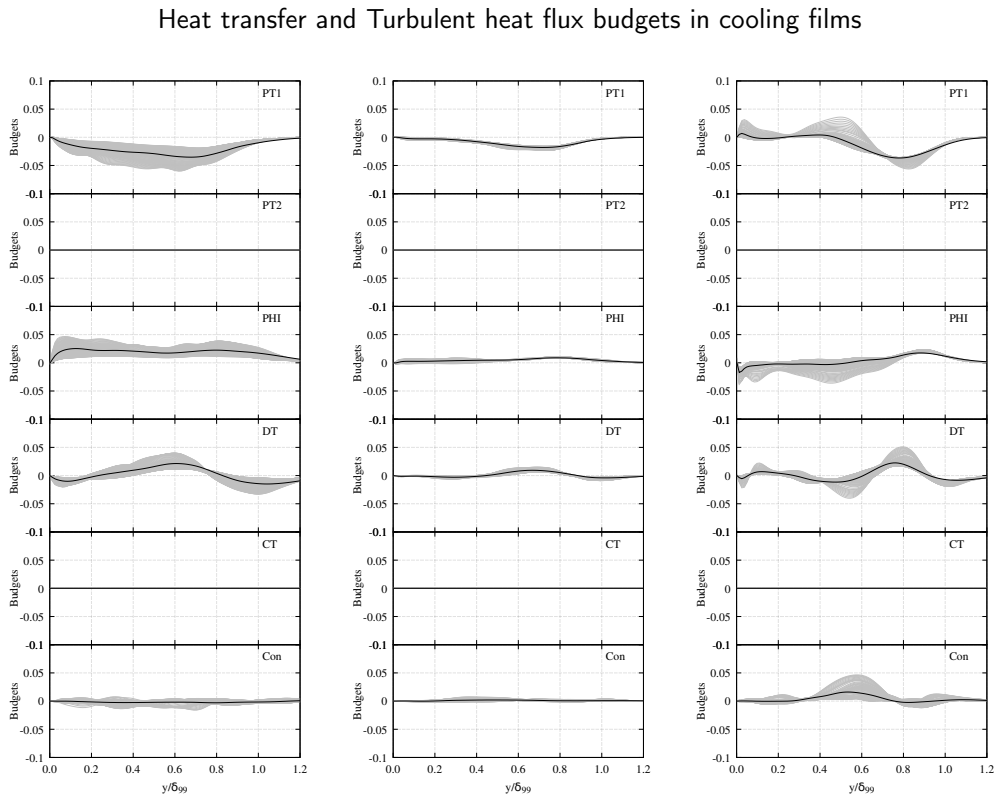
The self-similarity properties that emerge in the wall-normal profiles, streamwise profiles of mean quantities, Reynolds stresses and the budgets of Reynolds stresses have been pointed out in Hao and di Mare (2022), Hao and di Mare (2023a). These self-similarity properties cause graphs of quantities such as mean velocities or turbulence intensities taken at different



(a) $M = 0.5$ (b) $M = 1.0$ (c) $M = 1.5$

Figure 22: Budget terms of $\widetilde{v''T''}$ scaled by $(\bar{\rho}\Delta U^2 \Delta T (x/D)^{-\beta}/\delta_{99}$ for fan-shaped film at three blowing ratios. Grey lines: multiple curves on streamwise positions between $x/D = 5$ and $x/D = 15$, Black lines: Master curve (Average of multiple grey curves). Three columns from left to right are budgets of $M = 0.5$, $M = 1.0$, $M = 1.5$. For each column from the top to bottom are corresponding production due to the mean velocity and mean temperature $PT1$, Production due to the fluctuating strain rate $PT2$, Pressure-scrambling PHI, Turbulent viscous-thermal transport contribution DT, compressibility associated terms CT, and convection Con.

stream-wise positions to collapse onto each other if they are appropriately rescaled. The scaling quantities used are local quantities including the thickness of the jet layer, the velocity defect and the temperature defect picked up at a reasonably defined location across the layer. When the film presents an attached flow, these quantities are located at half of the jet layer thickness;



(a) $M = 0.5$ (b) $M = 1.0$ (c) $M = 1.5$

Figure 23: Budget terms of $\widetilde{v''T''}$ scaled by $(\bar{\rho}\Delta U^2 \Delta T(x/D)^{-\beta}/\delta_{99}$ for cylindrical film at three blowing ratios. Grey lines: multiple curves on streamwise positions between $x/D = 5$ and $x/D = 15$, Black lines: Master curve (Average of multiple grey curves). Three columns from left to right are budgets of $M = 0.5$, $M = 1.0$, $M = 1.5$. For each column from the top to bottom are correspondingly production due to the mean velocity and mean temperature $PT1$, Production due to the fluctuating strain rate $PT2$, Pressure-scrambling PHI, Turbulent viscous-thermal transport contribution DT, compressibility associated terms CT, and convection Con.

the velocity defect at the half-thickness point is adopted as the velocity scale; the temperature defect at the half-thickness point is adopted as the temperature scale. When the film presents a lifted flow, the largest velocity defect and the largest temperature defect in the upper part of the film are adopted. These quantities are the appropriate scales for the outer part of the jet. As for the near-wall region, there are already a few scaling proposed for near-wall flow in similar flow configurations. As an example, the u_τ scaling has been shown to apply close to the wall

Heat transfer and Turbulent heat flux budgets in cooling films

by Gupta, Choudhary, Singh, Prabhakaran and Dixit (2020), while they also proved that the buffer layer between the wall and the jet obeys a modified law of the wall as the establishment of the universal scaling near the wall is disturbed by reattachment, adverse pressure gradient, high turbulent intensities in the upper part of the jet.

This section will apply a more comprehensive external scaling to both the turbulent heat fluxes and their budgets of them, including the effect of the position. With this scaling, the budget terms taken at locations between x/D=5 and x/D=16 are shown to collapse in Fig. 20-23. The budget terms were scaled using the scaling factor $(\bar{\rho}\Delta U^2\Delta T(x/D)^{-\beta}/\delta_{99}$, and turbulent heat fluxes are scaled using the scaling factor $(\bar{\rho}\Delta U\Delta T)$. described in section 4.2. The wall-normal distances away from the wall are scaled by the boundary layer thickness δ_{99}. All quantities are evaluated on the median plane.

In Figures 20-23, it shows that the adopted scaling has the capability of making budget terms in the transport equation of turbulent heat fluxes (both streamwise and wall-normal components) collapse into narrow regions. The master curves are generated by averaging budget terms obtained on a series of streamwise positions in the wall jet far field *at the same nondimensional distance* δ_{99}. The shape of the master curves has been discussed in Sec. 4.2, with the same mechanism indicated. For each film cooling hole type, the shape and the scale of the master curves at different blowing ratios collapse to a single set of data. It also indicates that the amplitude of scaled turbulent heat transfer budget terms on the master curve hardly relies on the blowing ratio, but depends on the non-dimensional streamwise distance away from the cooling hole. In addition, the scaling parameter β is sensitive to the cooling hole type. β is taken as 0.5 for fan-shaped film cases, and as 0.9 for cylindrical film cases. The scaled budget terms are more close to identical shapes for the fan-shaped cases. Large differences are seen between scaled budget terms in cylindrical film cases, especially the wall-normal part, because

the mechanisms of jet flow in the cylindrical cases differ: at $M = 0.5$ the jet is attached, at $M = 1.5$ the jet is lifted off, at $M = 1.0$ the jet is in an intermediate status. It is significant to note that different heat transfers are scattered onto the same characteristics with the same scaling exponent β, even when the mechanisms of the heat transfer are totally different.

5. Conclusion

A detailed study of the structure of turbulent heat fluxes and turbulent heat flux budgets has been presented for fan-shaped and cylindrical cooling films. Three scaling methods are adopted for the general view in the three-dimensional field, the property at specific downstream positions on the centerline, and the self-similarity pattern of the collapsed characteristics along continuous downstream positions, respectively. Following a gradually deeper exploration using a gradually more comprehensive scaling method, a complete defect scaling method useful for turbulent heat flux budgets has been discovered by the end of this paper.

A qualitative study of the heat transfer characteristics is first shown. For the fan-shaped cases, the Favre-averaged temperature, the variance of temperature, and turbulent heat fluxes are concentrated in a weakly curved layer, with a structure that is essentially unchanged as the jet evolves downstream. For the cylindrical film, the blowing ratio controls the structure of the jet as well as the strength of the second motion in the $z - y$ plane. At higher blowing ratios, a potential core and a confined region become visible. A qualitative summary of the structure of the film in terms of jet edge, potential core, the lower edge of the jet, and confined region is proposed. The four regions are classified based on their positions and the relative magnitudes of the mean temperature, turbulent heat fluxes, and temperature variance in each region are highlighted. The potential core is characterized by low levels of temperature variance $\widetilde{T''T''}$. The confined region is characterized by low levels of wall-normal component of the turbulent heat flux $\widetilde{v''T''}$.

Heat transfer and Turbulent heat flux budgets in cooling films

A detailed examination of the turbulent heat flux budgets is then offered. It is shown that the structure of fan-shaped films stays as two layers and the budget of the $\widetilde{u''T''}$ turbulent heat fluxes is dominated by production due to mean velocity and temperature, and pressure scrambling in the jet edge. The budget of the $\widetilde{v''T''}$ is dominated by turbulent viscous-thermal transport contribution and production due to mean velocity and temperature. The production due to fluctuating strain is negligible in both geometries and at all positions examined. In cylindrical films at moderate blowing ratios, the presence of a potential core and confined region is reflected in the budgets a short distance downstream of the injection location by the apparent subdivision of the budget term profiles into a region identical to the fan shape case, and a region - closer to the wall - with essentially mirrored characteristics.

Furthermore, the self-similarity pattern has been discussed for the turbulent heat flux budgets using the final version of the scaling method. In principle, the magnitude of the budget terms varies as the film jet evolves downstream. A modified scaling law obtained from Hao and di Mare (2023b) is applied to the budgets of the turbulent heat fluxes, with the effect of position included as an exponential component. It is shown that the scaling law makes the magnitude of the budget terms invariant with the downstream position and highlights the universality of the shape of the budget term profiles. The existence of universal shapes for the budget terms highlights properties of self-similarity that have so far escaped clarification. Such properties indicate that the numerical prediction of the turbulent heat fluxes in film cooling flows and a large distance downstream of the films is not exceedingly problematic and that all inaccuracies are accrued in the early history of the film. Evidence for this observation is plentiful in literature (see e.g. Jiang, Murray, di Mare and Ireland (2022)).

Future work will focus on approximate theories for the evolution of the jet immediately downstream of the film.

Heat transfer and Turbulent heat flux budgets in cooling films

Nomenclature

Symbols

$< T''T'' >$ Favre-averaged temperature variance scaled by the temperature deficit, $< T''T'' >= \widetilde{T''T''}/\Delta T \Delta T$

$< T >$ Favre-averaged temperature scaled by the temperature deficit, $< T >= \widetilde{T}/\Delta T$

$< u''T'' >$ Favre-averaged streamwise turbulent heat flux scaled by the temperature deficit and velocity defect, $< u''T'' >= \widetilde{u''T''}/\Delta U \Delta T$

$< v''T'' >$ Favre-averaged wall-normal turbulent heat flux scaled by the temperature deficit and velocity defect, $< v''T'' >= \widetilde{v''T''}/\Delta U \Delta T$

β Exponent factor

δ_{ij} Kronecker delta

ϵ turbulent viscous-thermal dissipation

Φ_{Ti} Pressure-scrambling

$\widetilde{T''T''}$ Temperature variance

C_{Ti} compressibility associated terms

D_{Ti} turbulent viscous-thermal transport contribution

E Total energy

k_T Heat conduction coefficient

M_δ Mach number in the scaling form

Heat transfer and Turbulent heat flux budgets in cooling films

p	Pressure
Pr_δ	Prandtl number in the scaling form
q_i	Heat flux
Re_δ	Reynolds number in the scaling form
S_{kl}	Strain-rate tensor
T''	Turbulent temperature fluctuation
t	Time
$\bar{u}_c^+$	A van Driest transformation
ΔU	Streamwise velocity defect at $\delta_{99}/2$
δ_{99}	Boundary layer thickness, 99% far-field velocity point
δ_{v^*}	a semi-local viscous length
μ	viscosity
ρ'	Density fluctuation
ρ	Density
ρ_w	Near-wall density
σ_{ij}	Viscous stress tensor
$\sigma_{ij}^{(sgs)}$	Viscous stress tensor in the sub-grid scale
τ_w	wall shear stress

Heat transfer and Turbulent heat flux budgets in cooling films

$\widetilde{T}$ Favre-averaged temperature

$\widetilde{u''T''}$ Turbulent heat flux in the streamwise direction

$\widetilde{u}^{+}_{MI}$ a Mach-invariant scaling

$\widetilde{v''T''}$ Turbulent heat flux in the wall-normal direction

D Cooling hole diameter

f_{sgs} The budget term of sub-grid scale effect in the transport equation of turbulent heat flux

M Blowing ratio

Ma Mach number

P^1_{Ti} Production due to the mean velocity and mean temperature

P^2_{Ti} Production due to the fluctuating strain rate

q_T Turbulent heat flux vector

$q_T^{(sgs)}$ Turbulent heat flux vectorin the sub-grid scale

T'' Temperature fluctuation

T Temperature

T_w Wall temperature

T^+_{vd} The temperature transformation

u'' Velocity fluctuation in the streamwise direction

U	Mean velocity in the streamwise direction
u_τ	friction velocity
v''	Velocity fluctuation in the wall-normal direction
V	Mean velocity in the wall-normal direction
w''	Velocity fluctuation in the spanwise direction
W	Mean velocity in the spanwise direction
x	Streamwise distance from the center of the film-cooling hole
y	Coordinate in the Wall-normal direction
y^*	a wall-normal non-dimensional definition
y^+	Dimensionless wall distance
y_c^+	an integral length
z	Coordinate in the spanwise direction

Abbreviations

Con	Convection term
CT	Compressibility associated terms
DT	turbulent viscous-thermal transport contribution
eps	turbulent viscous-thermal dissipation
PHI	Pressure-scrambling

LES Large eddy simulation

$PT1$ Production due to the mean velocity and mean temperature

$PT2$ Production due to the fluctuating strain rate

Acknowledgments

Rolls-Royce plc is gratefully acknowledged for supporting this work and for granting permission for its publication. The authors sincerely thank Romero Eduardo, Frederic Goenaga, and Cristian Orozco Pineiro in Rolls-Royce plc for helpful discussion. The authors also acknowledge the use of the University of Oxford Advanced Research Computing (ARC) facility in carrying out this work. http://dx.doi.org/10.5281/zenodo.22558. Part of this work was also performed using resources provided by the Cambridge Service for Data Driven Discovery (CSD4) operated by the University of Cambridge Research Computing Service (www.csd3.cam.ac.uk), provided by Dell EMC and Intel using Tier-2 funding from the Engineering and Physical Sciences Research Council (capital grant EP/T022159/1), and DiRAC funding from the Science and Technology Facilities Council (www.dirac.ac.uk).

References

Bowersox, R.D.W., 2009. Extension of equilibrium turbulent heat flux models to high-speed shear flows. Journal of Fluid Mechanics 633, 61–70. URL: https://doi.org/10.1017/s0022112009007691, doi:10.1017/s0022112009007691.

Brun, C., Boiarciuc, M.P., Haberkorn, M., Comte, P., 2008. Large eddy simulation of compressible channel flow. Theoretical and Computational Fluid Dynamics 22, 189–212. URL: https://doi.org/10.1007/s00162-007-0073-y, doi:10.1007/s00162-007-0073-y.

Duan, L., Martín, M.P., 2011. Direct numerical simulation of hypersonic turbulent boundary layers. part 4. effect of high enthalpy. Journal of Fluid Mechanics 684, 25–59. URL: https://doi.org/10.1017/jfm.2011.252, doi:10.1017/jfm.2011.252.

Ellis, C.D., 2020. Turbulent closure analysis in heated separated and reattached flow using eddy-resolving data. Physics of Fluids 32, 045115. URL: https://doi.org/10.1063/1.5141750, doi:10.1063/1.5141750.

Flageul, C., Benhamadouche, S., Lamballais, É., Laurence, D., 2015. DNS of turbulent channel flow with conjugate heat transfer: Effect of thermal boundary conditions on the second moments and budgets. International Journal of Heat and Fluid Flow 55, 34–44. URL: https://doi.org/10.1016/j.ijheatfluidflow.2015.07.009, doi:10.1016/j.ijheatfluidflow.2015.07.009.

Foysi, H., SARKAR, S., FRIEDRICH, R., 2004. Compressibility effects and turbulence scalings in supersonic channel flow. Journal of Fluid Mechanics 509, 207–216. URL: https://doi.org/10.1017/s0022112004009371, doi:10.1017/s0022112004009371.

Gritsch, M., Schulz, A., Wittig, S., 1998. Adiabatic wall effectiveness measurements of film-cooling holes with expanded exits. Journal of Turbomachinery 120, 549–556. URL: https://doi.org/10.1115/1.2841752, doi:10.1115/1.2841752.

Gupta, A., Choudhary, H., Singh, A.K., Prabhakaran, T., Dixit, S.A., 2020. Scaling mean velocity in two-dimensional turbulent wall jets. Journal of Fluid Mechanics 891, A11. doi:10.1017/jfm.2020.132.

Hao, M., Hope-collins, J., di Mare, L., 2022. Generation of turbulent inflow data from realistic approximations of the covariance tensor. Physics of Fluids URL: https://doi.org/10.1063/5.0106664, doi:10.1063/5.0106664.

Hao, M., di Mare, L., 2022. A parametric study of reynolds stresses and turbulent heat fluxes in fan-shaped and cylindrical film cooling holes (under revision). International Journal of Heat and Mass Transfer .

Hao, M., di Mare, L., 2023a. Budgets of reynolds stresses in film cooling with fan-shaped and cylindrical holes. Physics of Fluids URL: https://doi.org/10.1063/5.0140670, doi:10.1063/5.0140670.

Hao, M., di Mare, L., 2023b. Scaling and similarity laws in three-dimensional wall jets. Physics of Fluids URL: https://doi.org/10.1063/5.0140671, doi:10.1063/5.0140671.

Hao, M., Wang, F., Hope-Collins, J., Rife, M.E., di Mare, L., 2020. Template-based hexahedral mesh generation for turbine cooling geometries, in: Volume 2C: Turbomachinery, American Society of Mechanical Engineers. URL: https://doi.org/10.1115/gt2020-14660, doi:10.1115/gt2020-14660.

Huang, J., Nicholson, G.L., Duan, L., Choudhari, M.M., Bowersox, R.D., 2020. Simulation and modeling of cold-wall hypersonic turbulent boundary layers on flat plate, in: AIAA Scitech 2020 Forum, American Institute of Aeronautics and Astronautics. URL: https://doi.org/10.2514/6.2020-0571, doi:10.2514/6.2020-0571.

Huang, P.G., Coleman, G.N., Bradshaw, P., 1995. Compressible turbulent channel flows: DNS results and modelling. Journal of Fluid Mechanics 305, 185–218. URL: https://doi.org/10.1017/s0022112095004599, doi:10.1017/s0022112095004599.

Jiang, Y., Murray, A., di Mare, L., Ireland, P.T., 2022. Mesh sensitivity of rans simulations on film cooling flow. International Journal of Heat and Mass Transfer .

Kawata, T., Tsukahara, T., 2022. Spectral analysis on transport budgets of turbulent heat fluxes in plane couette turbulence. Energies 15, 5258. URL: https://doi.org/10.3390/en15145258, doi:10.3390/en15145258.

Miura, T., MATSUBARA, K., SAKURAI, A., 2012. Turbulent-heat-flux and temperature-variance budgets in a single-rib mounting channel. Journal of Thermal Science and Technology 7, 120–134. URL: https://doi.org/10.1299/jtst.7.120, doi:10.1299/jtst.7.120.

Morkovin, M.V., 1962. Effects of compressibility on turbulent flows. Mécanique de la Turbulence 367, 26.

Muldoon, F., Acharya, S., 2006. Analysis of k and epsilon budgets for film cooling using direct numerical simulation. AIAA Journal 44, 3010–3021. URL: https://doi.org/10.2514/1.20597, doi:10.2514/1.20597.

8

Conclusions

8.1 | Reviews of Major Findings

The stated objective of this DPhil was to answer the question of "What are the flow patterns, turbulence structures and heat transfer characteristics in cooling films, and how can they be efficiently modelled?" Towards this target, three primary elements have been first implemented: the high resolution numerical scheme, the mesh generator, the inflow generator.

The major findings achieved in their pursuit are listed below:

LES is carried out on an array of film cooling cases at three blowing ratios and two hole types. Reliable Reynolds stresses and heat flux statistics are collected in these cases. A number of interesting qualitative features emerge from the results.

- LES simulations of modest cost can reproduce with high accuracy of the measured discharge characteristics for cylindrical and fan-shaped cooling films. The modest cost benefits from the hex mesh which saves a number of cells under the same level of grid quality, the high-resolution scheme which has a

competitive capability of discontinuity capturing compared with WENO but requires less computing time than WENO, the turbulence inflow generator which requires a shorter length of the development section.

- The jets acquire a layered structure with a developing boundary layer confined between the jet and the wall, and a free shear layer separating the jet from the mainstream, whereas the shear layer is self-similar in all cases studied, the near wall flow is not.

- It is shown that the structure of the wall jets produced by film-cooling devices can be divided into a near field and a far field.

- The near field is dominated by the changes in the structure of the jet as it merges with the main flow.

- The far field is dominated by the gradual mixing of the jet with the surrounding fluid. The far field approaches self-similar behaviour in the mean flow profiles and it is shown that an approximately self-similar behaviour can be achieved in the budget terms as long as an additional scaling factor containing the distance from the origin of the flow is introduced.

- A qualitative structure is proposed for cylindrical films, comprising a jet edge, a potential core, a lower edge and a confined region, with the qualitative criteria given based on the relative magnitude of mean temperatures, turbulent heat fluxes and temperature variance

A theory of scaling law has been proposed and self-similarity of velocity defect, Reynolds stress profiles for the outer part of three-dimensional wall jets are obtained

in the high-Reynolds-number limit. Reynolds stresses and turbulent heat fluxes are compared for different blowing ratios and two types of cooling holes in the parametric study.

- Numerical data indicate that the proposed theory is an accurate representation of the jet produced by a fan-shaped cooling film.

- The wall-normal velocity profiles, velocity defects, and Reynolds stress profiles have shapes essentially independent of the blowing ratio M.

- The jet produced by a fan-shaped film tends towards a self-similar flow profile very rapidly downstream of the injection point. The jet produced by a cylindrical film only approaches self-similar profiles at low blow ratios or at high blow ratios, but not at intermediate blow ratios (~ 1).

- The power laws obtained are shown to apply equally well to cylindrical films, albeit with modified exponents for the stream-wise decay of the velocity defect and growth of the jet layer thickness.

- the velocity defect, wall-normal velocity, and Reynolds stress profiles for the cylindrical film have shape sensitive to the blowing ratio M. It is not possible to identify a power law with respect to M that makes Reynolds stress profiles at various values of M collapse.

- The velocity and temperature defects at the center of the jets are suitable variables to establish similarity laws around the core of the jet.

- Analysis of the Reynolds stress and turbulent heat flux profiles shows that turbulent quantities reach self-similar behavior more slowly than the flow average quantities.

A detailed analysis of the mean velocity, temperature, Reynolds stress, and heat flux reveals that the approach to similarity implied by the proposed scaling law does take place, but at a different rate for different variables and for different film configurations. More precisely:

- The mean velocity and temperature fields produced by a fan-shaped film tend towards a self-similar flow profile very rapidly downstream of the injection point. The mean velocity and temperature fields produced by a cylindrical film only approach self-similar profiles at low blowing ratios or at high blowing ratios, but not at intermediate blowing ratios (~ 1).

- The similarity variables are the local velocity /temperature defect and the jet layer thickness. These similarity relations only apply to the outer part of the jet.

- The jets acquire a layered structure with a developing boundary layer confined between the jet and the wall, and a free shear layer separating the jet from the mainstream.

- The Reynolds stress and turbulent heat flux profiles show that the section of the jet resembling a free shear layer has essentially uniform and fairly isotropic Reynolds stress and has a distinct behavior from the boundary layer growing between the wall and the jet itself.

- For the fan-shaped cases, the Favre-averaged temperature, the variance of temperature, and turbulent heat fluxes are concentrated in a weakly curved layer, with a structure that is essentially unchanged as the jet evolves downstream.

- For the cylindrical film, the blowing ratio controls the structure of the jet as well as the strength of the second motion in the $z-y$ plane. At higher blowing ratios, a potential core and a confined region become visible. A qualitative summary of the structure of the film in terms of jet edge, potential core, the lower edge of the jet, and confined region is proposed. The four regions are classified based on their positions and the relative magnitudes of the mean temperature, turbulent heat fluxes, and temperature variance in each region are highlighted.

  The potential core is characterized by low levels of temperature variance $\widetilde{T''T''}$.

  The confined region is characterized by low levels of wall-normal component of the turbulent heat flux $\widetilde{v''T''}$

The results presented in this thesis allow a detailed analysis of the Reynolds stress and heat flux budgets. This analysis is crucial to advance the understanding of film cooling flows and their modeling for engineering purposes. The main findings can be thus summarized:

- It is shown that in fan-shaped films the general structure of the Reynolds stress budgets is not very different between the near and the far field.

- The opposite is true for cylindrical films, where the near field is dominated by localized regions of high turbulence intensity and turbulent shear stress. These

regions are found immediately downstream of the film and are characterized by high levels of anisotropy, due to the presence of the wall and of the confinement caused by the jet.

- It is also shown that the main source of turbulent kinetic energy in the outer part of the jets issuing from both fan-shaped and cylindrical films is the production term in the $u'u'$ budget. Energy extracted from the mean flow through this term is then fed into the normal Reynolds stresses via pressure redistribution terms.

- In the regions of high anisotropy immediately downstream of cylindrical films, most of the turbulent kinetic energy production takes place through the work done by the normal Reynolds stress $v'v'$ against the spanwise derivative of the mean spanwise velocity W. Energy extracted by this work is then fed to the other normal stresses via pressure redistribution.

- This process is absent in the jet produced by the fan-shaped film, where $\frac{\partial W}{\partial y}$ is small because the system of counter-rotating vortices is less well-defined, and sits much farther apart from the centerline and much closer to the wall.

- The budget of the $\widetilde{u''T''}$ turbulent heat fluxes is dominated by production due to mean velocity and temperature, and pressure scrambling in the jet edge. The budget of the $\widetilde{v''T''}$ is dominated by turbulent Turbulent viscous-thermal transport contribution and production due to mean velocity and temperature. The production due to fluctuating strain is negligible in both geometries and at all positions examined.

- In cylindrical films at moderate blowing ratios, the presence of a potential core and confined region is reflected in the budgets a short distance downstream of the injection location by the apparent subdivision of the budget term profiles into a region identical to the fan shape case, and a region - closer to the wall - with essentially mirrored characteristics.

- It is shown that the scaling law obtained in chapter 6 makes the magnitude of the budget terms invariant with the downstream position and highlights the universality of the shape of the budget term profiles.

8.2 | Future Work

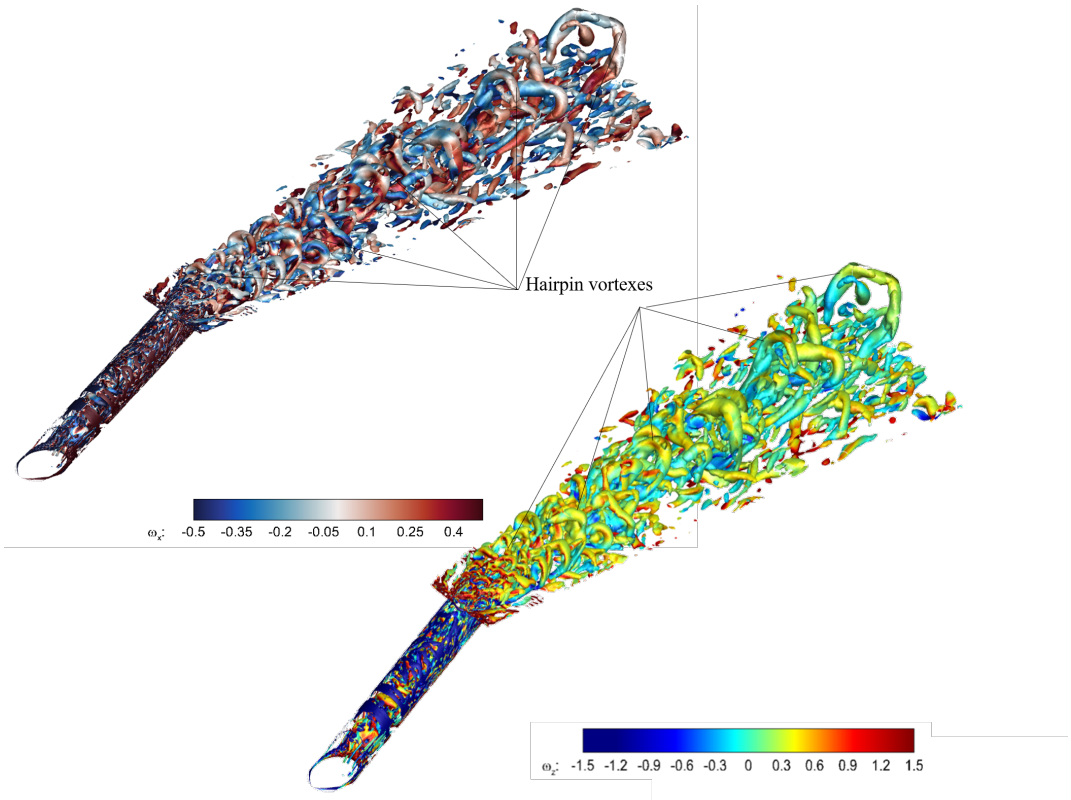
RANS simulations encounter difficulties in producing credible estimates for the film effectiveness in film cooling systems. Inaccuracies are generated in RANS-based simulations because of difficulties in matching measured flow rates for a given pressure drop across the film and because of difficulties in predicting the mixing process once the coolant is ejected from the film. A large number of published results focus on quantities of direct interest to the cooling system designer such as the film cooling effectiveness but overlook detailed distributions of the velocity and the Reynolds stress in the flow above the cooled surface. Velocity fields and Reynolds stress distributions are nonetheless the factors that ultimately determine the film cooling effectiveness by deciding the concentration of coolant near the surface. Development of RANS models feasible on film cooling flows could be expected based on the data of Reynolds stresses, turbulent heat fluxes as well as their budgets.

The LES implementation of this work can be extended onto a turbine with hundreds of cooling holes. The meshing method proposed in this thesis has been shown to apply to a turbine with hundreds of cooling holes. This means an accurate prediction of a whole turbine blade with multiple film cooling holes by LES is possible in the near future.

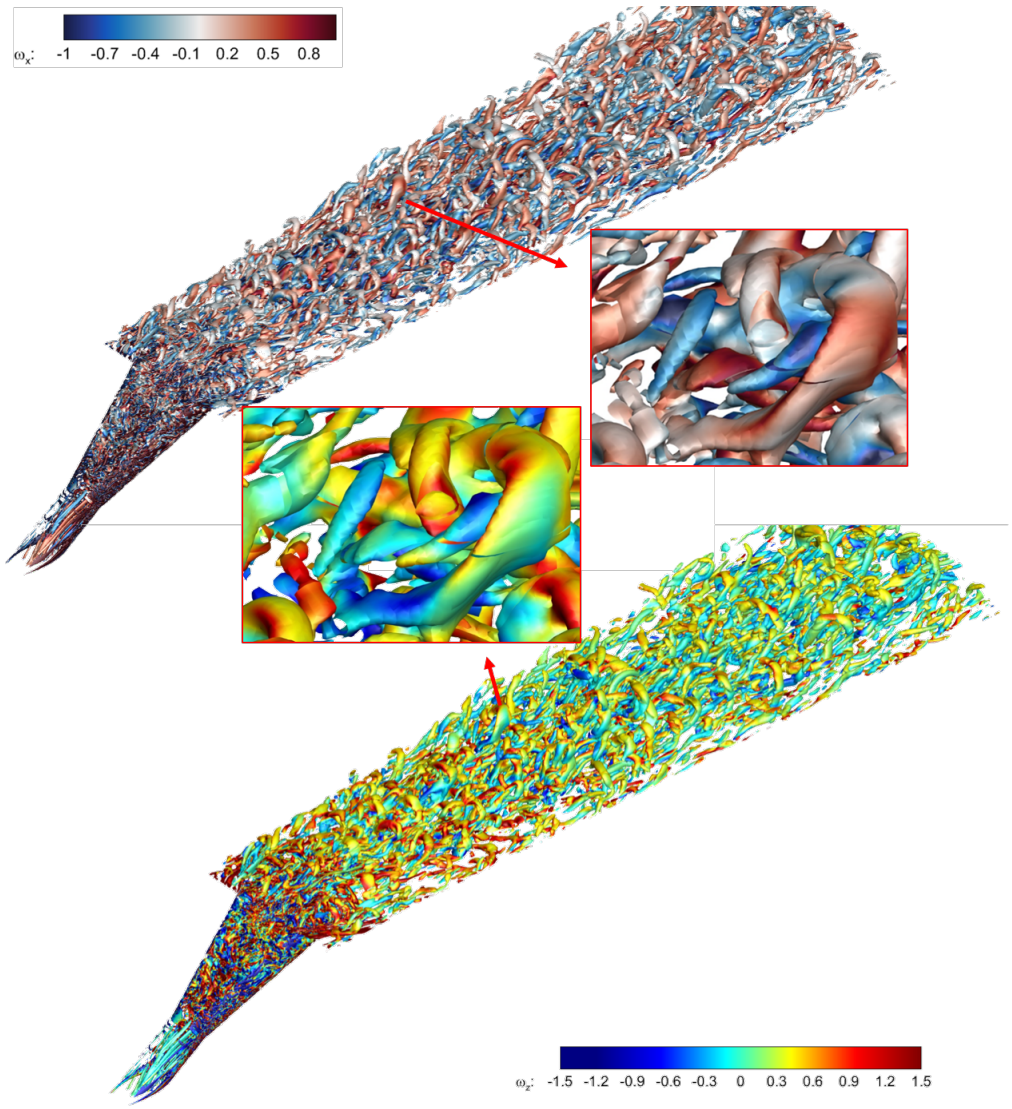
Furthermore, the work has an original chapter proposing the conjugate heat transfer method was unfortunately deleted due to the page limit required from the university department. This method is currently being developed and will be applied to film cooling cases very soon. The budget analysis on a film cooling case with the conjugate wall can be expected.

9

Appendix



(a)Cylindrical hole



(b)Fan-shaped hole

Figure 9.0: Hairpin vortices visualised by the iso-surface of Q-criteria colored by scaled streamwise and spanwise components of vorticity at BR=1.0

References

[1] Gas turbine rotor blade film cooling with and without simulated NGV shock waves and wakes. June 1990.

[2] J. Andreopoulos. Measurements in a jet-pipe flow issuing perpendicularly into a cross stream. *Journal of Fluids Engineering*, 104(4):493–499, December 1982. doi: 10.1115/1.3241892.

[3] Robert Artebrant and H. Joachim Schroll. Limiter-free third order logarithmic reconstruction. *SIAM Journal on Scientific Computing*, 28(1):359–381, January 2006. doi: 10.1137/040620187.

[4] A. Azzi and B. Jubran. Numerical modeling of film cooling from short length streamwise injection holes. *Heat and Mass Transfer*, 39(4):345–353, April 2003. doi: 10.1007/s00231-002-0320-0.

[5] Giovanna Barigozzi, Giuseppe Franchini, and Antonio Perdichizzi. The effect of an upstream ramp on cylindrical and fan-shaped hole film cooling: Part i — aerodynamic results. In *Volume 4: Turbo Expo 2007, Parts A and B*. ASMEDC, January 2007. doi: 10.1115/gt2007-27077. URL `https://doi.org/10.1115/gt2007-27077`.

[6] Giovanna Barigozzi, Giuseppe Franchini, and Antonio Perdichizzi. The effect of an upstream ramp on cylindrical and fan-shaped hole film cooling: Part II — adiabatic effectiveness

results. In *Volume 4: Turbo Expo 2007, Parts A and B*. ASMEDC, January 2007. doi: 10.1115/gt2007-27079. URL https://doi.org/10.1115/gt2007-27079.

[7] G. Bergeles, A. D. Gosman, and B. E. Launder. The turbulent jet in a cross stream at low injection rates: A three-dimensional numerical treatment. *Numerical Heat Transfer, Part B: Fundamentals*, 1(2):217–242, April 1978. doi: 10.1080/10407797809414307.

[8] G. Bergeles, A. D. Gosman, and B. E. Launder. Double-row discrete-hole cooling: an experimental and numerical study. *Journal of Engineering for Power*, 102(2):498–503, April 1980. doi: 10.1115/1.3230284.

[9] Mulugeta K. Berhe and Suhas V. Patankar. Investigation of discrete-hole film cooling parameters using curved-plate models. In *Volume 4: Heat Transfer Electric Power Industrial and Cogeneration*. American Society of Mechanical Engineers, June 1998. doi: 10.1115/98-gt-374. URL https://doi.org/10.1115/98-gt-374.

[10] David G Bogard and K Thole. Gas Turbine Film Cooling. *Journal of Propulsion and Power*, 22(2):249–270, 2006. ISSN 0748-4658. doi: 10.2514/1.18034.

[11] Frederick A. Buck, D. Keith Walters, Jeffrey D. Ferguson, E. Lee McGrath, and James H. Leylek. Film Cooling on a Modern HP Turbine Blade: Part I — Experimental and Computational Methodology and Validation. *Volume 3: Turbo Expo 2002, Parts A and B*, pages 823–833, 2002. doi: 10.1115/GT2002-30470.

[12] Ronald S Bunker. A review of shaped hole turbine film-cooling technology. *J. Heat Transfer*, 127(4):441–453, 2005.

[13] Ronald S. Bunker. Gas turbine cooling: Moving from macro to micro cooling. In *Volume 3C: Heat Transfer*. ASME, jun 2013. doi: 10.1115/gt2013-94277. URL https://doi.org/10.1115/gt2013-94277.

[14] Miroslav Čada and Manuel Torrilhon. Compact third-order limiter functions for finite volume methods. *Journal of Computational Physics*, 228(11):4118–4145, June 2009. doi: 10.1016/j.jcp.2009.02.020.

[15] Lionel Castillon, Gilles Billonnet, Jacques Riou, Stéphanie Péron, and Christophe Benoit. A Technological Effect Modeling on Complex Turbomachinery Applications With an Overset Grid Numerical Method. *Journal of Turbomachinery*, 136(10), 07 2014. ISSN 0889-504X. doi: 10.1115/1.4027997. 101005.

[16] D. Charbonnier, P. Ott, M. Jonsson, F. Cottier, and Th. Ko¨bke. Experimental and numerical study of the thermal performance of a film cooled turbine platform. In *Volume 3: Heat Transfer, Parts A and B*. ASMEDC, January 2009. doi: 10.1115/gt2009-60306. URL `https://doi.org/10.1115/gt2009-60306`.

[17] Hyung Hee Cho and Richard J Goldstein. Effect of hole arrangements on impingement/effusion cooling. In *KSME/JSME THERMAL and FLUID Engineering Conference*, pages 71–76, 1996.

[18] Phillip Colella and Paul R Woodward. The piecewise parabolic method (PPM) for gas-dynamical simulations. *Journal of Computational Physics*, 54(1):174–201, April 1984. doi: 10.1016/0021-9991(84)90143-8.

[19] A. O. Demuren, W. Rodi, and B. Scho¨nung. Systematic study of film cooling with a three-dimensional calculation procedure. *Journal of Turbomachinery*, 108(1):124–130, July 1986. doi: 10.1115/1.3262011.

[20] A.O. Demuren. Numerical calculations of steady three-dimensional turbulent jets in cross flow. *Computer Methods in Applied Mechanics and Engineering*, 37(3):309–328, May 1983. doi: 10.1016/0045-7825(83)90081-6.

[21] Alok Dhungel, Yiping Lu, Wynn Phillips, Srinath V. Ekkad, and James Heidmann. Film cooling from a row of holes supplemented with antivortex holes. *Journal of Turbomachinery*, 131(2), January 2009. doi: 10.1115/1.2950059.

[22] Erik Dick. *Fundamentals of turbomachines*, volume 109. Springer, 2015.

[23] Ahmed F El-Sayed. *Aircraft propulsion and gas turbine engines*. CRC press, 2017.

[24] WJ Feiereisen, E Shirani, JH Ferziger, and WC Reynolds. Direct simulation of homogeneous turbulent shear flows on the illiac iv computer: applications to compressible and incompressible modelling. In *Turbulent Shear Flows 3*, pages 309–319. Springer, 1982.

[25] Wen-Lung Fu, Lesley M. Wright, and Je-Chin Han. Buoyancy effects on heat transfer in five different aspect-ratio rectangular channels with smooth walls and 45-degree ribbed walls. In *Volume 3: Turbo Expo 2005, Parts A and B*. ASMEDC, January 2005. doi: 10.1115/gt2005-68493. URL `https://doi.org/10.1115/gt2005-68493`.

[26] Ian S. Gartshore, Marthe Salcudean, Y. Barnea, K. Zhang, and F. Aghadsi. Some effects of coolant density on film cooling effectiveness. In *Volume 2: Combustion and Fuels Oil and Gas Applications Cycle Innovations Heat Transfer Electric Power Industrial and Cogeneration Ceramics Structures and Dynamics Controls, Diagnostics and Instrumentation IGTI Scholar Award*. American Society of Mechanical Engineers, May 1993. doi: 10.1115/93-gt-076. URL `https://doi.org/10.1115/93-gt-076`.

[27] M. M. Gibson and B. E. Launder. Ground effects on pressure fluctuations in the atmospheric boundary layer. *Journal of Fluid Mechanics*, 86(3):491–511, June 1978. doi: 10.1017/s0022112078001251.

[28] P Glaister. Approximate Riemann Solutions Of The Shallow-Water Equations. *Journal of Hydraulic Research*, Vol.26(No.3):pp.293–306, 1988.

[29] Paul Glassman, Christine Miller, Thom Wozniak, and Clay Jones. A preventive dentistry training program for caretakers of persons with disabilities residing in community residential facilities. *Special Care in Dentistry*, 14(4):137–143, July 1994. doi: 10.1111/j.1754-4505.1994.tb01121.x.

[30] H A R Land M Glaz. NUMERICAL SOLUTION OF THE RIEMANN PROBLEM FOR TWO-DIMENSIONAL GAS DYNAMICS*. 14(6):1394–1414, 1993.

[31] R J Goldstein. Film Cooling. *Advances in Heat Transfer*, pages 321–379, 1971. ISSN 0065-2717. doi: 10.1016/S0065-2717(08)70020-0.

[32] R.J. Goldstein, E.R.G. Eckert, and F. Burggraf. Effects of hole geometry and density on three-dimensional film cooling. *International Journal of Heat and Mass Transfer*, 17(5): 595–607, May 1974. doi: 10.1016/0017-9310(74)90007-6.

[33] AD Gosman. *Heat and mass transfer in recirculating flows*. Academic press, 1969.

[34] Sigal Gottlieb and Chi-Wang Shu. Total variation diminishing runge-kutta schemes. *Mathematics of computation*, 67(221):73–85, 1998.

[35] L. Gräf and L. Kleiser. Large-eddy simulation of double-row compound-angle film cooling: Setup and validation. *Computers & Fluids*, 43(1):58–67, April 2011. doi: 10.1016/j.compfluid.2010.09.032.

[36] Günther Grötzbach. Direct numerical simulation of the turbulent momentum and heat transfer in an internally heated fluid layer. 1982.

[37] X. Guo, W. Schröder, and M. Meinke. Large-eddy simulations of film cooling flows. *Computers & Fluids*, 35(6):587–606, July 2006. doi: 10.1016/j.compfluid.2005.02.007.

[38] BR Haller and JJ Camus. Aerodynamic loss penalty produced by film cooling transonic turbine blades. 1984.

[39] J C Han and A B Mehendale. Flat-Plate Film Cooling With Steam Injection Through One Row and Two Rows of Inclined Holes. *Journal of Turbomachinery*, 108(1):137, 1986. ISSN 0889504X. doi: 10.1115/1.3262013.

[40] J C Han, P R Chandra, and S C Lau. Local Heat/Mass Transfer Distributions Around Sharp 180 deg Turns in Two-Pass Smooth and Rib-Roughened Channels. *Journal of Heat Transfer*, 110(1):91–98, 1988. ISSN 0022-1481. doi: 10.1115/1.3250478.

[41] Je-Chin Han. Fundamental Gas Turbine Heat Transfer. *Journal of Thermal Science and Engineering Applications*, 5(2):21007, 2013. ISSN 1948-5085. doi: 10.1115/1.4023826.

[42] Je-Chin Han, Sandip Dutta, and Srinath Ekkad. *Gas Turbine Heat Transfer and Cooling Technology, Second Edition*, volume 27. 2012. ISBN 1439855684. URL `https://books.google.com/books?id=Ly66eNVjtfEC{&}pgis=1`.

[43] Ami Harten. High resolution schemes for hyperbolic conservation laws. *Journal of Computational Physics*, 49(3):357–393, March 1983. doi: 10.1016/0021-9991(83)90136-5.

[44] B. A. HAVEN and M. KUROSAKA. Kidney and anti-kidney vortices in crossflow jets. *Journal of Fluid Mechanics*, 352:27–64, December 1997. doi: 10.1017/s0022112097007271.

[45] N. Hay, D. Lampard, and S. Benmansour. Effect of crossflows on the discharge coefficient of film cooling holes. *Journal of Engineering for Power*, 105(2):243–248, April 1983. doi: 10.1115/1.3227408.

[46] James D. Heidmann. A numerical study of anti-vortex film cooling designs at high blowing ratio. In *Volume 4: Heat Transfer, Parts A and B*. ASMEDC, January 2008. doi: 10.1115/gt2008-50845. URL `https://doi.org/10.1115/gt2008-50845`.

[47] Hirsch. *Numerical Computation of Internal and External Flows*. Elsevier, 2007. doi: 10.1016/b978-0-7506-6594-0.x5037-1. URL `https://doi.org/10.1016/b978-0-7506-6594-0.x5037-1`.

[48] Asif Hoda and Sumanta Acharya. Predictions of a film coolant jet in crossflow with different turbulence models. *Journal of Turbomachinery*, 122(3):558–569, February 1999. doi: 10.1115/1.1302322.

[49] D. G. Hyams and J. H. Leylek. A detailed analysis of film cooling physics: Part III— streamwise injection with shaped holes. *Journal of Turbomachinery*, 122(1):122–132, February 1997. doi: 10.1115/1.555435.

[50] Daniel G. Hyams, Kevin T. McGovern, and James H. Leylek. Effects of geometry on slot–jet film cooling performance. In *Volume 4: Heat Transfer Electric Power Industrial and Cogeneration*. American Society of Mechanical Engineers, June 1996. doi: 10.1115/96-gt-187. URL `https://doi.org/10.1115/96-gt-187`.

[51] D. Jackson, P. Ireland, and B. Cheong. Combined experimental and CFD study of a HP blade multi-pass cooling system. In *Volume 3: Heat Transfer, Parts A and B*. ASMEDC, January 2009. doi: 10.1115/gt2009-60070. URL `https://doi.org/10.1115/gt2009-60070`.

[52] Steven R. Jankovich, Steven E. Benzley, Jason F. Shepherd, and Scott A. Mitchell. The graft tool: An all-hexahedral transition algorithm for creating a multi-directional swept volume mesh, 1999.

[53] K Kadotani and RJ Goldstein. Effect of mainstream variables on jets issuing from a row of inclined round holes. 1979.

[54] Barry Koren. *A robust upwind discretization method for advection, diffusion and source terms*. Centrum voor Wiskunde en Informatica Amsterdam, 1993.

[55] B. Lad and L. He. Use of an Immersed Mesh for High Resolution Modeling of Film Cooling Flows. *Journal of Turbomachinery*, 135(1), 10 2012. ISSN 0889-504X. doi: 10.1115/1.4006398. 011022.

[56] B. Lad and L. He. An Immersed Mesh Block (IMB) Approach for Conjugate Heat Transfer Predictions. Turbo Expo: Power for Land, Sea, and Air, 06 2013. doi: 10.1115/GT2013-94383. URL `https://doi.org/10.1115/GT2013-94383`. V03BT11A007.

[57] B. Lad, L. He, and E. Romero. Validation of the immersed mesh block (IMB) approach against a cooled transonic turbine stage. In *Volume 4: Heat Transfer, Parts A and B*. American Society of Mechanical Engineers, June 2012. doi: 10.1115/gt2012-68779. URL `https://doi.org/10.1115/gt2012-68779`.

[58] B. Lad, L. He, and E. Romero. Validation of the Immersed Mesh Block (IMB) Approach Against a Cooled Transonic Turbine Stage. Turbo Expo: Power for Land, Sea, and Air, pages 1431–1443, 06 2012. doi: 10.1115/GT2012-68779. URL `https://doi.org/10.1115/GT2012-68779`.

[59] D. Lakehal, G.S. Theodoridis, and W. Rodi. Computation of film cooling of a flat plate by lateral injection from a row of holes. *International Journal of Heat and Fluid Flow*, 19(5): 418–430, October 1998. doi: 10.1016/s0142-727x(98)10022-x.

[60] B.L. Lapworth, M.G. Rose, and R.G.D. Nedar. Calculation of flow and heat transfer near the entrance to film-cooling holes using three-dimensional mesh embedding with solution

adaptation. *International Journal of Heat and Fluid Flow*, 17(2):155 – 166, 1996. ISSN 0142-727X. doi: https://doi.org/10.1016/0142-727X(95)00099-C.

[61] B.E. Launder. Modelling of turbulent flow in gas-turbine blading: achievements and prospects. *International Journal of Heat and Fluid Flow*, 3(4):171–184, December 1982. doi: 10.1016/0142-727x(82)90016-9.

[62] BE Launder, MA Leschziner, and M Sindir. The umist/ucd computations for the afosr-httm-stanford conference on complex turbulent flows. *Mechanical Engineering Department of the University of Manchester Institute of Science and Technology, Rep. No. TFD/82/1*, 1982.

[63] J. H. Leylek and R. D. Zerkle. Discrete-jet film cooling: A comparison of computational results with experiments. In *Volume 3A: General*. American Society of Mechanical Engineers, May 1993. doi: 10.1115/93-gt-207. URL `https://doi.org/10.1115/93-gt-207`.

[64] Xu-dong Liu. SOLUTION OF TWO-DIMENSIONAL RIEMANN PROBLEMS OF GAS DYNAMICS BY POSITIVE SCHEMES. 19(2):319–340, 1998.

[65] Antonio Marquina. Local piecewise hyperbolic reconstruction of numerical fluxes for nonlinear scalar conservation laws. *SIAM Journal on Scientific Computing*, 15(4):892–915, July 1994. doi: 10.1137/0915054.

[66] A.B. Mehendale, S. Ou, and J.C. Han. LEADING EDGE FILM COOLING HEAT TRANSFER INCLUDING THE EFFECT OF MAINSTREAM TURBULENCE. In *Transport Phenomena in Heat and Mass Transfer*, pages 304–315. Elsevier, 1992. doi: 10.1016/b978-0-444-89851-7.50032-7. URL `https://doi.org/10.1016/b978-0-444-89851-7.50032-7`.

[67] D. E. Metzger and M. K. Sahm. Heat transfer around sharp 180-deg turns in smooth rectangular channels. *Journal of Heat Transfer*, 108(3):500, 1986. doi: 10.1115/1.3246961.

[68] W. J. Mick and R. E. Mayle. Stagnation film cooling and heat transfer, including its effect within the hole pattern. *Journal of Turbomachinery*, 110(1):66–72, January 1988. doi: 10.1115/1.3262169.

[69] Frank Muldoon and Sumanta Acharya. Analysis of k and epsilon budgets for film cooling using direct numerical simulation. *AIAA Journal*, 44(12):3010–3021, December 2006. doi: 10.2514/1.20597.

[70] S. Na and T. I.-P. Shih. Increasing adiabatic film-cooling effectiveness by using an upstream ramp. In *Volume 3: Heat Transfer, Parts A and B*. ASMEDC, January 2006. doi: 10.1115/gt2006-91163. URL `https://doi.org/10.1115/gt2006-91163`.

[71] N. V. Nirmalan and L. D. Hylton. An experimental study of turbine vane heat transfer with leading edge and downstream film cooling. *Journal of Turbomachinery*, 112(3):477–487, July 1990. doi: 10.1115/1.2927683.

[72] Todd A. Oliver, David G. Bogard, and Robert D. Moser. Large eddy simulation of compressible, shaped-hole film cooling. *International Journal of Heat and Mass Transfer*, 140:498–517, September 2019. doi: 10.1016/j.ijheatmasstransfer.2019.04.119.

[73] Todd A. Oliver, David G. Bogard, and Robert D. Moser. Large eddy simulation of compressible, shaped-hole film cooling. *International Journal of Heat and Mass Transfer*, 140:498 – 517, 2019. ISSN 0017-9310. doi: https://doi.org/10.1016/j.ijheatmasstransfer.2019.04.119.

[74] S. Ou, A. B. Mehendale, and J. C. Han. Influence of high mainstream turbulence on leading edge film cooling heat transfer: Effect of film hole row location. *Journal of Turbomachinery*, 114(4):716–723, October 1992. doi: 10.1115/1.2928024.

[75] Steven J. Owen, Matthew L. Staten, Scott A. Canann, and Sunil Saigal. Advancing front quadrilateral meshing using triangle transformations, 1998.

[76] S Stephen Papell, Chi-Rong Wang, and Robert W Graham. Film-cooling effectiveness with developing coolant flow through straight and curved tubular passages. Technical report, 1982.

[77] S. V. Patankar, D. K. Basu, and S. A. Alpay. Prediction of the three-dimensional velocity field of a deflected turbulent jet. *Journal of Fluids Engineering*, 99(4):758–762, December 1977. doi: 10.1115/1.3448902.

[78] M. A. Puso and J. Solberg. A stabilized nodally integrated tetrahedral. *International Journal for Numerical Methods in Engineering*, 67(6):841–867, 2006. doi: 10.1002/nme.1651.

[79] J.-F. Remacle, R. Gandham, and T. Warburton. GPU accelerated spectral finite elements on all-hex meshes. *Journal of Computational Physics*, 324:246–257, November 2016. doi: 10.1016/j.jcp.2016.08.005.

[80] P. Renze, W. Schröder, and M. Meinke. Large-eddy simulation of film cooling flows with variable density jets. *Flow, Turbulence and Combustion*, 80(1):119–132, August 2007. doi: 10.1007/s10494-007-9080-8.

[81] W. Rodi and S.K. Srivatsa. A locally elliptic calculation procedure for three-dimensional flows and its application to a jet in a cross-flow. *Computer Methods in Applied Mechanics and Engineering*, 23(1):67–83, July 1980. doi: 10.1016/0045-7825(80)90079-1.

[82] P L Roe. Characteristic-based schemes for the euler equations. *Annual Review of Fluid Mechanics*, 18(1):337–365, January 1986. doi: 10.1146/annurev.fl.18.010186.002005.

[83] Philip L Roe. Some contributions to the modelling of discontinuous flows. *Large-scale computations in fluid mechanics*, pages 163–193, 1985.

[84] PL Roe. *Numerical algorithms for the linear wave equation.* Royal Aircraft Establishment, 1981.

[85] CHRISTIAN SAUMWEBER, ACHMED SCHULZ, SIGMAR WITTIG, and MICHAEL GRITSCH. Effects of entrance crossflow directions to film cooling holes. *Annals of the New*

York Academy of Sciences, 934(1):401–408, January 2006. doi: 10.1111/j.1749-6632.2001.tb05876.x.

[86] D. L. Schmidt, B. Sen, and D. G. Bogard. Film cooling with compound angle holes: Adiabatic effectiveness. *Journal of Turbomachinery*, 118(4):807–813, October 1996. doi: 10.1115/1.2840938.

[87] Chi-Wang Shu and Stanley Osher. Efficient implementation of essentially non-oscillatory shock-capturing schemes. *Journal of Computational Physics*, 77(2):439–471, August 1988.

[88] A. K. Sinha, D. G. Bogard, and M. E. Crawford. Film-cooling effectiveness downstream of a single row of holes with variable density ratio. *Journal of Turbomachinery*, 113(3):442–449, July 1991. doi: 10.1115/1.2927894.

[89] D Spalding and S Patankar. Heat and mass transfer. *Morgan-Grampian, London, England*, pages 15–68, 1967.

[90] A. Suresh and H.T. Huynh. Accurate monotonicity-preserving schemes with runge–kutta time stepping. *Journal of Computational Physics*, 136(1):83–99, September 1997. doi: 10.1006/jcph.1997.5745.

[91] P. K. Sweby. High resolution schemes using flux limiters for hyperbolic conservation laws. *SIAM Journal on Numerical Analysis*, 21(5):995–1011, October 1984. doi: 10.1137/0721062.

[92] Toshihiko Takahashi, Kazunori Watanabe, Tomoharu Fujii, and Terutaka Fujioka. Numerical Analysis of Temperature Distribution of a Film-Cooled and TBC Coated Blade. Turbo Expo: Power for Land, Sea, and Air, pages 691–702, 06 2008. doi: 10.1115/GT2008-50730. URL `https://doi.org/10.1115/GT2008-50730`.

[93] B. Tartinville and Ch. Hirsch. Modelling of Film Cooling for Turbine Blade Design. Turbo Expo: Power for Land, Sea, and Air, pages 2219–2228, 06 2008. doi: 10.1115/GT2008-50316. URL `https://doi.org/10.1115/GT2008-50316`.

[94] M. E. Taslim and A. Khanicheh. Experimental and Numerical Study of Impingement on an Airfoil Leading Edge With and Without Showerhead and Gill Film Holes. *Journal of Turbomachinery*, 128(2):310, 2006. ISSN 0889504X. doi: 10.1115/1.2137742.

[95] J. R. Taylor. Heat Transfer Phenomena in Gas Turbines. *The American Society of Mechanical Engineers*, 80:1–12, 1980.

[96] Joe F Thompson, Zahir U.A Warsi, and C Wayne Mastin. Boundary-fitted coordinate systems for numerical solution of partial differential equations—a review. *Journal of Computational Physics*, 47(1):1–108, jul 1982. doi: 10.1016/0021-9991(82)90066-3.

[97] E.F. Toro. *Riemann solvers and numerical methods for fluid dynamics.* 2009. ISBN 3540659668. doi: 10.1007/978-3-540-49834-6.

[98] ER Turner, MD Wilson, LD Hylton, and RM Kaufman. Turbine vane external heat transfer. volume 1: analytical and experimental evaluation of surface heat transfer distributions with leading edge showerhead film cooling. Technical report, 1985.

[99] Bram van Leer. Towards the ultimate conservative difference scheme. v. a second-order sequel to godunov's method. *Journal of Computational Physics*, 32(1):101–136, July 1979. doi: 10.1016/0021-9991(79)90145-1.

[100] D. K. Walters and J. H. Leylek. A systematic computational methodology applied to a three-dimensional film-cooling flowfield. *Journal of Turbomachinery*, 119(4):777–785, October 1997. doi: 10.1115/1.2841188.

[101] D Keith Walters, James H Leylek, and Frederick A Buck. Film Cooling on a Modern HP Turbine Blade: Part II — Compound-Angle Round Holes. *Volume 3: Turbo Expo 2002, Parts A and B*, pages 1095–1101, 2002. doi: 10.1115/GT2002-30613.

[102] Adrian James White. Film cooling of gas turbine blades. 1983.

[103] S. Wittig, A. Schulz, M. Gritsch, and K. A. Thole. Transonic film-cooling investigations: Effects of hole shapes and orientations. In *Volume 4: Heat Transfer Electric Power*

Industrial and Cogeneration. American Society of Mechanical Engineers, June 1996. doi: 10.1115/96-gt-222. URL https://doi.org/10.1115/96-gt-222.

[104] Paul Woodward and Phillip Colella. The numerical simulation of two-dimensional fluid flow with strong shocks. *Journal of Computational Physics*, 54(1):115–173, 1984. ISSN 10902716. doi: 10.1016/0021-9991(84)90142-6.

[105] Lesley M Wright, Sarah A Blake, Dong-Ho Rhee, and Je-Chin Han. Effect of Upstream Wake With Vortex on Turbine Blade Platform Film Cooling With Simulated Stator-Rotor Purge Flow. *ASME Conference Proceedings*, 2007(47934):125–134, 2007. ISSN 0889504X. doi: 10.1115/GT2007-27092.

[106] Takashi Yamane and Kazuomi Yamamoto. Introduction of combined usage of overset grid method in conjugate heat transfer simulation. In *Volume 3: Heat Transfer, Parts A and B*. ASMEDC, January 2009. doi: 10.1115/gt2009-59832. URL https://doi.org/10.1115/gt2009-59832.

[107] Takashi Yamane and Kazuomi Yamamoto. Introduction of Combined Usage of Overset Grid Method in Conjugate Heat Transfer Simulation. Turbo Expo: Power for Land, Sea, and Air, pages 737–746, 06 2009. doi: 10.1115/GT2009-59832. URL https://doi.org/10.1115/GT2009-59832.

[108] Savas Yavuzkurt and Melaku Habte. Effect of Computational Grid on Performance of Two-Equation Models of Turbulence for Film Cooling Applications. Turbo Expo: Power for Land, Sea, and Air, pages 133–143, 06 2008. doi: 10.1115/GT2008-50153. URL https://doi.org/10.1115/GT2008-50153.

[109] Jörg Ziefle and Leonhard Kleiser. Assessment of a film-cooling flow structure by large-eddy simulation. *Journal of Turbulence*, 9:N29, January 2008. doi: 10.1080/14685240802232855.